From Layered Intrusions to Mid-Ocean Rides: The Petrography and Chemistry of Basaltic Magmas

by

Benjamin W. Wernette

Earth and Ocean Sciences
Duke University

Date: _____
Approved:

_____
Emily Klein, Advisor

_____
Alan Boudreau

_____
Drew Coleman

_____
Avner Vengosh

Dissertation submitted in partial fulfillment of
the requirements for the degree of Doctor
of Philosophy in
Earth and Ocean Sciences in the Graduate School
of Duke University

2020

ABSTRACT

From Layered Intrusions to Mid-Ocean Rides: The Petrography and Chemistry of Basaltic Magmas

by

Benjamin W. Wernette

Earth and Ocean Sciences
Duke University

Date: _____
Approved:

_____
Emily Klein, Advisor

_____
Alan Boudreau

_____
Drew Coleman

_____
Avner Vengosh

An abstract of a dissertation submitted in partial
fulfillment of the requirements for the degree
of Doctor of Philosophy in
Earth and Ocean Sciences in the Graduate School of
Duke University

2020

Copyright by
Benjamin W. Wernette
2020

Abstract

The geochemical evolution of basaltic magmas, in a variety of settings, has been the subject of countless studies. In some instances, basaltic magmas evolve to form economic transition and precious metal ore bodies. The metals extracted from these ore bodies are of critical importance to a wide variety of industries, such as automotive manufacturing. On a larger scale, basaltic magmas evolve to form the oceanic crust, the interface between the Earth's mantle and the oceans. These are just two examples of how basaltic magmas are entwined with life on Earth and together represent the focus of this dissertation.

The second chapter of this dissertation uses detailed petrography to characterize the late-stage evolution of the Eocene Skaergaard Intrusion, Greenland. Significantly, this study identifies textural and chemical evidence that suggests that late hydrothermal fluids modified the Skaergaard transition (copper) and precious metal (silver, gold, platinum) budget.

The third chapter examines the major and trace element concentrations, as well as the $^{87}Sr/^{86}Sr$ ratios, for a suite of basaltic lavas dredged from the Cocos-Nazca Spreading Center, the Dietz Volcanic Ridge, and the East Pacific Rise. Prior to this study, this region of the Pacific basin was sparsely sampled. Notably, this study determines that lavas from the Cocos-Nazca Spreading Center are chemically depleted and are

likely sourced from mantle that differs from that characteristic of normal mid-ocean ridge basalt.

Finally, the fourth chapter examines the size distribution, morphology, and chemical composition of plagioclase in plagioclase phyric lavas from the Cocos-Nazca Spreading Center. A variety of plagioclase morphologies, textures, and chemical compositions are reported. Importantly, this study demonstrates that combining size distribution analysis with textural and compositional information can provide nuanced information about the processes occurring beneath mid-ocean ridges.

Contents

Abstract i

List of Tables vii

List of Figures viii

Acknowledgements xii

1.Introduction 1

2. Sulfides, native metals, and associated trace minerals of the Skaergaard Intrusion, Greenland: Evidence for late hydrothermal fluids 3

2.1 Chapter Summary 3

2.2 Introduction 4

2.3 Geologic Background and Summary of Previous Studies 6

2.4 Sampling and Methods 11

2.5 Results 12

2.5.1 Summary of Stratigraphic Trends 12

2.5.2 General Description of Sulfide Assemblages and Associated Trace Minerals . 14

2.5.3 Occurrence of Precious and Transition Metals 19

2.5.4 Fluid Inclusions 25

2.6 Discussion 26

2.6.1 Sulfides and Associated Minerals 26

2.6.2 Evidence for Volatiles in the Skaergaard Intrusion 29

2.6.3 Precious Metals in an Exsolved Volatile Phase 31

2.6.4 Temperature and Timing 33

2.6.5 Modelling Silver Solubility 35

2.6.6 Evaluating Existing Genetic Models for the Skaergaard Intrusion Metal Budget 41

2.6.7 Genetic Model 43

2.7 Conclusions 44

3. The major element, trace element, and $^{87}Sr/^{86}Sr$ characteristics of basaltic lavas from the Cocos-Nazca Spreading Center 46

3.1 Chapter Summary 46

3.2 Introduction 48

3.3 Geological Background 51

3.4 Sample Description 56

3.5 Methods 57

3.6 Results 60

3.6.1 Major Elements 60

3.6.1.1 Cocos-Nazca Spreading Center 60

3.6.1.2 Dietz Volcanic Ridge 64

3.6.2 Trace Elements 66

3.6.2.1 Cocos-Nazca Spreading Center 66

3.6.2.2 Dietz Volcanic Ridge 68

3.6.3 $^{87}Sr/^{86}Sr$ Isotope Analyses 69

3.7 Discussion 70

3.7.1 Comparing the Cocos-Nazca Spreading Center to the Galapagos Spreading Center 70

3.7.2 The Unusual Chemical Depletion of Cocos-Nazca Lavas 71

3.7.3 Local East Pacific Rise and Incipient Rift Lavas 75

3.7.4 Dietz Volcanic Ridge 77

3.7.5 Comparing Cocos-Nazca Lavas to Other Highly Depleted MORB and the Global Occurrence of Depleted MORB 77

3.7.6 Modeling the Depleted Nature of Cocos-Nazca, Incipient Rift, and local East Pacific Rise Lavas 81

3.7.7 A Tectonic Model for the Local East Pacific Rise and Cocos-Nazca Lavas 86

3.8 Conclusions 91

4. The size distribution, morphology, and chemical composition of plagioclase in plagioclase-bearing lavas from the Cocos-Nazca Spreading Center 93

4.1 Chapter Summary 93

4.2 Introduction 94

4.3 Crystal Size Distribution - Theory 96

4.4 Review of Crustal Processes at Mid-Ocean Ridges and Previous CSD Studies 100

4.5 The Cocos-Nazca Spreading Center and Lava Samples 106

4.6 Petrography 109

4.7 Methods 113

4.7.1 Crystal Size Distribution Calculations for Cocos-Nazca Samples 113

4.7.2 Electron Microprobe Analyses 116

4.8 Results 117

4.8.1 Crystal Size Distribution 117

4.8.2 Plagioclase Compositional Zoning 119

4.9 Discussion 122

4.9.1 Cocos-Galapagos and Cocos-Nazca 122

4.9.2 Conceptual Model for the Cocos-Galapagos and Cocos-Nazca Plagioclase-Bearing Lavas 123

4.9.3 Plagioclase Ultraphyric Lavas 129

4.10 Conclusions 132

5. Conclusions 133

Appendix A: Supplementary Material for Chapter 1 134

Appendix B: Supplementary Material for Chapter 2 156

Appendix C: Supplementary Material for Chapter 3 178

References 184

List of Tables

Table 1: Summary of sulfide assemblages. 15

Table 2: Area and perimeter measurements (microns) for native metals. 16

Table 3: Compilation of representative studies examining plagioclase phenocrysts in MORB. 102

Table 4: Crystal size distribution (CSD) data collected for samples from the Cocos-Galapagos (C-G) and Cocos-Nazca (C-N) spreading domains. 115

Table 5 (pages 141-161): Sulfide assemblages and associated minerals. 135

Table 6: Comparison of recommended certificate Zr concentrations (ppm) and concentrations calculated by method of additions for two basalt standards. 159

Table 7: Comparison of HFSE data collected during Fall 2018 and Fall 2019. 162

Table 8: Major element, trace element, and $^{87}Sr/^{86}Sr$ for basaltic glass and whole rock samples from the Cocos-Nazca Spreading Center, Dietz Volcanic Ridge, and EPR. 163

Table 9: Mineral-melt distribution coefficients used in melting calculations. 171

Table 10: Trace element concentrations (ppm) used in melting calculations. 173

Table 11: Example batch melting calculation using the PM - 5% Melt concentrations... 174

Table 12: Trace element concentrations (ppm) for each lithology (harzburgite and lherzolite). 175

Table 13: REEBOX PRO model inputs. 176

Table 14: Microprobe determined plagioclase core and rim major element compositions for plagioclase from the Cocos-Nazca Spreading Center. 180

Table 15: Crystal size distribution results for plagioclase ultraphyric basalts (PUB) from the literature. 183

List of Figures

Figure 1: Simplified geologic map of the Skaergaard Intrusion with the approximate location of samples used in this study denoted. 8

Figure 2: Stratigraphy of the Skaergaard Intrusion with approximate location of samples used in this study denoted by white stars. 13

Figure 3: False color EDS maps of sulfide occurrences. 20

Figure 4: False color EDS maps of silver occurrences in the Skaergaard Intrusion. 21

Figure 5: a) Back-scattered electron image of an apparent fluid inclusion in clinopyroxene containing native Ag with trace quantities of quartz. 22

Figure 6: EDS false color composition map of native Au in plagioclase with associated halite and sylvite. 23

Figure 7: False color EDS images of precious metal occurrences. 24

Figure 8: Photomicrographs of fluid inclusions in olivine. 26

Figure 9: Variation in loss on ignition data reported by Keays and Tegner (2016) as a function of lithologic unit.. 28

Figure 10: Numerical calculation of Ag enrichment in end-member basaltic liquids and evolving vapor as a function of fraction of silicate liquid remaining. 37

Figure 11: Numerical calculations simulating the dissolution of Ag in sulfide-free (top) and sulfide-bearing (bottom) systems. See text for further discussion. 40

Figure 12: Bathymetric map of the eastern equatorial Pacific (top) and the Cocos-Nazca Spreading Center (bottom).. 49

Figure 13: Schematic illustration of the evolution of the Cocos-Nazca Spreading Center from 2 Ma to present.. 53

Figure 14: Longitudinal variation (102.5°W to 90.5°W) of La/Sm_N (top) and $^{87}Sr/^{86}Sr$ (bottom).. 56

Figure 15: Covariation diagrams for glasses and two whole rock samples from the Cocos-Nazca Spreading Center. 62

Figure 16: Along-axis variations in MgO, K_2O/TiO_2, $Na_{8.0}$, $Fe_{8.0}$, La/Sm_N, Nb/Y, and $^{87}Sr/^{86}Sr$ for glass and whole rock samples from the Cocos-Nazca and adjacent EPR..... 63

Figure 17: Along-axis variations in MgO, K_2O/TiO_2, $Na_{8.0}$, $Fe_{8.0}$, La/Sm_N, Nb/Y, and $^{87}Sr/^{86}Sr$ for glass from the Dietz Volcanic Ridge and adjacent EPR. 65

Figure 18: Bulk silicate earth-normalized trace element spider diagrams for Cocos-Nazca Spreading Center and neighboring features. 67

Figure 19: K_2O/TiO_2 vs $^{87}Sr/^{86}Sr$ for basaltic glass from the Cocos-Nazca, the Dietz Volcanic (DVR), and the adjacent EPR (labeled). 70

Figure 20: Comparison of regional geochemical data. 73

Figure 21: La/Sm_N vs Nb/Y for lavas from the Cocos-Nazca, local EPR, and Dietz Volcanic Ridge. 75

Figure 22: Comparative bulk silicate earth-normalized trace element spider diagrams.. 79

Figure 23 (next page): Results of melting calculations.. 84

Figure 24: Segment averaged longitudinal changes in $Fe_{8.0}$ (A), La/Sm_N (B), and Nb/Y (C). The x-axis is the EPR and individual Cocos-Nazca segments (2 – 9). 88

Figure 25: Cartoon depicting one possible explanation for the depleted nature of the Cocos-Nazca Spreading Center lavas.. 90

Figure 26: Idealized crystal length vs ln (population density). 99

Figure 27: Multibeam bathymetry map of the Cocos-Nazca Spreading Center and the surrounding region. 107

Figure 28: Longitudinal variations in (A) dredge depth, (B) mantle Bouguer anomaly inferred relative crustal thickness, and (C) plagioclase mode. 108

Figure 29: Examples of plagioclase-phyric lavas sampled from the Cocos-Nazca Spreading Center. 110

Figure 30: Plagioclase photomicrographs for PUB lavas from the Cocos-Nazca Spreading Center.....112

Figure 31: Correlation between plagioclase true volume (measured by point counting) and CSD calculated volume. 116

Figure 32: Crystal size distribution plots for plagioclase from (A) the Cocos-Galapagos spreading regime, and (B) the Cocos-Nazca spreading regime. 118

Figure 33: CSD slope vs CSD intercept for both the > 1 mm and < 1 mm size fractions. 119

Figure 34 (next page): Distribution of plagioclase core and rim $An_{\#}$ for samples D15-2 (A), D20-3 (C), and D49-1 (E).....120

Figure 35: A physical model that explains the observed CSDs. 125

Figure 36: Crystal size distribution curves for plagioclase that crystallized during rapid ($\Delta T/\Delta t$ = 60°C/hr) and slow cooling ($\Delta T/\Delta t$ = 7°C/hr) experiments.. 128

Figure 37: Comparisons of plagioclase ultraphyric basalt found elsewhere.....131

Figure 38: Covariation plot of Zr data (ppm) collected using DCP and ICP-MS. The black line is the line of unity (1:1). Poor agreement is observed between the two methods. ...156

Figure 39: Covariation plot of Sr data (ppm) collected using DCP and ICP-MS. The black line is the line of unity (1:1). 157

Figure 40: Method of addition results for NBS 688 (top) and USGS BHVO (bottom). ...158

Figure 41: Comparison of Zr concentrations (ppm) collected by ICP-MS (x-axis) and DCP (y-axis). 160

Figure 42: Comparison of high field strength element data measured on ICP-MS following either two-acid digestions or $LiBO_2$ flux-fusion.. 161

Figure 43: *REEBOX PRO* thermodynamic output.....176

Figure 44: Example of a scanned plagioclase-bearing MORB (sample D22-1, A) and the outlines generated and measured by *ImageJ* (B). 178

Figure 45: Examples of end-member *CSDSlice* models. KN-63D/1 is from the Knipovich ridge while D22-1 is from the Cocos-Nazca Spreading Center. 179

Acknowledgements

First, I would like to thank my advisor, Dr. Emily Klein, for teaching me how think scientifically and challenging me to grow professionally. Second, I would like to thank my committee members, Dr. Alan Boudreau, Dr. Drew Coleman, and Dr. Avner Vengosh, for acting as mentors and cheerleaders. Stimulating and often amusing conversations with Dr. Paul Baker, Dr. Alex Glass, and Dr. Gary Dwyer were reinvigorating. Gary dedicated much of his time to helping me with analytical procedures and troubleshooting a variety of issues. Ryan Mills at the University of North Carolina – Chapel Hill was incredibly helpful on a number of different occasions.

I would also like to thank my colleagues, Erin Benson, Rachel Coyte, Dr. Andrew Kondash, Dr. Nancy Lauer, Jun Shepard, Dr. Wout Salenbien, Zhen Wang, Dr. Enrico Zorzetto, and the SR1806 science party for their friendship and support. Aleta Donald, Briana Kleiner, and Lizzy Nist were incredibly helpful and their contributions to this dissertation cannot be overstated. This work was funded in part by the National Science Foundation.

Finally, I would like to thank my family for their unrelenting love and support. My father, D'Arcy Wernette, frequently shared words of wisdom and countless dad jokes. My mother, Dr. Catherine Wernette, provided endless empathy and

encouragement. Last, I would like to thank my incredible wife, Mary Wernette. Your love and companionship buoy me in the roughest of waters.

1. Introduction

The study of igneous rocks has shed light on a wide variety of processes important to an overall understanding of the evolution of the Earth. For example, the detailed study of intrusive igneous bodies has revealed the sequence of minerals that precipitate from a cooling and crystallizing magma and how this influences the composition of the magma from which they precipitated (McBirney, 1975). Further, the study of mid-ocean ridge basalts, the eruptive product of the global mid-ocean ridge system, has provided insight into the chemical heterogeneity of the Earth's mantle and how the Earth segregated into numerous chemical reservoirs through time (Hart, 1988; Hofmann, 1997). In both instances, numerous observations at a variety of scales (e.g., mineral, rock, regional) were used to elucidate large-scale processes. This dissertation continues this tradition by using detailed petrographic and geochemical observations to better understand large-scale processes related to the evolution of igneous systems.

The second chapter of this dissertation reports detailed petrographic observations of sulfide minerals, native metals, and trace minerals in rocks from the Eocene Skaergaard Intrusion of east Greenland. Significantly, these observations reveal a link between the evolution of late-stage hydrothermal fluids and the modification of the Skaergaard transition and precious metal budget and distribution. The third chapter of this dissertation utilizes major and trace element geochemistry with $^{87}Sr/^{86}Sr$ ratios to

characterize a suit of lavas from the Cocos-Nazca Spreading Center of the eastern equatorial Pacific. As a whole, these lavas are chemically unique when compared to other lavas in the region and an intimate relationship with the nearby East Pacific Rise is revealed. Finally, the fourth chapter of this dissertation examines morphologies and chemical compositions of plagioclase crystals found in these same lavas. Combining the two methodologies reveals information about how magmas ascend through the oceanic crust prior to eruption on the seafloor. Ultimately, it is determined that plagioclase morphologies and chemical compositions reflect fundamental changes in how magmas are processed prior to eruption along the Cocos-Nazca Spreading Center.

2. Sulfides, native metals, and associated trace minerals of the Skaergaard Intrusion, Greenland: Evidence for late hydrothermal fluids

Published as: Wernette, B., Li, P., and Boudreau, A., 2019, Sulfides, native metals, and associated trace minerals of the Skaergaard intrusion, Greenland: evidence for late hydrothermal fluids: Mineralium Deposita, doi: 10.1007/s00126-019-00924-1.

2.1 Chapter Summary

Sulfide assemblages, precious metals, transition metal alloys, and associated accessory phases were characterized throughout the Skaergaard intrusion to better constrain the sulfide saturation history of the intrusion and the role of late magmatic volatiles in modify the Skaergaard metal budget and distribution. Sulfides in and below the Middle Zone of the Layered Series of the intrusion are readily replaced by low-Ti magnetite. The ratio ∑(low-Ti magnetite mode)/∑(sulfide mode), indicating oxidation of sulfides, reaches maximum values in the Lower Zone of the Layered Series. Sulfide assemblages below the Middle Zone are typically accompanied by minor biotite, apatite, and rare calcite as well as trace compositionally distinctive clinopyroxene and orthopyroxene. The occurrence of Ag, Au, Pt, Cu and metal alloys outside of the Middle Zone is further evidence of the Skaergaard intrusion parental magma being S-poor. Native Ag, commonly accompanied by trace amounts of Cl, occurs both in and below the Middle Zone. Evidence of coexisting precious metal + brine assemblages exists where native metals are accompanied by sylvite ± halite and Ag is accompanied by Ag

halides. Ag occurrences in the Middle Zone are of irregular morphology with trace Cl ± S ± calcite. Further evidence supportive of a metal + brine assemblage is observed where Ag + quartz is found in an apparent open clinopyroxene-hosted fluid inclusion consisting of Na, Si, Cl, Ca, K, and S. Ag is used to model the behavior of precious metals and transition metals in the presence of an exsolving fluid phase. Numerical modeling suggests that, in a sulfide-bearing system, residual Ag concentrations and concentrations in the exsolved fluid are most affected at the point where sulfide is lost to a separating volatile fluid phase. It is suggested that, owing to the low-S nature of the Skaergaard system, fractional crystallization and early fluid saturation produced enrichment of Ag, with other precious and transition metals, in the interstitial silicate liquid much higher than normal due to delayed sulfide saturation. As this interstitial liquid evolved, Ag was lost to an exsolved volatile phase of high salinity and migrated upward. A similar process likely occurred for Au and other elements with high affinities for Cl.

2.2 Introduction

In layered mafic intrusions (LMIs), evidence for the existence of volatile phases is preserved in fluid inclusions, apatite composition, and halogen geochemistry (e.g., Boudreau and McCallum, 1989; Hanley et al., 2008). Of debate, however, is whether these fluids play a significant role in the processes responsible for generating, or

modifying, the stratiform platinum-group element (PGE)-sulfide ore bodies for which LMIs are known. Conventionally, these deposits are thought to form as the result of gravitationally driven downward movement of immiscible sulfide liquid droplets in the magma chamber. Large sulfide liquid/silicate liquid partition coefficients (e.g., Mungall and Brenan, 2014) and large silicate liquid/sulfide liquid mass ratios (R-factor, Campbell and Naldrett, 1979) allow for the extreme enrichment of transition and noble metals as well as PGE in immiscible sulfide droplets. Experimental results confirm that these are reasonable assumptions (Fleet et al., 1993).

Conversely, others have suggested that stratiform mineralization is the result of upward moving exsolved fluid, rich in halides, allowing for the efficient transport of transition and precious metals vertically through an igneous body (e.g., Boudreau and McCallum, 1992). Theoretical work (Shinohara, 1994) supports this model and experimental work performed on rhyolitic and granitic systems (Candela and Holland, 1984; Simon et al., 2008; Frank et al., 2011) and theoretical work done on LMIs (Boudreau and McCallum, 1992; Meurer et al., 1999) suggest the importance of exsolved halide-bearing volatiles. Together these end-member models are referred to as the "orthomagmatic" and "hydromagmatic" models, respectively.

Complicating our understanding of LMIs is that the larger intrusions (i.e., Bushveld and Stillwater Complex) show evidence of multiple magma injections and

prolonged cooling histories for which the preservation of original igneous textures and chemistry is uncertain. It is generally agreed that the small Paleogene Skaergaard intrusion of southeast Greenland cooled and crystallized as a closed system (Holness et al., 2007). Of both scientific and commercial interest is the fact that the Skaergaard intrusion contains a zone enriched in Au and PGEs known as the Platinova Reef (Andersen et al., 1998; Holwell and Keays, 2014; Godel et al., 2014; Nielsen et al., 2015). It is because of this that the Skaergaard intrusion provides a unique opportunity to investigate how metalliferous LMIs evolve through time. In this study, we examine sulfide assemblages and their associated phases and characterize the occurrence of precious and transition metals outside of the Platinova Reef to better understand the role of exsolved volatiles in the distribution and modification of metals in LMIs and the sulfide saturation history of the Skaergaard Intrusion.

2.3 Geologic Background and Summary of Previous Studies

For extensive reviews, readers are directed to the early studies of Wager and Deer (1939) and the more recent summary of Nielsen (2004). Briefly, the Skaergaard Complex is a ~ 55 Ma (Brooks and Gleadow, 1977; Hirschman et al., 1997) intrusion located in southeast Greenland (Figure 1). The intrusion formed during the Paleogene rifting of Greenland from Eurasia (Nielsen, 1975). The Complex is hosted uncomformably in Archean gneiss and, from bottom to top, is composed of the Layered

and Upper Border Series. At its margin, the Complex is composed of the Marginal Border Series. The Layered Series is thought to have grown upward from the floor of the intrusion while the Upper Border and Marginal Border Series crystallized from the roof and the walls of the intrusion inward, respectively. The Layered Series is subdivided into the Lower (LZ), Middle (MZ), and Upper Zone (UZ) according to the presence of index minerals.

For the MZ, Wager et al. (1957) describe a Cu-rich sulfide assemblage consisting of chalcopyrite and bornite. The upper ~ 100 m of the MZ is host to the Triple Group, a sequence of layered gabbros (Nielsen et al., 2015) that contain zones of anomalously high Au and PGE concentrations (Andersen et al., 1998). Individual layers within the Triple Group have been correlated across the intrusion (Andersen et al., 1998; Holwell and Keays, 2013; Nielsen et al., 2015) and discrete Pd-, Au-, and Cu-rich subzones, or "offsets", have been identified (Bird et al., 1991; Andersen et al., 1998; Nielsen et al., 2005; Holwell and Keays, 2014). Collectively, these metalliferous subzones are known as the Platinova Reef. Several petrogenetic models for the Platinova Reef have been proposed and broadly align with the orthomagmatic or hydromagmatic endmember models.

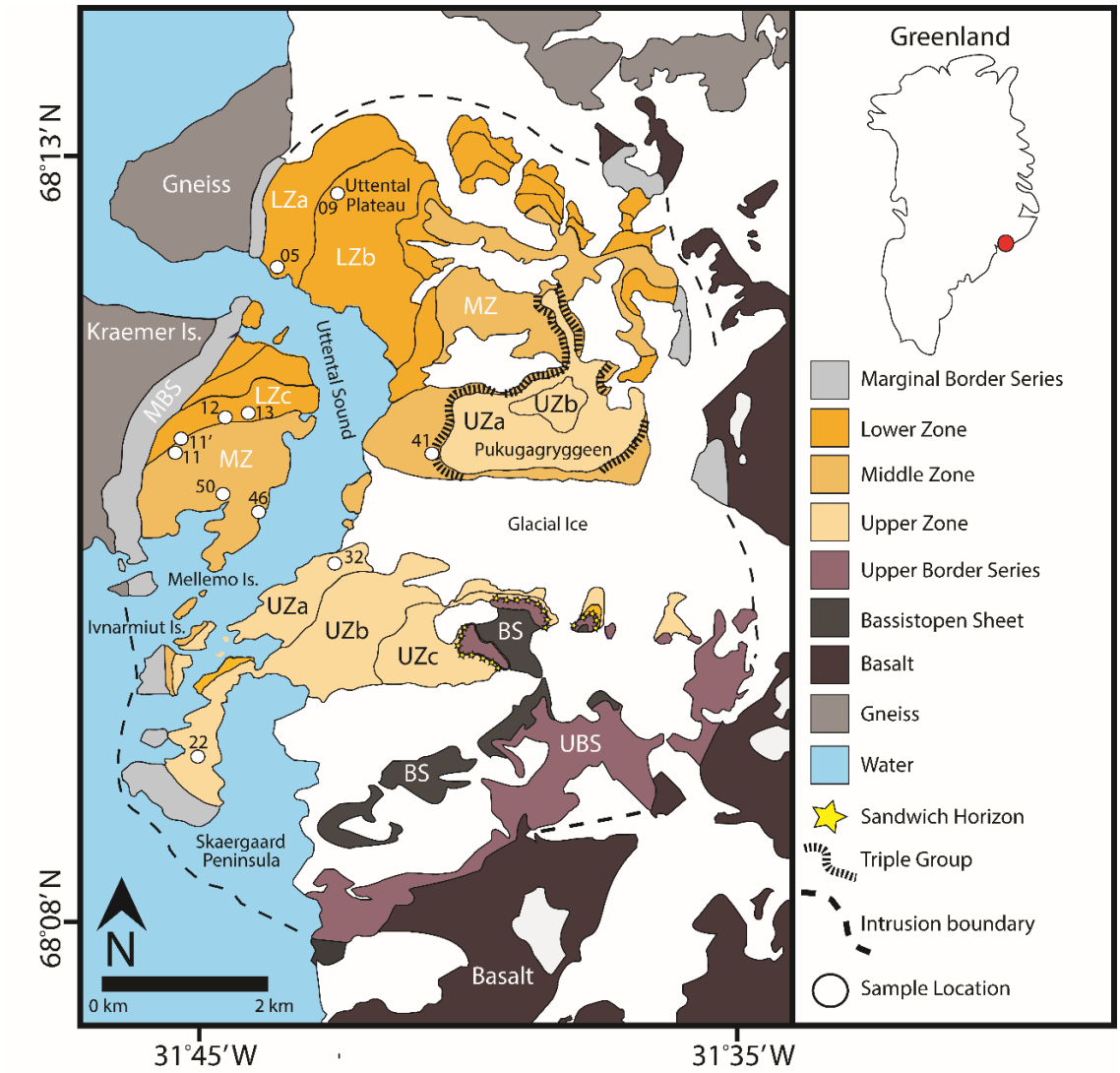

Figure 1: Simplified geologic map of the Skaergaard Intrusion with the approximate location of samples used in this study denoted. Geologic map modified after McBirney (1989).

Previous workers have suggested that the Platinova Reef is the result of Rayleigh fractionation processes acting to concentrate PGEs in sulfide (Holwell and Keays, 2014). In this model, large $D^{sulfide/silicate}$ values act to concentrate PGE in early formed layers (Pendergast, 2000; Holwell and Keays, 2014). To explain high PGE tenors in sulfide and the observed Pd, Au, Cu offsets of the Platinova Reef, Holwell and Keays (2014) proposed a multistage sulfide saturation model whereby early formed sulfide droplets concentrate chalcophile elements as they settle through the magma chamber. In their model, re-dissolution of this early sulfide as it moves into hotter magma along the floor of the chamber acts to concentrate chalcophile elements in the magma. This is followed by a second local (or in-situ) sulfide saturation event that generates low-volume high-tenor sulfides. The observed Pd, Au, and Cu offsets are thought by Howell and Keays (2014) to reflect variations in $D^{sulfide/silicate}$. Indeed, Godel et al. (2014) found textural evidence supportive of in-situ sulfide nucleation in the Platinova Reef. Andersen et al. (1998) suggested that compaction of cumulates forced sulfides to migrate vertically generating the observed metal offsets while potentially oxidizing existing sulfides. Analogous to the model of Andersen et al. (1998), Nielsen et al. (2015) proposed that the precious metal distribution observed in the Platinova Reef can be explained by the upward migration of Fe-rich melts rich in volatiles and precious metals. Andersen (2006) proposed that late hydrothermal fluids transported precious metals vertically along

grain boundaries and fluid pathways. In this model, redox barriers limit the PGE carrying capacity of the hydrothermal fluid acting to separate the stratigraphic occurrence of Pd from Au.

Anomalously high Cu/S ratios observed throughout the Skaergaard stratigraphy (Cu/S = 1 – 7, Keays and Tegner, 2016) have been attributed to early shallow-level degassing and S loss (Li and Boudreau 2017), late S loss to hydrothermal fluids (Andersen, 2006), magmatic oxidation (Wohlgemuth-Ueberwasser et al., 2013), or anomalous Cu/S ratios in the Skaergaard parental magma source region (Keays and Tegner 2016). Andersen (2006) concluded that sulfide texture and mineralogy in the LZ is well explained by an exsolved hydrothermal fluid oxidizing and replacing preexisting sulfides with low-Ti magnetite and redistributing Cu, S, and precious metals to different stratigraphic levels. Li and Boudreau (2017) arrived at a similar conclusion after conducting a modal analysis of sulfides found in the Lower Zone and Marginal Border Series. Conversely, Godel et al. (2014) note that LZ sulfides are generally not accompanied by low-Ti magnetite, ultimately suggesting that late hydrothermal fluids did not oxidize magmatic sulfide assemblages.

There are a number of detailed studies of precious metal distribution through the Platinova Reef (Bird et al., 1991; Godel et al., 2014; Nielsen et al., 2015; Holwell et al., 2016; Keays and Tegner, 2016). These studies focus on characterizing the volumetrically

significant Cu, Au, Pd, and Pt occurrences within the Reef. In the Platinova Reef, researchers have observed the occurrence of Ag in native form (Nielsen et al., 2015), electrum (Holwell et al., 2015), Au-Cu-Ag alloys (Bird et al., 1991 and Cabri et al., 2005), as well as Au-PGE alloys (Andersen et al., 1998). Additionally, Holwell et al. (2015) note Ag concentrations of ~ 250 ppm in sulfides from the Triple Group. Reef occurrences of Au include native Au (Bird et al., 1991), tetra-auricupride (AuCu, Cabri et al., 2005; Nielsen et al., 2015), and Au-Cu-Pd alloys (Nielsen et al., 2015). Pd and Pt form the precious metal minerals (PMMs) skaergaardite and nielsenite while Cu is a constituent of PMMs or metal alloys. Away from the Plainova Reef, Andersen et al. (2017) note the occurrence of Ag in Au-Cu-Ag alloys found in marginal basement schists that formed as the Skaergaard magma interacted with its Archean host rock. In addition, they also found electrum (Au-Ag) and various Bi-bearing PMM.

2.4 Sampling and Methods

A. Boudreau collected samples in 1990. Three samples, SK90-5, SK90-9, and SK90-13, were published in a previous study (Li and Boudreau, 2017) and were re-examined and included in this study for completeness. In total, 11 polished thin sections were systematically scanned using the Cameca CAMEBAX microprobe at Duke University. Sulfide assemblages and accessory phases were characterized using energy dispersive spectrometry (EDS, accelerating voltage = 20 KeV, beam current = 15 nA) and

X-ray composite maps. The same methods were used to identify and characterize the occurrences of Ag, Au, Pt, Cu and metal alloys. Sulfides, native metals, metal alloys, and accessory minerals were imaged and imported into the photo processing software IMAGE-J (Schneider et al. 2012) for area and perimeter measurements. Where reported, semi-quantitative plagioclase data were collected using EDS. Uncertainties are An# ± 4.

2.5 Results

2.5.1 Summary of Stratigraphic Trends

As summarized in Figure 2 and discussed in detail below, stratigraphic trends show a general decrease in chalcopyrite (and a corresponding increase in bornite) from LZ through MZ before chalcopyrite and digenite join the sulfide assemblage in the UZ. Similarly, the relative modal abundance of low-Ti magnetite as a fraction of the sulfide assemblage is highest in LZ samples (Figure 2). The abundance of late hydrous minerals (biotite and amphibole) are typically higher in and below the MZ and broadly parallels the bulk rock loss on ignition (LOI) stratigraphic trends reported by Keays and Tegner (2016). The sulfide-magnetite assemblages occur at both grain boundaries and within primocryst silicate minerals. Further, the relative proportion of accessory minerals, such as calcite, biotite, apatite and compositionally distinctive orthopyroxene and clinopyroxene, as a function of a given sulfide assemblage is greatest in samples from the LZ.

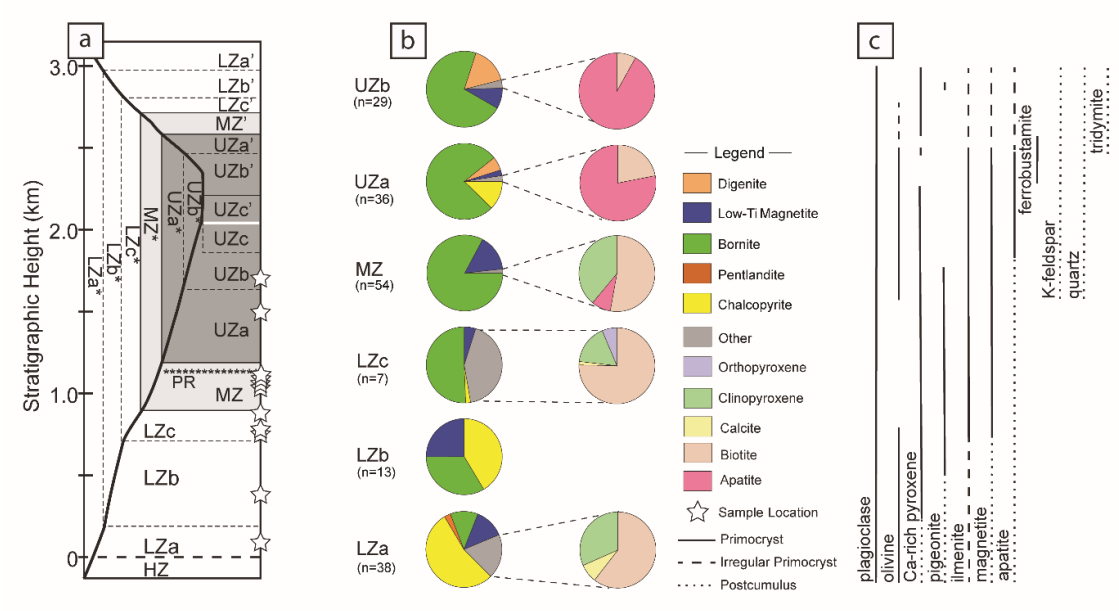

Figure 2: a) Stratigraphy of the Skaergaard Intrusion with approximate location of samples used in this study denoted by white stars. b) Sulfide assemblage proportion oxides and sulfides (left column) and other accessory minerals (right column). Stratigraphic zone corresponds to the stratigraphic zone in (a) and n is the number of individual sulfide assemblages studied for each stratigraphic zone. c) From Naslund (1984) the stratigraphic extent of primocryst minerals (solid lines), irregular primocryst minerals (dashes), and late postcumulus minerals (dotted lines).

Occurrences of native Ag, Au, Pt, and Cu are generally restricted to MZ and LZ samples and native Ag is more common than Pt or Au in terms to total grains observed (12 grains of Ag vs 3 for Au and Pt, respectively). Similarly, halite and sylvite were found only in those samples from and below the MZ. Native Ag is commonly associated with trace quantities of Cl. Although uncertain owing to the low total number of grains observed, there is a suggestion that the size and total number of individual Ag grains per thin section broadly increases up stratigraphy. A brief description of the individual

sulfide (n = 165) and metal and metal-alloy (n = 18) occurrences are presented in tables 1 and 2, respectively. Comprehensive descriptions of individual sulfide assemblages can be found in Appendix A. Sulfides occurring in late crosscutting albite + titanite veins are not included in this dataset.

2.5.2 General Description of Sulfide Assemblages and Associated Trace Minerals

LZa: Sulfides, mainly chalcopyrite and bornite, are typically found interstitial to olivine and plagioclase. Pentlandite is observed in limited quantities and generally comprises a small proportion of individual assemblages (average of ~ 4 vol. %). Sulfides are commonly non-uniform in morphology and are commonly replaced, in part, by low-Ti magnetite (Figure 3a, b). Native Cu is observed where sulfides are extensively replaced by low-Ti magnetite (Figure 3a). Hydrous minerals, such as biotite and amphibole, are observed truncating sulfides or mantling sulfide assemblages (Figure 3b, c). Minor calcite is found mantling sulfides with no evidence of other low or high temperature silicate alteration. When observed, calcite is rounded and commonly no greater than 20 μm in size. Anhedral clino- and orthopyroxene also locally mantle sulfides. When adjacent,

Table 1: Summary of sulfide assemblages.

		Sulfide Assemblage Total Area (μm²)					Associated Trace Minerals (μm²)				
Zone	**No. sulfide occurrences**	**Chalcopyrite**	**Pentlandite**	**Bornite**	**Digenite**	**Ti-Poor Magnetite**	**Biotite**	**Apatite**	**Calcite**	**Cpx**	**Opx**
LZa	38	31727	1594	6930	263	7467	6674	15	869	3489	-
LZb[1]	13	751	-	608	-	455	-	-	-	-	-
LZc	7	549	-	4768	-	233	4287	-	84	959	361
MZ	54	-	-	537079	-	100690	5776	902	-	4257	-
UZa	36	59997	-	374590	28443	11710	2612	9259	-	-	-
UZb	29	-	-	196081	44156	9432	1959	22154	-	-	-

[1]Data from Li and Boudreau, 2017

Table 2: Area and perimeter measurements (microns) for native metals.

ID	Zone	Occurrence	Area	Perimeter	Notes
SK90-5-B2	LZa	Ag	21	17	In plagioclase with trace Cl-bearing phase
SK90-5-H2	LZa	Ag	392	148	In olivine with trace Na, K, and Cl
SK90-5-K2	LZa	Ag	535	275	Olivine-plagioclase grain boundary with trace Cl and associated Ag-halides (Figure 4c)
SK90-5-O	LZa	Ag	15	15	Interstitial to cpx, apatite, and plagioclase (Figure 4a)
SK90-5-L	LZa	Ag	57	9	In plagioclase near margin. No Cl signature observed (Figure 4b)
SK90-5-S	LZa	Pt	133	70	In Ti-rich magnetite
SK90-5-Au	LZa	Au	64	40	In plagioclase with coexisting halite and sylvite (Figure 6)
SK90-13-Q	LZc	Ag	364	95	At pyroxene-pyroxene grain boundary with trace Cl and S
SK90-11-1	MZ	Ag-Au	679	239	Ag - Au intergrowth with Cu and calcite (?) in plagioclase (Figure 4e)
SK90-11-1b-J	MZ	Ag	493	177	In plagioclase with trace Cl and associated Cu, Au
SK90-50-B-1	MZ	Ag	371	207	In plagioclase with trace calcite, S, Cl (Figure 4d)
SK90-50-B-2	MZ	Ag	18	38	Mantling barite.
SK90-50-0	MZ	Ag-Zn	4	8	Ag-Zn alloy and associated native Cu in cpx with trace Cl (Figure 4f)
SK90-50-E	MZ	Ag	35	7	In apparent fluid inclusion in cpx (Figure 5)
SK90-50-0-1	MZ	Cu	31	15	In cpx with notable Cl signature and associated Ag-Zn alloy (Figure 4f)
SK90-41b-BB	MZ	Cu	20	24	Cu in high-Ti magnetite with associated trace silver
SK90-41b-GG	MZ	Pt-Au	174	63	At plagioclase-cpx grain boundary with trace apatite and Fe-Mg amphibole (Figure 7a)
SK90-32-AA	UZb	Pt	92	50	In plagioclase near cpx and sulfide assemblage (Figure 7b)

plagioclase is increasingly calcic near sulfide assemblages (An# ~ 66, Figure 3a) but less calcic away from sulfide assemblages (An# ~ 50).

LZb: Chalcopyrite and bornite make up the entire sulfide assemblage with near equal proportions of low-Ti magnetite replacing the sulfides (Li and Boudreau, 2017).

LZc: Observed sulfide proportions by area average 9% chalcopyrite and 91% bornite. Sulfides occur both within silicates (cores and margins) and at silicate grain boundaries. Low-Ti magnetite is less abundant relative to LZa. Biotite truncates silicate grain boundaries or crosscuts sulfides. Calcite was observed in a single sulfide assemblage. As for LZa, plagioclase becomes increasingly calcic towards sulfide assemblages where An# is similar to that observed in LZa.

MZ: The sulfide assemblage below the Platinova Reef consists entirely of bornite with variable amounts of low-Ti magnetite. It is important to note that this differs from the MZ bornite and chalcopyrite assemblage reported by Wager et al. (1957). Sulfides are interstitial to, or found entrained within, silicates. Sulfide morphology is typically irregular and is positively correlated with the abundance of secondary silicates or low-Ti magnetite. Biotite and amphibole are observed in limited quantities mantling sulfides, and calcite is only associated with native Ag or Ag-halides.

At pyroxene grain boundaries, olivine is locally observed enclosing sulfide assemblages and, in some cases, low-Ti magnetite (Figure 3d). When present, an increase in plagioclase anorthite content in adjacent plagioclase is observed.

UZa: The sulfide assemblage is composed entirely of bornite (82%), chalcopyrite (13%), and minor digenite (5%). Low-Ti magnetite is observed replacing sulfides in quantities similar to that observed in LZc. Apatite is regularly associated with sulfides, typically surrounding the periphery of the mineral. Sulfides are notably non-uniform in composition with Cu-rich, S-poor areas (Figure 3e). Anhydrite is observed in limited abundance where sulfides are in direct contact with plagioclase. Additionally, plagioclase becomes increasingly calcic towards sulfide assemblages. Near sulfide An# are as high as 72 (Figure 3f).

UZb: Bornite and minor digenite comprise the entire sulfide assemblage. Sulfides are commonly rounded and found at silicate-silicate or silicate-oxide grain boundaries and less commonly within high-Ti magnetite. Additionally, sulfides are found interstitial to modally abundant apatite. Low-Ti magnetite is seen in minor abundance and biotite is observed in only one assemblage.

2.5.3 Occurrence of Precious and Transition Metals

Below the MZ, native Ag occurs as discrete rounded grains near the cores of major minerals such as plagioclase, interstitial to late phases such as clinopyroxene and apatite (Figure 4a), or at primocryst grain boundaries (Figure 4b, c). In MZ samples, Ag occurs both as well-rounded grains and irregular shaped grains in silicate minerals (Figure 4d) or at silicate grain boundaries. Those occurrences of irregular morphology (6 out of 12) are accompanied by trace amounts of Cl ± S ± calcite (Figure 4d, e) and Ag-halides (Figure 4d). Less common are Ag grains occurring with Au intergrowths and trace Cu with notable trace quantities of Cl (Figure 4e). Ag was not observed above UZa. One occurrence of note (MZ), which is interpreted as a ruptured fluid inclusion, is native Ag found in clinopyroxene with quartz and trace quantities of Na, Si, Cl, Ca, K, and S (Figure 5).

Grains of native Au or Pt are much less common than native Ag. Native Au occurs as intergrowths with Ag in the MZ (Figure 4e) and as singular occurrences with halite and sylvite in plagioclase in LZa (Figure 6). In LZa, native Pt was found within high-Ti magnetite. Further, Pt-sulfides and Pt-Au alloys are observed at primocryst grain boundaries with trace Fe-Mg amphibole and apatite in MZ samples (Figure 7a). Of note is one occurrence of Pt in plagioclase in UZb (Figure 7b).

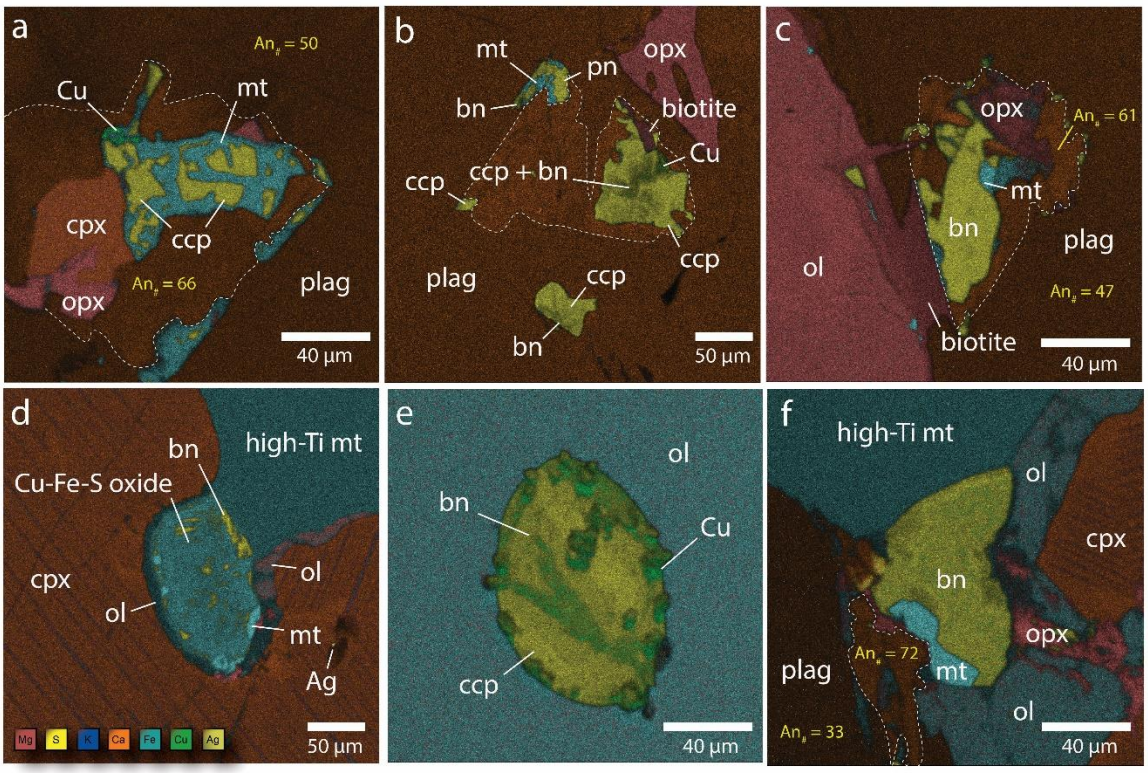

Figure 3: False color EDS maps of sulfide occurrences. a) Sample SK90-5 (LZa) Sulfide assemblage readily altered to magnetite. Note Cu occurring where much of the sulfide has been lost and that plagioclase immediately surrounding the assemblage is more calcic (brighter orange, white dashed line) b) Sample SK90-5 (LZa) Polysulfide assemblage cross-cut by magnetite and biotite. Note that plagioclase immediately surrounding the assemblage is more calcic (brighter orange, white dashed line). c) Sample SK90-5 (LZa) Sulfide assemblage truncated by biotite, orthopyroxene, and low-Ti magnetite. Note that the area immediately surrounding the sulfide is more calcic plagioclase (brighter orange, white dashed line). d) Sample SK90-50 (MZ) Interstitial sulfide from the Middle Zone that is entirely oxidized. Note the minor Ag occurrence. e) Sample SK90-32A (UZa) Rounded sulfide with areas of high and low S concentrations with no sign of host silicate alteration. f) SK90-32A (UZa) Interstitial bornite replaced by low-Ti magnetite. Note near sulfide high-Ca plagioclase (brighter orange, white dashed line). All images are EDS false color composition maps. Elements and corresponding colors are given in 3d.

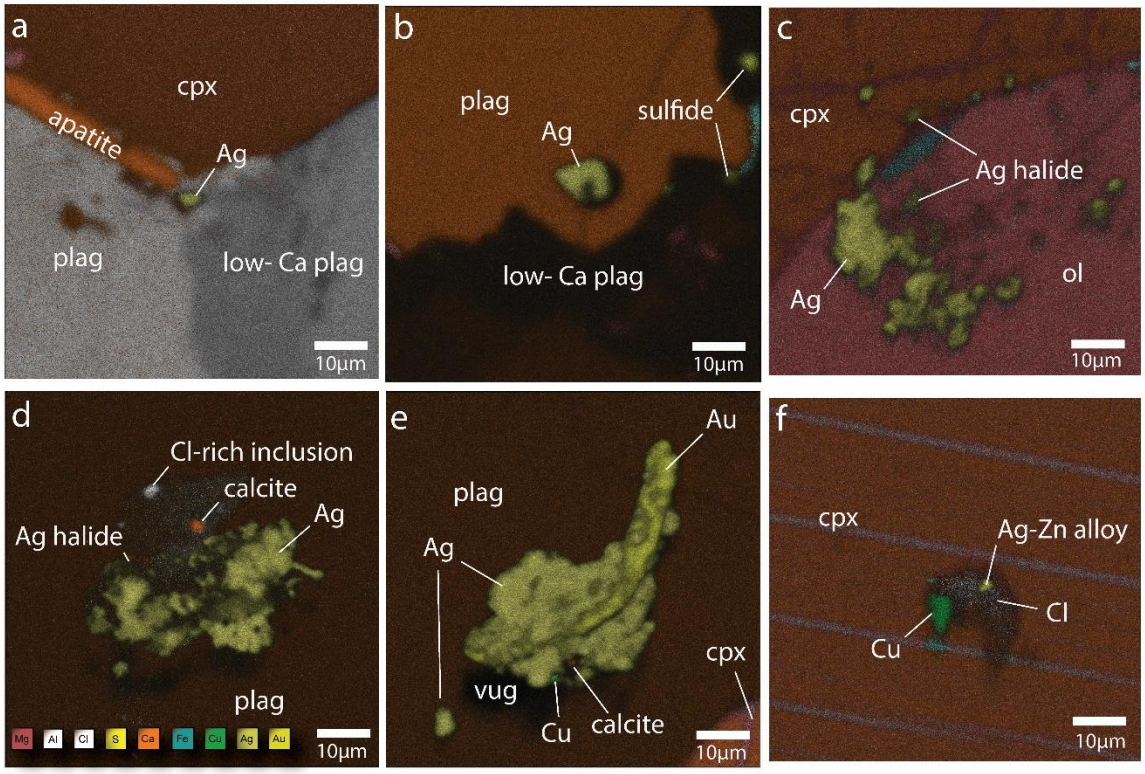

Figure 4: False color EDS maps of silver occurrences in the Skaergaard Intrusion. a) SK90-5 (LZa) Ag interstitial to plagioclase, apatite, and clinopyroxene. b) SK90-5 (LZa) Native Ag in plagioclase near grain boundary. c) SK90-5 (LZa) Native Ag with associated Ag halides at olivine-clinopyroxene grain boundary. d) SK90-50 (MZ) Native Ag in plagioclase with calcite and Cl-rich inclusion. e) SK90-11-1b (MZ) Ag-Au intergrowth in plagioclase. f) SK90-50 (MZ) Ag-Zn alloy with associated native Cu in a chlorine rich inclusion in clinopyroxene. All images are EDS false color composition maps. For elements and corresponding colors, readers are directed to the key in 4d.

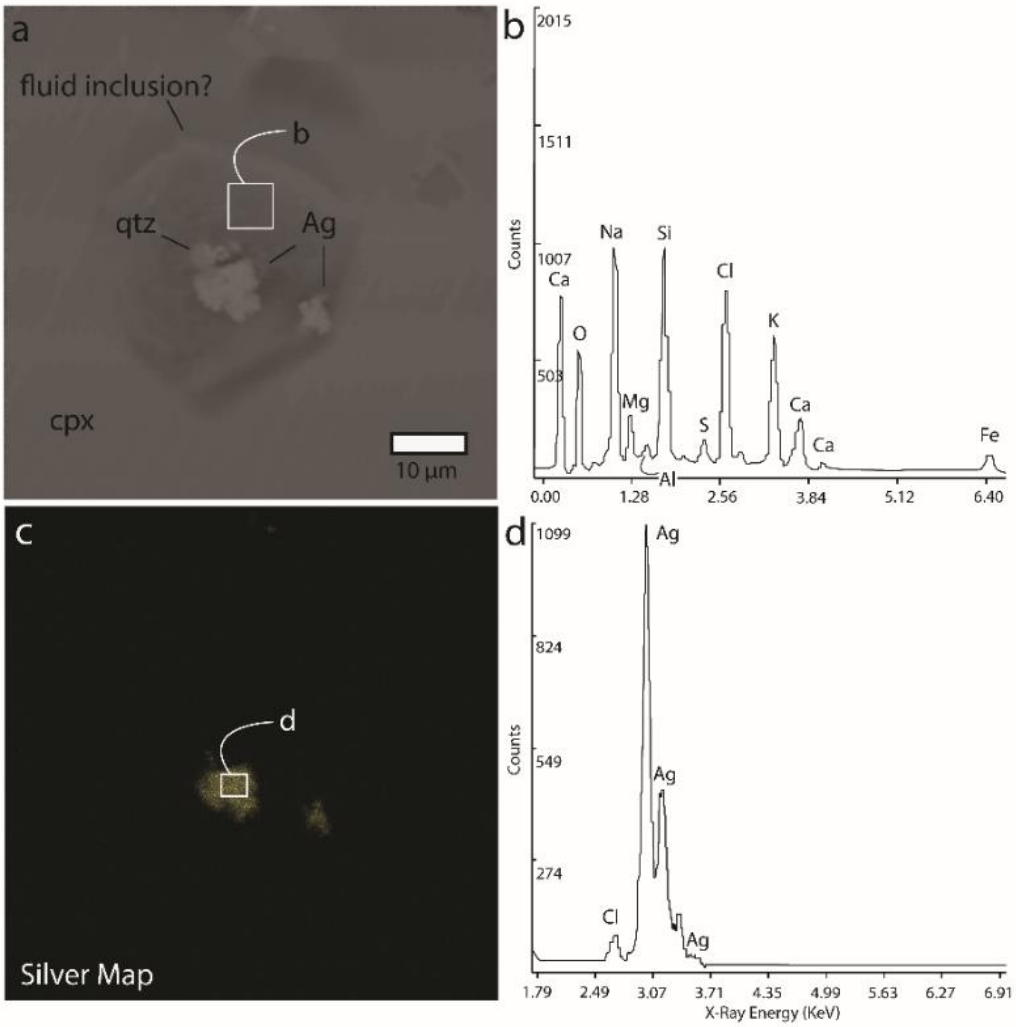

Figure 5: a) Back-scattered electron image of an apparent fluid inclusion in clinopyroxene containing native Ag with trace quantities of quartz. b) Semi-quantitative X-Ray spectra for the field outlined in (a). Note the abundance of Ca, Na, Si, Cl, and K. c) EDS false color composition map for Ag. Same field of view as (a). d) Semi-quantitative X-Ray Spectra for the field outlined in (c). Note the composition is almost entirely Ag with trace Cl.

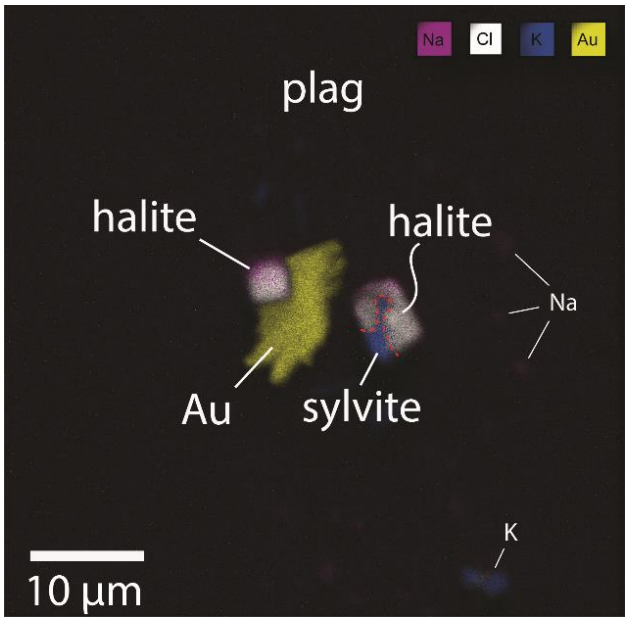

Figure 6: EDS false color composition map of native Au in plagioclase with associated halite and sylvite. Blue regions represent areas of high K concentration while purple regions represent areas of high Na concentration. Elements and corresponding colors are also given.

Native Cu is seen where significant replacement, or loss, of S from sulfide minerals appears to have occurred (LZa, Figure 3a). In some samples, however, Cu "colloids" are observed at sulfide grain boundaries without evidence of sulfur loss or silicate replacement in LZ and UZ samples (Figure 3e). In MZ samples, Cu is observed in high-Ti magnetite and pyroxene with associated trace Ag. Finally, trace quantities of Cu are observed in pyroxenes from LZb and LZc and amphiboles from the MZ.

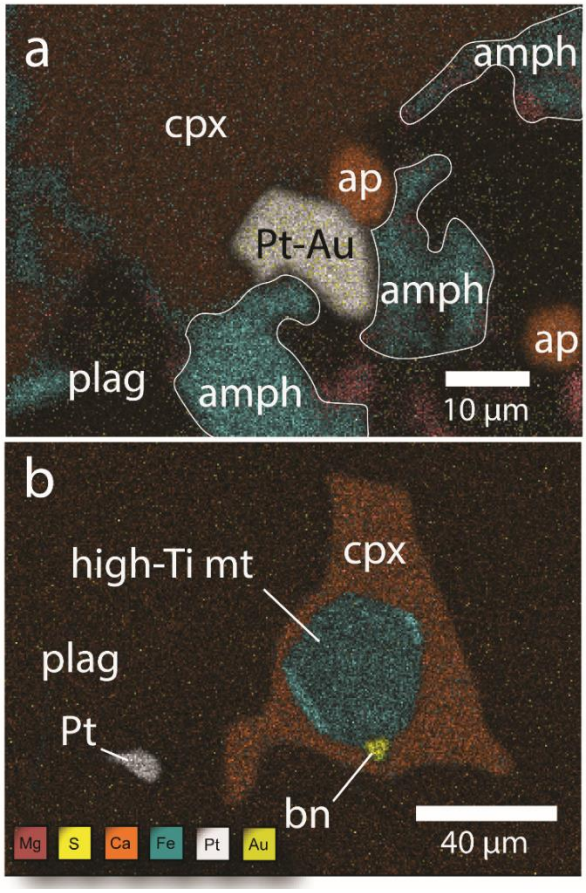

Figure 7: False color EDS images of precious metal occurrences. a) Pt-Au alloy at plagioclase-clinopyroxene grain boundary with associated Fe-Mg amphiboles and apatite from sample SK90-41b (MZ). b) Native Pt in plagioclase in sample SK90-32 (UZb). Both images are EDS false color composition maps. Elements and corresponding colors are given in 7b.

Approximately 70 % of the occurrences of precious and transition metals outside of the mineralized Platinova Reef are accompanied by trace Cl or are spatially associated with hydrous minerals such as biotite and amphibole. Furthermore, about 40 % of the occurrences are either at, or close to, grain boundaries while the remaining 60 % occur in primocryst minerals. Finally, except for one instance of Ag near sulfide (Figure 3d),

precious metals are not observed near sulfide minerals, perhaps reflecting different precipitation processes.

2.5.4 Fluid Inclusions

Fluid inclusions were not observed below the MZ; however, the former presence of a high temperature fluid is inferred from the presence of sylvite inclusions in clinopyroxene and plagioclase primocrysts from LZa and LZc and halite crystals at silicate grain boundaries in LZa. Within the MZ, fluid inclusions were observed as singular occurrences in pyroxene or as inclusion trails in olivine (Figure 8).

The fluid inclusions in pyroxene, inadvertently opened during thin section preparation, are no greater than 50 μm in diameter. They contain Ag, Ag-Zn alloys, Cu and trace quantities of Cl, Na, Ca, and K. Fluid inclusions in olivine can be categorized into three principle groups that form inclusion trails, consisting of elongate or oblate shaped fluid inclusions ~ 40 μm in diameter. One population of inclusions parallels olivine fracture surfaces, while the other two are not associated with any identifiable fracture surface and differ only in size and density of the inclusions (Figure 8). Broadly, inclusions in olivine number in the dozens and are categorized as consisting of ~ 80 % vapor fill with a small proportion of fluid (Figure 8b, d). Where observed, solids make up ~ 10 % of fluid inclusion volume (Figure 8b). All olivine in sample SK90-50 (MZ) host fluid inclusions.

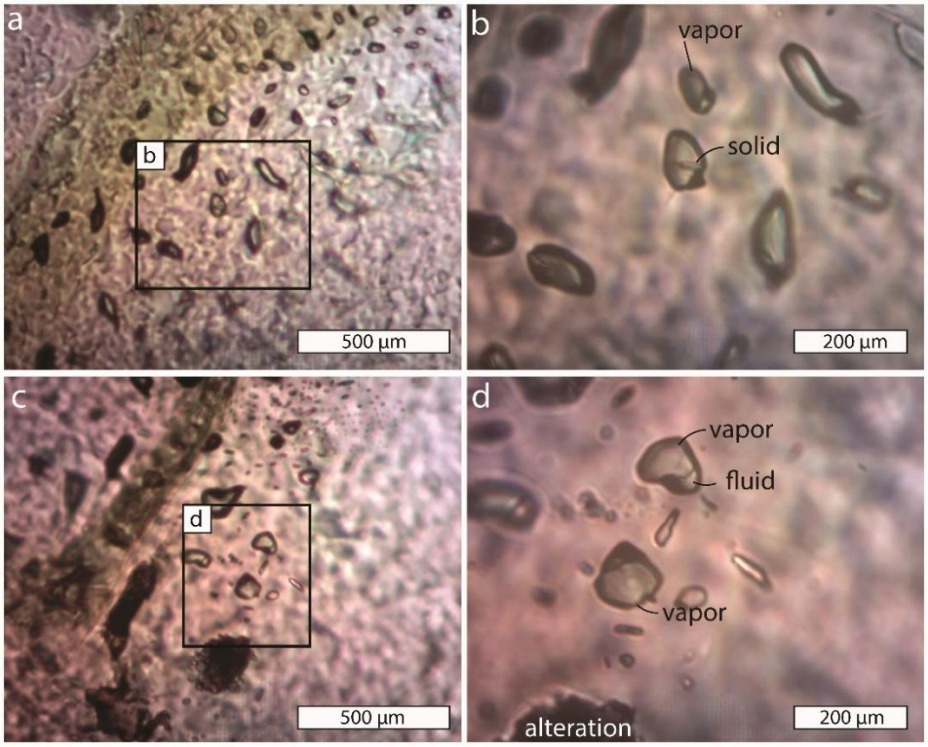

Figure 8: Photomicrographs of fluid inclusions in olivine. a) Plane polarized photomicrograph (PPP) of fluid inclusions in olivine from SK90-50 (MZ). b) PPP of the field outlined in (a). Note the crystalline solid phase present in one fluid inclusion and the ~ 90 % vapor fill in the other. c) PPP of an additional cluster of fluid inclusions in olivine from SK90-50. d) Plane polarized photomicrograph of the field outlined in (c). The larger fluid inclusions are composed of a vapor + fluid. Note the population of smaller elongate inclusions.

2.6 Discussion

2.6.1 Sulfides and Associated Minerals

As noted above, the Ti-free magnetite has been previously interpreted to be replacement of the original sulfide assemblage as the result of S loss (Andersen, 1998; Andersen, 2006; Li and Boudreau, 2017); our observations are consistent with these

interpretations. Specifically, sulfides in and below UZa are commonly replaced by low-Ti magnetite as the result of S loss via fO_2-neutral reactions:

$$\underset{cpy}{CuFeS_2} + \underset{vapor}{1.15H_2O} \rightarrow \underset{mt}{0.27Fe_3O_4} + \underset{bn}{0.19Cu_5FeS_4} + \underset{\text{------ vapor ------}}{1.15H_2S + 0.04SO_2} \quad (1)$$

and

$$\underset{cpy}{CuFeS_2} + \underset{\text{--------- vapor --------}}{1.11H_2O + 2HCl + SO_2} \rightarrow \underset{mt}{0.33Fe_3O_4} + \underset{\text{---- vapor ----}}{CuCl_2 + 2.11H_2S} \quad (2)$$

(Li and Boudreau, 2017). Evidence of sulfur loss by these reactions is ubiquitous from LZa through UZa. Additionally, the abrupt decrease in secondary, or late hydrous minerals above the MZ is consistent with loss on ignition (LOI) data reported by Keays and Tegner (2016) where values approach 1 wt. % below UZa but are closer to 0.2 wt. % in, and above, UZa (Figure 9). Similarly, the enrichment in the An content in plagioclase suggests silica and Na loss to a silica-undersaturated fluid via:

$$\underset{plagioclase}{2.0CaNaAlSi_{2.5}O_8} + \underset{\text{--- vapor ---}}{4.0H_2O + 4.0H^+} \rightarrow \underset{anorthite}{CaAl_2Si_2O_8} + \underset{\text{---------- vapor ----------}}{3.0H_4SiO_4 + Ca^{2+} + 2.0Na^+} \quad (3)$$

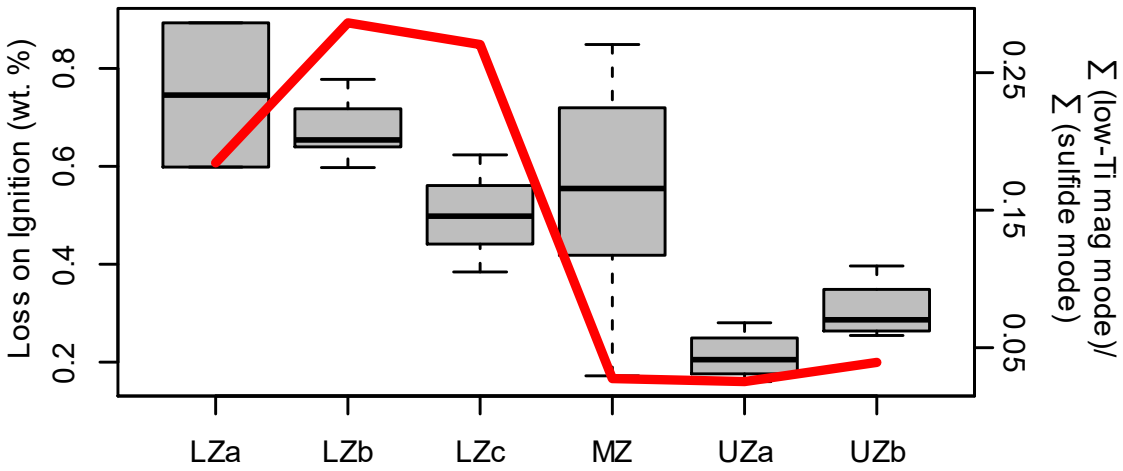

Figure 9: Variation in loss on ignition data reported by Keays and Tegner (2016) as a function of lithologic unit. Also plotted in red is the Σ(low-Ti magnetite mode)/Σ(sulfide mode).

Support for this is the observation that Ca content, increase toward sulfide assemblages in LZa through UZa (Figure 3a, b, c, and f). Further, silica loss can produce olivine at pyroxene grain boundaries via the reaction:

$$\underset{\textit{orthopyroxene}}{2.0(Mg_{0.5}Fe_{0.5})SiO_3} + \underset{\textit{vapor}}{2.0H_2O} \rightarrow \underset{\textit{olivine}}{(MgFe)_2SiO_4} + \underset{\textit{vapor}}{H_4SiO_4} \quad (4)$$

Similar observations have been made at the 2.7 Ga Stillwater Complex (Meurer et al., 1997) where discordant troctolites were explained by silica loss to reactive fluids. Further work is needed to confirm that olivine observed in MZ samples are metasomatic in nature though fluid inclusions in olivine (Figure 8) are consistent with this hypothesis.

2.6.2 Evidence for Volatiles in the Skaergaard Intrusion

The reactants involved in equations 1 through 4 require a sulfide-undersaturated volatile phase to produce the observed assemblages. Direct evidence for a fluid includes (i) the fluid inclusions with associated Ag and quartz that retain trace quantities of Ca, Na, Cl, and S and (ii) MZ clinopyroxene hosted Ag-Zn alloys with Cu and trace Cl. Moreover, the association of Ag with Cl in MZ and LZ samples suggests their concentration mechanism is the same. Further, native Au with proximal halite and sylvite (Figure 6) is supportive of a coexisting metal + brine assemblage. Finally, the occurrence of Pt-Au at clinopyroxene-plagioclase grain boundaries with associated Fe-Mg amphiboles suggests that PGE interacted with a hydrous fluid.

More broadly, Sonnenthal (1992) described Cl-bearing fluid inclusions in late anorthositic pegmatites of the UZ while Larsen et al. (1992) describe brine inclusions containing up to ~ 22 wt. % NaCl in gabbroic pegmatites in and below the MZ. Sonnenthal (1992) determined that Cl-bearing fluid inclusions were trapped between 500 and 800°C while Larsen et al. (1992) estimate a much narrower range of 655-770°C. These saline conditions and temperatures might reflect those appropriate for the transport of Ag by an aqueous $NaAgCl_2$ complex, as predicted by Yin and Zajacz (2018). Further, Larsen et al. (1992) suggest that fluid inclusions present within interstitial phases suggests a crystal + (evolved) silicate liquid + exsolved fluid assemblage,

consistent with the presence of apatite, biotite, and salts. This agrees with our observation of fluid inclusions in interstitial olivine (MZ) and plagioclase with apparent silicate and iron-rich melt inclusions (MZ) as described by Jakobsen et al. (2011). Na enrichment will occur during reaction (3) where plagioclase is converted to anorthite by a silica-undersaturated fluid. It is noted that, in some instances, plagioclase near sulfide assemblages preserve An# ~ 62 near oxidized sulfides while An# of ~ 52 is preserved away from sulfides (Figure 3a, b, c). UZa plagioclase preserve larger variations, with one instance of near sulfide An# ~ 72 while An# away from the sulfide is ~ 33 (Figure 3f), suggesting this process becomes more efficient, and total Na^+ increases, up stratigraphy.

Finally, evidence for volatiles in other LMIs include saline fluid and halide melt inclusions (Hanley et al., 2008) in the Archean Stillwater Complex, apatite halogen geochemistry of samples from the Archean Stillwater and Bushveld Complexes (Boudreau et al., 1986), and $H_2O \pm NaCl \pm CO_2 \pm CH_4$ inclusions in quartz reported for the Bushveld Complex (Ballhaus and Stumpfl, 1985). Of note is the similarity in fluid inclusion compositions from the Bushveld Complex described by Ballhaus and Stumpfl (1985) to those from the Skaergaard Complex described by Larsen et al. (1992). The solutions described by Larsen et al. (1992) and Sonnenthal (1992) are saline in nature, so the observation of halite and sylvite at silicate grain boundaries reflect the former presence of a high temperature fluid rich in Cl. These fluids are of interest in LMIs

because of their ability to transport precious and transition metals through an igneous body.

2.6.3 Precious Metals in an Exsolved Volatile Phase

Magmatic volatile phases are an important control on the distribution of precious metals in epithermal systems (Heinrich et al., 2004) and Cu-Au porphyry systems (Candela, 1989; Heinrich et al., 2004; Simon et al., 2008a). In addition, volatiles have also been argued to be important for metal distribution in layered mafic intrusions (Boudreau and McCallum, 1992; Meurer et al., 1999, Hanley et al., 2008). Previous studies of the Skaergaard intrusion have invoked magmatic volatile phases to explain dendritic anorthosite and pegmatite found in UZa (Sonnenthal, 1992), oxidized sulfides found throughout the stratigraphy (Andersen, 2006), and unusually high Cu/S ratios (Anderson, 2006). Further, Godel et al. (2014) assert that in the lowermost zone (Pd5) of the Platinova Reef, Au occurs at silicate ground boundaries and is never enclosed by oxide minerals further implying that Au mineralization is not of primary magmatic origin.

Several researchers (Simon et al., 2008a; Frank et al., 2011; Zajacz et al., 2013; Yin and Zajacz, 2018) have studied the behavior of silver in S-poor granitic and rhyolitic systems. Zajacz et al. (2008) show that the Ag fluid-silicate liquid partition coefficient ($D^{fluid/silicate}$) increases linearly with the molarity of Cl, m_{Cl}, in the exsolved fluid phase

such that $D^{fluid/silicate}$ for Ag is $\cong$ 4 x m_{Cl}. Indeed, Cl has an affinity for the aqueous phase with $D^{fluid/silicate}$ values between 20 and 40 (Holland, 1972) or between .9 and 6 in molten basalts (Webster et al., 1999). A pertinent question is whether an exsolved Cl-bearing fluid phase can transport significant quantities of Ag as a neutral chloride complex:

$$\underset{melt}{AgO_{0.5}} + \underset{vapor}{HCl} \rightarrow \underset{vapor}{AgCl} + 0.5H_2O \quad (5)$$

(Simon et al., 2008b) and by inference, other Cl soluble metals such as Au, Cu, and Zn. Yin and Zajacz (2018) suggest that at higher temperatures (~ 900°C), the neutral $NaAgCl_2$ is the favored Ag species in Cl-bearing exsolved fluids via the modified H_2-neutral reaction:

$$\underset{melt}{AgO} + \underset{vapor}{NaCl + HCl + 0.5SO_2} \rightarrow \underset{vapor}{NaAgCl_2 + 0.5H_2SO_4} \quad (6)$$

Na cations can come from reaction (3) suggesting that the conversion of plagioclase to anorthite by a silica-undersaturated fluid is intimately related to the transport of Ag as illustrated by reaction (6). Less well understood is the behavior of Ag in basaltic systems. Early studies investigated the concentration of Ag and other precious metals in MORBs to understand their potential as protoliths to greenstone Au deposits (Keays and Scott, 1976). Recent experimental results have allowed for the determination of Ag $D^{sulfide/silicate}$ of about 1000 (Li and Audetet, 2012). Indeed, the investigation of sulfide globules in MORB glasses lead to the determination of a similar

$D^{sulfide/silicate}$ of 1138 ± 245 (Patten et al., 2013). Workers have observed that MORB Cu/Ag values remain constant at ~ 3500 with decreasing Mg#, suggesting the two elements behave similarly throughout MORB fractionation (Jenner, 2017). Additionally, similar Cu/Ag values are observed in arc and back-arc environments prior to sulfide saturation (Jenner et al., 2010). Further support for the associated nature of Cu and Ag is found in mantle peridotites where Cu/Ag values are nearly identical to those observed in MORB (Wang and Becker, 2015). Zajacz et al. (2013) determined Ag solubilities for basaltic liquids to be ~ 11 and ~ 5.5 ppm for sulfide-bearing and sulfide-free compositions, respectively. Because of the late S saturation in the S-poor Skaergaard system, it is appropriate to further investigate the partitioning of Ag into coevolving vapor in basaltic liquids. Doing so will allow for a better understanding of Ag behavior in S-poor intrusions.

2.6.4 Temperature and Timing

Temperature constraints might allow for better understanding of Ag (and other precious and transition metals) mobilization during the Skaergaard cooling history. Physical relations such as the interstitial nature of Ag in LZ samples and proximity to grain boundaries suggests that Ag precipitation occurred late in the intrusion's cooling history but early enough to be locally entrained during overgrowth of primocrysts by crystallization of interstitial liquid. Further, ~ 40 % of the precious metal occurrences

reported here occur at primocryst grain boundaries (see Table 2) and in some instances, these occurrences are in close proximity to hydrous minerals (Figure 7a). Utilizing clinopyroxene solvus thermometry, Manning and Bird (1986) determined minimum temperature of formation for late clinopyroxene rich veins to be between ~ 500 and 750°C which is within the range of temperatures reported for fluid inclusions by Sonnenthal (1992) and Larsen et al. (1992). It is suggested that this is a viable minimum temperature range for the precious metals reported here.

What remains unclear is why Ag is observed exclusively in native form in lithologies below the MZ while Ag occurs as both alloys and native Ag and in sulfides in the MZ in general and in the Platinova Reef in particular (Bird et al., 1991; Andersen et al., 1998; Cabri et al., 2005; Holwell et al., 2015). High Ag $D^{sulfide/silicate}$ of ~ 1000 (Li and Audetet, 2012; Patten et al., 2013) suggest that Ag should be retained in sulfide, if any is present. One possible explanation is that the LZ magma was simply undersaturated in sulfide. Another scenario could be that LZ S was lost to an exsolving volatile phase (e.g., Li and Boudreau, 2017), leaving behind small amounts of Ag with little or no S. In that case, one would expect to see alloys with Cu in approximate proportion to the metal concentration of the original sulfide. That this is not generally seen suggests that metals have been effectively separated during volatile exsolution and transport.

2.6.5 Modelling Silver Solubility

To illustrate Ag enrichment during crystallization and degassing, a simple partitioning model is calculated using Rayleigh fractionation (Shaw, 1970):

$$C_{liq} = C_o * F^{\bar{D}-1} \tag{7}$$

Where C_{liq} and C_o represent the concentration of Ag in the silicate liquid and the initial concentration, respectively. F corresponds to the weight fraction of silicate liquid remaining; D is the bulk partition coefficient of Ag in the system given by:

$$\bar{D} = D^{vap/liq} * X_{vap} + \sum(D_i^{xtal/liq} * X_i) \tag{8}$$

$D^{vap/liq}$ is the Ag vapor/liquid partition coefficient, $D_i^{xtal/liq}$ corresponds to the Ag crystal/liquid partition coefficient for each mineral phase i. X_i and X_{vap} are the weight fraction of crystal i and vapor separating from a silicate liquid, respectively. Because Ag does not readily partition into common silicate minerals (Adam and Green, 2006; Greaney et al., 2017), $D_{Ag}^{xtal/liq}$ is equal to 0. Ultimately, the concentration of Ag in the vapor as crystallization proceeds is given by:

$$C_{vapor} = C_o * F^{\bar{D}-1} * D^{vap/liq} \tag{9}$$

Simon et al. (2008b) determine that $D_{Ag}^{vap/liq}$ in rhyolitic systems is 32 and $D_{Ag}^{brine/liq}$ is ~ 1000. For the purposes of this calculation, a conservative $D_{Ag}^{vap/liq}$ of 10 is used. Because the initial Ag concentration of the Skaergaard silicate liquid is unknown,

end-member calculations are carried out for a mid-ocean ridge basalt (MORB) (C_{Ag} = 0.0718 ppm, sample: T3-72D254-16-4, Keays and Scott, 1976) and a Hawaiian basalt from the Kilauea Iki lava lake (C_{Ag}= 0.09 ppm, sample: 67-3-6.8, Greaney et al., 2017) under sulfide-free conditions. In this example, Kilauea Iki is thought to be analogous to a sulfide-undersaturated degassing cumulate pile.

As illustrated in Figure 10, Ag increases in both the volatile and liquid phase as the weight fraction of silicate liquid decreases. Also plotted is a dashed line corresponding to Ag saturation in a S-free basaltic liquid (~ 5.5 ppm, Zajacz et al., 2013). For MORB liquid, extreme fractionation (F = 0.002) is required before MORB liquid reaches Ag saturation values of ~ 5.5 ppm. Because $D_{Ag}^{vap/liq}$ is 10, coevolving MORB vapor saturates in Ag much sooner during the evolution of the liquid (F = 0.02). The evolution of the Hawaiian basalt is identical in behavior except that saturation of Ag in the liquid and vapor occurs earlier in the evolution of the liquid (F = 0.015 and 0.15, respectively). In the absence of sulfide, Ag (and other metals with a similar affinity for Cl) will preferentially concentrate in the coevolving vapor phase. This observation is confirmed by a number of studies that investigate gas condensates from volcanic fumaroles (Yudovskaya et al., 2006; Yudovskaya et al., 2008; Chaplygin et al., 2015).

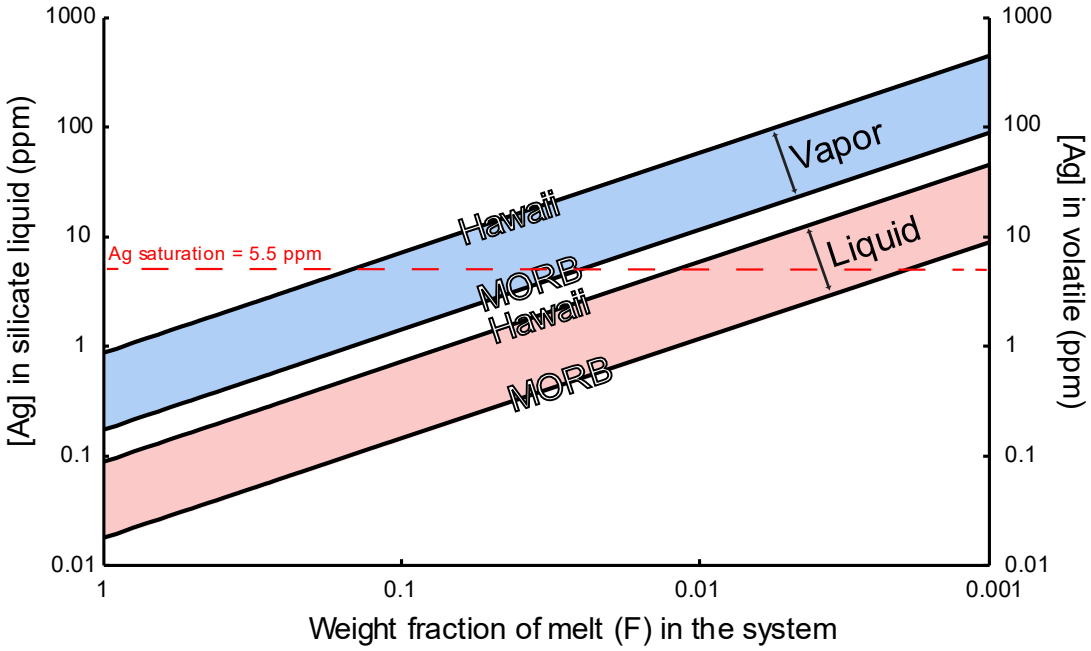

Figure 10: Numerical calculation of Ag enrichment in end-member basaltic liquids and evolving vapor as a function of fraction of silicate liquid remaining. Ag concentrations for the liquid (red) and co-existing vapor (blue) are shown for Hawaiian basalt and MORB. The horizontal red dashed line indicates the saturation level of Ag in a S-free basaltic liquid (~ 5.5 ppm, Zajacz et al., 2013). See text for further discussion.

In the following, the partitioning of Ag into a volatile phase in both sulfide-free (Case 1) and sulfide-bearing (Case 2) systems is examined. We follow the methods of Boudreau and McCallum (1992) where fractional vaporization from an interstitial liquid is assumed like fractional melting and is described by equation (10);

$$\frac{C_r}{C_o} = \left(1 - F_{vap}\right)^{\left(\frac{1}{D}-1\right)} \tag{10}$$

Where, C_r = the residual concentration of the element of interest, C_o = the initial concentration of the element of interest, F_{vap} = the weight fraction of vapor exsolving from the silicate liquid and D = bulk partition coefficient given by equation (11);

$$D = \left(\frac{X_{liq}}{D_{liq}}\right) + X_{sulf} * \left(\frac{D_{sulf}}{D_f}\right) \tag{11}$$

Where, X_{liq} = the weight fraction of silicate liquid remaining in the system, X_{sulf} = the weight fraction of sulfide in the system, D_f = the fluid/silicate liquid partition coefficient while D_{sulf} = the sulfide/silicate liquid partition coefficient for the element of interest. Finally, the concentration of the element of interest in the separated fluid at any interval is given by:

$$\frac{C_f}{C_o} = \frac{1}{D} * \frac{C_r}{C_o} \tag{12}$$

where, C_f = the concentration in the exsolved fluid.

Case 1. The partitioning of Ag into an exsolved fluid in a sulfide-free system (Figure 11a, b). Here, it is assumed that 75% silicate liquid has crystallized to form silicate minerals while 25% interstitial silicate liquid remains. The liquid is undersaturated in volatiles. The interstitial liquid is considered to saturate in Cl-bearing vapor at 5% such that for every 1% silicate liquid crystallized, 5% of that is Cl-bearing vapor. Initial Cl concentrations of 1, 5, 10, and 20 mol are assumed corresponding to modest values of 12.5, 62.5 125, and 250 ppm (ϱ = 2.8 g/cm^3) or $D_{Ag}^{fluid/silicate}$ values of 4,

20, 40, and 80, respectively (Zajacz et al., 2008). Cl is perfectly incompatible in the solids prior to vapor saturation so that concentrations increase exponentially as crystallization takes place. As shown in Figure 11a and b, residual concentrations are most affected by larger Ag fluid/silicate liquid partition coefficients where residual Ag concentrations are half the original value after ~ 20% silicate liquid has crystallized and the bulk weight fraction H_2O has evolved to ~ 0.012. Similarly, Ag in the exsolved fluid is highest in the early stages of fluid evolution before values diminish due to dilution (Figure 11b).

Case 2. Figure 11c and d show a similar calculation for a sulfide-bearing system composed of 74.9% crystals, 25% silicate liquid, and .1% sulfide liquid. Cl molarities remain unchanged from *Case 1*. It is assumed that the liquid is sulfide saturated at 400 ppm S. Each fraction of water evolved contains 5% S which is subtracted from the starting S content before each subsequent calculation. The Ag sulfide/silicate liquid partition coefficient is taken to be 1000 (Jenner, 2017) while Ag fluid/silicate liquid partition coefficient values are as in the S-free calculation. Calculations suggest that minimal change is observed in residual concentration prior to sulfide being completely exhausted (vertical blue line, Figure 11c, d). This is in large due to the high Ag sulfide/silicate liquid partition coefficient values suggesting the partitioning of silver into a fluid in a sulfide-bearing system is controlled by the amount of sulfide present.

Indeed, for each $D_{Ag}^{fluid/silicate}$ value, concentration in the exsolved fluid is maximized after sulfide is entirely exhausted (Figure 11d).

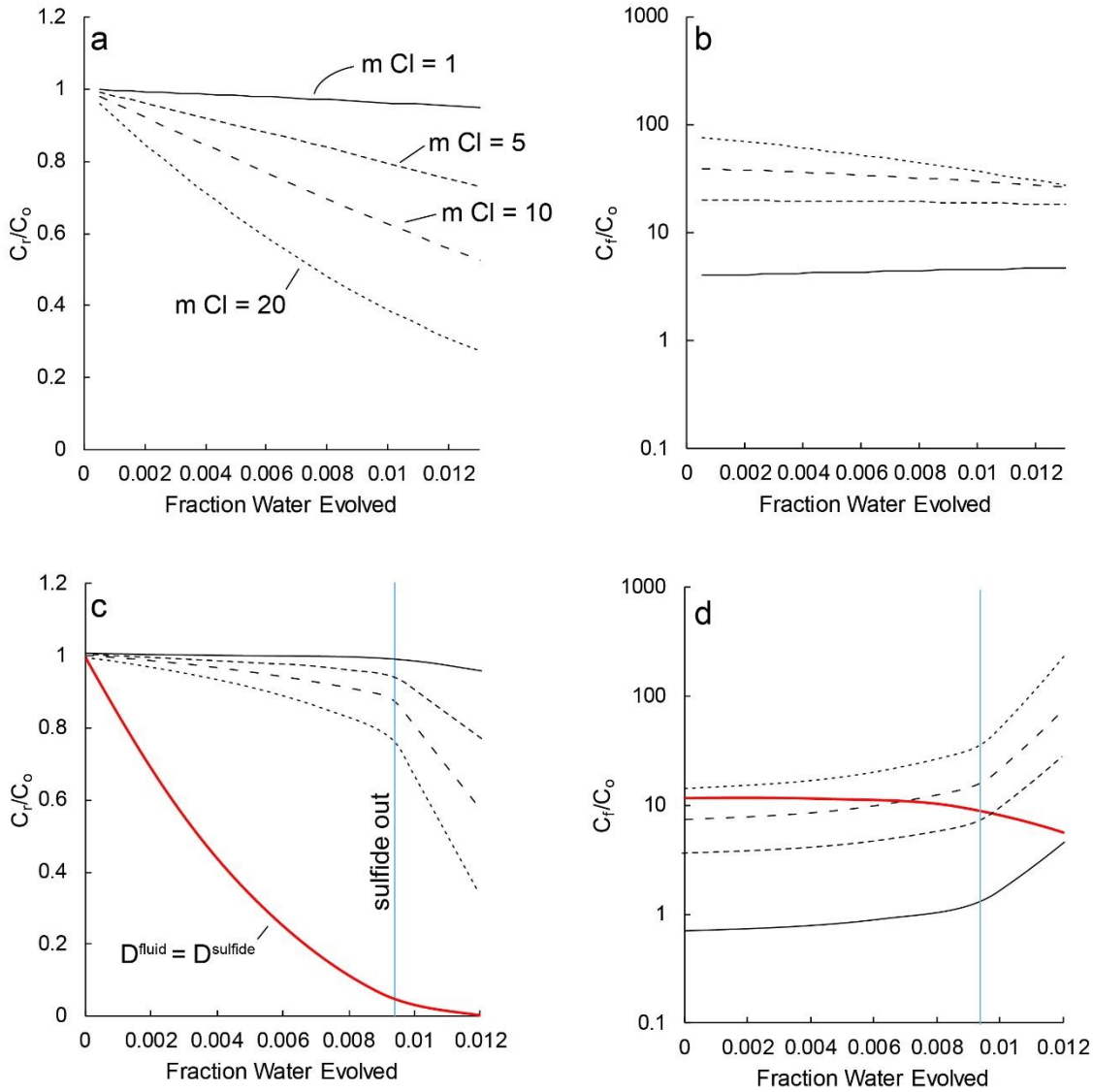

Figure 11: Numerical calculations simulating the dissolution of Ag in sulfide-free (top) and sulfide-bearing (bottom) systems. See text for further discussion.

In either scenario, calculations suggest that a volatile phase efficiently removes Ag from the residual silicate liquid. In the sulfide-free system, the earliest exsolved fluid (X_{water} < .002) experiences the highest enrichment in Ag that decreases as Ag is removed from the system. The residual silicate liquid experiences a gradual reduction in Ag content as vapor is lost. In the sulfide-bearing system, Ag in the residual silicate liquid is most affected after sulfide is totally resorbed during S loss to the vapor (at X_{water} ~ .0094). This suggests that, if sulfide is present, Ag will be preferentially partitioned into sulfide unless large fractions of volatiles evolve from the interstitial silicate liquid or $D_{Ag}^{fluid/silicate}$ values are sufficiently high.

2.6.6 Evaluating Existing Genetic Models for the Skaergaard Intrusion Metal Budget

Although this contribution is based on a limited number of samples, reconciling observations presented here with the late-stage evolution of the Skaergaard and existing genetic models for the Platinova Reef is worthwhile. Godel et al. (2014) and Nielsen et al. (2015) suggest that discordant Au mineralization in the Platinova Reef is explained by the late-stage evolution of hydrothermal fluids. Textural observations presented in this study confirm the existence of metal + brine assemblages and support the ideas of Godel et al. (2014) and Nielsen et al. (2015). The limited number of PGE outside of the Reef with the observed absence of Pd might reflect differences in $D^{sulfide/silicate}$ where $D^{sulfide/silicate}$ Pd > Pt >> Au > Ag ≈ Cu (Mungall and Brenan, 2014). It is possible that

existing sulfide would scavenge PGE preferentially based on $D^{sulfide/silicate}$ values. Limited sulfide availability would prevent the partitioning of lower $D^{sulfide/silicate}$ elements (e.g., Au, Ag, Cu) into sulfide allowing for concentration in the evolving silicate liquid where exsolved hydrothermal fluids might ultimately transport these metals along grain boundaries. One obvious complication to this hypothesis is the observation that a distinct Cu-sulfide zone exists in the Platinova Reef and this occurrence is commonly attributed to orthomagmatic processes (Holwell and Keays, 2014; Keays and Tegner, 2016). Further, native Cu reported in this study is spatially related to sulfide minerals and is likely the result of oxidation processes.

The limited number of PGE and PGM observed outside of the Reef might be the result the limited number of samples examined in this study. While little can be said about the petrogenesis of the Platinova Reef, it is important to emphasize that our results indicate that late magmatic hydrothermal fluids are, in some instances, directly linked to precious metals, particularly Ag and Au. For both Ag and Au, evidence suggestive of a coexisting metal + Cl-bearing phase are observed. If fluids contemporaneously oxidized magmatic sulfides, the S lost from below the Platinova Reef and its transport upward could give rise to sulfide saturation in the upper parts of the crystal pile. In this case, the exsolved fluid would consist of metals complexed as Cl and S species. Variable redox sensitivity (Cl^+ vs HS^-) would act to separate metals

transported as Cl complexes (Ag) from those transported as S complexes (Au) (Li and Boudreau, 2019). In this scenario, the net result would not be unlike the Pd, Au, Cu offsets described by others (Bird et al., 1991; Andersen et al., 1998; Nielsen et al., 2005; Holwell and Keays, 2014).

2.6.7 Genetic Model

A model is proposed where Ag, with other Cl soluble elements having low $D^{mnrl/melt}$ partition coefficients, Au in particular, becomes increasingly concentrated in the residual liquid during crystallization. At low liquid/silicate mineral mass fraction (F), Ag is concentrated in the interstitial liquid. At this point, or shortly thereafter, enough silicate liquid volume has crystallized to allow for the separation of H_2O, CO_2, Cl and other volatile components with low $D^{mnrl/melt}$partition coefficients. Owing to its relatively high $D^{fluid/silicate}$ partition coefficient, Ag partitions into the exsolved fluid as Ag-chloride or perhaps Na-Ag-chloride. The exsolved fluid transporting Ag will travel vertically along grain boundary networks, and fluid pathways, interacting with other interstitial phases. Heating of the fluid as it moves into hotter regions can lead to S and SiO_2 loss from the host assemblage while leaving behind a small portion of the Ag-bearing volatile phase. Eventual cooling of the fluid can cause Ag precipitation or, when a fluid-undersaturated interstitial liquid is encountered, re-dissolution of the fluid initiates the precipitation of Ag and perhaps an increased volatile content for that section

of the intrusion. Minor amounts of metal + volatile are trapped in the interstitial liquid and are presumed to have generated textures seen in Figure 4a, and Figure 7. The cumulative effect of this process most affected the MZ where the silicate liquid became saturated in fluid + vapor early enough to preserve fluid inclusions in olivine, clinopyroxene, and plagioclase.

2.7 Conclusions

Evidence for S loss is present throughout the Skaergaard stratigraphy, with the relative proportion of low-Ti magnetite replacing sulfide being most extensive in the LZ. Native Ag is regularly associated with trace quantities of Cl in and below the MZ, consistent with a coexisting metal + brine assemblage. Ag, and other Cl soluble metals can be readily mobilized by an exsolved volatile Cl-bearing phase in both sulfide-free and sulfide-bearing liquids. This contribution has implications for the origins of the Platinova Reef. In particular, our work supports the assertions of Godel et al. (2014) and Nielsen et al. (2015) who attribute Au mineralization to late hydrothermal fluids. Ultimately, it is suggested that a late fluid rich in halides transported Ag and perhaps other precious metals vertically through the Skaergaard cumulate pile. Numerical modeling suggests that the Kilaeua Iki lava lake may be analogous to a S-free degassing cumulate pile. Indeed, it is possible that Ag and Au are readily mobile provided the magma is S-poor or experienced an early sulfide saturation event. Finally, this

contribution presents new evidence supportive of late hydrothermal processes in LMIs and suggests that similar work may clarify late-stage evolution of other intrusions, particularly those intrusions where evidence of hydrothermal activity has been reported (e.g., Stillwater, Bushveld).

3. The major element, trace element, and $^{87}Sr/^{86}Sr$ characteristics of basaltic lavas from the Cocos-Nazca Spreading Center

3.1 Chapter Summary

The Cocos-Nazca Spreading Center is a westward propagating rift located ~ 30 km east of the fast spreading East Pacific Rise (EPR) in the equatorial Pacific Ocean. During a research cruise in 2018, the Cocos-Nazca Spreading and adjacent regions were geophysically surveyed and basaltic rock samples were collected during 60 dredges. Glass and whole rock major element concentrations, trace element concentrations, and $^{87}Sr/^{86}Sr$ ratios for basaltic lavas from the Cocos-Nazca Spreading Center, the adjacent EPR, and the Dietz Volcanic Ridge south of the Cocos-Nazca are reported here. Lavas from the Cocos-Nazca Spreading Center are relatively primitive (Mg# = 55 – 65) and limited in their overall chemical variability. Comparisons to regional, northern EPR, and global mid-ocean ridge basalts (MORB) indicate that these lavas are unusually depleted with respect to incompatible trace elements (e.g., La/Sm_N as low as 0.38). Mantle melting calculations suggest that Cocos-Nazca lava compositions are consistent with a mantle source that is more depleted than would be expected for lavas generated from typical depleted MORB mantle (Workman and Hart, 2005). This is attributed to prior melt extraction at the adjacent EPR, and subsequent re-melting of depleted mantle beneath the Cocos-Nazca rift. For segments within the deep western Cocos-Galapagos spreading

domain (segments 2-4), a systematic decrease in segment-averaged $Fe_{8.0}$, La/Sm_N, and Nb/Y with distance from the Cocos-Nazca gore tip correlates with an increase in spreading rate and is attributed to a small increase in mean extent and pressure of melting eastward across this domain. For segments within the eastern Cocos-Nazca spreading domain (segments 5-9), segment-averaged $Fe_{8.0}$, La/Sm_N, and Nb/Y are relatively constant. This coincides with constant spreading rates and an overall increase in segment maturity. These observations are attributed to the establishment of a stable mantle melting regimes beneath segments in this eastern domain.

In contrast to the depleted nature of lavas from the Cocos-Nazca rift, basalts from the Dietz Volcanic Ridge, which forms the southern boundary of the Galapagos microplate, are geochemically considered normal-MORB to transitional-MORB (La/Sm_N from 0.69 to 0.87). Comparisons to other lavas in the region indicate that these are among the most enriched compositions found west of 98°W. Coupled with a ridge axis that is almost 700 m shallower than the adjacent EPR, this supports the hypothesis of Smith et al. (2013) that the formation of the southern boundary of the Galapagos Microplate, now represented by the Dietz Volcanic Ridge, was linked to the development of a mini hotspot in the region.

Like the Cocos-Nazca Spreading Center, EPR lavas sampled 30 km west of the Cocos-Nazca rift tip, as well as samples collected previously from the

Incipient Rift north of the Cocos-Nazca Spreading Center are chemically depleted relative to typical northern EPR samples. Available geochemical data thus suggests a large-scale regional depletion in source composition, apparently not seen elsewhere along mid-ocean ridges.

3.2 Introduction

The Cocos-Nazca Spreading Center (Cocos-Nazca, Figure 12) is a v-shaped, westward propagating, rift located in the eastern equatorial Pacific (Lonsdale, 1988). To the east, the Cocos-Nazca merges into the more commonly known Galapagos gore (Holden and Dietz, 1972). The tip of Cocos-Nazca spreading center is located approximately 30 km east of the EPR and rifts into ~ 0.4 Ma oceanic crust that was accreted at the EPR (Lonsdale, 1988). The position of the rift tip relative to the EPR has remained fixed for the last ~1 Ma (Lonsdale, 1988; Smith et al., 2013). Early workers (Hey, 1977; Lonsdale, 1988; Lonsdale, 1992) identified and characterized key tectonic features in this region, including in the east, the Galapagos hotspot and platform, the Galapagos Spreading Center, the Dietz Volcanic Ridge, and the Incipient Rift (Figure 12). Investigations over four decades have led to an understanding of much of the tectonic evolution of this part of the eastern equatorial Pacific on both large and small scales (Hey, 19777; Lonsdale, 1988; Francheteau et al., 1990; Lonsdale, 1995; Schouten et al., 2008; Smith et al., 2011; Smith et al., 2013; Smith et al., 2020).

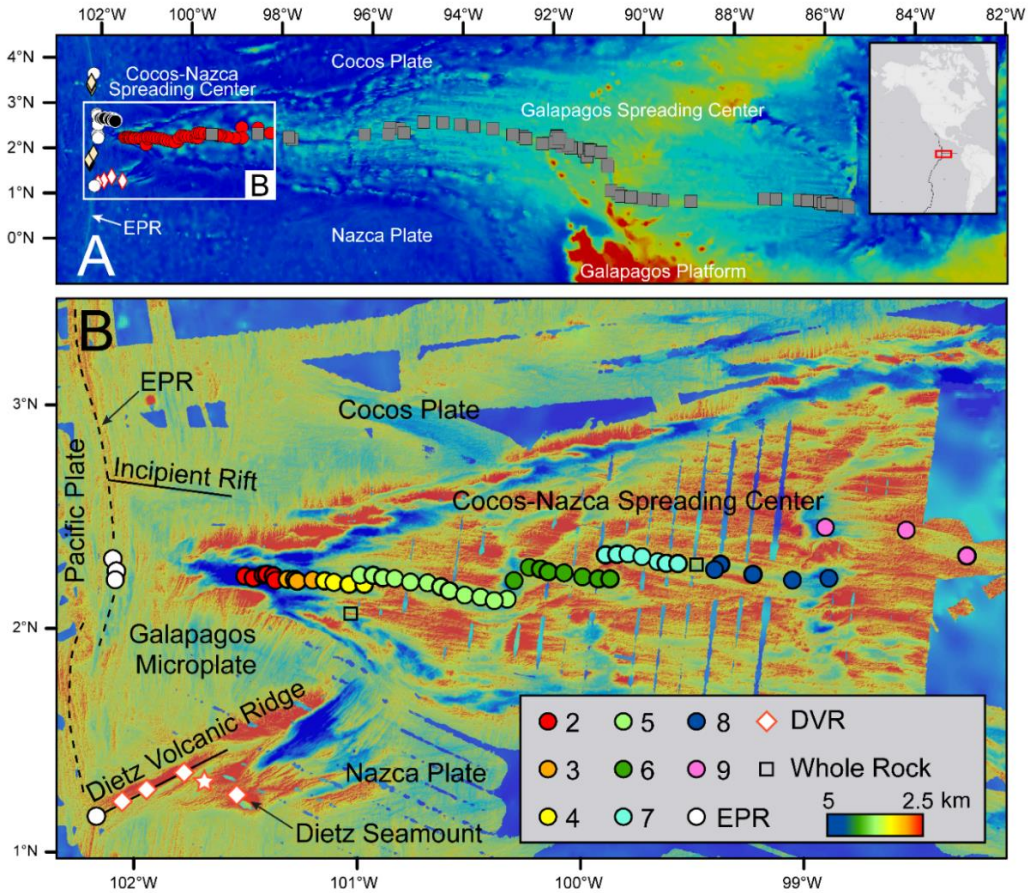

Figure 12: Bathymetric map of the eastern equatorial Pacific (top) and the Cocos-Nazca Spreading Center (bottom). A) Satellite bathymetry map (data from: www.marine-geo.org) of the eastern equatorial Pacific region in the vicinity of the Galapagos and Cocos-Nazca spreading centers, with sample locations for this and previous studies. The inset shows the field of (A) in relation to North and South America. Red circles = Cocos-Nazca Spreading Center, grey squares = Galapagos Spreading Center, white circles = EPR, black circles = Incipient Rift, white diamonds = Dietz Volcanic Ridge, and beige diamonds = AHA Nemo cruise (Smithka and Perfit, 2013; M. Perfit, personal communication). B) Multi-beam map of the Cocos-Nazca Spreading Center and the surrounding area. Points correspond to individual dredge locations and are color coded according to ridge segment (2 through 9 in the legend), EPR, and Dietz Volcanic Ridge. The locations of the two whole rock samples analyzed are shown as squares with black outlines and the approximate location of the Dietz hotspot (Smith et al., 2013) is shown as a white star with a red outline.

For example, geophysical studies have led to a better understanding of the temporal evolution of the Galapagos and Cocos-Nazca Spreading Centers and the associated subduction of the Farallon plate in this region (e.g., Hey, 1977; Lonsdale, 1995). In addition, westward propagation of the Cocos-Nazca has given rise to a series of northwest-southeast trending transient rifts to the north at ~ 2°40′N (Incipient Rift, Schouten et al., 2008) and northeast-southwest trending transient rifts to the south at ~ 1°15′N. Unlike the Cocos-Nazca, these transient rifts formed true ridge-ridge-ridge configurations with their adjacent EPR segments. The recent (< 1.4 Ma) development of the southern boundary of the Galapagos microplate has been attributed to a mini hotspot in the region (Smith et al., 2013).

Geochemical investigations of lavas recovered from this region have provided information about the influence of the Galapagos hotspot on the neighboring Galapagos Spreading Center. For example, it has been demonstrated that the geochemical influence of the Galapagos hotspot on the neighboring Galapagos Spreading Center is greatest near the hotspot (~ 91°W) and diminishes with increasing distance from the hotspot (Detrick et al., 2002; Cushman et al., 2004). The Galapagos Spreading Center (Detrick et al., 2002; Cushman et al., 2004) and Galapagos hotspot (White et al., 1993) have been relatively well-sampled and studied, as has the Hess Deep (Franchetau et al., 1990; Franchetau et al., 1991; Gillis et al., 1993; Gillis et al., 2014). In contrast, there has been

only limited previous sampling of ~ 360 km of the Cocos-Nazca rift, the adjacent East Pacific Rise (EPR), or the Dietz Volcanic Ridge to the south (Figure 12a).

To better understand the geochemical and geophysical evolution of the Cocos-Nazca spreading center and the processes that occur during the transition from initial rifting to magmatic seafloor spreading, a 37-day scientific cruise aboard the *R/V Sally Ride* (Leg 1806) was conducted during April and May 2018. Here, we report geochemical analyses of lavas collected from the region. Interpretations of geophysical and geologic data collected are reported by Zheng et al. (2019) and Smith et al. (2020).

3.3 Geological Background

The Cocos-Nazca rift acts to separate three major tectonic plates in the region with the Pacific plate located west of the north-south trending EPR and the Cocos and Nazca plates located north and south of the Cocos-Nazca rift, respectively (Figures 12 and 13c). The Incipient Rift (~2°40'N) and Dietz Volcanic Ridge (~1°15'N) form true ridge-ridge-ridge triple junctions with their local EPR segments and are found north and south of the Cocos-Nazca, respectively. The Dietz Volcanic Ridge forms the southern boundary of the Galapagos microplate (Schouten et al., 2008; Smith et al., 2013). Southeast of the Dietz Volcanic Ridge, at approximately (1°12'N, 101°30'W), is a large (~ 2500 mbs) seamount. The current position of the 'mini hotspot' described by Smith et al. (2013) is between the Dietz Volcanic Ridge and the seamount, at ~ 101°36'N.

The genetic relationship between the Cocos-Nazca rift, the Incipient Rift and the Dietz Volcanic Ridge were described in a model of regional stresses advanced by Schouten et al. (2008), Smith et al. (2011), and Mitchell et al. (2011). In this model compressive forces related to the propagation of the Cocos-Nazca rift are minimized at the points where the Incipient Rift and the Dietz Volcanic Ridge intersect the EPR, leading over time to the development of a series of symmetric transient rifts to the north and south of the Cocos-Nazca Spreading Center (Figure 13). After 1.4 Ma, the southern transient rifts ceased movement and became 'fixed', forming the Dietz Volcanic Ridge and the southern boundary of the Galapagos microplate (Smith et al., 2013). This change at about 1.4 Ma is attributed to presence of a 'mini hotspot' that migrated across the EPR to its current location just northwest of the Dietz seamount (Smith et al., 2013). Westward propagation of the Cocos-Nazca created the 5500 m deep Hess Deep basin (Hey et al., 1977; Lonsdale, 1988; Francheteau et al., 1990; Francheteau et al., 1992) that exposes upper mantle lithologies and has been the site of multiple submersible (Francheteau et al., 1990) and ocean drilling program (e.g., ODP Leg 147; Gillis et al., 1993; IODP Expedition 345; Gillis et al., 2014) studies, which have provided important information about the structure of the oceanic crust (Francheteau et al., 1991; Gillis et al., 2014), melt migration processes (Lissenberg et al., 2013), as well as fluid-rock interaction (e.g., Gillis et al., 2001).

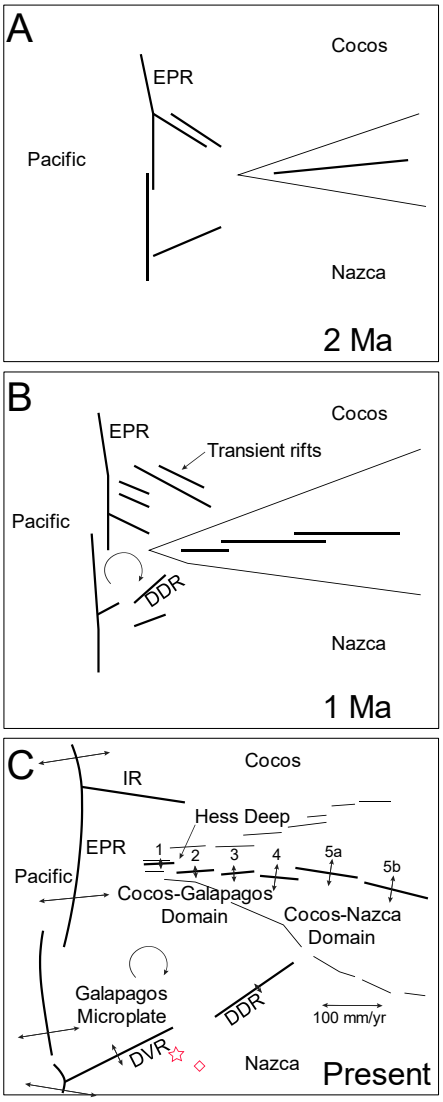

Figure 13: Schematic illustration of the evolution of the Cocos-Nazca Spreading Center from 2 Ma to present. Figure after Schouten and Smith (2008) and Smith et al. (2020). C) Cocos-Nazca segments are labeled (1-5). It is important to note that Smith et al. (2020) separate segments 5 and 6 into two 'subsegments'. Arrows are scaled to reflect spreading rate. The Cocos-Galapagos and Cocos-Nazca spreading domains are labeled. Abbreviations: EPR = East Pacific Rise, DVR = Dietz Volcanic Ridge, DDR = Dietz Deep Rift. The approximate location of the Dietz seamount and Dietz hotspot of Smith et al. (2013) are shown as a diamond and star, respectively. The Cocos-Galapagos and Cocos-Nazca domains are found within the Cocos-Nazca Spreading Center.

Along the Cocos-Nazca rift, in its current configuration, in the west rifting occurs between the Cocos plate and the Galapagos microplate (segments 1-3, Smith et al., 2020; Figure 13c). Ultra-slow to slow spreading rates between 19 and 29 mm/year are calculated for this domain. To the east, spreading occurs between the Cocos and Nazca plates (segments 4 through 9), with a calculated spreading rate of approximately 48 mm/year. The west-to-east increase in segment spreading rate is accompanied by a general increase in segment length, segment offset distance, and crustal thickness inferred from mantle Bouguer anomalies (Zheng et al., 2019; Smith et al., 2020) and an overall shoaling in axial ridge depth (4500 – 3500 m). The change in spreading domain is manifest in a 10-degree change in ridge axis strike (087° for Cocos-Galapagos, 097° for Cocos-Nazca, Smith and Schouten, 2018). Importantly, Smith and Schouten (2018) suggest that the transition from initial amagmatic to sparsely magmatic rifting to magmatic seafloor spreading is established by segment 3, within the Cocos-Galapagos spreading domain.

East of our study area, the Cocos-Nazca merges into the intermediate-spreading (50 mm/year, DeMets et al., 1994) Galapagos Spreading Center (Figure 12a), whose morphology (Canales et al., 2002; Sinton et al., 2003; Christie et al., 2005) and axial lava chemistry (Cushman et al., 2004; Christie et al., 2005) is strongly influenced by the Galapagos hotspot at ~ 91°W. Segmentation and axial morphology in this region is

complex with multiple propagating rifts at 95°30′W, 95°15W, and 85°W (Christie and Sinton, 1981). Geochemical indicators of an enriched mantle source correlate with thickening of the crust and are thought to reflect the influence of the Galapagos hotspot (Detrick, 2002; Cushman et al., 2004; Christie et al., 2005). For example, enriched-MORB (E-MORB) compositions are observed east of 92°36′W (Figure 14) in close proximity to the Galapagos hotspot, while transitional-MORB (T-MORB, between the 95°30′W propagator and 92°36′W) and normal-MORB (N-MORB, between 98°W and the 95°30′W propagator) are observed with increasing distance away from the hotspot (Detrick et al., 2002; Cushman et al., 2004). Using trace element and H_2O concentrations in basalt, Detrick et al. (2002) placed the western extent of the Galapagos hotspots geochemical influence at ~ 95°30′W. Using radiogenic isotopes (Sr, Nd, Pb), Schilling et al. (2003) extended the western boundary to ~ 99°30′W (within our study area), although this was based on limited sampling (two samples reported between 100°W and 98°W).

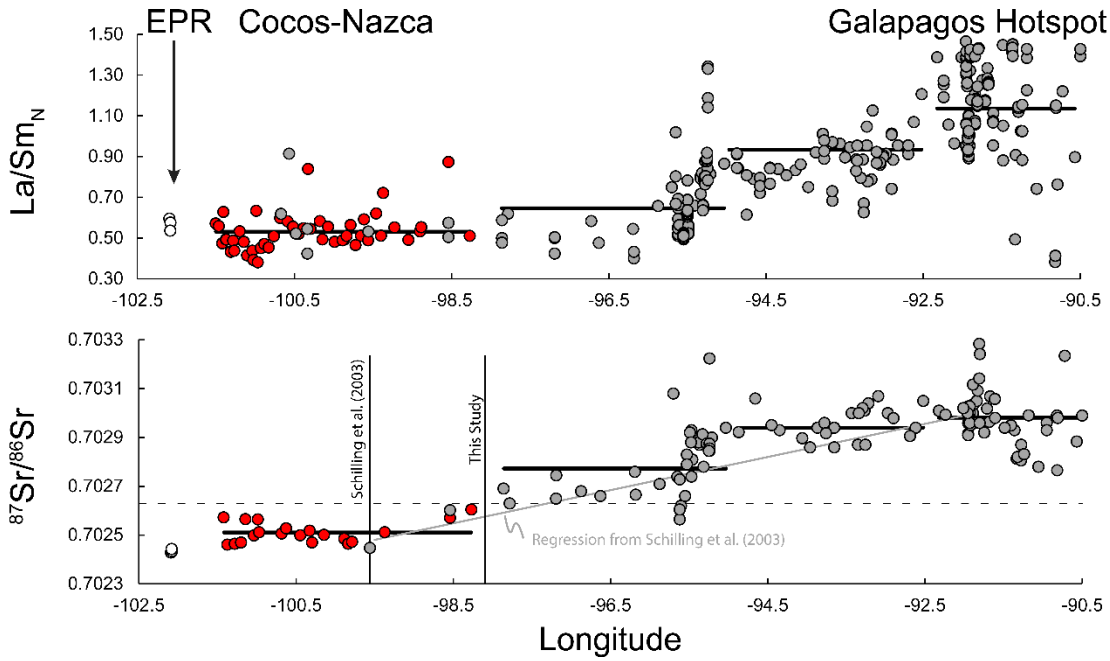

Figure 14: Longitudinal variation (102.5°W to 90.5°W) of La/Sm$_N$ (top) and ^{87}Sr/^{86}Sr (bottom). Figures include data from the EPR (white circles, this study), Cocos-Nazca Spreading Center (red circles, this study), and the Galapagos Spreading Center (grey squares, PetDB, www.earthchem.org/petdb). The horizontal black lines in both figures represent the average La/Sm$_N$ and ^{87}Sr/^{86}Sr values for the Cocos-Nazca (101°W to 98°W), Galapagos Spreading Center N-MORB (98°W to 95°W), Galapagos Spreading Center T-MORB (95°W to 92°36'W), and Galapagos Spreading Center E-MORB (east of 92°36'W). The dashed line in the lower figure corresponds to a reference ^{87}Sr/^{86}Sr ratio of 0.70263. The vertical lines labeled Schilling et al. (2003) and This study correspond to the western extent of the Galapagos hotspot chemical signature determined by Schilling et al. (2003) and determined in this study. ^{87}Sr/^{86}Sr ratios from the literature are corrected to a measured NBS 987 ^{87}Sr/^{86}Sr of 0.710254 following the methods of Jenkyns et al. (1995).

3.4 Sample Description

Lavas were collected April-May 2018 aboard the *R/V Sally Ride* (Leg SR1806). Of the 66 deployed dredges, basaltic lavas were recovered in 60 dredges. In general,

collected rocks range from small (≤ 2 cm in diameter) glass nodules to large (> 100 cm in diameter) pillows. Where present, plagioclase is the main phenocryst. Of note is the occurrence of phyric (20 % of the collected samples have ≥ 5 % plagioclase) and plagioclase ultraphyric basalts (> 15% plagioclase, Lange et al., 2013a). The size distribution, morphological, and chemical characteristics of plagioclase in the plagioclase-phyric lavas are the subject of Chapter 3. A comprehensive description of dredges and samples is available from the University of California San Diego and Scripps Institution of Oceanography Geologic Data Center (http://gdc.ucsd.edu/), and geologic sample repository (https://scripps.ucsd.edu/collections/gc).

3.5 Methods

Geochemical analyses were performed on one sample from each dredge that recovered basalt. This includes 49 glass and two whole rock samples from the Cocos-Nazca rift, five glass samples from the EPR, and four glass samples from the Dietz Volcanic Ridge (Figure 12b). Basaltic glass was handpicked using a binocular microscope at Duke University to avoid alteration and phenocrysts. Whole rock samples were powdered in an agate mortar to < 60 μm and homogenized prior to preparation for chemical analysis.

Major elements and high abundance trace elements (Zn, Mn, Co, Cu, Sr, Ni, V, Ba, Sc, Cr, Y, and Zr) were measured using a Fisons SpecterSpan 7 Direct Current

Plasma Emission Spectrometer (DCP) at Duke following the methods of Klein et al. (1991). Each sample was run in triplicate and the average is reported (Appendix B, Table 8). Low-abundance trace elements were measured using a Thermo-Fisher VG PlasmaQuad 3 Inductively Coupled Plasma Mass Spectrometer (ICP-MS) at Duke following a two acid ($HF-HNO_3$) digestion procedure modified after Cheatham et al. (1993). For each method, standards used for calibration include U.S. Geological Survey BHVO-1 and BIR, NBS-688, and an internal standard, K1919, from the same flow as USGS BHVO-1.

Trace elements analyzed by both DCP and ICP-MS (V, Cr, Co, Ni, Zn, Sr, Y, Zr, and Ba) were compared and found to be in excellent agreement (e.g., correlation coefficient $R^2 > 0.90$) for all elements except Zr ($R^2 \sim 0.5$). For a majority of samples, Zr values measured by ICP-MS were significantly lower (by as much as 65%) than those measured by DCP. Previous studies have reported difficulties in the analysis of HFSEs arising from incomplete acid digestion of mineral phases (e.g., zircon) and/or precipitation of HFSE-bearing fluoride minerals during $HF-HNO_3$ digestions (e.g., Yokoyama et al., 1999; Nikolaeva et al., 2008 and references therein). To determine whether our discrepancies in Zr measurements were due to the $HF-HNO_3$ digestion procedure used for ICP-MS analyses, a subset of 19 samples were reanalyzed using both the DCP and ICP-MS following $LiBO_2$ flux-fusion. For analysis by ICP-MS, solutions of

fused samples were centrifuged and diluted 100-fold. This procedure led to excellent agreement in Zr values measured by DCP and ICP-MS ($R^2 \approx 0.97$), suggesting that our initial low Zr values by ICP-MS were due to incomplete digestion using the two-acid technique. It was also investigated whether other HFSE were potentially affected by incomplete acid dissolution by comparing ICP-MS analyses of flux-fused solutions and HF-HNO_3 digested solutions of the same samples. Interestingly, this comparison showed generally good agreement, with Nb, Hf, and Ta R^2 values of 0.98, 0.98, and 0.85, respectively. All of the Zr data presented in this chapter was collected following a flux-fusion. See Appendix B for additional information.

In addition to major and trace elements, $^{87}Sr/^{86}Sr$ ratios were collected for a subset of 27 samples. Following a cation separation, $^{87}Sr/^{86}Sr$ ratios were analyzed using a VG Sector 54 thermal ionization mass spectrometer at the University of North Carolina at Chapel Hill following the methods of Miller et al. (1995). $^{87}Sr/^{86}Sr$ ratios are relative to NBS 987 ($^{87}Sr/^{86}Sr = 0.710254$, $2\sigma = 0.000015$, n = 30). All data are normalized to an $^{88}Sr/^{86}Sr$ of 0.1194, assuming exponential fractionation. Internal precision for each analysis is better than the reproducibility of the standard. Basalt samples are assumed to be zero age such that no age correction was applied.

3.6 Results

3.6.1 Major Elements

3.6.1.1 Cocos-Nazca Spreading Center

Cocos-Nazca lavas are relatively primitive (Mg# ≈ 55 – 65) with limited variability in MgO (~ 7.5 – 9.5 wt. %; Table 8). To first order, lavas from the Cocos-Nazca rift system show major element variations (Figure 15a-c) consistent with fractionation of a tholeiitic parental liquid (up to ~ 20% crystallization). Compared to data representing the range in worldwide major element compositions, on the plot of MgO vs Na_2O, Cocos-Nazca lavas fall within the field for the southern EPR. On plots of MgO vs FeO_T and Al_2O_3, however, Cocos-Nazca lavas extend from the field for southern EPR lavas and into the field for lavas from the Kolbeinsey ridge. Liquid lines of decent (LLD) calculated for two relatively primitive samples (D40-1 and D56-1) at 1 kbar total pressure are roughly parallel to the overall observed trends for the Cocos-Nazca data on major element covariation diagrams.

Longitudinal variations indicate that significant intra- and intersegment variability exists in MgO (Figure 16a). In addition, K_2O/TiO_2 ratios are variable from segments 2 through 6 (Figure 16b, K_2O/TiO_2 ≈ 0.05 - 0.11) with little systematic behavior apart from segment 3 where all lavas cluster around 0.07. With the exception of one sample from segment 9 with K_2O/TiO_2 = 0.17, lavas from segment 7, 8, and 9 are much more limited in variability and similar to values observed at the EPR (K_2O/TiO_2 ≈ 0.07).

$Na_{8.0}$ and $Fe_{8.0}$ are fractionation corrected Na_2O and FeO_T concentrations (at MgO = 8 wt. %) and to first order represent, respectively, the mean extent and the mean pressure of mantle melting (Klein and Langmuir, 1987). When compared to the global range in $Na_{8.0}$ (1.5 – 3.5, Klein and Langmuir, 1987), segment averaged $Na_{8.0}$ is limited in variability (Figure 16c), ranging from 2.5 to 2.9, similar to values observed at the local EPR (2.3 to 2.7, this study). Segment averaged $Fe_{8.0}$ (Figure 5d) decreases modestly from west to east (~ 10.5 to ~ 9.5) and is broadly coincident with an observed shallowing of Cocos-Nazca axial ridge depth.

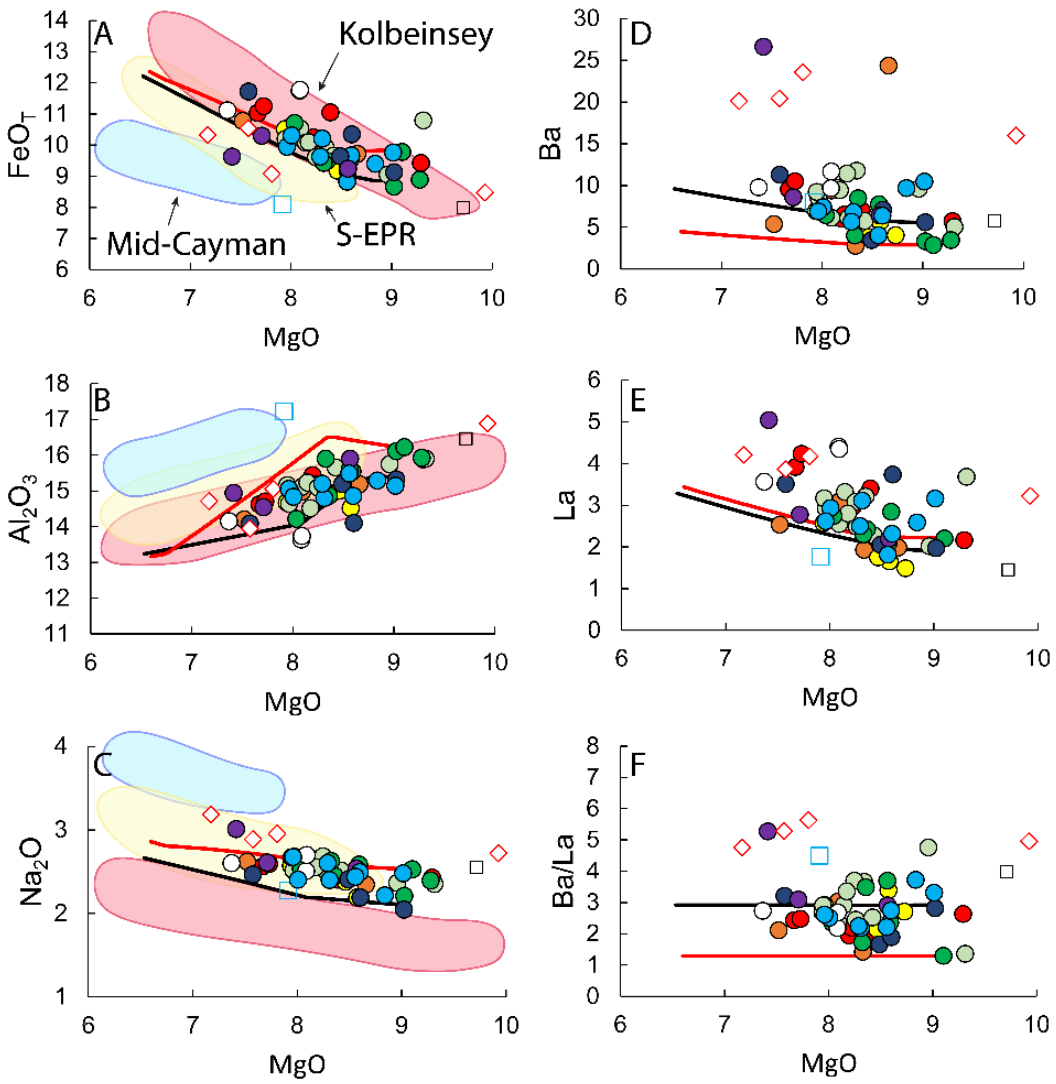

Figure 15: Covariation diagrams for glasses and two whole rock samples from the Cocos-Nazca Spreading Center. Also included are lavas from the adjacent EPR (white circles) and the Dietz Volcanic Ridge (white diamonds with red outline). The liquid lines of decent (LLD) are calculated for samples D40-1 and D56-1 using the program COMAGMAT (Ariskin et al., 1993) at 1kbar total pressure and fO_2 = QFM. Fields for Kolbeinsey Ridge, southern-EPR, and Mid-Cayman Rise (PetDB, www.earthchem.org/petdb) are shown for comparison. Symbols as in Figure 12.

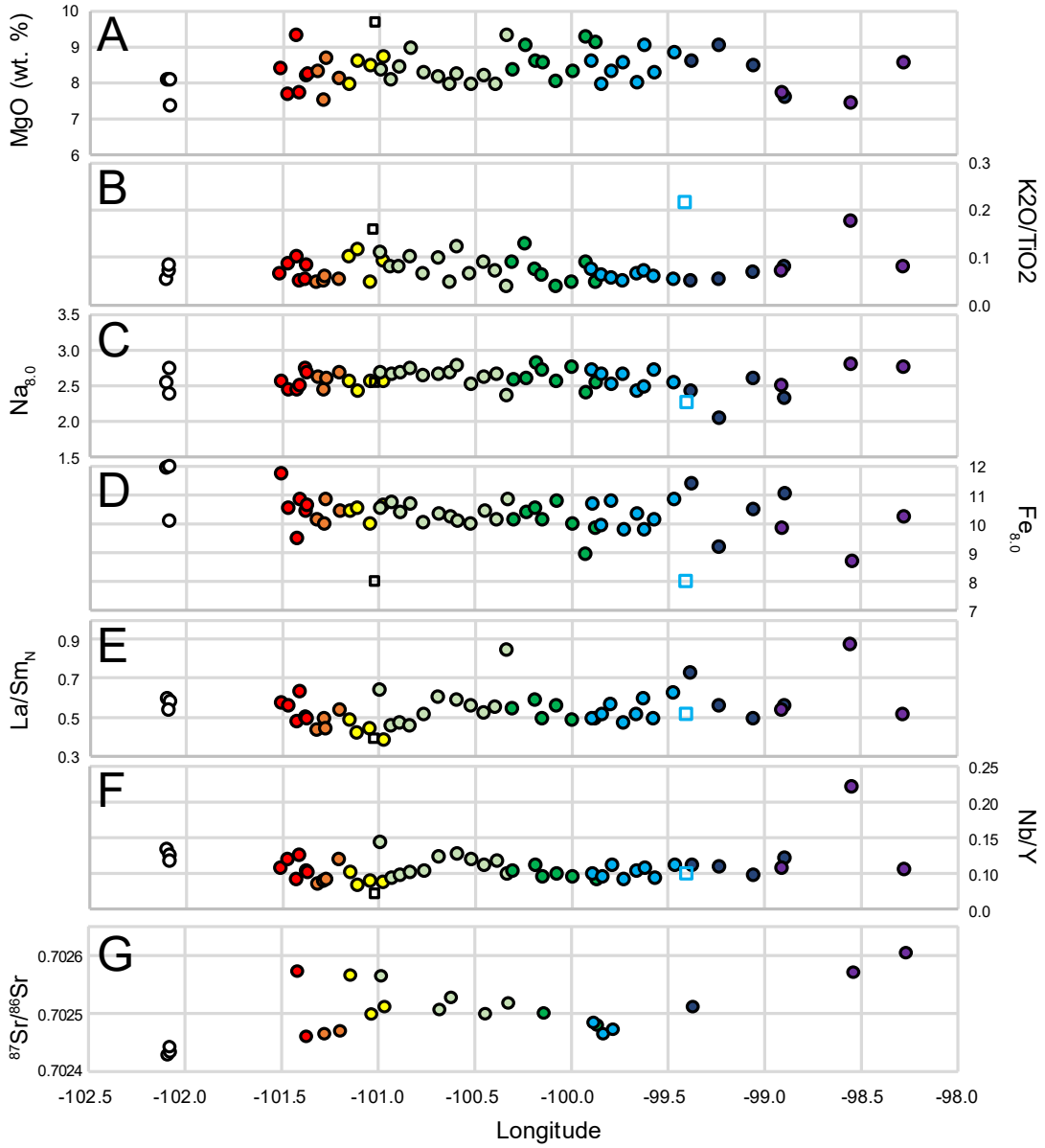

Figure 16: Along-axis variations in MgO, K_2O/TiO_2, $Na_{8.0}$, $Fe_{8.0}$, La/Sm_N, Nb/Y, and $^{87}Sr/^{86}Sr$ for glass and whole rock samples from the Cocos-Nazca and adjacent EPR. Symbols as in Figure 12. The algorithm of Klein and Langmuir (1987) is used to calculate $Na_{8.0}$ and $Fe_{8.0}$.

3.6.1.2 Dietz Volcanic Ridge

Major element variations for samples from the Dietz Volcanic Ridge and the adjoining EPR show values that are similar to those of the Cocos-Nazca (Figure 15). On average, however, at a given MgO, Dietz Volcanic Ridge lavas tend to have higher concentrations of Na_2O and lower concentrations of FeO_T.

Spatial variations along the Dietz Volcanic Ridge (Figure 17a) show a general decrease in MgO extending from the usually high values at the easternmost sampling site (D61; MgO ~ 9.9 wt. %) to lower values westward, with the lowest value (MgO ~ 7 wt. %) sampled where the Dietz Volcanic Ridge links to the EPR. This is broadly consistent with increasing degrees of crystal fractionation from east to west. Similarly, K_2O/TiO_2 is highest for the seamount sample (Figure 17b) and progressively decreases westward before increasing slightly at the adjoining EPR. Assuming a constant source composition, spatial variations in $Na_{8.0}$ (Figure 17c) would suggest a progressive increase in extent of melting from the DVR ($Na_{8.0}$ = ~ 3.4) though the adjacent EPR ($Na_{8.0}$ = ~ 2.5) and a corresponding decrease in the mean depth of melting ($Fe_{8.0}$ from 11.7 to 9.7).

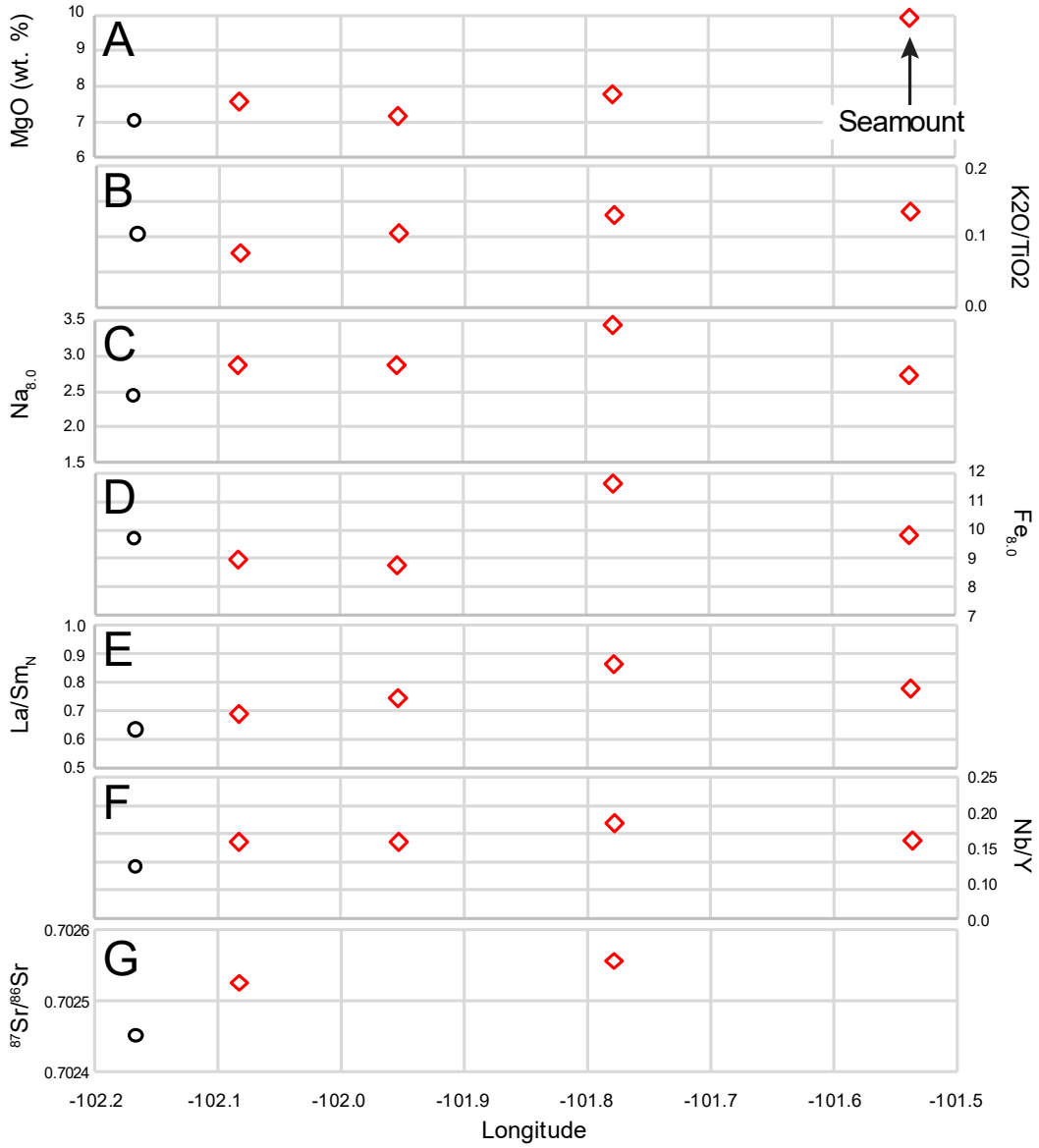

Figure 17: Along-axis variations in MgO, K_2O/TiO_2, $Na_{8.0}$, $Fe_{8.0}$, La/Sm_N, Nb/Y, and $^{87}Sr/^{86}Sr$ for glass from the Dietz Volcanic Ridge and adjacent EPR. Symbols are as in Figure 1. The algorithm of Klein and Langmuir (1987) is used to calculate $Na_{8.0}$ and $Fe_{8.0}$.

3.6.2 Trace Elements

3.6.2.1 Cocos-Nazca Spreading Center

Cocos-Nazca samples have trace element signatures that are unusually depleted (e.g., La/Sm_N as low as 0.38) even compared depleted-MORB (D-MORB, $La/Sm_N < 0.60$) as defined by Gale et al. (2013). On plots of MgO vs Ba, La, and Ba/La (Figure 15d-f), the Cocos-Nazca data as a whole show significant variability at constant MgO. Indeed, the calculated LLDs bisect the scatter of Cocos-Nazca lavas, and trace element variations are not easily explained by fractionation of a single or limited range of parental melt compositions. In general, primitive mantle normalized trace element diagrams (Figure 18) show similar trace element patterns within and between individual Cocos-Nazca segments. As a whole, Cocos-Nazca lavas are depleted in the LREEs and generally preserve a modest negative Eu anomaly, consistent with the fractionation of plagioclase. More variability is observed for the highly incompatible, fluid mobile, trace elements (Cs, Rb, Ba). Of note is the sporadic depletion in high-field strength elements (HFSEs) Nb and Zr. Lavas anomalously low in Nb and Zr concentrations are those that fall below the canonical Nb/Ta and Zr/Hf values for MORB (Nb/Ta = 15.5, Workman and Hart, 2005; Zr/Hf = 39, Salters and Stracke, 2004). It is important to note that the anomalously low HFSE values are not attributed to the analytical issue addressed in the Methods section above.

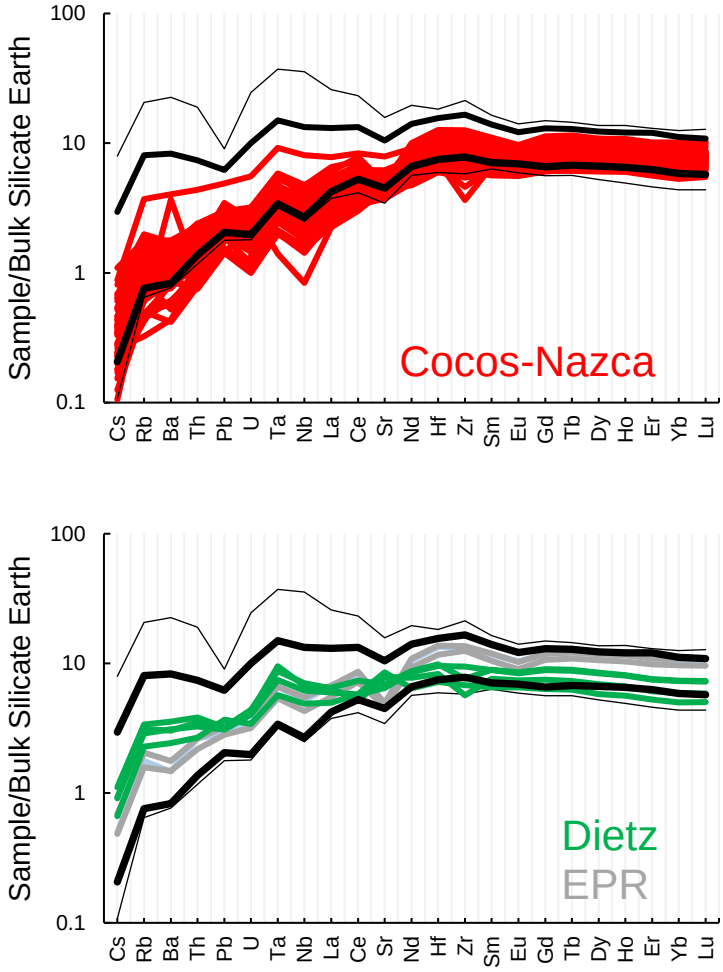

Figure 18: Bulk silicate earth-normalized trace element spider diagrams for Cocos-Nazca Spreading Center (top), Dietz Volcanic Ridge (green, bottom), and the local EPR (grey, bottom). For reference, the entire variation (thin black line) and 95 % variation (thick black line) of northern-EPR data from the compilation of Mallick et al. (2019) is given in each. Data are normalized to the bulk silicate earth values of Sun and McDonough (1995).

Figure 16 shows the longitudinal variation in trace element ratios La/Sm_N (Figure 16e) and Nb/Y (Figure 16f). For western segments (2 through 4), semi-systematic along-axis variations exist for primitive mantle normalized La/Sm_N and Nb/Y. In general, high

values are observed in western segments (2) that progressively decrease through segment 4. Eastern segments (5 – 9) exhibit more overall variability, though segment averaged La/Sm_N and Nb/Y for these segments typically reflect the mean of western segments (2, 3, and 4).

3.6.2.2 Dietz Volcanic Ridge

In contrast to the highly depleted nature of samples from the Cocos-Nazca rift, two samples from the Dietz Volcanic Ridge have trace element systematics that are transitional in nature ($La/Sm_N > 0.75$, Gale et al., 2013). The other two Dietz Volcanic Ridge samples are nearly transitional (La/Sm_N of 0.74 and 0.68) and have similar bulk silicate earth-normalized trace element patterns that are similar to their transitional counterparts (Figure 18). Significantly, highly incompatible trace element concentrations (Cs, Rb, Ba) for Dietz Volcanic Ridge lavas are elevated with respect to lavas from the Cocos-Nazca Spreading Center. Dietz Volcanic Ridge lavas also have positive Sr anomalies. Longitudinal variations La/Sm_N (Figure 17e) and Nb/Y (Figure 17f) highlight that the most trace element enriched sample occurs at the end of the Dietz Volcanic Ridge ($La/Sm_N = 0.87$), rather than at the point of the Dietz seamount ($La/Sm_N = 0.78$), different than what is observed for major elements (Figure 17a, b). Broadly, a west to east along-axis increase in trace element concentrations is observed (Figure 17).

3.6.3 $^{87}Sr/^{86}Sr$ Isotope Analyses

The overall variability of $^{87}Sr/^{86}Sr$ ratios for samples from the Cocos-Nazca rift, the Dietz Volcanic Ridge, and the local EPR is limited, ranging from 0.70243 to 0.70261 (Figures 19). There is a weak overall positive correlation between $^{87}Sr/^{86}Sr$ trace element ratios indicative of incompatible element enrichment (e.g., K_2O/TiO_2). The lowest $^{87}Sr/^{86}Sr$ values in our data set occur in the EPR samples. Interestingly, the highest values are found along the easternmost Cocos-Nazca segment (segment 9), and not in samples from the Dietz Volcanic Ridge, although the latter were found to be transitional in terms of rare earth element patterns. Apart from the finding that $^{87}Sr/^{86}Sr$ is lowest at the EPR and highest in segment 9, there is little systematic variation among samples along the Cocos-Nazca ridge segments between the two. For the two Dietz Volcanic Ridge samples analyzed, $^{87}Sr/^{86}Sr$ increases from west to east, in agreement with the observed longitudinal variations in La/Sm_N and Nb/Y (Figure 17g).

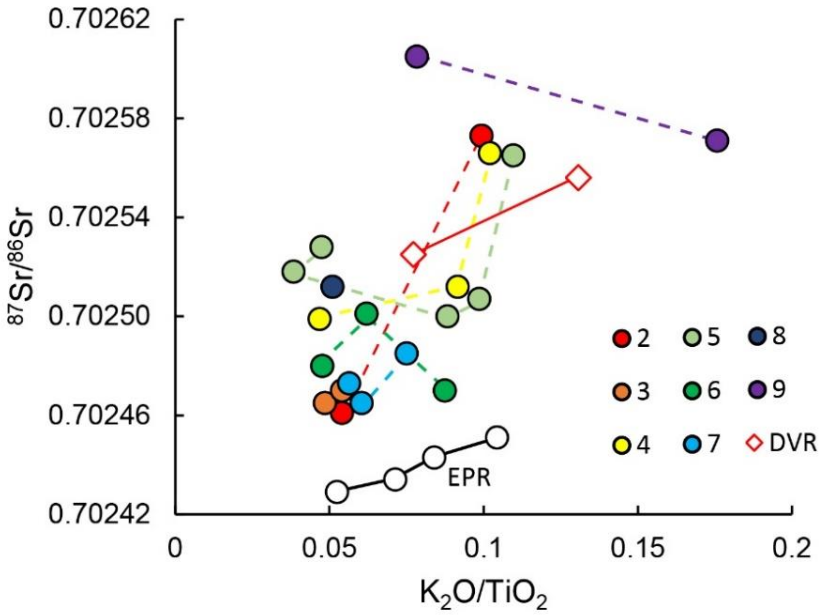

Figure 19: K_2O/TiO_2 vs $^{87}Sr/^{86}Sr$ for basaltic glass from the Cocos-Nazca, the Dietz Volcanic (DVR), and the adjacent EPR (labeled). Samples from the same ridge segment are connected by a line to aid in the discrimination of trends.

3.7 Discussion

3.7.1 Comparing the Cocos-Nazca Spreading Center to the Galapagos Spreading Center

The Cocos-Nazca Spreading Center merges eastward with the Galapagos Spreading Center at approximately 98°W. Along the Galapagos Spreading center, trace element systematics in general reveal that N-MORB is observed between 98°W and 95°W while T-MORB is observed between 95°W and 92°36'W (Detrick et al., 2002; Cushman et al., 2004). Lavas east of 92°36'W (E-MORB, Cushman et al., 2004) are

among the most enriched in the region and are clearly influenced by the Galapagos hotspot (e.g., Detrick et al., 2002; Cushman et al., 2004).

Longitudinal variations in La/Sm_N indicate that with only two exceptions the Cocos-Nazca Spreading Center lavas are depleted relative to those found further to the east (east of 95°30′W, see Figure 14). Similarly, spatial variations in $^{87}Sr/^{86}Sr$ ratios reveal that the average Cocos-Nazca Spreading Center $^{87}Sr/^{86}Sr$ ratio ($^{87}Sr/^{86}Sr = 0.70251$) is more depleted relative to those found further to the east, apart from the low values observed at the 95°30′W propagator (Figure 14). Interestingly, all available $^{87}Sr/^{86}Sr$ ratios west of ~ 98°16′W are below ~ 0.70263 while the majority of those to the east of ~ 98°16′W are above this value, perhaps marking the western extent of the Galapagos hotspot. This observation is in broad agreement (within ~ 115 km) with that of Schilling et al. (2003) who, based on radiogenic isotopes (Sr, Nd, Pb), placed the western extent of the Galapagos hotspot at ~ 99°30′W. An isotopic 'low' exists in EPR samples just west of Cocos-Nazca Spreading Center.

3.7.2 The Unusual Chemical Depletion of Cocos-Nazca Lavas

Cocos-Nazca lavas are primitive (Mg# 55-65), characteristically depleted, and limited in overall trace element variability. In a regional context, the Cocos-Nazca lavas are among the most depleted relative to N-MORB from the Galapagos Spreading Center (Figure 20a, b, c). Together, these characteristics are suggestive of a Cocos-Nazca source

region that is highly depleted with limited dispersed enriched heterogeneities. This contrasts with models of mantle source heterogeneities envisioned to explain MORB that appear to be mixtures of enriched and depleted end-member source compositions elsewhere along the EPR (Castillo et al., 2000).

Having established that the Cocos-Nazca lavas are depleted in a regional context, it is useful to compare their compositions to those expected to be sourced from typical MORB mantle (depleted MORB mantle, DMM, Workman and Hart, 2005). Figure 21 is a plot of La/Sm_N vs Nb/Y. Also included in this figure are the data from the recent compilation of northern-EPR data of Mallick et al. (2019) (small black dots) and a pooled melt composition (up to 15 %) calculated using the adiabatic decompression melting program *REEBOX PRO* (Brown and Lesher, 2016).

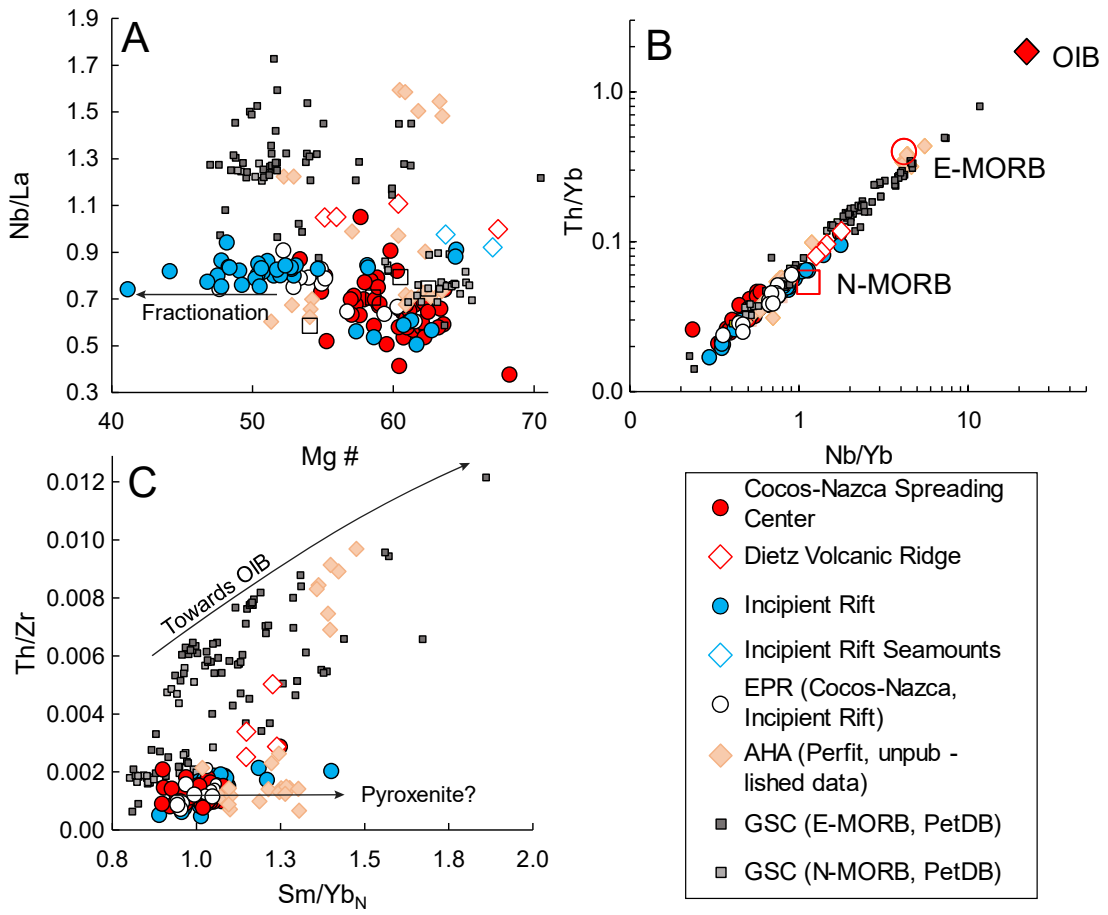

Figure 20: Comparison of regional geochemical data. Plots include data from the Cocos-Nazca Spreading Center (this study), Incipient Rift (Hanna, 2004), Dietz Volcanic Ridge (this study), local EPR (this study; Hanna, 2004), 1°40'N OSC (unpublished, M. Perfit), and Galapagos Spreading Center (PetDB). Symbols are as given in Figure 1a. A) Mg# vs Nb/La illustrates the depleted nature of Cocos-Nazca, Incipient Rift, and local EPR lavas. Note also that IR samples are more fractionated than lavas from the other localities. B) Nb/Yb vs Th/Yb covariation diagram. N-MORB is from Niu et al. (1997), E-MORB is from Lehnert et al. (2002), OIB is from Sun and McDonough (1995). C) Sm/Yb$_N$ vs Th/Zr covariation diagram illustrates the limited chemical variability observed in Cocos-Nazca, Incipient Rift, and local EPR lavas.

For the pooled melt composition, the starting composition is that of DMM. Figure 21 indicates that either exceedingly large extents of melting of DMM are required to produce Cocos-Nazca compositions or that the Cocos-Nazca source region is depleted with respect to DMM. That Cocos-Nazca lavas are the result of large extents of melting is seen as unlikely for a number of reasons. First, the Cocos-Nazca is spreading at rates as low as 19 mm/year. Second, mantle Bouguer anomaly inferred crustal thickness for the Cocos-Nazca is as low as 4 km, implying limited overall melt productivity. Third, Cocos-Nazca ridge segment morphologies (axial graben) are not consistent with large melt fluxes (axial highs are observed at the EPR). Finally, this hypothesis would imply that Cocos-Nazca lavas are generated from larger extents of melting than northern-EPR lavas where total spreading rates exceed 130 mm/year. It is for these reasons Cocos-Nazca lavas are more likely derived from a mantle source that is unusually depleted with respect to incompatible trace elements.

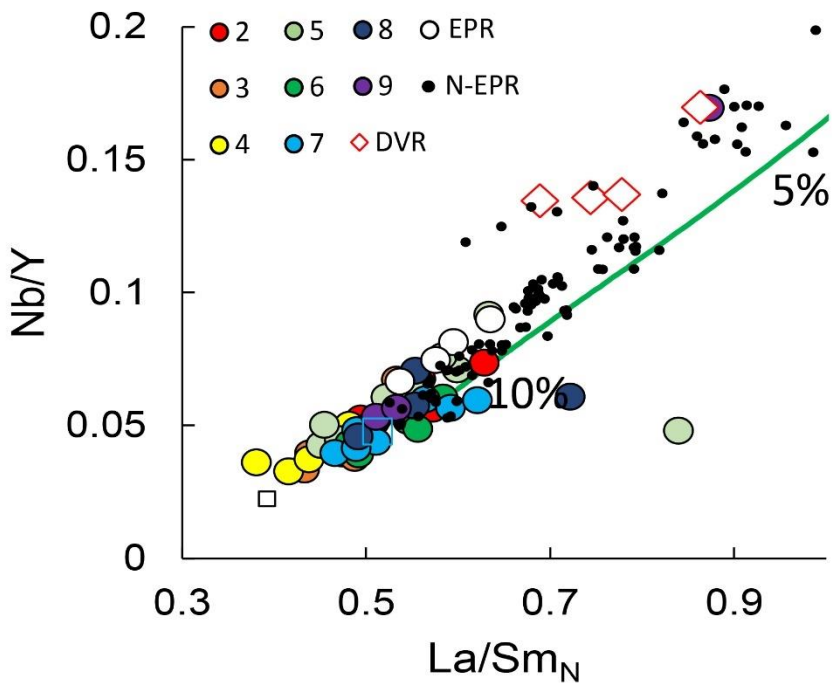

Figure 21: La/Sm$_N$ vs Nb/Y for lavas from the Cocos-Nazca, local EPR, and Dietz Volcanic Ridge. Also shown (small black dots) are the northern-EPR data from Mallick et al. (2019). The solid green line are the pooled melt compositions for melting of DMM (Workman and Hart, 2005) calculated using the adiabatic decompression melting program *REEBOX PRO* (Brown and Lesher, 2016). La and Sm values are normalized to the primitive mantle concentrations in Sun and McDonough (1995).

3.7.3 Local East Pacific Rise and Incipient Rift Lavas

Though sparsely sampled, the EPR lavas west of the tip of the Cocos-Nazca rift (at ~ 2°15′N) are also unusually depleted when compared to the recent compilation of northern-EPR data by Mallick et al. (2019) (Figure 21). Aside from the one transitional lava at segment 9 (Nb/Yb = 1.79), Cocos-Nazca lavas (Nb/Yb ≈ 0.23 - 0.90) also differ from N-MORB (Nb/Yb = 1.14, Figure 20b). Further, EPR lavas near the Incipient Rift at ~

2°40′N are among the most depleted in the region (La/Sm_N as low as 0.38). Similarly, lavas from the 3°30′N overlapping spreading center (Smithka and Perfit, 2013) are depleted with respect to the high field strength elements (Figure 20a, b, c). Interestingly, these lavas have elevated Sm/Yb_N relative to other similarly depleted lavas in the region (Figure 20c), perhaps indicative of source heterogeneities (more pyroxene?) unique to these lavas (Perterman and Hirschmann, 2003).

Incipient Rift lavas are slightly more chemically diverse and more evolved than those from the Cocos-Nazca (Mg# 50-60). Western Incipient Rift lavas (near the EPR) are chemically similar to local, on-axis EPR lavas suggesting the two locations share a common source. Indeed, this geochemical link between the adjacent EPR and the Incipient Rift was also identified by Hanna (2004). A ~ 400 m decrease in ridge depth from the EPR to the Incipient rift suggests that one possible explanation for this exists where magmas dike laterally from the adjacent EPR into the Incipient Rift region.

Despite the widespread occurrence of depleted lavas, some normal to transitional lavas exist in the region (west of 98°W). It is important to note that these occurrences are generally restricted to features like overlapping spreading centers, seamounts, or the Dietz Volcanic Ridge. Unpublished AHA-NEMO lavas from the EPR overlapping spreading centers at 1°40′N (M. Perfit, personal communication) range from depleted to enriched compositions (Figure 20c). Like E-MORB from the Galapagos

Spreading Center, the enriched lavas from the 1°40′N overlapping spreading center extend towards the trace element signatures of E-MORB and OIB (Figure 20b, c). For the Incipient, there are two on-axis seamounts that are both more enriched (La/Sm_N = 0.85 and 0.89) and more primitive (Mg# > 60) than their axial lava counterparts and similar in composition to lavas from the Dietz Volcanic Ridge.

3.7.4 Dietz Volcanic Ridge

Lavas from the Dietz Volcanic Ridge range in extent of fractionation (Mg# 55-68) and are enriched (La/Sm_N up to 0.89) relative to lavas from the Cocos-Nazca and Incipient Rift (see Figure 20 and Figure 21). Like those data from the 1°40′N overlapping spreading centers and the Incipient Rift seamounts, samples from the Dietz Volcanic Ridge are among the most enriched samples west of 98°W. This, together with an approximately 650 m decrease in axial ridge depth when compared to the local EPR (EPR = 2975 mbs, DVR = 2324 mbs), supports the theory of Smith et al. (2013) who attribute the Dietz Volcanic Ridge and the formation of the southern boundary of the Galapagos microplate to a "mini hotspot" in the region around 1.4 Ma.

3.7.5 Comparing Cocos-Nazca Lavas to Other Highly Depleted MORB and the Global Occurrence of Depleted MORB

As noted above, an unusual feature of Cocos-Nazca lavas west of 98°W is their depletion in with respect to the compatible trace element ratios (La/Sm_N < 0.60, Nb/Yb < 1.15, Th/Yb < 0.05) and high field strength element ratios that frequently deviate from

canonical values (canonical Nb/Ta = 15, Zr/Hf = 39). Because unusually depleted MORB have been recovered elsewhere, it is useful to compare the Cocos-Nazca lavas to anomalously depleted MORB found elsewhere in the Pacific basin and to global MORB more broadly.

Anomalously depleted near-EPR lavas have been reported for major transform faults such as Siqueiros (Perfit et al., 1996; Hays, 2004) and Garrett (Hekinian et al., 1992; Wendt et al., 1999) as well as near-axis seamounts (e.g., Fornari et al., 1988; Niu and Batiza, 1997; Hall et al., 2006). Figure 22 shows bulk silicate earth-normalized trace element diagrams (Cs-Lu) for the Cocos-Nazca rift (Figure 22a), Siqueiros Transform (Figure 22b), Garrett Transform (Figure 22b), and near-EPR seamounts analyzed by Niu and Batiza (1997) (Figure 22c). Also shown in Figure 22a are data for the EPR west of the Cocos-Nazca rift tip (grey lines). For reference, the variation of northern-EPR data compiled by Mallick et al. (2019) is given in each figure. The 95 % variation is also provided in each figure and is used to eliminate statistically anomalous data that would otherwise influence comparisons.

For Cocos-Nazca lavas (Figure 22a), the more depleted lavas are those whose bulk silicate earth-normalized values fall below the lower limit of the northern EPR 95 % field. Indeed, 24 out of the 47 on-axis Cocos Nazca samples plot beneath this line. These lavas are particularly depleted in the highly incompatible trace elements (Cs to Nb) and

are not spatially confined to a particular ridge segment. Overall, similar depletions are only observed for lavas from the Garrett transform (Figure 22b), though Garrett lavas extend to even more depleted values of highly incompatible elements than Cocos-Nazca lavas (Ba, in particular).

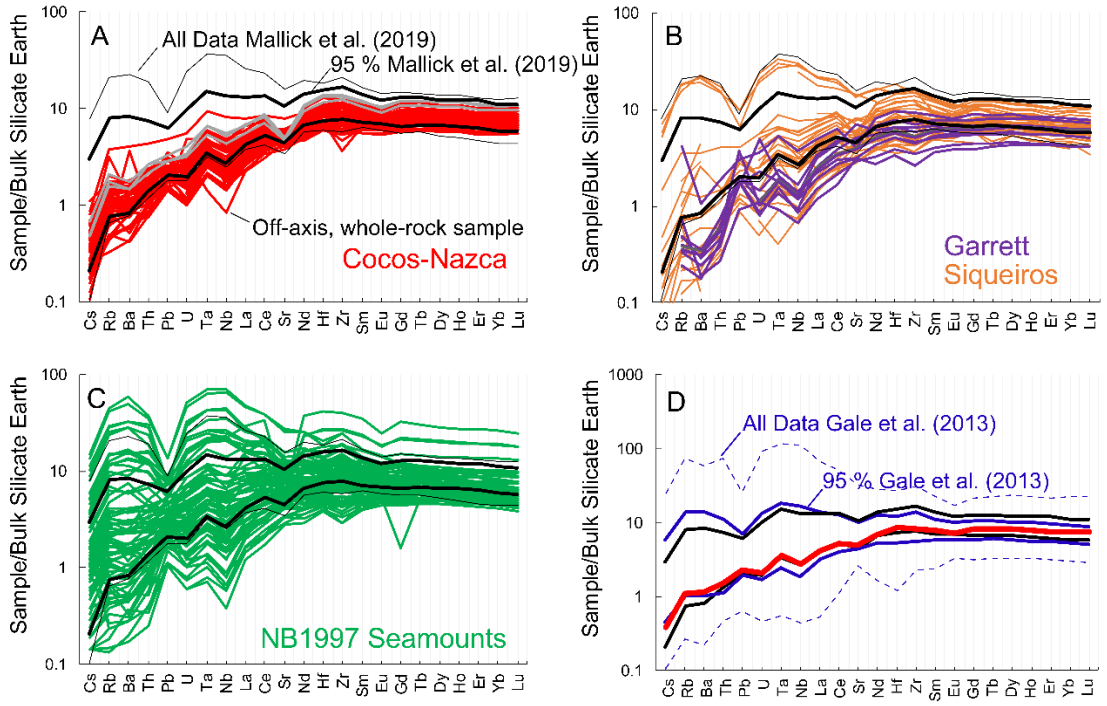

Figure 22: Comparative bulk silicate earth-normalized trace element spider diagrams for lavas from the Cocos-Nazca Spreading Center (this study), Garrett fracture zone (Wendt et al., 1999), Siqueiros fracture zone (PetDB, www.earthchem.org/petdb), and 5°N - 15°N near-EPR seamounts (Niu and Batiza, 1997). Normalizing bulk silicate earth values are from Sun and McDonough (1995). The entire variation of northern-EPR data compiled by Mallick et al. (2019) is given in Figure 10a, b, and c (thin black lines). The 95 % variation of northern-EPR data is provided in each figure (thick black lines). D) Comparison of the average on-axis Cocos-Nazca glass composition (red line) to the variation reported for global MORB (Gale et al., 2013).

Figure 22d compares the on-axis average of Cocos-Nazca lavas (bold red line, 360 km length scale) to the global compilation of Gale et al. (2013). Like the northern-EPR data, the entire range of values from Gale et al. (2013) as well as the 95 % variation is provided. The 95 % variation for global MORB is remarkably similar to that of northern-EPR data with notably higher limits on Cs and Rb and lower limits on Ta, Nb and the REEs. For the Cocos-Nazca, the average of on-axis lavas is nearly identical to the lower limit of the 95 % variation of northern-EPR data, suggesting the mean Cocos-Nazca composition is depleted relative to lavas from the northern-EPR and in a global sense. It is important to note that the above discussion is not intended to suggest that highly depleted MORB are unique to localities orthogonal to the fast-spreading EPR or the Pacific basin more broadly. Indeed, the compilation of Gale et al. (2013) (Figure 22d) highlights that although outside of the 95 % variation, highly depleted MORB exist globally.

For the Siqueiros transform (Perfit et al., 1996; Hays, 2004) and the 5°N – 15°N near-EPR seamounts (Niu and Batiza, 1997), a combination of depleted and enriched compositions are reported, and are attributed to incomplete mixing of diverse melts (Siqueiros) or anomalously depleted source compositions (5°N – 15°N near-EPR seamounts). For the 5°N – 15°N near-EPR seamounts, Lundstrom et al. (1998) suggested that the highly depleted lavas can be explained by a two-stage melting model. Similarly,

depleted to transitional lavas from Garrett (Hekinian et al., 1992; Wendt et al., 1999) are attributed to a mantle source that experienced prior depletion during melting at the adjacent EPR (Wendt et al., 1999). Due to their similarities in chemistry (depleted) and geography (orthogonal to the EPR), these localities provide a useful guide for identifying the processes that lead to the depleted compositions observed at the Cocos-Nazca Spreading Center.

3.7.6 Modeling the Depleted Nature of Cocos-Nazca, Incipient Rift, and local East Pacific Rise Lavas

The preceding sections established that Cocos-Nazca, Incipient Rift, as well as local EPR lavas are unusually depleted in incompatible trace elements and require an unusual source composition. Melting of a depleted mantle end member (e.g., Salters and Stracke, 2004; Workmann and Hart, 2005) does not produce the chemical signatures observed in these lavas (Figure 21). Similarly depleted lavas have been reported for the Garrett transform (Hekinian et al., 1992; Wendt et al., 1999) and near-EPR seamounts (Niu and Batiza, 1997). Particularly striking for these localities is the prevalence of Nb/Ta and Zr/Hf values that differ markedly from canonical values (Nb/Ta << 15.5, Workman and Hart, 2005), and have bulk silicate earth-normalized REE ratios that are unusually depleted compared to MORB worldwide (e.g., Gale et al., 2013).

Lundstrom et al. (1998) explored the origins of anomalously low Nb/Ta and Zr/Hf in MORB and suggested that these lavas result from melting of a mantle source

that experienced prior melting and removal of enriched components. They performed a series of experiments in the diopside-anorthite-albite system that established that the partitioning of HFSEs into pyroxene is a function of pyroxene alumina content. Their results indicate that at higher Al_2O_3 concentrations (~ 5 wt.%), $D_{Ta,Hf}^{cpx/liq}$ is greater than $D_{Nb,Zr}^{cpx/liq}$, providing a mechanism whereby HFSE pairs can become fractionated from one another. Al^{4+} is moderately incompatible during melting of DMM and is well correlated with extent of melting indicators in residual peridotites such as Cr# of spinel (Niu and Hekinian, 1997) and HREE concentrations in peridotite clinopyroxenes (Hellebrand et al. 2001). As melt fraction (F) increases, alumina content in the residual peridotite decreases (Niu and Hekinian, 1997), ultimately decreasing the Nb/Ta and Zr/Hf values of the residual peridotite (Lundstrom et al. 1998).

Numerical calculations are used to identify possible source compositions for the depleted Cocos-Nazca lavas. For these calculations, two different methods are used. The first is a simple batch melting calculation following the methods of Lundstrom et al. (1998) while the second is a pooled melt calculation using the adiabatic decompression melting program *REEBOX PRO* (Brown and Lesher, 2016). The initial calculations start with a spinel lherzolite source composition (mineral modes of DMM, Workmann and Hart, 2005) with the trace element signature of primitive mantle (Sun and McDonough, 1995). The 1 GPa melting reaction; $0.56\ Opx\ +\ 0.72\ Cpx\ +\ 0.04\ Spin\ =\ 0.34\ Oliv\ +$

1 *Melt* (Wasylenki et al. 2003) is used. It is important to note that spinel is not included in these calculations as its modal proportion is small, as is its relative influence on the trace elements of interest (e.g., McKenzie and O'Nions, 1991). The residuum of the initial melting event (F = 5 %) undergoes subsequent batch melting following the same melting reaction, resulting in melts that are uniquely depleted with respect to HFSEs (red line, Figure 12).

A second calculation is carried out using the adiabatic decompression melting program, *REEBOX PRO* (Brown and Lesher, 2016). For this calculation, a two-stage melting process was used. An initial source composition of DMM undergoes a first stage melting event, resulting in a chemically depleted harzburgite + lherzolite residuum (proportions = 60:40; bulk mineralogy = 0.68 Ol + 0.22 Opx + 0.10 Cpx). The bulk trace element concentration is a weighted average of the highly depleted harzburgite (La/Sm_N = 0.17) and the lherzolite, whose trace element signature is that of depleted DMM (La/Sm_N = 0.4, Workman and Hart, 2005). This residuum then undergoes a second stage adiabatic decompression melting and the pooled melt composition at each decompression step is used to evaluate whether such a process is capable of generating the chemical signatures observed in Cocos-Nazca, Incipient Rift, and local EPR lavas (black line, Figure 23). For additional information related to calculations, see Appendix B.

Figure 23 shows the results of these calculations with Cocos-Nazca rift, Incipient Rift and EPR data, as well as data from the Garrett transform (Wendt et al., 1999) and the northern-EPR (Mallick et al., 2019). Samples from the Cocos-Nazca rift, Incipient Rift, and local EPR plot between the DMM and Lundstrom et al. (1998) melting curves, while the *REEBOX PRO* melting curve generally acts to bisect the data.

Figure 23 (next page): Results of melting calculations. DMM is the pooled melting curve generated by *REEBOX PRO* (Brown and Lesher, 2016) using the average depleted MORB mantle mineral mode and chemical composition of Workman and Hart (2005). Lundstrom et al. (1998) melting is the batch melting curve generated for a source that has experienced prior melt depletion (La/Sm_N = 0.2) following the methods of Lundstrom et al. (1998). For this calculation, $D^{ol/liq}$ and $D^{opx/liq}$ partition coefficients are from Salters and Stracke (2004) while $D^{cpx/liq}$ partition coefficients are from Lundstrom et al. (1998). Residuum melting REEBOX is the pooled melt composition at each decompression step of a harzburgite + lherzolite source using the adiabatic decompression melting program *REEBOX PRO* (Brown and Lesher, 2016). For additional information, readers are directed to Appendix B.

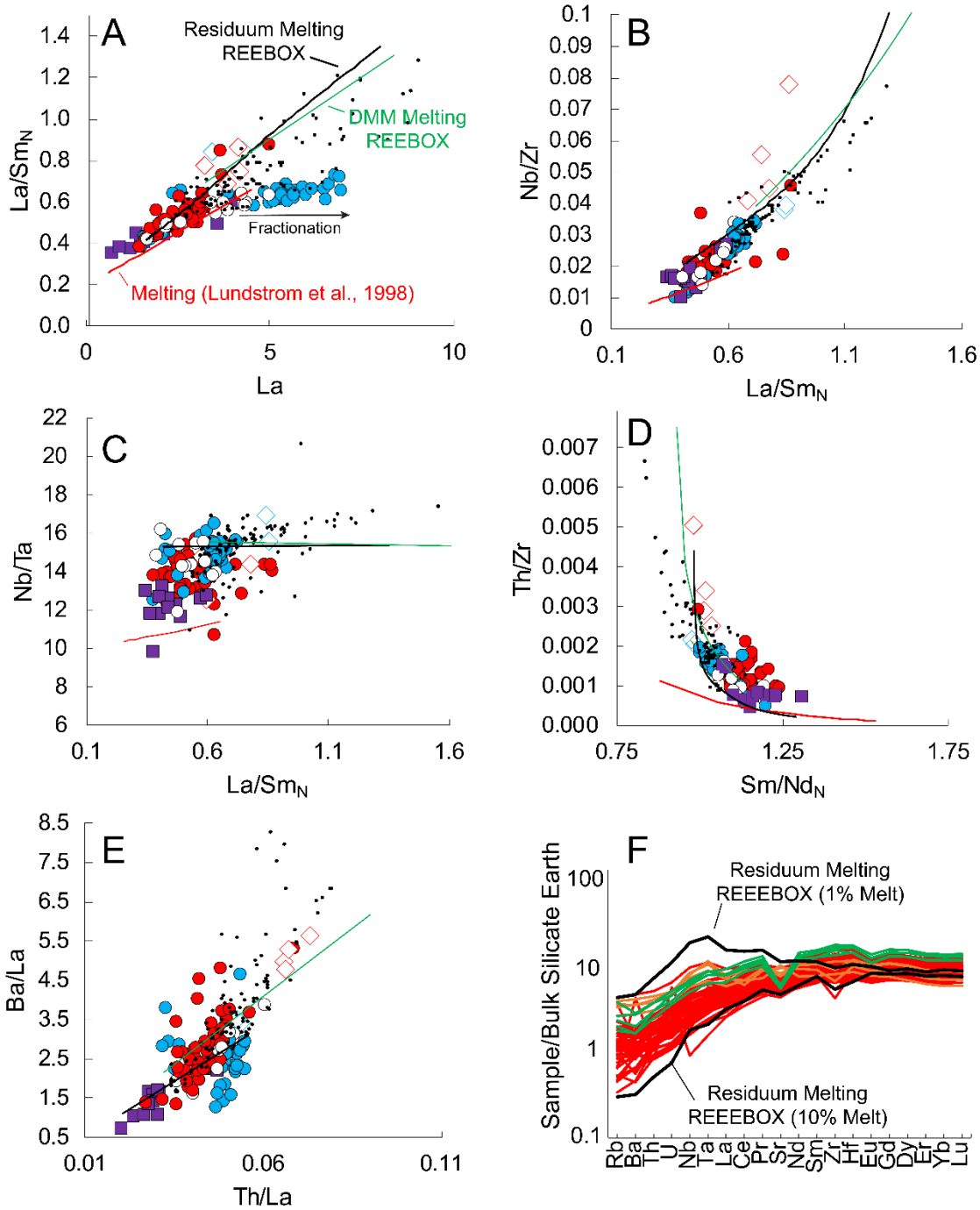
A
Residuum Melting
REEBOX
DMM Melting
REEBOX
Fractionation
Melting (Lundstrom et al., 1998)
La/Sm$_N$
La
B
Nb/Zr
La/Sm$_N$
C
Nb/Ta
La/Sm$_N$
D
Th/Zr
Sm/Nd$_N$
E
Ba/La
Th/La
F
Residuum Melting
REEEBOX (1% Melt)
Residuum Melting
REEEBOX (10% Melt)
Sample/Bulk Silicate Earth
Rb Ba Th U Nb Ta La Ce Pr Sr Nd Sm Zr Hf Eu Gd Dy Er Yb Lu

This observation suggests that the anomalously depleted nature of these lavas may result from the pooling of melts derived from the harzburgite + lherzolite source. However, this is not true for Nb/Ta (Figure 23c). This is a consequence of the lherzolite lithology crossing the solidus at greater depth than the harzburgite such that the Nb/Ta of the lherzolite dominates the composition of the pooled melts derived from the residuum.

Figure 23 confirms that a two-stage melting model can explain the depleted nature of these lavas in REE (Figure 23a, d) and HFSE (Figure 23b, c) space. Importantly, the pooled melt compositions generated by *REEBOX PRO* account for much of the observed trace element variability in Cocos-Nazca lavas (Figure 23f).

3.7.7 A Tectonic Model for the Local East Pacific Rise and Cocos-Nazca Lavas

The calculations discussed above suggest that a two-stage melting model is one possible explanation for the depleted nature of Cocos-Nazca, Incipient Rift, and local EPR lavas. Importantly, this model accounts for the chemical variations observed in these lavas without reference to the tectonic or the physical processes governing melt generation in the region. For the Cocos-Nazca rift, averages of the western, immature segments (segments 2, 3, and 4) show a stepwise decrease in $Fe_{8.0}$, La/Sm_N, and Nb/Y (Figure 24) that coincides with an increase in spreading rate, suggesting a progressive increase in mean extent of melting from segment 2 (19 mm/year) to 4 (48 mm/year).

Segments further east (segments 5-9) are spreading at intermediate spreading rates (48 mm/year) and show little systematic change in segment averaged $Fe_{8.0}$, La/Sm_N, and Nb/Y, though outliers do exist. This coupled with little change in axial ridge depth and mantle Bouguer anomaly inferred crustal thickness suggests the development of a stable melting regime beneath these segments.

In general, numerical modeling suggests that Cocos-Nazca lavas are likely derived from an unusually depleted source region. Any tectonic model should take into account the proximity of the Cocos-Nazca to the fast-spreading EPR. A scenario is envisaged where the Cocos-Nazca propagates westward and overrides mantle that has experienced prior melt extraction at the adjacent EPR (Figure 25). Prior melt extraction leads to a more refractory, depleted, source region that is likely similar to the harzburgite + lherzolite mantle described in the modeling section. It is important to emphasize that this tectonic model is similar to that proposed for the Garrett transform by Wendt et al. (1999) and results in a two-stage process as suggested for near-EPR seamounts by Lundstrom et al. (1998).

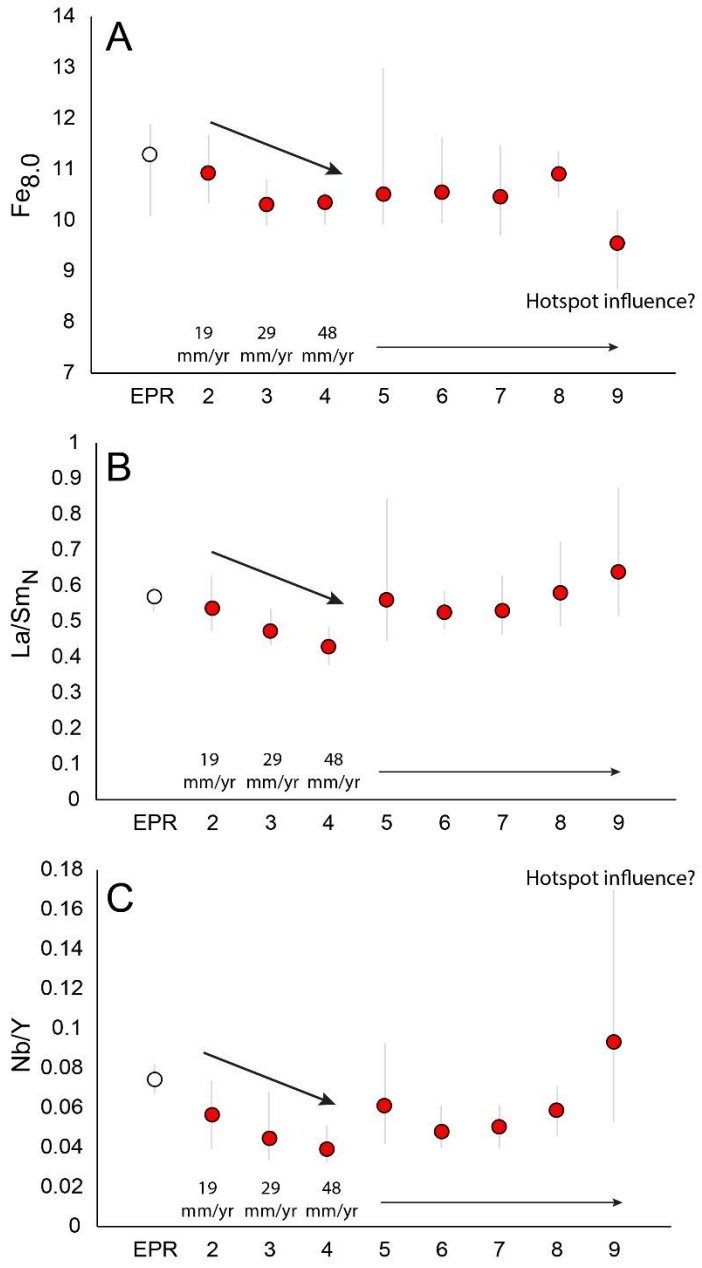

Figure 24: Segment averaged longitudinal changes in $Fe_{8.0}$ (A), La/Sm_N (B), and Nb/Y (C). The x-axis is the EPR and individual Cocos-Nazca segments (2 – 9). Filled symbols are the average value for each ridge segment while the minimum and maximum values are given by the grey lines. Arrows denote observed trends in western segments. Spreading rates are also provided (19, 29, and 48 mm/year).

The observed west to east increase in segment length, segment spreading rate, and mantle Bouguer anomaly inferred crustal thickness suggests an overall increase in melt productivity away from the Rift tip. For the western segments (2-4), the observed stepwise decrease in trace element ratios is further support for increasing melt productivity away from the gore tip. For the segments found further east (5-9), relatively constant segment averaged trace element ratios likely reflect the existence of a stable mantle melting regime beneath each segment.

For the local EPR, lava compositions are more depleted than their northern-EPR counterparts and are consistent with melting of a depleted harzburgite + lherzolite source. This is particularly true for EPR lavas adjacent to the Incipient Rift. Together, these observations suggest that the formation of unusually depleted on-axis lavas may also be a characteristic of this region. There are several possible explanations for this observation. First, it is possible that as a result of the northwestern absolute plate motion of the Pacific plate (Figure 25; Wang et al., 2018) the local EPR is continually melting mantle that has experienced previous melt depletion, assuming a relatively wide triangular melting regime like that depicted in Figure 25. Interestingly, Miocene EPR lavas from the off-axis Deep Sea Drilling Project (Leg 9, site 82 at ~ 2°35'N, ~106°56'W, and site 83 at ~ 04°02'N, 95°44'W) are normal-MORB (Geldmacher et al., 2013), suggesting that, if this hypothesis is correct, this is a recent phenomenon (< 5 Ma). It is

also possible that the compressive forces from the westward propagation of the Cocos-Nazca (Schouten et al., 2008) act to limit pooling of melts envisioned to be produced throughout the melting regime (Klein and Langmuir, 1987; Langmuir et al., 1992). In this scenario, melts produced by lower degrees of melting with more enriched trace element signatures may be prevented from mixing to form the pooled melts that erupt on the seafloor.

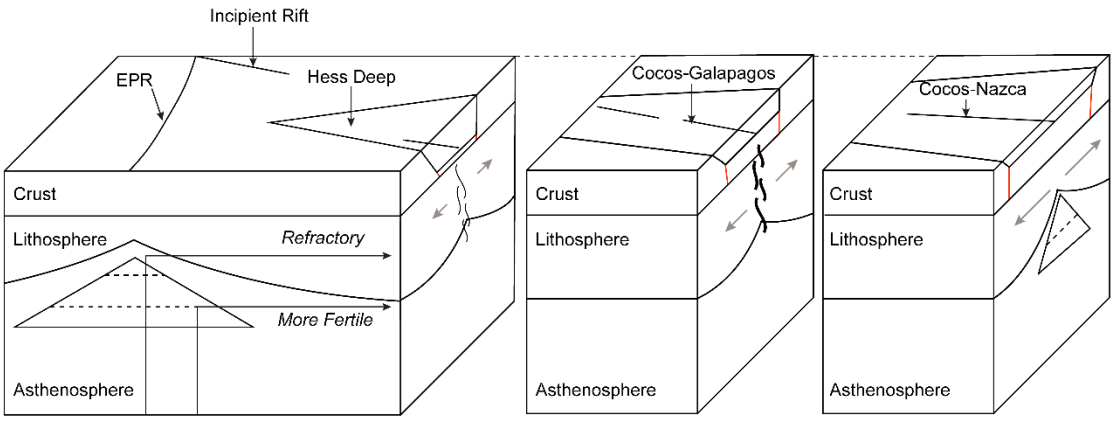

Figure 25: Cartoon depicting one possible explanation for the depleted nature of the Cocos-Nazca Spreading Center lavas. In this example, mantle that has experienced less adiabatic decompression melting beneath the EPR (left panel, 'More Fertile') is transported laterally to the Cocos-Nazca Spreading Center where it is then melted once more. For the Cocos-Nazca, the extent of mantle melting increases from west to east as reflected by the geophysical and geochemical data. A stable mantle melting regime is established beneath the Cocos-Nazca spreading domain (left most panel). Grey arrows are scaled to reflect Cocos-Nazca spreading rates of 19, 29, and 48 mm/year. Vertical red lines mark crust generated at the Cocos-Nazca versus crust created at the EPR. The bulk mantle beneath the Cocos-Nazca Spreading Center is similar to the harzburgite + lherzolite source discussed in the modeling section. In general, this model is similar to that proposed for the Garrett transform by Wendt et al. (1999).

3.8 Conclusions

In terms of major elements, Cocos-Nazca lavas are broadly consistent with fractionation of a tholeiitic parental liquid. Notably, these lavas are unusually depleted with respect to the incompatible trace elements (La/Sm_N as low as 0.38) and in some cases, high field strength element ratios that deviate from canonical (Nb/Ta from ~ 10 to 16, canonical Nb/Ta = 15.5). Trace element concentrations between and within individual segments are variable and cannot be explained by fractionation alone, requiring variations in mantle source composition and/or extents and pressures of melting. Numerical calculations indicate that these lavas are consistent with the pooled melt compositions derived from an unusually depleted harzburgite + lherzolite source. A model is proposed that suggests that as the Cocos-Nazca propagates westward, it overrides mantle that experienced prior melt extraction at the adjacent EPR, leading to a more refractory, and depleted, source region. For immature Cocos-Nazca ridge segments (2, 3, and 4), segment averaged $Fe_{8.0}$, La/Sm_N, and Nb/Y, show a stepwise decrease from west to east that is correlated with an increase in spreading rate. This may be due to an increase in mean F associated with increased spreading.

EPR segments adjacent to both the Cocos-Nazca and Incipient Rift are also depleted in trace element compositions relative to northern-EPR. Two scenarios are proposed to account for the depleted nature of these lavas. First, it is possible that the

northwestern absolute plate motion of the Pacific plate requires that the local EPR is always sourcing melt from a previously depleted mantle. Second, it is possible that the compressive forces from the propagation of the Cocos-Nazca acts to inhibit shallow level melt mixing such that the enriched component of the EPR melt is limited or absent from the pooled melt chemical signature.

Finally, the Dietz Volcanic Ridge is transitional in nature, with enrichments in the highly incompatible trace elements (Ba, Nb, Ta) and a positive Sr anomaly. These lavas are among the most enriched in the region. Numerical modeling indicates that these lavas are more enriched than would be predicted for melts sourced from a typical depleted mantle composition. It is suggested that this, in combination with an almost 700 m decrease in axial ridge depth relative to the local EPR, supports the hypothesis of Smith et al. (2013) the formation of the southern boundary of the Galapagos (~ 1.4 Ma) microplate is related to the existence of a mini hotpot in the region.

4. The size distribution, morphology, and chemical composition of plagioclase in plagioclase-bearing lavas from the Cocos-Nazca Spreading Center

4.1 Chapter Summary

The crystal size distribution, morphology, and chemical composition (An#) of plagioclase crystals from the two domains that exist within the Cocos-Nazca Spreading Center (Cocos-Galapagos and Cocos-Nazca) are reported. For the Cocos-Galapagos, log linear plagioclase crystal size distributions are observed. For the Cocos-Nazca, plagioclase crystal size distributions are distinctly curved and extend to larger sizes. For the studied samples, a variety of plagioclase morphologies (acicular, tabular, rounded) show textures associated with crystal – melt disequilibria (resorbed cores, sieve texture). For the Cocos-Nazca domain, crystals of all sizes (< 1 mm up to 7 mm) plagioclase (core and rim) compositions are not in equilibrium with their host glass, suggesting that plagioclase are xenocrystic in origin. It is suggested that the observed range in plagioclase sizes, morphologies, and compositions sampled a variably aged nucleation front at crustal levels by an aphyric magma. Faster cooling rates, or smaller bodies of magma, result in a limited distribution of plagioclase sizes in the nucleation front resulting in log linear crystal size distributions.

For the Cocos-Galapagos domain, faster cooling rates and/or smaller bodies of magma, are based on the small and limited size range of crystals, as well as indicators of

low melt productivity including the ultra-slow to slow spreading rates and thin crust inferred from mantle Bouguer anomalies. For the Cocos-Nazca domain, a wide range in erupted crystal sizes and compositions is suggestive of slower cooling rates and/or larger bodies of magma. This is attributed to greater melt productivity consistent with faster spreading rates and thicker crust. Together, these observations suggest that the large-scale differences in the physical characteristics observed between the two domains are also reflected in difference in the crystal populations in the erupted lavas.

4.2 Introduction

Mid-ocean ridge volcanism accounts for the majority of worldwide extrusive volcanic activity. Decades of study of the geochemistry and petrology of mid-ocean ridges basalts (MORBs) have yielded a wealth of information about the chemical and physical conditions of the sub-oceanic mantle, the processes that occur during mantle melting, and the evolution of melts during transport to the surface (Klein and Langmuir, 1987; Saunders, 1988; Hart, 1988; White and Klein, 2014). Recent advances in seismic imaging of the distribution of melt at crustal and upper mantle depths beneath mid-ocean ridges (e.g., Toomey et al., 1990; Cannat, 1993; Singh et al., 2006; Carbotte et al., 2015) has led to renewed interest in studying the shallow-level processes of magma evolution, in light of new physical constraints (Rubin et al., 2009; Wanless and Behn, 2017). A thorough understanding of magma evolution and crystallization beneath the

ridge axis also provides important constraints on models of the development of the architecture of the igneous crust, particularly the relationship between the plutonic and extrusive units (Sinton and Detrick, 1992; Karson, 2019).

Many studies have illustrated that the mode and chemical composition of the crystal assemblage in erupted basalts provides information about processes that occur at crustal and upper mantle depths prior to eruption on the seafloor (Rhodes et al., 1979; Kuo and Kirkpatrick, 1982; Bryan, 1983; Alt et al., 1993; Nielsen et al., 1995, Hellevang and Pederson, 2008; Zellmer et al., 2011; Lange et al., 2013a; Drignon et al., 2018; Bennett et al., 2019). Such studies have used MORB phenocrysts to constrain the timescale of eruption events (Costa et al., 2010; Zellmer et al., 2011), the complexity of melt pathways (Wanless and Shaw, 2012; Lange et al., 2013a; Drignon et al., 2018; Bennett et al., 2019), the diversity of magma compositions crystals interact with (Rhodes et al., 1979; Kuo and Kirkpatrick, 1982; Nielsen et al., 1995; Lange et al., 2013a), and magma mixing events (Rhodes et al., 1979; Kuo and Kirkpatrick, 1982). Early experimental studies determined the temperatures that minerals (olivine, plagioclase, clinopyroxene) begin to crystallize and how the crystallization of these minerals changes the bulk composition of the magma from which they were formed (Bender et al., 1978; Stolper, 1980) Recently, experimental studies examining how plagioclase grow in a cooling magma indicate that prolonged crystallization of basaltic liquids results in crystal agglomeration and

coarsening (Pupier et al., 2008; Ni et al., 2014; Giuliani et al., 2020). Together, natural and experimental studies suggest that the physiochemical conditions of a given ridge will be reflected in the size, morphology, and chemical composition of the crystal assemblage.

In this study, plagioclase-bearing lavas from the Cocos-Nazca Spreading Center are analyzed to supplement the geochemical study of basaltic glass presented in Chapter 2. Specifically, the plagioclase crystal size distribution and phenocryst characteristics (morphology, composition) are used to explore magmatic processes that occur within the crust and possible differences in these processes as a function of spreading rate.

4.3 Crystal Size Distribution - Theory

The theory governing crystal size distribution analysis (CSD) was first applied to geologic systems by Marsh (1988) and specifically to igneous petrology by Cashman and Marsh (1988). CSD analysis has been used to study a variety of geologic sub-disciplines including planetary geology (Neal et al., 2015), volcanology (Morgan et al., 2007), igneous petrology (Higgins, 1996; Higgins, 1998; Boorman et al., 2004), and metamorphic petrology (Cashman and Ferry, 1988). CSD analysis is particularly useful because it is a non-destructive technique that provides researchers with quantitative data to explore processes such as closed system fractionation, crystal accumulation, and magma mixing (Marsh, 1988). The following overview is based on the work of Marsh (1988), Cashman and Marsh (1988), and Higgins (1996; 1998; 2002).

Crystal size population density is the total number of crystals, n, within a given crystal size range, L, per unit volume. Graphically, population density equates to the slope of a line plotting crystal size against total number of crystals:

$$N(L) = \int L_o n(L) dL \tag{13}$$

Population density is the volume of crystals divided by the size interval and has the units mm^{-4}. When plotting ln (population density) vs L (Figure 26a), closed system behavior in igneous systems typically results in a straight line whose slope is proportional to $-1/G\tau$, where G is the crystal growth rate and τ is the crystal residence time (Marsh, 1988). If no crystals are removed from the system, crystal growth rate is related to the time-dependent nucleation rate. Ultimately, the slope of a given CSD reflects the thermal conditions a crystal population experiences. Similarly, the y-intercept of this plot is equivalent to the nucleation number density which reflects the number of nucleation sites per unit volume (Marsh, 1988). If a given magmatic system experiences rapid undercooling, there will be an increase in the overall nucleation number density while the opposite is true for a magmatic system that experiences slower cooling (Marsh, 1988). For example, Giuliani et al. (2020) report 962 plagioclase crystals after rapid quenching experiments ($\Delta T/\Delta t$ = 60°C/hr) while only 17 plagioclase crystals are reported for the same measured area after cooling rate was slowed substantially ($\Delta T/\Delta t$ = 1°C/hr). Perturbations resulting in non-linear behavior can be

interpreted as the consequence of a physical process acting to modify a given CSD. For example, the idealized CSD curve is deflected downward by crystal fractionation (Figure 26a) and upward by crystal accumulation (Figure 26a). Mixing of magmas with different thermal histories results in a kinked CSD. Concurrent decreases in y-intercept values with shallowing of CSD slope is often interpreted as crystal coarsening (Figure 26b). For comparison, Figure 26c shows plagioclase data from the Makaopuhi lava lake (Cashman and Marsh, 1988) and illustrates closed system behavior in a natural setting.

The idealized coarsening process given in Figure 26b follows the Communicating Neighbors theory (Dehoff, 1991), rather than the Lifshitz – Slyozov – Wagner theory (LSW, Lifshitz and Slyozov, 1961; Wagner, 1961). Communicating Neighbors theory posits that crystal growth depends on crystals interacting with one another (i.e., inter-crystalline diffusion) as well as a suspending fluid whereas LSW theory suggests that crystals interact only with a suspending fluid (no inter-crystalline diffusion). The limitations of LSW theory as it relates to natural systems has been addressed by Voorhees (1992) and the efficacy of using Communicating Neighbors theory to model crystal aging in anorthosites was demonstrated by Higgins (1998).

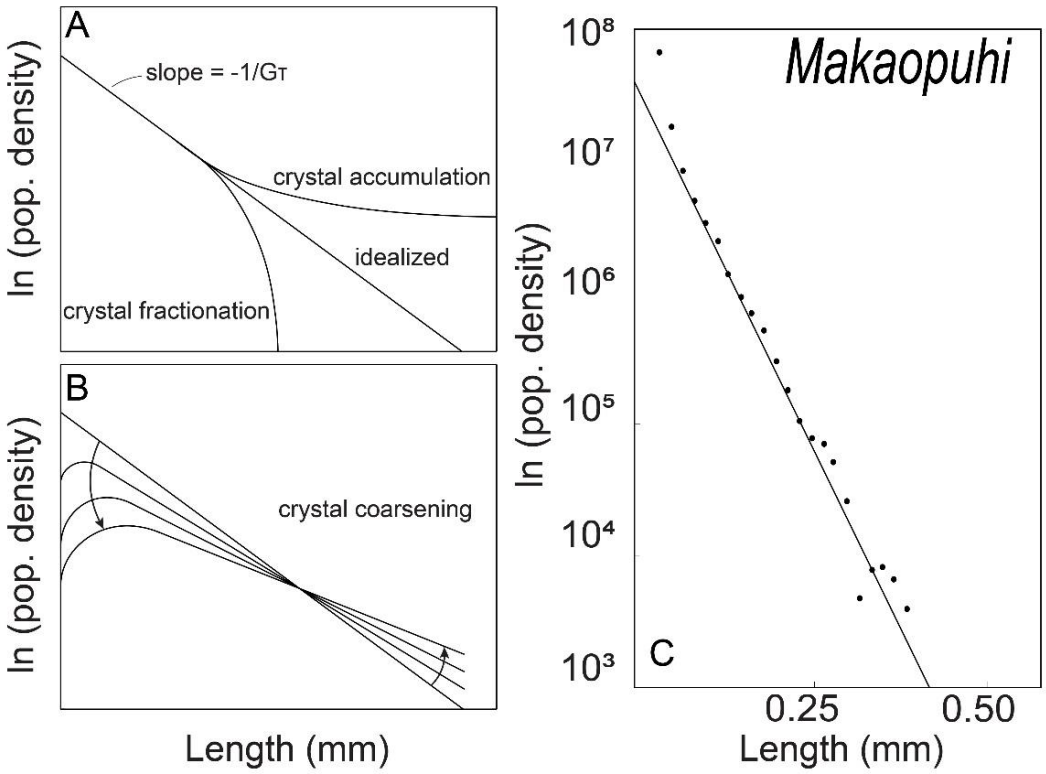

Figure 26: Idealized crystal length vs ln (population density). A) Idealized refers to closed system behavior. Also provided is the expected influence of crystal fractionation and accumulation on the idealized CSD from Marsh (1988). The slope of the idealized CSD is proportional to -1/Gτ, where G is the crystal growth rate and τ is the crystal residence time. The CSD intercept is the nucleation density. B) Theoretical influence of crystal coarsening following Communicating Neighbors theory (Dehoff, 1991) on the idealized CSD modified from Higgins (2006). C) Natural example of closed system behavior for plagioclase from the Makaopuhi lava lake (Cashman and Marsh, 1988).

4.4 Review of Crustal Processes at Mid-Ocean Ridges and Previous CSD Studies

Early workers envisaged sub-axial magma chambers as large, molten reservoirs beneath mid-ocean ridges (e.g., Cann, 1974). Utilizing seismic reflection and seismic tomography, subsequent studies (e.g., Herron et al., 1978; Toomey et al. 1990; Sinton and Detrick, 1992; Cannat, 1993; Singh et al., 2006) refined this model to our current understanding that along fast-spreading ridges, axial magma chambers (AMCs) are thin (hundreds of meters thick), narrow (1-2 km across-axis), continuous bodies (up to tens of km along-axis) that overlie a seismically distinct mush zone (melt + crystals). Further, studies have related the expulsion of magma from the AMC to the eruption of lavas on the seafloor (e.g., Xu et al., 2014). For magmatically robust intermediate-spreading centers, a crustal structure similar to fast-spreading ridges is predicted (Carbotte et al., 2015). Although less frequently observed, seismically imaged AMCs have also been reported for slow-spreading ridges (Pagli et al., 2012; Combier et al., 2015). However, magma bodies at these ridges are thought to be ephemeral with 'pods' of mush distributed throughout the crust and a thin zone of melt beneath the segment center (Cannat, 1996; Carbotte et al., 2015). These geophysical studies provide information on the distribution of melt at depth and can be combined with petrologic and geochemical studies to better understand the processes that occur as primary mantle melts migrate from depth to the seafloor.

The crystal cargo of erupted basalts records the sum of all processes experienced by a crystal population prior to eruption. Examples of previous studies that have examined MORB phenocrysts and their relevant observations are provided in Table 3. In general, a variety of minerals are erupted in MORB as phenocrysts (plagioclase, olivine, clinopyroxene, spinel), however plagioclase most frequently dominates the rock mode (see Table 3). The eruption of plagioclase-phyric lavas with large and abundant plagioclase crystals is rare at fast-spreading ridges, but occurs commonly along intermediate, slow, and ultra-slow spreading centers (Lange et al., 2013a, Nielsen et al., 2020). This has led to the conclusion that the physical processes at slower spreading ridges are more amenable to the growth of larger plagioclase crystals and their transport to the seafloor (Lange et al., 2013a; Lange et al., 2013b; Drignon et al., 2018). One such hypothesis is that the presence of axial magma chambers at fast spreading centers acts to decrease magma ascent velocities allowing crystals to settle out of melt stalled in the crust (Lange et al., 2013a, b).

Table 3: Compilation of representative studies examining plagioclase phenocrysts in MORB.

Ridge	Reference	Mineralogy	Plagioclase Mode	Size Range	Morphology	Zonation	Notes
Gakkel	Bennett et al., 2019	Pl, Ol	0.4 - 50 %	< 1 mm ("microlites") - 14 mm	Tabular, Resorbed, Acicular, Skeletal	Normal, Reverse, Oscillatory, Sector, Patchy	Authors note that tabular and resorbed plagioclase have higher An# compared to acicular and skeletal plagioclase.
	Nielsen et al., 2017; Nielsen et al., 2020	Pl, Ol	≥ 15 %	≤ 10 mm	Tabular	None, Simple	Report that plagioclase in PUB are not as texturally complex as reported by Bennett et al., 2019. Plagioclase major element chemistry does not vary significantly while trace element chemistry is highly variable.
	Zellmer et al., 2011	Pl	> 45 %	≤ 2 mm - 10 mm	Tabular	Concentric, Non-concentric	Reported plagioclase An# range from 79 to 84.
Southwest Indian Ridge	Nielsen et al., 2020	Pl, Ol	≥ 15 %	< 5 mm - 30 mm	Tabular	None	Authors report high An# cores, low An# rims.
Mohns and Knipovich	Hellevang and Pederson, 2008	Pl, Ol, Cpx	10 - 54 %	≤ 12 mm	Tabular, Resorbed, Acicular, Skeletal	None, Normal, Reverse, Sector	Authors report that massive plagioclase with An# between 84 and 88. Lower An# are reported for skeletal plagioclase.
Mid-Atlantic	Costa et al., 2010	Pl, Ol, Cpx	≤ 10 %	≤ 4 mm			Authors report core An# between 75 and 88. Reported rim An# range from 55 to 65.
Costa Rica	Alt et al., 1993; Costa et al., 2010	Pl, Cpx, Spn	≤ 10 %	0.1 mm - 5 mm	Tabular, Acicular	Normal, Reverse, Oscillatory	Authors report that plagioclase is in equilibrium with a primitive magma (MgO > 11 wt. %).
Gorda	Nielsen et al., 1995	Pl, Ol, Spn	20 - 40 %	≤ 20 mm		Normal	Authors report homogenous plagioclase with minimal core-rim variation.
Galapagos	Eason and Sinton, 2006	Pl, Ol	≤ 15 %	≤ 2 mm	Tabular	Normal, Reverse	Reported no textures associated with disequilibrium (i.e., resorbtion).
Juan de Fuca	Sours-Page et al., 1999	Pl, Ol, Spn	10 - 30 %	2 - 20 mm			
	Nielsen et al., 2020	Pl, Ol	≥ 15 %	≤ 5 mm			

Note: compiled size range, morphology, zonation, and notes pertain only to plagioclase

The occurrence of plagioclase ultraphyric basalts (PUB, > 15 vol. % plagioclase, Lange et al. 2013a) has been reported for both subaerial (Cullen et al., 1989; Hansen and Gronvold, 2000; Valer et al., 2917) and submarine localities (Hellevang and Pederson, 2008; Lange et al., 2013a; Bennett et al., 2019). These basalts are unusual because of their often-exceedingly high abundance of plagioclase (up to ~ 50 vol. %, Bennett et al., 2019). This is particularly strange because as magmas become more crystalline their probability of erupting decreases (Marsh, 1996; Marsh, 2013). Because of this, PUB formation has been attributed to plagioclase flotation (Galapagos archipelago, Cullen et al., 1989) or injections of primitive melts that incorporate plagioclase as xenocrysts (Hellevang and Pederson, 2008; Lange et al., 2013a, b; Drignon et al., 2018). In the former, it is thought that density contrasts allow for plagioclase to accumulate as it floats in a dense magma. For the latter, injections of primitive melts ascend faster than plagioclase xenocrysts settle, allowing for the accumulation of plagioclase. In either scenario, many studies have established that studying PUB provides information about the upper mantle and crust beneath mid-ocean ridges. For example, Lange et al. (2013a, b) established that diverse $^{87}Sr/^{86}Sr$ ratios are preserved in plagioclase in PUB and that this variability is equal to the $^{87}Sr/^{86}Sr$ variability observed in lavas along first-order ridge segments (i.e., transform to transform). This suggests that plagioclase interact with a wide variety of magma compositions throughout their growth. Further, melt inclusions in PUB

plagioclase reveal plagioclase growth histories that extend to upper mantle depths (Drignon et a., 2018). The overall paucity of olivine crystals in these lavas has been attributed to density differences between plagioclase (ϱ ~ 2.8 g/cm^3) and olivine (ϱ ~ 3.2 g/cm^3) and variable ascent velocities that effectively separate plagioclase crystals from olivine crystals (see Lange et al., 2013a). In general, limited abundances of olivine are reported for PUB lavas (Nielsen et al., 2020).

Similarly, a wide range in liquid compositions have also been reported for mineral-hosted melt inclusions for ridges at all spreading rates (Nielsen et al., 1995; Michael et al., 2002; Danyushevsky et al., 2003; Danyushevsky et al., 2004; Drignon et al., 2018). Further, olivine- and plagioclase-hosted melt inclusion studies (Wanless and Shaw, 2012; Wanless and Behn, 2017; Drignon et al., 2018; Bennet et al., 2019) have revealed that the crystal cargo carried by magmas can be scavenged from below the crust. Indeed, Wanless and Behn (2017) suggested that crystallization at all spreading rates may occur at such depths (up to 10 km). For the ultra-slow spreading Mohns and Knipovich ridges, Hellevang and Pederson (2008) attribute diverse crystal morphologies in a single sample to complicated melt pathways that incorporate crystals (xenocrysts) from different depths in the crust. A detailed study of plagioclase morphologies from the ultra-slow spreading Gakkel ridge, led Bennet et al. (2019) to a similar conclusion.

Thus, studies of crystal morphology and chemical composition can be used to identify diverse processes that crystals experiences prior to eruption.

CSD analysis of MORB, which typically requires more than 200 crystals for accurate results (Morgan and Jerram, 2005), is not generally practical owing to the paucity of phenocrysts in most samples (e.g., Batiza and Niu, 1992). The few CSD studies that do exist for MORB have been used to examine conditions of magma evolution and ascent. For PUB samples from the Mohns and Knipovich ridges, flat CSD slopes at larger crystal sizes led Hellevang and Pederson (2008) to conclude that large plagioclase crystals are xenocrystic and accumulate at crustal depths and are then carried to the surface sometime later. Experimental studies of crystal growth in basaltic liquids at different cooling rates ($\Delta T/\Delta t$ from 1°C/hr to 60°C/hr) show clear differences in the size and distribution of crystals when cooled slowly (1°C/hr) as opposed to rapid quenching (60°C/hr, Giuliani et al., 2020). In addition, for MORB popping rocks (MORB that crystallized from vapor-saturated magma), linear vesicle size distributions (which employs the same governing theory as CSD) led Sarda and Graham (1990) to conclude that bubbles nucleate continuously during magma ascent. While there have been few studies applying CSD theory to MORB, for samples with sufficient crystallinities CSD theory has the potential to provide information about the processes crystals experience prior to entrainment in the magma that transports them to the seafloor.

4.5 The Cocos-Nazca Spreading Center and Lava Samples

The Cocos-Nazca Spreading Center (Figure 27) is a v-shaped propagating ridge whose tip is located just east of the fast-spreading EPR at ~ 2°10'N (Lonsdale, 1988). The Cocos-Nazca Rift is propagating at a rate that is equal to the local EPR half spreading rate, or ~ 60 mm/year (Hey, 1977; Lonsdale, 1988). Along its western end, near its tip, spreading occurs between the Cocos plate and the Galapagos microplate. To the east, beginning at ~ 101°W, spreading occurs between the Cocos and Nazca plates (Hey, 1977; Lonsdale, 1988; Smith and Schouten, 2018; Smith et al., 2020). The Cocos-Nazca rift is composed of series of second-order ridge segments. Changes from Cocos-Galapagos to Cocos-Nazca spreading are also reflected in a 10-degree change in segment orientation (087° vs 097°, Smith et al., 2020). Moving eastward from the gore tip, axial ridge depth (Figure 28a) decreases and crustal thickness inferred from mantle Bouguer anomalies increases (Figure 28b, Zheng et al., 2019; Smith et al., 2020). These changes are accompanied by increases in ridge segment length and spreading rate (Smith et al., 2020). Changes in spreading domain at ~ 101°W reflect the transition from tectonic rifting to magmatic seafloor spreading.

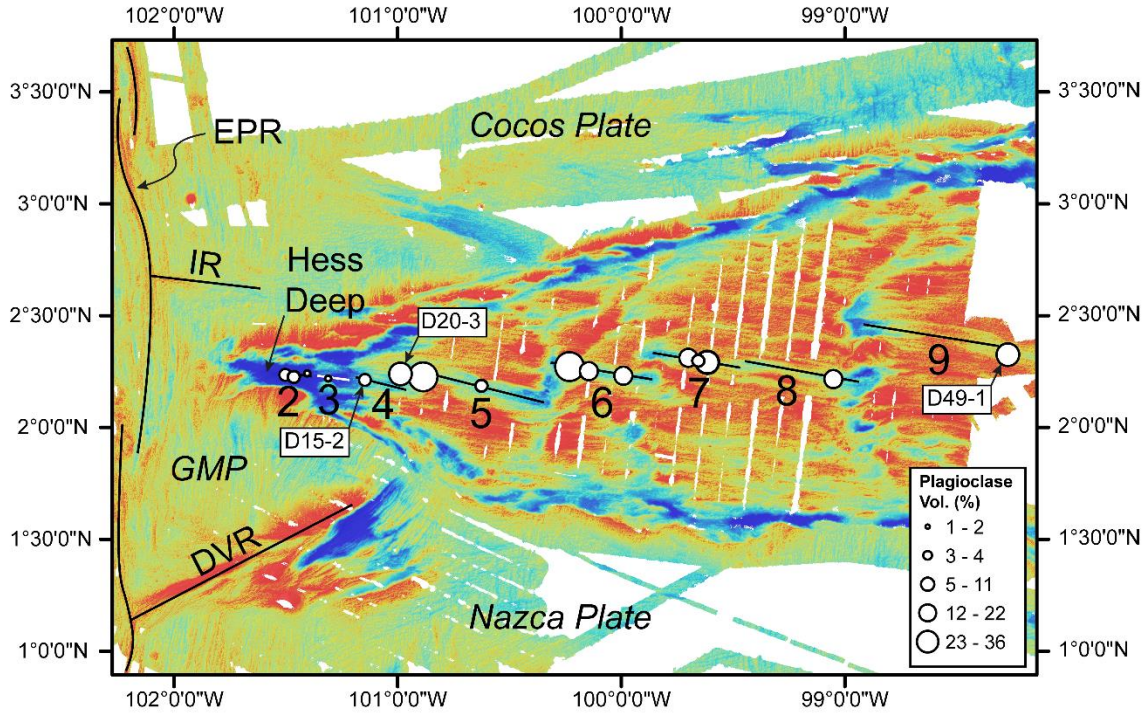

Figure 27: Multibeam bathymetry map of the Cocos-Nazca Spreading Center and the surrounding region. Locations of 16 samples (Table 4) discussed in this study are shown as white circles, the size of which corresponds to plagioclase volume percent (see legend). Individual segments are labeled (2 through 9) as are the individual samples selected for petrographic and microprobe analyses (D15-2, D20-3, and D49-1). Abbreviations are as follows: EPR is the East Pacific Rise, IR is the Incipient Rift, GMP is the Galapagos Microplate, DVR is the Dietz Volcanic Ridge.

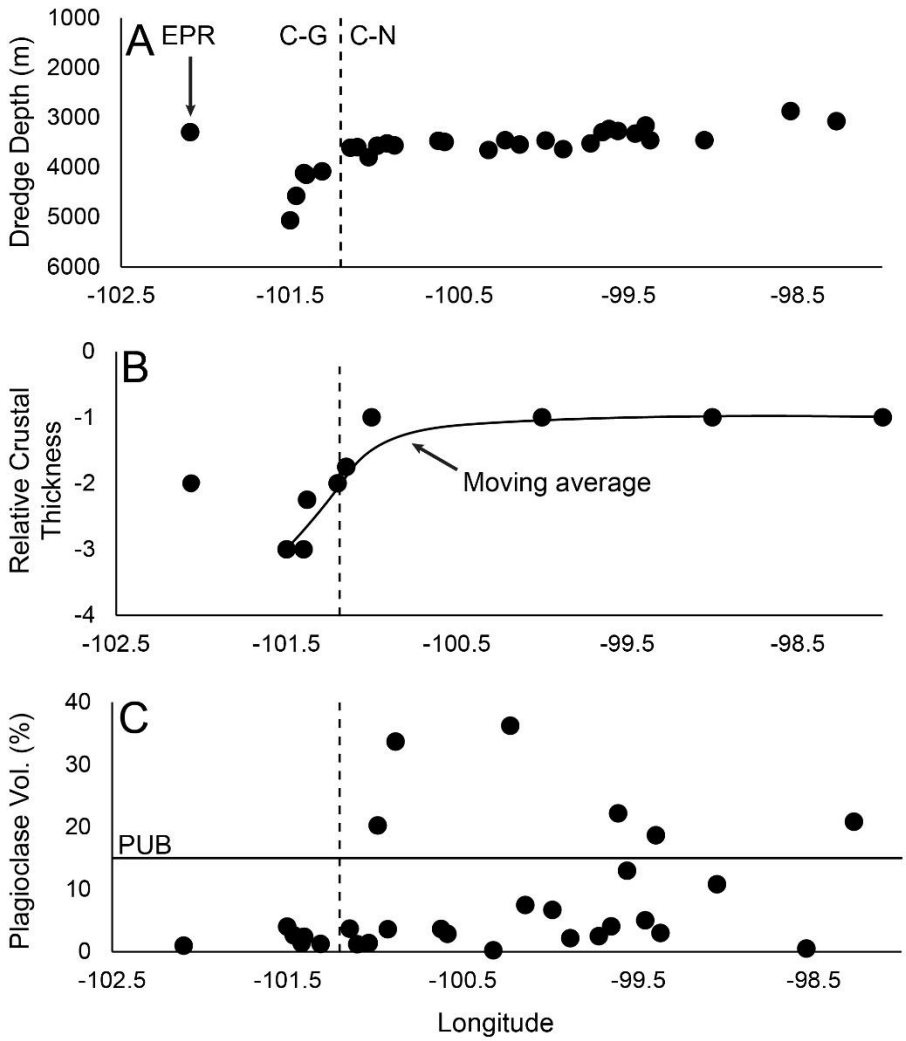

Figure 28: Longitudinal variations in (A) dredge depth, (B) mantle Bouguer anomaly inferred relative crustal thickness, and (C) plagioclase mode. The vertical dashed line marks the transition from Cocos-Galapagos to Cocos-Nazca spreading. The solid line in (B) represents the moving average of the Bouguer anomaly inferred relative crustal thickness. The horizontal line in (C) labeled 'PUB' represents the transition from plagioclase phyric to plagioclase ultraphyric basalts (PUB, > 15 vol. %, Lange et al., 2013a). Dredge depth, and plagioclase volume represent variations of a broader, representative, dataset. Data in (B) is from Zheng et al. (2019).

Lava samples were dredged in April-May 2018 aboard the *R/V Sally Ride* (Leg 1806). Lavas are generally fresh with little alteration and minimal vesicularity. The majority of samples have glassy rinds and plagioclase is the dominant crystalline phase (see Figure 29). In general, these lavas are limited in their chemical variability and are depleted relative to both the adjacent EPR and compared to the majority of MORB world (Gale et al., 2013). The geochemistry of these lavas is discussed in detail in Chapter 2. Aphyric to sparsely phyric lavas occur along the entire length of the Cocos-Nazca rift. However, the occurrence of highly-phyric lavas with plagioclase phenocrysts that extend to greater sizes is restricted to the Cocos-Nazca domain (Figure 28c). Five out of the 16 studied lavas are plagioclase ultraphyric basalts (PUB, > 15 vol. % plagioclase, Lange et al., 2013a).

4.6 Petrography

Three samples representing a range in phenocryst contents and distance from the rift tip were examined in detail. From west to east, these are samples D15-2, D20-3, and D49-1 (Figure 29); the latter two are PUB samples with 20.2 and 20.8 vol. % plagioclase, respectively.

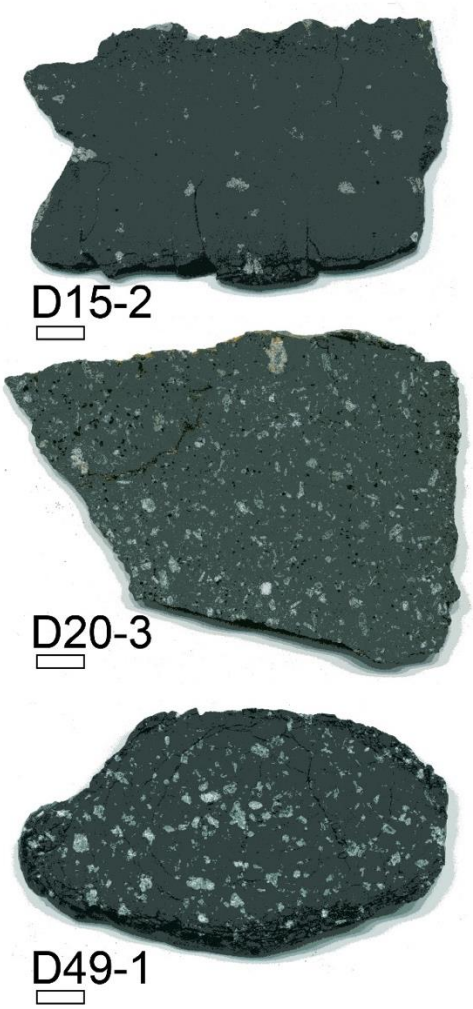

Figure 29: Examples of plagioclase-phyric lavas sampled from the Cocos-Nazca Spreading Center. D15-2 is sparsely phyric while D20-3 and D49-1 are plagioclase ultraphyric basalts (PUB, > 15 vol. % plagioclase, Lange et al., 2013a). Scale bar is 1 cm. D15-2 is from segment 4 while D20-3 is from segment 5 and D49-1 is from segment 9. Additional information for each sample is provided in Table 4.

Sample D15-2 is sparsely phyric (~ 3.7 vol. % plagioclase) and is characterized by a population of ≤ 1 mm acicular and skeletal plagioclase. This sample also contains several monomineralic plagioclase glomerocrysts that range from 1 to 4 mm in diameter. Olivine microphenocrysts (< 0.5 mm) are present but account for only a small proportion of the total crystal content of this sample (< 1 %). Like D15-2, both PUB lavas have a population of ≤ 1 mm acicular and skeletal plagioclase. However, these samples are characterized by large (1 – 4 mm, up to 7 mm) tabular crystals and also each have a population of large (> 1 mm) acicular and rounded crystals. Textural evidence of crystal disequilibria is most evident in the two PUB samples (~ 40 % of PUB plagioclase show disequilibria textures), although also observed in D15-2. Such evidence includes resorbed cores, resorbed edges, and sieve textures. Photomicrographs of different crystal morphologies and disequilibria textures are shown in Figure 30.

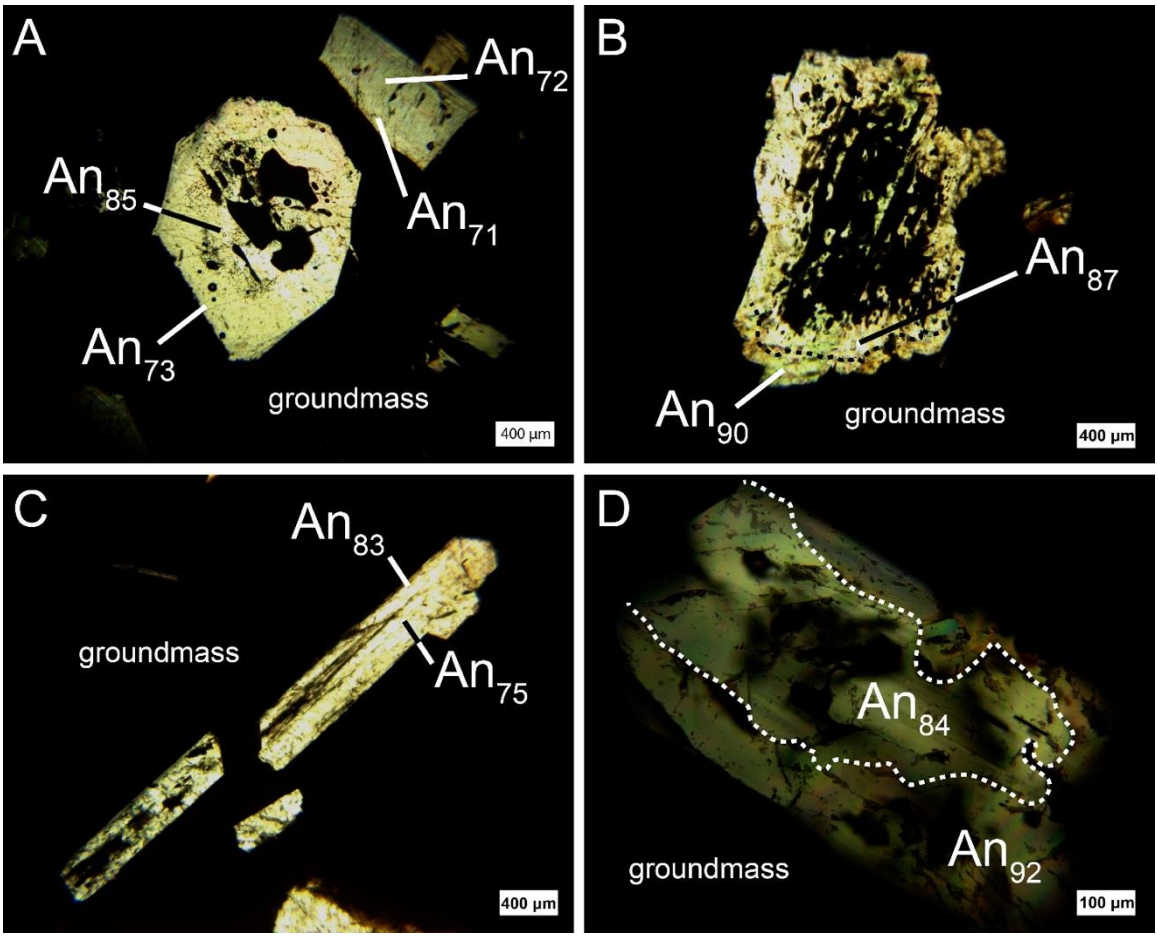

Figure 30: Plagioclase photomicrographs for PUB lavas from the Cocos-Nazca Spreading Center. A) Plane-polarized light photomicrograph of plagioclase D20-3_2 (center) and D20-3_3. Note the rounded nature of the center plagioclase, the resorbed core, and the normal zonation. B) Plane polarized light photomicrograph of a large tabular crystal (D49-1_9) with sieve texture. The optically determined core – rim boundary is highlighted by the dashed black line. C) Large acicular plagioclase in D49-1 without obvious disequilibria textures. D) Cross-polarized light photomicrograph of plagioclase D49-1_8. The low An# core is outlined in white. Note the reverse zoning in this plagioclase. The number following the sample ID refers to the specific plagioclase analyzed for that particular sample. See Appendix C for microprobe analyses.

4.7 Methods

4.7.1 Crystal Size Distribution Calculations for Cocos-Nazca Samples

Cut slabs for 16 representative samples scanned and the images were imported into the image processing software *ImageJ* (Schneider et al., 2012). Plagioclase phenocrysts were identified by adjusting the color threshold and measured. Partial crystals along the margins, glomerocrysts, and crystals with a measured area of < .01 mm^2 were excluded from the dataset. Following the methods of Boorman et al. (2004), the measured feret major and minor axes were imported into the program *CSDSlice* (Morgan and Jerram, 2006) to determine the best-fit short, intermediate, and long axes for conversion from 2- to 3D. The feret major axis is the greatest measured distance between two points of a given crystal while the feret minor axis is the minimum distance between two points of a given crystal. For all samples, the best-fit modeled 3-D shape has $R^2 \geq 0.70$ with mean $R^2 \approx 0.85$. Examples of plagioclase outlines and the modeled 3-D fit are given in Appendix C.

For 3-D size distribution calculations, plagioclase measurements (feret major, feret minor) were imported into the program *CSD Corrections* (Higgins, 2000; Higgins, 2002) with the best-fit short, intermediate, and long axes determined by *CSDSlice.* For all CSD calculations, we use the standard default of 5 bins per log unit and a roundness of 0.6. Roundness is determined using *ImageJ* and is equal to 1/aspect ratio, where aspect

ratio is the major axis/minor axis. Size intervals with one crystal are not statistically significant and introduce errors in CSD regression calculations. Consequently, these crystals are intentionally removed from the dataset. Similarly, size bins with a 2σ of infinity are also excluded due to a limited number of crystals present in that particular size range. See Table 4 for a summary of CSD calculations. Data accuracy was assessed by comparing plagioclase volume measured by intersection data (point counting, 'True Volume') to plagioclase volume determined by CSD ($R^2 = 0.95$, Figure 31).

Table 4: Crystal size distribution (CSD) data collected for samples from the Cocos-Galapagos (C-G) and Cocos-Nazca (C-N) spreading domains.

Sample	Domain	Long	Lat	No. of Crystals[1]	S:I:L	Shape Score[2]	Max L (mm)	Volume %	Intercept	Slope	Intercept < 1 mm	Slope < 1 mm	Intercept > 1 mm	Slope > 1 mm
D05-2	C-G	-101.50	2.24	278	1:1.4:2.2	0.86	5.32	4.02	2.32	-4.67	3.60	-7.70	-1.92	-1.88
D06-2	C-G	-101.46	2.23	82	1:1.4:2.0	0.72	3.04	3.59	1.04	-2.19	2.74	-6.43		
D08-2	C-G	-101.41	2.24	214	1:1.3:2.0	0.90	1.29	2.37	2.54	-4.61	3.50	-6.83	-2.00	-1.50
D08-3	C-G	-101.41	2.24	217	1:1.4:2.0	0.72	4.60	11.16	1.19	-2.48	3.15	-6.88	-2.15	-1.18
D11-2	C-G	-101.31	2.22	143	1:1.6:1.6	0.83	0.74	0.87	4.04	-11.30	4.17	-11.78		
D01-1	C-N	-99.66	2.30	155	1:1.4:2.2	0.86	4.80	4.05	1.96	-4.42	2.54	-5.80	-2.20	-1.60
D15-2	C-N	-101.15	2.21	89	1:1.2:1.9	0.88	2.50	3.69	0.88	-2.58	2.70	-6.60	-1.70	-1.40
D20-3	C-N	-100.99	2.24	1506	1:1.4:2.2	0.89	4.53	20.23	2.03	-2.24	3.81	-5.70	-1.49	-1.00
D22-1	C-N	-100.89	2.23	490	1:1.4:1.8	0.95	8.58	33.66	0.48	-1.59	2.66	-5.81	-2.29	-0.80
D26-3	C-N	-100.63	2.19	431	1:1.4:1.8	0.88	5.11	3.62	1.75	-4.24	3.01	-7.50	-1.60	-2.00
D34-2	C-N	-100.23	2.27	822	1:1.4:1.8	0.91	5.91	36.21	1.74	-2.13	3.67	-6.26	-0.97	-1.18
D36-1	C-N	-100.15	2.25	622	1:1.4:1.8	0.92	7.19	10.21	1.24	-2.72	2.90	-6.59	-1.94	-1.26
D38-7	C-N	-99.99	2.23	491	1:1.5:1.8	0.90	3.55	6.76	1.40	-3.19	2.39	-5.43	-1.84	-1.52
D47-2	C-N	-99.70	2.31	1458	1:1.4:1.9	0.90	2.61	8.12	3.80	-5.06	4.06	-6.10	-0.56	-1.87
D48-1	C-N	-99.62	2.29	837	1:1.4:1.9	0.92	4.98	22.16	1.27	-2.03	3.09	-5.59	-1.27	-1.09
D49-1	C-N	-98.27	2.33	587	1:1.4:1.9	0.90	6.79	20.85	0.86	-2.01	2.60	-5.40	-1.48	-1.12
D54-1	C-N	-99.05	2.22	1059	1:1.4:1.9	0.92	5.96	10.82	1.16	-2.44	2.89	-6.30	-1.73	-1.25

[1]*Number of crystals is the total number of crystals included in each measurement*

[2]*Shape score is the correlation coefficient for the modelled 3-D shape collected using CSDSlice (Morgan and Jerram, 2006)*

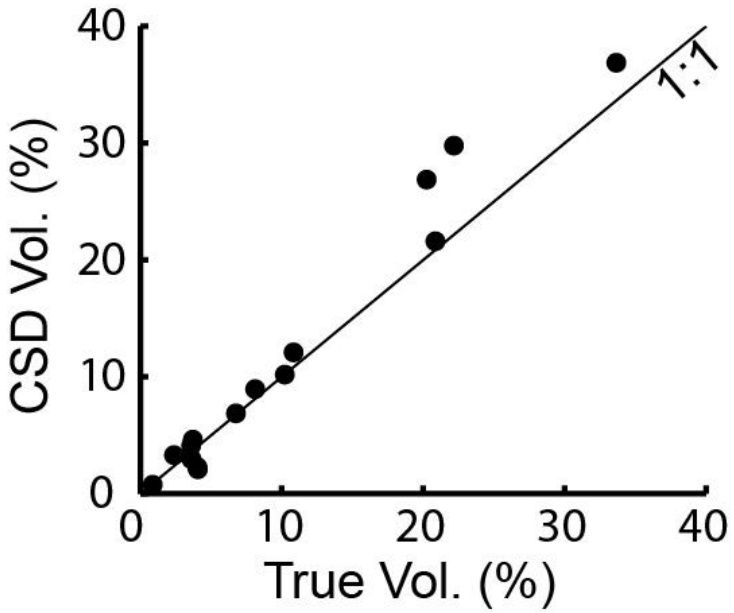

Figure 31: Correlation between plagioclase true volume (measured by point counting) and CSD calculated volume.

4.7.2 Electron Microprobe Analyses

To further elucidate the CSD analyses of the 16 sparsely phyric to plagioclase ultraphyric basalts, plagioclase crystals in three samples (D15-2, D20-3, and D49-1) were analyzed by electron microprobe (An#) characterization. In total, major element compositions of 47 plagioclase core – rim pairs were analyzed using the Cameca CAMEBAX Electron Microprobe at Duke University. For all analyses, a defocused beam (~ 15 μm in diameter) was used with a beam current and accelerating voltage of 15 nA and 15 KeV, respectively. Repeat analyses of an in-house bytownite standard reveal an overall standard deviation of ± 0.6 % corresponding to an An# error of ± 2.71. An# is the

molar ratio Ca/(Ca + Na + K). Core – rim pair compositions and standard repeat analyses can be found in Appendix C.

4.8 Results

4.8.1 Crystal Size Distribution

The sparsely phyric lavas from the Cocos-Galapagos spreading regime have the smallest grain sizes (≤ 0.5 – 4 mm) and are the only samples with approximately log-linear distributions on crystal size distribution plots (crystal length vs ln population density, Figure 32a). Size distributions for lavas from the Cocos-Nazca spreading regime, in contrast, show a characteristic concave upward curvature and extend to larger crystal sizes (up to 10 mm, Figure 32b). Because CSDs for samples with larger phenocrysts are curved, the CSD slope and intercept cannot be assumed to describe the crystallization conditions of the entire crystal population in that sample. Therefore, for these samples, each is separated into two size ranges (> 1 mm and < 1 mm) with roughly linear distributions. CSD slope and intercept values are calculated for each size range and denoted as either > 1 mm or < 1 mm (see Table 4); this provides a measure of the different thermal histories for the > 1 mm and < 1 mm crystal populations in each of these samples. Using this approach, Figure 33 shows CSD slopes and intercepts for all 16 samples studied, which as a whole, show a broad inverse correlation ('all sizes', Figure 33).

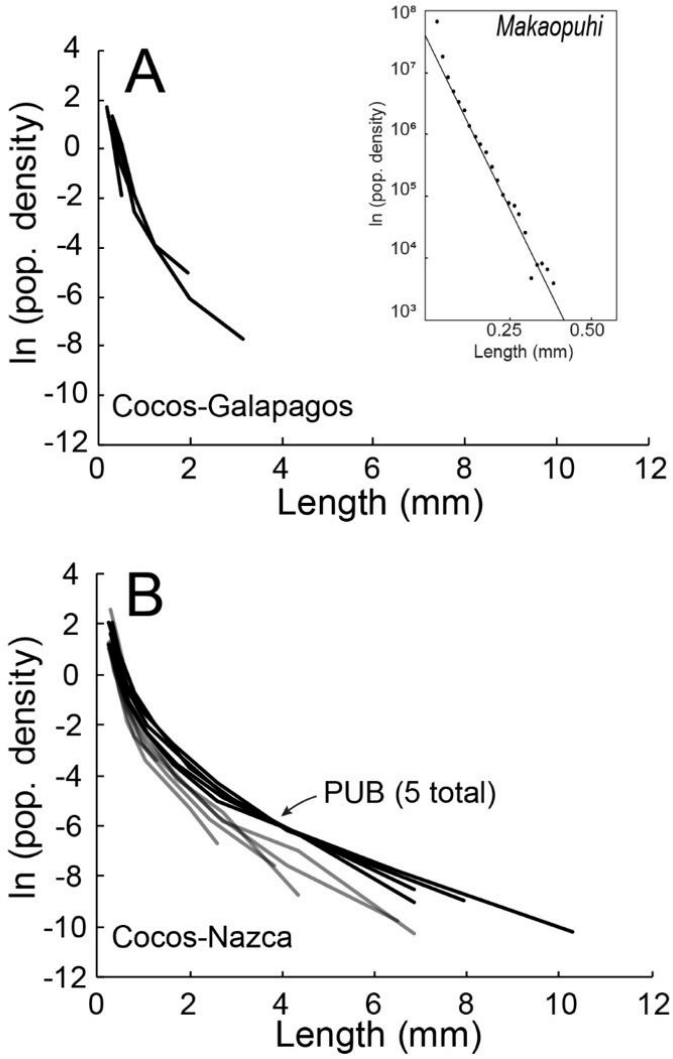

Figure 32: Crystal size distribution plots for plagioclase from (A) the Cocos-Galapagos spreading regime, and (B) the Cocos-Nazca spreading regime. The inset in (A) is the size distribution plot for Makaopuhi lava lake from Cashman and Marsh (1988). The linear distribution of the Makaopuhi lava lake sample is indicative of closed system behavior.

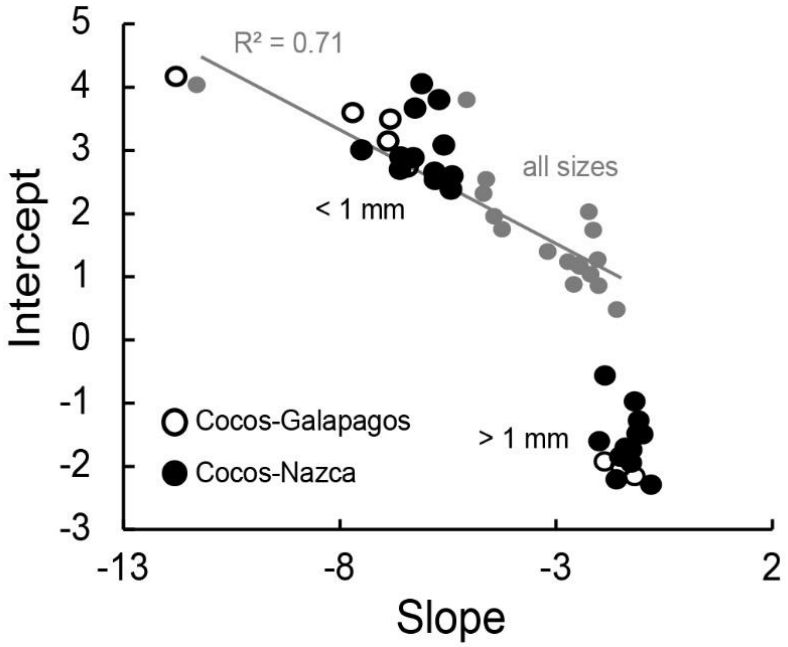

Figure 33: CSD slope vs CSD intercept for both the > 1 mm and < 1 mm size fractions. The points in grey labeled 'all sizes' represents the simple linear regression for each CSD without separation into > 1 and < 1 mm size ranges.

4.8.2 Plagioclase Compositional Zoning

Plagioclase An# analyses are presented in Figure 34 (see Appendix C, Table 14 for individual analyses). In general, plagioclase core and rim compositions are highly variable within and between individual samples (An# range from 63 to 84, 70 to 88, and 76 to 92 for D15-2, D20-3, and D49-1, respectively). There is a crude trend where higher An# core compositions are associated with larger crystals (Figure 34b, d), though high An# are also observed in smaller (< 1 mm) plagioclase crystals. For all samples, normal

and reverse chemical zonation is observed and is associated with all crystal morphologies and disequilibrium textures (see Figure 30).

Also shown in Figure 34 are the calculated equilibrium An# values for each sample, based on glass compositions presented in Chapter 2 (Appendix B, Table 8). For all three samples, a large proportion of plagioclase crystals (both core and rim) are not in equilibrium with their host glass composition (Figure 34a, c, e). For samples D15-2 and D20-3, there is an overall tendency for rims to approach compositions expected to be in equilibrium with the host glass. This is not the case for sample D49-1, where the proportion of crystals in equilibrium with their host glass is lowest (4 out of 18 crystals, Figure 34b, d).

Figure 34 (next page): Distribution of plagioclase core and rim $An_{\#}$ for samples D15-2 (A), D20-3 (C), and D49-1 (E). The solid pink line is the $An_{\#}$ in equilibrium with the host glass and was calculated using MELTS (Ghiorso and Sack, 1995; Asimow and Ghiorso, 1998). The dashed blue line is the $An_{\#}$ in equilibrium with the host glass with 0.5 wt. % H_2O added to the glass composition. Equilibrium $An_{\#}$ were calculated using the glass major element composition. Increasing pressure acts to decrease equilibrium $An_{\#}$. Core – rim variations as a function of crystal size are also given for samples D15-2 (B), D20-3 (D), and D49-1 (F).

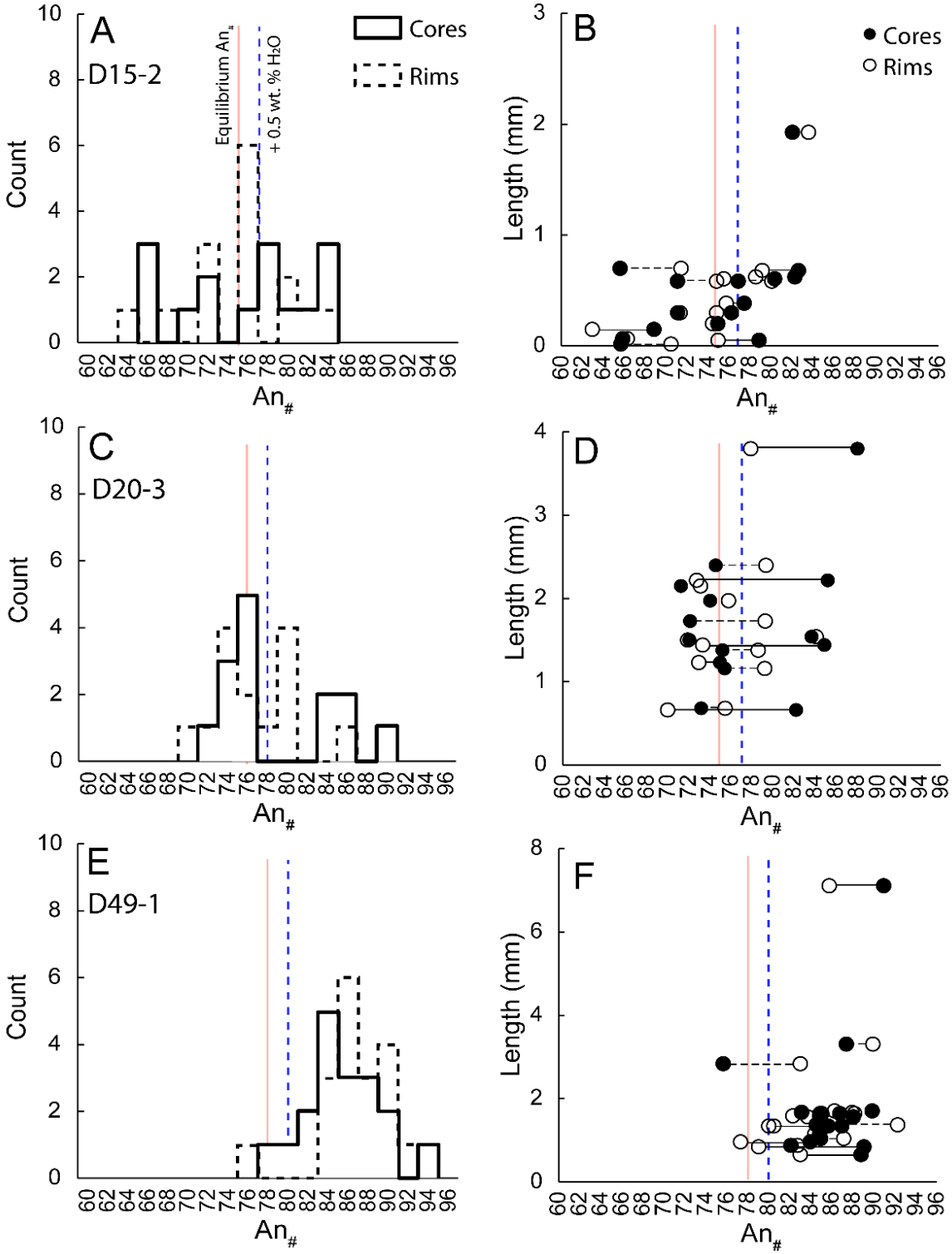
A
D15-2
Cores
Rims
Equilibrium An#
+ 0.5 wt. % H2O
Count
An#
B
Cores
Rims
Length (mm)
An#
C
D20-3
Count
An#
D
Length (mm)
An#
E
D49-1
Count
An#
F
Length (mm)
An#

4.9 Discussion

4.9.1 Cocos-Galapagos and Cocos-Nazca

The plagioclase CSDs for the Cocos-Galapagos spreading domain are near log linear while those from the Cocos-Nazca have larger crystals and are distinctly curved. Further, plagioclase from the Cocos-Nazca preserve textures (resorbed cores, sieve textures) indicative of crystal-melt disequilibria. Initial interpretations of the log linear CSD trends for the < 1 mm size fraction might suggest rapid cooling and crystallization of a magma (e.g., Marsh, 1988) without significant modification by crystal aging. This interpretation is supported by basalt cooling experiments where similar CSD trends are observed for plagioclase that nucleated during rapid quenching ($\Delta T/\Delta t$ = 60°C/hr, Giuliani et al., 2020). If this were true, however, these crystals would be in equilibrium with their host glass. Although rims tend toward equilibrium compositions, the majority of the crystals including the < 1 mm size fraction are rarely in equilibrium with their host glass, the opposite of what is expected for a 'microlite' population. Consequently, the simple explanation of mixing of a single size population into a system with a log linear CSD (the "crystal accumulation curve" in Figure 28a) seems unlikely.

In contrast, for the Cocos-Nazca spreading domain, the broad curvature of the CSDs (Figure 32b) and the negative correlation between CSD slope and CSD intercept (Figure 33) for the > 1 mm size fraction is consistent with crystal accumulation and/or

crystal coarsening of the larger grains (Higgins, 1998). A similar CSD pattern is reported for plagioclase from Reunion Island and interpreted to be the result of plagioclase incorporation (Marsh, 1996). Texturally, the sparsely phyric and highly-phyric lavas have a complex population of plagioclase crystals, the majority of which have textures associated with crystal – melt disequilibria. The existence of both normal and reverse zonation suggests a history of crystal super heating and under cooling. Further, the < 1 mm plagioclase populations that are, in general, not in chemical equilibrium with their host glass (An#) suggests that crystals of all sizes were incorporated as xenocrysts in a migrating magma. This is most evident for sample D49-1 where all but one crystal core are more anorthitic than what is expected for the host glass. For samples D15-2 and D20-3, the tendency for core – rim pairs to be bisected by the melt equilibrium An# composition (Figure 34b, d) suggests that crystals may react with their host magma such that the plagioclase rim compositions approach equilibrium with their host magma. This is not observed for sample D49-1, suggesting the host magma incorporated plagioclase with less time for xenocrysts to react and equilibrate with their host magma.

4.9.2 Conceptual Model for the Cocos-Galapagos and Cocos-Nazca Plagioclase-Bearing Lavas

To explain the mixed population of < 1 mm and > 1 mm crystals and the general lack of equilibrium with their host magma, a conceptual model is developed. It is suggested that the CSDs represent the incorporation of crystals that initially formed at a

crystallization front (steep and linear CSDs) and aged crystals (flat CSDs) deeper in the mush zone. Figure 35 is a half-space cartoon depicting a possible explanation for the observed size distributions, morphologies, and compositions of plagioclase crystals from the Cocos-Galapagos and Cocos-Nazca domains. Here, a crustal mush with a range of plagioclase sizes reflecting their relative age is shown. The 'rigid front' is the point where crystallinities exceed 50 % and the mush behaves like a solid (Marsh, 1996; Marsh, 2013). Crystals nucleate and begin to grow at the nucleation front (blue line). Selective sampling of this crystal population produces a CSD with a steep slope, a high intercept value, and limited crystal lengths (Figure 35a). Deeper in the crystallization front, growth occurs by aging such that this crystal population produces a CSD with a downturn at small sizes (Figure 35b). It is important to note that CSD patterns similar to that observed in Figure 35b are observed for plagioclase in gabbros from the Oman ophiolite (Garrido et al., 2001). If all crystals outside of the rigid front are entrained by an ascending aphyric magma, the resulting CSD will reflect the sum of all crystal populations outside of the rigid front (black line, Figure 35c). Slower cooling rates will both produce fewer crystal nuclei at the nucleation front (lower CSD intercepts) and allow more time for crystal aging deeper in the crystallization front. The net result of slower cooling is to produce larger plagioclase and flatter CSDs. The hypothetical CSD resulting from slower cooling is also given in Figure 35 (green line, Figure 35c).

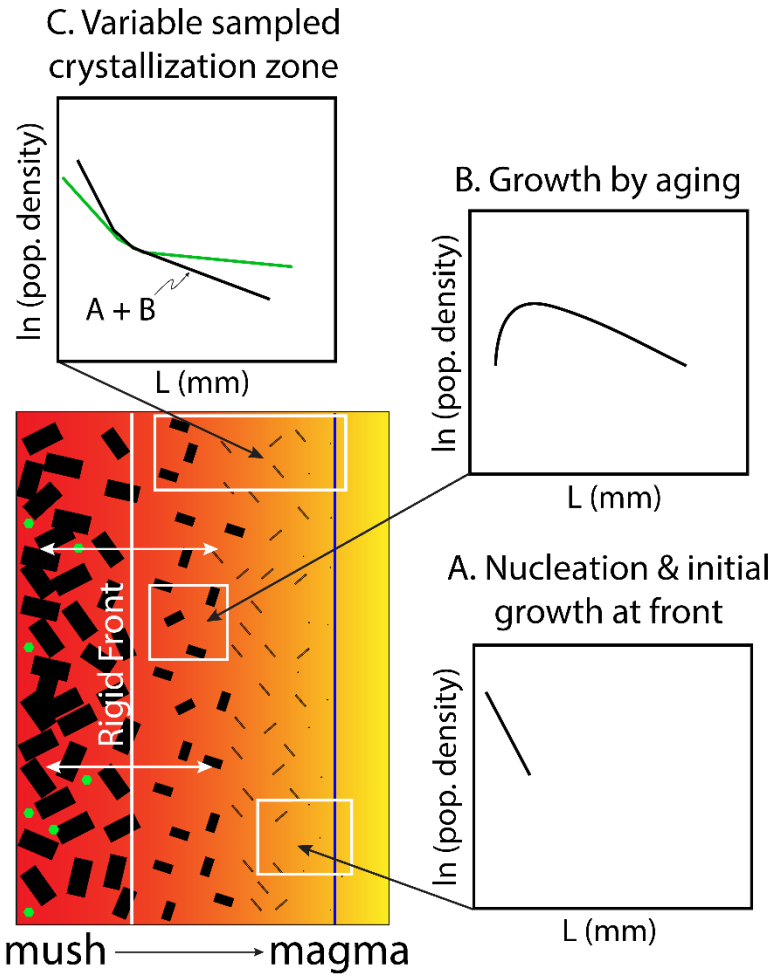

Figure 35: A physical model that explains the observed CSDs. A) Half-space cartoon depicting a cooling pod of magma in the oceanic crust. The rigid front marks the transition from rigid mush, where the mush behaves as a solid, to crystals suspended in magma. The blue line marks the nucleation front. A) Nucleation and growth at the nucleation front results in a CSD with a steep slope, high intercept value, and limited crystal sizes. B) Away from the nucleation front, crystals continue to grow by aging such that the CSD has a downturn at smaller crystal sizes. C) Sampling of the entire crystal population outside of the rigid front results in the black CSD curve. If cooling rate is increased, the rigid front migrates to the right such that the only eruptible crystals are small. If cooling rate is decreased, the rigid front moves to the left such that more aged crystals are eruptible. The green line in (C) is the predicted CSD for a crystal population that experiences slower cooling relative to the black CSD in (C).

One problem with the conceptual model described above is the observation that there is no characteristic downturn at smaller crystal sizes for Cocos-Nazca crystal size distributions. One possibility, as shown in Figure 35, is that the Cocos-Nazca lavas entrain variably aged crystals such that the characteristic downturn at smaller sizes is effectively 'erased'. One concern with this conceptual model is the open system nature of crustal mushes where a variety of processes, like temperature fluctuations, can modify the crystal size population (Mills et al., 2011).

Figure 36 compares crystal size distribution curves for plagioclase populations from Guiliani et al. (2020) that crystallized at rapid ($\Delta T/\Delta t$ = 60°C/hr) and slow cooling rates ($\Delta T/\Delta t$ = 7°C/hr). In this scenario, the size distribution for the rapidly cooling population is analogous to that observed in Figure 35a. Similarly, the size distribution for the slowly cooling population is analogous to that observed in Figure 35b. Combining the two crystal populations results in a mixed population of crystals that 'erases' the downturn associated with the slower cooling (aging) population (mixed population, Figure 36). Importantly, Figure 36 confirms that the signatures of crystal aging are potentially obscured when multiple size populations with different cooling histories are entrained by a migrating magma.

For the Cocos-Galapagos, it is suggested that the steep slopes, high intercept values, and limited crystal sizes reflect selectively sampling the nucleation front or

sampling of a faster cooling mush (cooler crust or smaller magma body). In both scenarios, a limited range of plagioclase sizes exists outside of the rigid front that can be incorporated into an ascending magma. For the Cocos-Nazca, a slower cooling mush (warmer crust or larger magma body) produces a wider range of plagioclase sizes and compositions. Those crystals deeper in the nucleation front would have more time to age. This variable crystal population outside of the rigid front is incorporated into an ascending magma and reacts (resorbed cores, sieve textures, normal and reverse zoning) such that plagioclase approach equilibrium with the carrier magma. Importantly, this scenario explains the presence of < 1 mm crystals that are not in chemical equilibrium with their host glass. It is important to emphasize that the above discussion does not preclude the nucleation of plagioclase microlites during magma ascent to the seafloor. In fact, this process almost certainly occurred for sample D15-2, where some of the < 1 mm plagioclase (cores and rims) are in equilibrium with the host glass composition. Instead, this physical model provides a simple way to explain a majority of the plagioclase size distributions, morphologies, and compositions discussed in this study.

Together, these observations highlight the differences between the two spreading domains. For the Cocos-Galapagos domain, the observed CSD patterns might reflect rapid cooling, crystallization of a smaller body of magma, the existence of simple melt pathways with limited opportunities to entrain plagioclase, or all three. For the Cocos-

Nazca domain, the occurrence plagioclase ultraphyric basalts suggest more complex melt pathways with an increase in the number of opportunities for ascending magmas to entrain plagioclase.

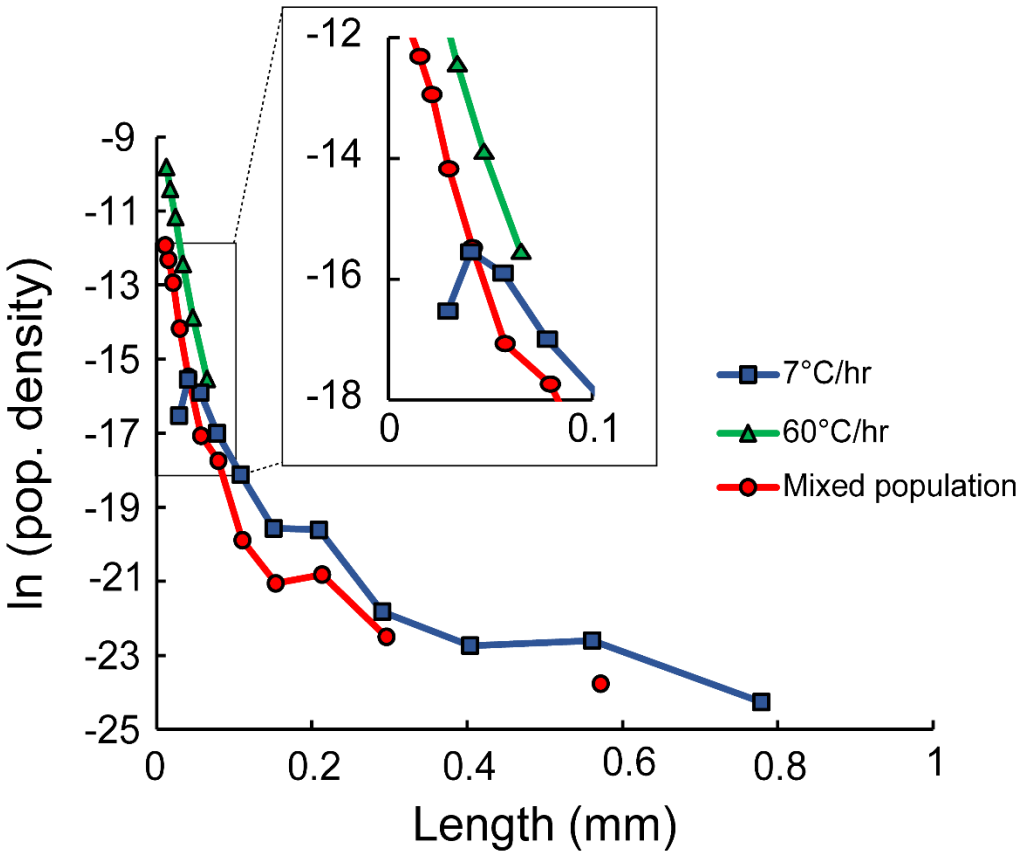

Figure 36: Crystal size distribution curves for plagioclase that crystallized during rapid (ΔT/Δt = 60°C/hr) and slow cooling (ΔT/Δt = 7°C/hr) experiments. Data is from Giuliani et al. (2020). The mixed population is the resulting crystal size distribution after combining the rapid and slow cooling populations. Importantly, mixing of the two populations removes the crystal aging signature seen in the slow cooling crystal size distribution.

4.9.3 Plagioclase Ultraphyric Lavas

For PUB lavas, the existence of large plagioclase (that can be incorporated into an ascending magma) requires sufficient time for prolonged growth and reflects the physiochemical conditions experienced during nucleation and growth. Figure 37a compares axial ridge depth to plagioclase volume (%) for PUB from the Cocos-Nazca Spreading Center, the Blanco transform, the Juan de Fuca ridge, the Southwest Indian Ridge, and the Knipovich ridge. In general, a broad correlation exists between plagioclase phenocryst content and axial ridge depth (Figure 37a, $R^2 = 0.30$), suggesting that high magma fluxes (shallow ridge depths) are associated with phyric lavas. This is counterintuitive because plagioclase length is proportional to the growth rate multiplied by the time allowed to grow. Large fluxes of magma (shallow depths) should result in shorter residence times, smaller plagioclase, and fewer plagioclase in the mode. Figure 37b illustrates that there is no correlation between ridge spreading rate and plagioclase volume (%) for the same dataset (excluding those data from the Blanco fracture zone), although available data is limited. A strong correlation among PUB lavas is observed when comparing CSD slope to CSD intercept for the > 1 mm size population ($R^2 = 0.91$, Figure 37c). As noted above, this distribution can be interpreted as crystal accumulation at crustal levels and/or crystal coarsening (Marsh, 1998; Higgins, 2006). Because these samples are not genetically related, this observed correlation might suggest that PUB

from the Southwest Indian Ridge more efficiently entrained plagioclase prior to eruption while PUB from the Cocos-Nazca did not. Figure 37c highlights that there are differences in PUB CSDs for the > 1 mm size fraction and raises the question: does this reflect some fundamental process governing PUB formation?

One possible explanation for the observed differences among PUB lava CSDs exists where those lavas with shallow CSD slopes and low CSD intercept values (SWIR, Figure 37c) simply reflect environments where the growth of larger plagioclase is favored (i.e., slower cooling rates or larger magma bodies). Indeed, Nielsen et al. (2020) report euhedral morphologies and limited chemical zonation for plagioclase megacrysts (up to 2 cm long) in PUB from the Southwest Indian Ridge and the Blanco fracture zone. These are characteristics of prolonged growth in a mush (Marsh, 2013). In this scenario, it is possible that slower cooling rates in a crustal mush leads to an increase in the number of aged crystals outside of the rigid front (see Figure 35). Ultimately, these aged crystals are incorporated into an ascending magma resulting in coarse lavas that appear to have aged relative to other PUB lavas.

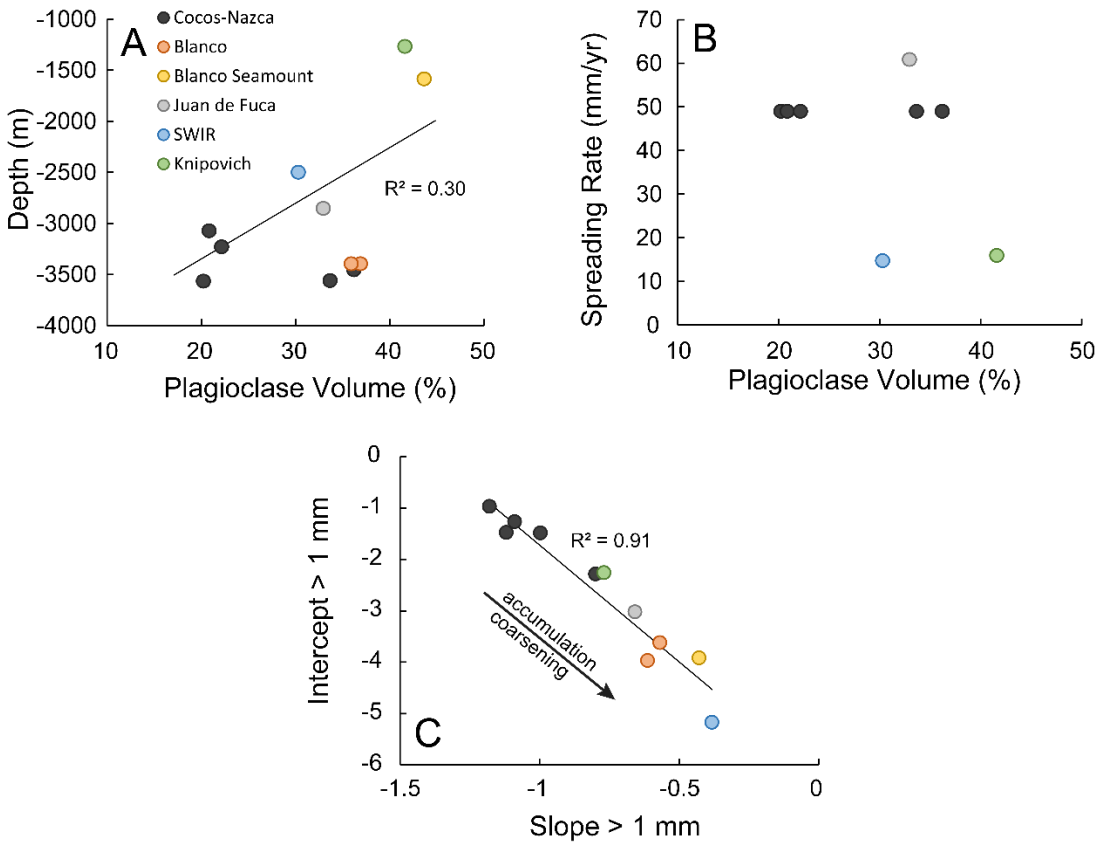

Figure 37: Comparisons of plagioclase ultraphyric basalt found elsewhere. A) Correlation between plagioclase volume (%) and axial ridge depth for PUB lavas discussed in the text. B) Comparing plagioclase volume (%) to ridge spreading rate. It is important to note that data from the Blanco fracture zone are excluded from this plot. C) Correlation between CSD slope and intercept for the > 1 mm size fraction for PUB lavas from various spreading centers. The arrow represents the possible interpretations for a linear data array in this space (Marsh, 1998; Higgins, 2006; Higgins, 2008). Data for Blanco, Juan de Fuca, and the Southwest Indian ridge are from Lange et al. (2013a) and Nielsen et al. (2020). Data for Knipovich are from Hellevang and Pederson (2008). For information related to PUB CSD calculations and plagioclase equilibrium An#, readers are directed to Appendix C.

4.10 Conclusions

Crystal size distributions (CSDs) for plagioclase-bearing lavas from the Cocos-Galapagos and Cocos-Nazca spreading centers differ, perhaps reflecting the transition from tectonic to magmatic spreading and the development of a more complex magma plumbing system. Plagioclase from one sparsely phyric lava and two PUB lavas have a variety of morphologies (acicular, skeletal, tabular, rounded) and resorption textures (resorbed cores, sieve textures). Plagioclase An# are highly variable within and between samples. For two samples, the chemical composition of plagioclase core – rim pairs approach equilibrium with their host glass, suggesting that plagioclase crystals react with their carrying magma. The presence of small (< 1 mm) plagioclase that are not in equilibrium with their host glass might originate at a nucleation front. A simple physical model is proposed that accounts for the observed variability in plagioclase CSDs, textures, and chemical compositions.

Comparisons of CSDs for PUB lavas from different spreading centers reveal that differences exist among PUB lava size distributions. For these lavas, slower cooling rates in a crustal mush might lead to an increase in the number of aged (large) crystals that exists outside of the rigid front. These aged crystals are incorporated into an ascending magma leading to the eruption of coarse PUB lavas that appear to have aged (or entrained more plagioclase) relative to other PUB lavas.

5. Conclusions

This dissertation uses detailed petrographic and geochemical observations to examine a variety of processes occurring within igneous systems. The second chapter establishes a connection between the late-stage hydrothermal evolution of the Skaergaard Intrusion of east Greenland and the modification of the Skaergaard transition and precious metal budget. Significantly, this work highlights that layered intrusions are complex systems with multiple processes acting in concert to form these bodies. The third chapter of this dissertation reports geochemical data for the previously sparsely sampled Cocos-Nazca Spreading Center of the eastern equatorial Pacific. In general, these data are unique to the region and a genetic link between the Cocos-Nazca Spreading Center and the neighboring East Pacific Rise is established. The fourth chapter of this dissertation reports detailed morphological and chemical measurements of plagioclase crystals in lavas erupted at the Cocos-Nazca Spreading Center. More broadly, this chapter establishes that crystal size distribution theory can be used to elucidate processes occurring at crustal levels beneath mid-ocean ridges. Ultimately, observed morphological and chemical differences in plagioclase crystals provide information about how crustal processes evolve as a spreading center matures.

Appendix A: Supplementary Material for Chapter 1

Sulfides and accessory minerals were systematically studied using the Cameca CAMEBAX microprobe at Duke University. Table 5 is given in the following pages and provides a detailed accounting of the occurrences reported in Chapter 1.

Table 5 (pages 141-161): Sulfide assemblages and associated minerals. Samples SK90-11 (LZc), SK90-12 (LZc), SK90-11-1b (MZ), and SK90-41b (MZ) are not included in this table as either no sulfides were observed, or sulfides were entirely altered.

ID	SK90-5-A	SK90-5-AA-1	SK90-5-AA-2	SK90-5-AA-3	SK90-5-B	SK90-5-B-2	SK90-5-BB	SK90-5-C
Stratigraphic Zone	**LZa**	**LZa**	**LZa**	**LZa**	**LZa**	**LZa**	**LZa**	**LZa**
Chalcopyrite	540	626	432	202	400	172		
Pyrrhotite								
Pentlandite							693	
Bornite							4142	431
Covellite								
Ti-Poor magnetite		145						
Native Cu								
Biotite		422		45				
Apatite		15						
Calcite								
Clinopyroxene								
Orthopyroxene								
Ca-plag near assemblage?								
Notes	Between olivine and cpx	Olivine-plag grain boundary with associated biotite	In plag	In plag with trace biotite	Intracrystalline (plag)	Grain boundary sulfide (plag - cpx)	In plag with trace biotite	Grain boundary (olivine - plag)

ID	SK90-5-CC-1	SK90-5-CC-2	SK90-5-CC-3	SK90-5-CC-4	SK90-5-D	SK90-5-E	SK90-5-F	SK90-5-FF-1
Stratigraphic Zone	**LZa**	**LZa**	**LZa**	**LZa**	**LZa**	**LZa**	**LZa**	**LZa**
Chalcopyrite	4992	390	1282	1537	861	2499	219	2510
Pyrrhotite								
Pentlandite		426	262					
Bornite						1123		
Covellite								263
Ti-Poor magnetite		394		800	329		664	
Native Cu								
Biotite	551				893	114		1798
Apatite								
Calcite								
Clinopyroxene					1205			
Orthopyroxene								
Ca-plag near assemblage?	Y							
Notes	In plag near grain boundary	In plag	In plag	In plag	Sulfide in cpx	In plag	With low-Ti magnetite	In plag

ID	SK90-5-FF-2	SK90-5-G	SK90-5-GG-1	SK90-5-GG-2	SK90-5-H	SK90-5-HH	SK90-5-II	SK90-5-K
Stratigraphic Zone	**LZa**	**LZa**	**LZa**	**LZa**	**LZa**	**LZa**	**LZa**	**LZa**
Chalcopyrite	2066	763	85	132	859	183	190	1376
Pyrrhotite								
Pentlandite								
Bornite			98				25	113
Covellite								
Ti-Poor magnetite				6				93
Native Cu								
Biotite		724						
Apatite								
Calcite		198	27					
Clinopyroxene								
Orthopyroxene								
Ca-plag near assemblage?								
Notes	Cu colloids at grain margins. Desulfurization?	Trace calcite	In plag with trace calcite and biotite - near boundary	At plag - olivine boundary	In plag	At cpx-olivine boundary	At cpx-olivine boundary with trace biotite	In late plag-rich vein, sulfide oxidized

ID	SK90-5-KK	SK90-5-L	SK90-5-M	SK90-5-N	SK90-5-P	SK90-5-R	SK90-5-T	SK90-5-U
Stratigraphic Zone	**LZa**	**LZa**	**LZa**	**LZa**	**LZa**	**LZa**	**LZa**	**LZa**
Chalcopyrite	363				357	974	2156	612
Pyrrhotite								
Pentlandite				213				
Bornite		262						
Covellite								
Ti-Poor magnetite					276	836	256	171
Native Cu			100	21				
Biotite							1061	
Apatite								
Calcite							475	
Clinopyroxene								
Orthopyroxene								
Ca-plag near assemblage?			Y					
Notes	In plag	Bornite intracrystalline to sodic plag	"Myrmekitic" texture. S loss with Cu	Pentlandite with native Cu in plag	Sulfide assemblage in plag (An50) with magnetite	Intracrystalline sulfide assemblage (plag)	Sulfide assemblage in plag at ol-plag boundary, minor biotite and calcite	Olivine - plag boundary

ID	SK90-5-V	SK90-5-W-1	SK90-5-W-2	SK90-5-W-3	SK90-5-Y	SK90-5-Z	SK90-13-A	SK90-13-B
Stratigraphic Zone	**LZa**	**LZa**	**LZa**	**LZa**	**LZa**	**LZa**	**LZc**	**LZc**
Chalcopyrite	462	1787	1564	307	701	127		
Pyrrhotite								
Pentlandite								
Bornite					459	278	67	434
Covellite								
Ti-Poor magnetite	577	2336	514			71		
Native Cu		109						
Biotite		1066					28	179
Apatite								
Calcite				32	137			84
Clinopyroxene	317	1732		235				
Orthopyroxene								
Ca-plag near assemblage?								Y
Notes	Oxidized chalcopyrite with minor opx - textural disequilibria	In plag	In plag	Oxidized ccp in plag	In plag with minor calcite, trace biotite	Between cpx and plag, trace KCl	In plag, trace Cl	Cu inclusion in carbonate. Note Cl anomaly

ID	SK90-13-C	SK90-13-D	SK90-13-E	SK90-13-F	SK90-13-G	SK90-22-A	SK90-22-AA	SK90-22-B
Stratigraphic Zone	**LZc**	**LZc**	**LZc**	**LZc**	**LZc**	**UZb**	**UZb**	**UZb**
Chalcopyrite			349		200			
Pyrrhotite								
Pentlandite								
Bornite	116	1469	597	1375	710	5003	931	8287
Covellite							3537	
Ti-Poor magnetite		40	139		54		256	
Native Cu								
Biotite				4080				
Apatite								
Calcite								
Clinopyroxene	646				313			
Orthopyroxene			361					
Ca-plag near assemblage?				Y	Y			
Notes	Between plag, note Fe-Mg-Al silicate	In cpx with minor low-Ti magnetite	In cpx with trace opx	In plag with biotite	At cpx-plag boundary	Bornite in olivine	Intracrystalline covellite to olivine, minor Ti-poor mt	Rounded bornite in plag with associated vug

ID	SK90-22-BB	SK90-22-CC	SK90-22-D	SK90-22-DD	SK90-22-E	SK90-22-EE	SK90-22-F	SK90-22-H
Stratigraphic Zone	**UZb**	**UZb**	**UZb**	**UZb**	**UZb**	**UZb**	**UZb**	**UZb**
Chalcopyrite								
Pyrrhotite								
Pentlandite								
Bornite	11040	5692	1725	1000	1099	2198	5616	472
Covellite								
Ti-Poor magnetite	2421	4018		195				
Native Cu								
Biotite								
Apatite		2874						
Calcite								
Clinopyroxene								
Orthopyroxene								
Ca-plag near assemblage?								
Notes	Irregular grain boundaries, half surrounded by biotite	Interstitial with secondary Fe-Mg silicate.	Bornite with trace apatite in olivine	Interstitial to apatite and cpx	In Ti-magnetite	Bornite between high-Ti mt and cpx	Largely at cpx-olivine boundary	In plag

ID	SK90-22-I	SK90-22-J	SK90-22-K	SK90-22-L	SK90-22-M	SK90-22-N	SK90-22-O	SK90-22-P
Stratigraphic Zone	**UZb**	**UZb**	**UZb**	**UZb**	**UZb**	**UZb**	**UZb**	**UZb**
Chalcopyrite								
Pyrrhotite								
Pentlandite								
Bornite	266	12992	1384	154	878	30835	24629	53722
Covellite								
Ti-Poor magnetite			518					
Native Cu								
Biotite								
Apatite								
Calcite								
Clinopyroxene								
Orthopyroxene								
Ca-plag near assemblage?								
Notes	In plag	At cpx/Ti-magnetite boundary	In cpx	In Ti-magnetite	In plag	Associated trace apatite Ti-magnetite and cpx	In cpx with associated Ti-magnetite	Part of Ti-magnetite bleb with trace apatite

ID	SK90-22-R	SK90-22-S	SK90-22-T	SK90-22-U	SK90-22-V	SK90-22-W	SK90-22-X	SK90-22-Y
Stratigraphic Zone	**UZb**	**UZb**	**UZb**	**UZb**	**UZb**	**UZb**	**UZb**	**UZb**
Chalcopyrite								
Pyrrhotite								
Pentlandite								
Bornite			4557		19097	666	3562	277
Covellite	6209	1470		12305				
Ti-Poor magnetite								
Native Cu								
Biotite							1959	
Apatite		17497					1783	
Calcite								
Clinopyroxene								
Orthopyroxene								
Ca-plag near assemblage?								
Notes	In Ti-magnetite	At olivine-plag boundary with associated apatite	Bornite between grain boundaries of Ti-rich magnetite with cpx and olivine	Covellite interstitial to plag and cpx	Irregular bornite	Rounded bornite at high-Ti magnetite/plag boundary	Bornite with biotite interstitial to large apatite and plag	Rounded bornite in olivine

ID	SK90-22-Z	SK90-32A-C	SK90-32A-A	SK90-32A-AA	SK90-32A-B	SK90-32A-BB	SK90-32A-CC	SK90-32A-D
Stratigraphic Zone	**UZb**	**UZa**	**UZa**	**UZa**	**UZa**	**UZa**	**UZa**	**UZa**
Chalcopyrite								
Pyrrhotite								
Pentlandite								
Bornite		1562	8938			21327		5813
Covellite	20635				312		6201	
Ti-Poor magnetite	2024					1771		
Native Cu								
Biotite								
Apatite								
Calcite								
Clinopyroxene								
Orthopyroxene								
Ca-plag near assemblage?						Y	Y	
Notes	Covellite between large euhedral apatite	Surrounded by chlorite	Grain boundary between olivine and cpx	Sulfide with associated high-Ti magnetite in cpx, note native Pt	Interstitial between olivine, high-Ti magnetite and cpx	Plag becomes more calcic towards assemblage, note olivine at cpx grain boundary	Cpx and plag boundary	Rounded in olivine

ID	SK90-32A-DD	SK90-32A-E	SK90-32A-EE	SK90-32A-F	SK90-32A-FF	SK90-32A-G	SK90-32A-GG	SK90-32A-H
Stratigraphic Zone	**UZa**	**UZa**	**UZa**	**UZa**	**UZa**	**UZa**	**UZa**	**UZa**
Chalcopyrite	2096				2893			
Pyrrhotite								
Pentlandite								
Bornite	913	16771	9168	4676	10630	7772		1115
Covellite							14147	
Ti-Poor magnetite	818	652			2280	1586		
Native Cu								
Biotite				2612				
Apatite						394		
Calcite								
Clinopyroxene								
Orthopyroxene								
Ca-plag near assemblage?					Y	Y		
Notes	At boundary between olivine and Ti-magnetite	Bornite in cpx	In cpx, minor opx at boundary	At plag-cpx boundary	Note sulfate and calcic plagioclase	An near the assemblage, potential low T alteration overprinting	In cpx, minor opx at boundary	Fe-silicate replacing sulfide, olivine present at boundary

ID	SK90-32A-HH	SK90-32A-I	SK90-32A-II	SK90-32A-J	SK90-32A-JJ	SK90-32A-K	SK90-32A-KK	SK90-32A-L
Stratigraphic Zone	**UZa**	**UZa**	**UZa**	**UZa**	**UZa**	**UZa**	**UZa**	**UZa**
Chalcopyrite							895	
Pyrrhotite								
Pentlandite								
Bornite	92222	8922	9888	4549	18718	9796	2500	46726
Covellite			3320					
Ti-Poor magnetite			414	289	1223			
Native Cu								
Biotite								
Apatite	8241							304
Calcite								
Clinopyroxene								
Orthopyroxene								
Ca-plag near assemblage?					Y		Y	
Notes	Texture indicates S loss	Surrounded by olivine in cpx	In olivine	Co-Cu-S, surrounded by olivine	Plag becomes more calcic towards assemblage	In olivine	Surrounded by olivine note plag is more calcic, anhydrite is present	Surrounded by olivine. Apatite is F-rich

ID	SK90-32A-LL	SK90-32A-M	SK90-32A-MM	SK90-32A-N	SK90-32A-O	SK90-32A-P	SK90-32A-Q	SK90-32A-R
Stratigraphic Zone	**UZa**	**UZa**	**UZa**	**UZa**	**UZa**	**UZa**	**UZa**	**UZa**
Chalcopyrite						566		
Pyrrhotite								
Pentlandite								
Bornite	18728		43131	134	4647	1397	1985	3940
Covellite		4257		206				
Ti-Poor magnetite	487		1469		325	296		
Native Cu								
Biotite								
Apatite								320
Calcite								
Clinopyroxene								
Orthopyroxene								
Ca-plag near assemblage?	Y		Y	Y				
Notes	Bornite between plag, olivine, and high-Ti magnetite	Sulfide is altered, silicate appears intact, note Cl	Surrounded by olivine, plag is more calcic	Plag becomes more calcic towards assemblage	Between high-Ti magnetite, note plag composition near assemblage	At boundary between olivine and plag	In pyroxene with minor high-Ti magnetite, proximal Ag	High-F apatite

ID	SK90-32A-U	SK90-32A-V	SK90-32A-W	SK90-32A-Y	SK90-32A-Z	SK90-41b-A	SK90-41b-B	SK90-41b-BB
Stratigraphic Zone	**UZa**	**UZa**	**UZa**	**UZa**	**UZa**	**MZ**	**MZ**	**MZ**
Chalcopyrite	3826	1265			48456			
Pyrrhotite								
Pentlandite								
Bornite		2917	7019	8686		24411	2988	
Covellite								
Ti-Poor magnetite					100	1970	2062	
Native Cu	3284							
Biotite								
Apatite								
Calcite								
Clinopyroxene								
Orthopyroxene								
Ca-plag near assemblage?							Y	
Notes	In olivine, no alteration	Between olivine and high-Ti mt. Note sulfate present away from assemblage	At cpx-plag boundary	In olivine	In olivine	In cpx	Presence of olivine	Native Ag and Cu in Ti-rich magnetite

ID	SK90-41b-C	SK90-41b-CC	SK90-41b-D	SK90-41b-DD	SK90-41b-E	SK90-41b-EE	SK90-41b-F	SK90-41b-FF
Stratigraphic Zone	**MZ**	**MZ**	**MZ**	**MZ**	**MZ**	**MZ**	**MZ**	**MZ**
Chalcopyrite								
Pyrrhotite								
Pentlandite								
Bornite	692	2749	219		19427		16688	923
Covellite								
Ti-Poor magnetite		72					439	129
Native Cu								
Biotite								
Apatite								
Calcite								
Clinopyroxene					4257			
Orthopyroxene								
Ca-plag near assemblage?								
Notes	Fe-Mg-Al Silicate	Surrounded by cpx and microcrystalline olivine			Cpx-plag boundary		Cpx-plag boundary	Bornite with olivine

ID	SK90-41b-G	SK90-41b-GG	SK90-41b-H	SK90-41b-HH	SK90-41b-I	SK90-41b-II	SK90-41b-J	SK90-41b-K
Stratigraphic Zone	**MZ**	**MZ**	**MZ**	**MZ**	**MZ**	**MZ**	**MZ**	**MZ**
Chalcopyrite								
Pyrrhotite								
Pentlandite								
Bornite	3789		27621	10815	2565	4715	16748	34937
Covellite								
Ti-Poor magnetite			1589	1205		2270	1498	
Native Cu								
Biotite								
Apatite		102						674
Calcite								
Clinopyroxene								
Orthopyroxene								
Ca-plag near assemblage?						Y		
Notes	Cl inclusion in bornite	150 microns of Pt-Au alloy with associated Cl-F apatite	Bornite in Ti-magnetite, notable Cl	Apatite present between euhedral olivine	Cu-Fe-Mg-Al-Silicate perhaps augite? 1:3 Si:O	Sulfide surrounded by olivine, note anorthite by sulfide oligoclase away from sulfide	Between cpx and plag, note olivine mantling	Sulfides with associated olivine mantling sulfide

ID	SK90-41b-L	SK90-41b-M	SK90-41b-N	SK90-41b-O	SK90-41b-P	SK90-41b-Q	SK90-41b-R	SK90-41b-S
Stratigraphic Zone	**MZ**	**MZ**	**MZ**	**MZ**	**MZ**	**MZ**	**MZ**	**MZ**
Chalcopyrite								
Pyrrhotite								
Pentlandite								
Bornite	11246	87266	312		1197	20959	2765	671
Covellite								
Ti-Poor magnetite	1292				410		1380	
Native Cu								
Biotite								
Apatite			28					
Calcite								
Clinopyroxene								
Orthopyroxene								
Ca-plag near assemblage?					Y	Y		
Notes	Surrounded by olivine		Olivine, cpx and plag present	Pt sulfide	Surrounded by olivine, at olivine-plag boundary	Interstitial to cpx, plagioclase and Ti-magnetite	Abundant olivine around the sulfide	In cpx

ID	SK90-41b-T	SK90-41b-U	SK90-41b-V	SK90-41b-W	SK90-41b-X	SK90-41b-Y	SK90-41b-Z	SK90-50-A
Stratigraphic Zone	**MZ**	**MZ**	**MZ**	**MZ**	**MZ**	**MZ**	**MZ**	**MZ**
Chalcopyrite								
Pyrrhotite								
Pentlandite								
Bornite	6095		6488	4673	17031	3264	2465	2184
Covellite								
Ti-Poor magnetite			205		708	574		
Native Cu								
Biotite								
Apatite	98							
Calcite								
Clinopyroxene								
Orthopyroxene								
Ca-plag near assemblage?				Y				
Notes	Trace cpx and opx with minor apatite	In cpx	At Ti-magnetite/cpx boundary	Fe-Mg-Al silicate with trace Cl	Cpx-plag boundary	Sulfide surrounded by olivine all in cpx	Sulfide surrounded by olivine all in cpx	Bornite with proximal Ag

ID	SK90-50-AA	SK90-50-BB	SK90-50-CC	SK90-50-DD	SK90-50-EE	SK90-50-FF	SK90-50-I	SK90-50-II
Stratigraphic Zone	**MZ**	**MZ**	**MZ**	**MZ**	**MZ**	**MZ**	**MZ**	**MZ**
Chalcopyrite								
Pyrrhotite								
Pentlandite								
Bornite	450	2816	1585	26934	421	1280	2539	1341
Covellite								
Ti-Poor magnetite	168	51021	87	593	13216	9533	281	211
Native Cu								
Biotite								
Apatite								
Calcite								
Clinopyroxene								
Orthopyroxene								
Ca-plag near assemblage?								
Notes		Almost entirely low-Ti magnetite	Secondary olivine?			Secondary olivine? Highly oxidized sulfide	Sulfide found within olivine	Cl anomaly

ID	SK90-50-J	SK90-50-JJ	SK90-50-L	SK90-50-M	SK90-50-N	SK90-50-O	SK90-50-P	SK90-50-Q
Stratigraphic Zone	**MZ**	**MZ**	**MZ**	**MZ**	**MZ**	**MZ**	**MZ**	**MZ**
Chalcopyrite								
Pyrrhotite								
Pentlandite								
Bornite		27637	23352	2266	14625	226	197	9989
Covellite								
Ti-Poor magnetite		1624			153	1247	5540	
Native Cu								
Biotite				922				4854
Apatite								
Calcite								
Clinopyroxene								
Orthopyroxene								
Ca-plag near assemblage?								
Notes			In pyroxene with plag and high-Ti magnetite				Recrystallized olivine?	

ID	SK90-50-R	SK90-50-W	Sk90-50-Y
Stratigraphic Zone	**MZ**	**MZ**	**MZ**
Chalcopyrite			
Pyrrhotite			
Pentlandite			
Bornite	59906	23219	2393
Covellite			
Ti-Poor magnetite		1088	125
Native Cu			
Biotite			
Apatite			
Calcite			
Clinopyroxene			
Orthopyroxene			
Ca-plag near assemblage?			
Notes	Bornite in cpx with high-Ti magnetite	High Fe-Mg-Al silicate surrounds both bornite and magnetite	

Appendix B: Supplementary Material for Chapter 2

High abundance trace element data were collected using a Direct Current Plasma Emission Mass Spectrometer (DCP) following a $LiBO_2$ flux-fusion after the methods of Klein et al. (1991). Low abundance trace elements were collected using an Inductively Coupled Plasma Mass Spectrometer (ICP-MS) following a two-acid (HF and HNO_3) digestion. Where possible, trace element data collected using the different methods were used to compare inter-instrument/method accuracy and precision. For Zr, initial measurements indicated poor agreement between the two methods (Figure 38).

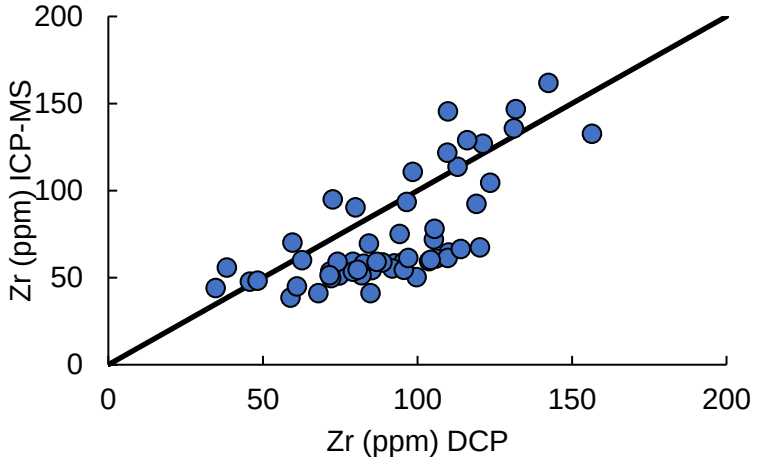

Figure 38: Covariation plot of Zr data (ppm) collected using DCP and ICP-MS. The black line is the line of unity (1:1). Poor agreement is observed between the two methods.

For Sr and other high abundance trace elements (e.g., Ba, Ni, Cu), excellent agreement is observed for the two methods for Sr (Figure 39), suggesting that the

analytical problems are unique to Zr and possibly other HFSEs. For HFSEs, Okina et al. (2016) demonstrated that recovery may be limited when using a two-acid digestion procedure, and Tanaka et al. (2003) reported that at high HF activity, the precipitation of fluoride minerals limits HFSE concentrations in solution.

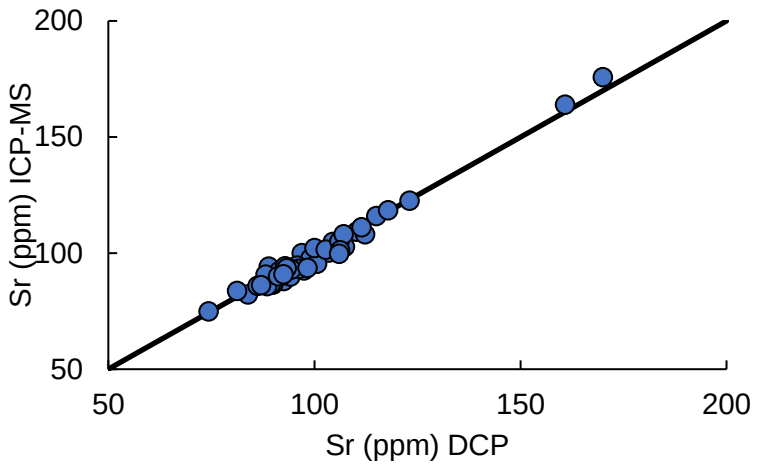

Figure 39: Covariation plot of Sr data (ppm) collected using DCP and ICP-MS. The black line is the line of unity (1:1). Excellent agreement is observed between the two methods.

To determine whether analytical problems were the result of instrumentation or digestion procedures, we used method of addition to independently determine Zr concentrations for two rock standards (NBS 688 and USGS BHVO). For this, we prepared four solutions of each standard following a $LiBO_2$ flux-fusion after the methods of Klein et al. (1991). Three out of the four solutions were spiked with 0.3, 0.6 and 0.9 μg/mL of 250 ppm ultra-pure Zr standard solution (Sigma-Aldrich), respectively, while

one of the solutions was left unmodified. Each solution was measured, in duplicate, by DCP. The average measured counts for each solution were plotted against the quantity of Zr spike added (Figure 40) and the linear relationship was used to determine the Zr concentration of the unspiked solution (Table 6).

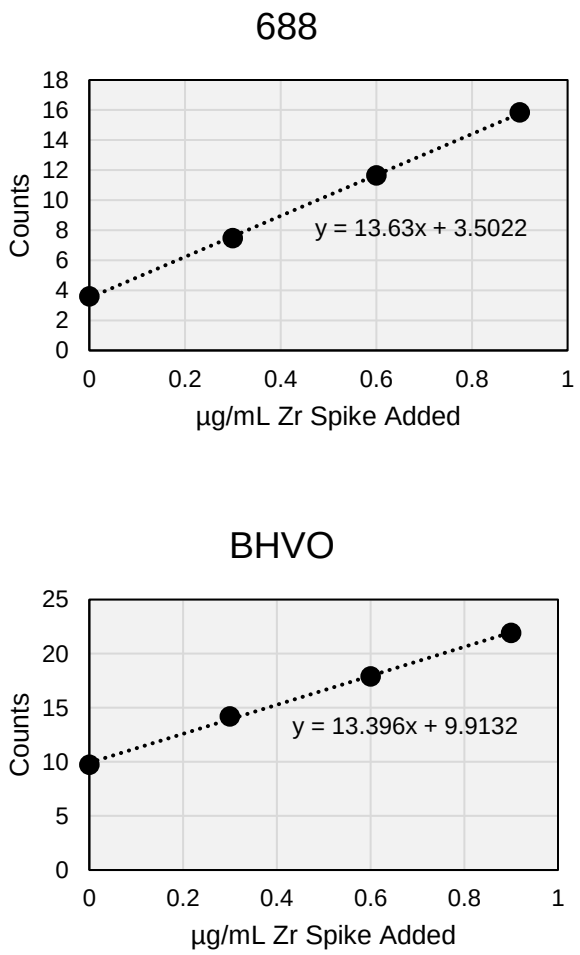

Figure 40: Method of addition results for NBS 688 (top) and USGS BHVO (bottom). Unmodified Zr concentrations are calculated using the line equation given in each plot.

Standard certificate values for Zr, Zr values calculated by method of addition, and the difference between the two values are shown in Table 6. In general, method of addition calculated values are in good agreement with the standard certificate values, suggesting that both the flux-fusion digestion and the DCP measurements of that solution are accurate for determining Zr concentrations in basaltic glass.

Table 6: Comparison of recommended certificate Zr concentrations (ppm) and concentrations calculated by method of additions for two basalt standards.

Standard ID	Certificate Value	Calculated	% Difference
NBS 688	67	64	4.7
USGS BHVO	184	185	0.54

After confirming that flux-fusion digestion and DCP measurements accurately determine Zr concentrations of NBS 688 and USGS BHVO, a subset of 19 samples were reanalyzed by ICP-MS following a flux-fusion digestion. This subset of samples was selected based on initially low Nb/Ta and Zr/Hf values. The initial flux-fusion solution was centrifuged and diluted 100x before being analyzed by ICP-MS. Figure 41 compares Zr concentrations determined by DCP and ICP-MS following flux-fusion digestion. Agreement between the two instruments is very good, especially when compared to the initial measurements (see Figure 38).

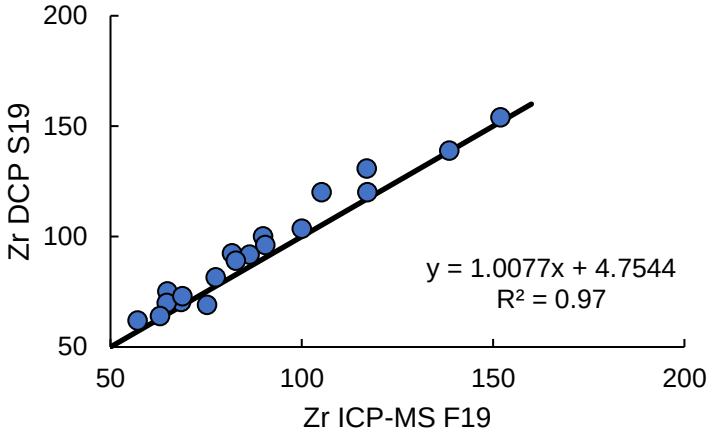

Figure 41: Comparison of Zr concentrations (ppm) collected by ICP-MS (x-axis) and DCP (y-axis). F19 denotes to data collected during the Fall of 2019 while S19 denotes data that was collected during the summer of 2020. The solid black line is the line of unity (1:1).

Other HFSEs (Nb, Hf, Ta) were also measured to determine whether these elements are similarly influenced by digestion procedure. Figure 42 examines Nb, Hf, and Ta data of the 19 samples following a two-acid digestion and a $LiBO_2$ flux-fusion. For this subset of samples, excellent agreement between the two digestion methods is observed for Nb (Figure 42a) and Hf (Figure 42c). For Ta, agreement between the two methods is not as strong ($R^2 = 0.85$, Figure 42b). Ta values that deviate from unity are those with originally highly anomalous Nb/Ta (≈ 7-10).

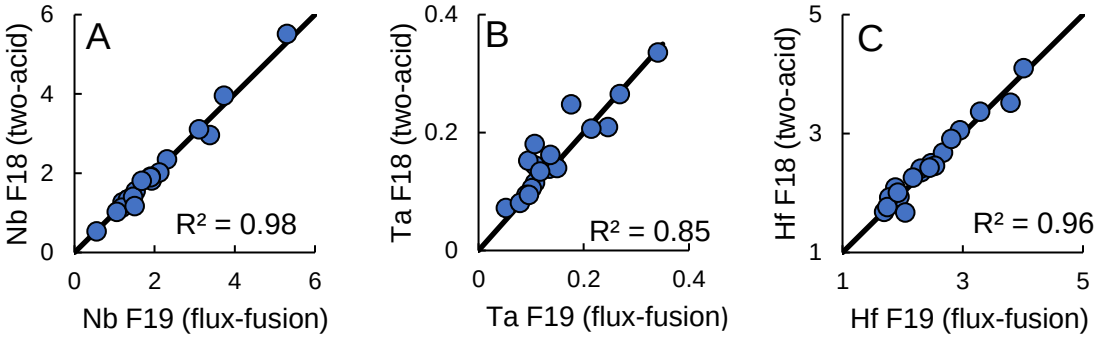

Figure 42: Comparison of high field strength element data measured on ICP-MS following either two-acid digestions or $LiBO_2$ flux-fusion. Solid black line is the line of unity (1:1).

Table 7 compares HFSE data collected during the Fall of 2018 and 2019 using the two different digestion procedures. Also provided are the Zr/Hf and Nb/Ta values for each sample. For this study, all Zr data were collected using the DCP at Duke University following a flux-fusion digestion. For Ta, samples with anomalously low Nb/Ta, were re-analyzed using ICP-MS following a flux-fusion digestion. The reported data for these samples were those digested using the flux-fusion procedure. Table 8 is a compilation of all major element, trace element, and $^{87}Sr/^{86}Sr$ data reported in Chapter 2.

Table 7: Comparison of HFSE data collected during Fall 2018 and Fall 2019. Fall 2018 data were collected following a two-acid digestion. Fall 2019 data were collected following a flux-fusion. Zr data for both were collected following a flux-fusion digestion.

	Fall 2018[1]						Fall 2019[2]					
Sample	**Zr**	**Hf**	**Nb**	**Ta**	**Zr/Hf**	**Nb/Ta**	**Zr**	**Hf**	**Nb**	**Ta**	**Zr/Hf**	**Nb/Ta**
D02-4	139.0	3.5	3.0	0.2	39.5	14.1	138.6	3.8	3.4	0.2	36.5	13.7
D05-4	120.2	3.1	2.3	0.2	39.4	9.5	105.2	3.0	2.3	0.2	35.6	13.1
D08-2	130.9	3.4	3.1	0.2	38.9	15.0	116.9	3.3	3.1	0.2	35.5	14.5
D12-1	92.5	2.5	1.3	0.1	37.1	9.3	81.8	2.5	1.3	0.1	33.1	12.3
D18-1 (WR)	62.0	1.7	0.5	0.1	36.8	7.4	57.1	1.7	0.6	0.1	33.8	10.6
D30-1	75.2	2.1	1.5	0.1	36.0	13.5	64.8	1.9	1.5	0.1	34.6	14.2
D35-1	91.9	2.3	1.8	0.1	39.1	13.1	86.4	2.3	1.9	0.1	37.4	14.3
D36-1	70.5	1.9	1.3	0.2	36.4	8.3	68.4	1.9	1.2	0.1	35.2	12.6
D38-1	89.1	2.4	1.3	0.1	37.0	12.7	82.8	2.3	1.3	0.1	36.0	13.2
D40-1	81.6	2.3	1.1	0.1	36.2	12.0	77.5	2.2	1.2	0.1	35.7	13.0
D45-1	103.7	2.7	2.0	0.1	38.8	13.8	99.9	2.7	2.1	0.1	37.4	14.7
D46-2	70.0	1.9	1.0	0.1	36.4	12.7	64.7	1.8	1.1	0.1	36.4	13.3
D48-1	100.2	2.5	1.9	0.1	40.7	13.7	89.9	2.5	1.9	0.1	35.4	12.7
D50-3	120.1	2.9	5.5	0.3	41.3	16.4	117.1	2.8	5.3	0.3	41.6	15.6
D56-1	64.1	1.8	1.4	0.1	36.4	14.9	62.9	1.7	1.5	0.1	36.1	15.3
D57-5	96.3	2.4	1.9	0.2	39.7	11.7	90.5	2.4	1.9	0.1	37.0	13.9
D58-1	69.1	1.7	1.2	0.2	41.3	6.5	75.3	2.0	1.5	0.1	36.8	14.1
D59-1	73.1	2.0	1.8	0.1	36.5	13.5	68.8	1.9	1.7	0.1	35.8	14.3
D66-1	154.2	4.1	4.0	0.3	37.6	14.9	151.9	4.0	3.7	0.3	37.8	13.9

[1]Fall 2018 data collected on the ICP-MS following a two-acid digestion. Zr data are from the DCP following a flux-fusion digestion. [2]Fall 2019 data were collected using ICP-MS following a flux-fusion digestion.

Table 8: Major element, trace element, and $^{87}Sr/^{86}Sr$ for basaltic glass and whole rock samples from the Cocos-Nazca Spreading Center, Dietz Volcanic Ridge, and EPR.

Sample	D01-1	D02-4	D03-1	D04-2	D05-4	D06-5	D07-1	D08-1
Latitude	2.30	2.31	2.26	2.22	2.24	2.23	2.24	2.24
Longitude	-99.66	-102.09	-102.08	-102.08	-101.50	-101.46	-101.42	-101.41
Depth	3293	3296	3231	3259	5065	4570	4115	4151
Segment	7	EPR	EPR	EPR	2	2	2	2
SiO_2 (wt. %)	50.63	50.79	51.54	51.56	50.48	50.59	50.18	50.52
MgO	8.04	8.14	8.22	7.44	8.55	7.70	9.41	7.79
CaO	12.04	11.17	10.58	11.42	11.77	11.34	11.87	11.43
MnO	0.18	0.21	0.21	0.20	0.20	0.20	0.17	0.20
TiO_2	1.63	1.97	2.04	1.86	1.70	1.86	1.29	1.86
FeO_T	10.36	11.82	11.96	11.22	11.26	11.07	9.54	11.34
Na_2O	2.42	2.52	2.74	2.63	2.45	2.57	2.46	2.61
K_2O	0.11	0.10	0.15	0.16	0.11	0.16	0.13	0.09
Al_2O_3	14.90	13.73	13.96	14.29	15.22	14.68	16.08	14.83
P_2O_5	0.13	0.17	0.18	0.17	0.12	0.18	0.10	0.15
SUM	100.44	100.63	101.58	100.96	101.87	100.34	101.24	100.82
Sr (ppm)	97.12	92.29	98.19	92.56	97.28	96.96	99.02	104.55
Ba	7.41	9.67	11.68	9.79	6.98	9.53	5.71	10.51
Zn	86.71	110.24	104.41	91.15	87.62	96.72	75.19	91.14
Cu	72.27	62.96	54.75	59.32	73.77	68.73	76.26	64.71
Ni	109.13	112.07	137.91	91.86	111.50	99.82	173.05	97.55
V	331.46	360.45	391.26	382.88	305.25	373.91	274.37	331.18
Sc	39.56	40.76	40.72	41.15	40.41	42.04	38.17	40.90
Cr	362.94	215.32	235.48	256.13	259.11	254.00	376.38	240.85
Y	38.87	41.55	48.36	42.39	40.94	46.39	32.48	42.13
Zr	110.13	138.56	142.40	131.20	105.21	131.87	85.21	116.94
Co	46.86	53.45	52.89	49.90	50.12	50.45	47.46	49.35
Rb	0.73	1.06	1.23	0.95	0.71	1.03	0.37	0.95
Nb	2.05	3.38	3.61	2.83	2.31	3.13	1.28	3.10
Cs	0.01	0.01	0.01	0.01	0.01	0.01	0.00	0.01
La	2.94	4.41	4.35	3.57	3.40	3.92	2.17	4.24
Ce	10.18	13.51	14.43	12.03	10.75	13.15	7.84	12.17
Pr	1.82	2.40	2.52	2.11	1.90	2.30	1.40	2.20
Nd	9.76	13.18	13.66	11.65	10.63	12.53	7.95	11.75
Sm	3.65	4.71	4.81	4.23	3.78	4.46	2.91	4.29
Eu	1.23	1.60	1.57	1.39	1.31	1.49	1.06	1.39
Gd	4.97	6.46	6.45	5.81	5.23	6.14	4.04	5.60
Tb	0.94	1.21	1.20	1.08	1.00	1.13	0.77	1.06
Dy	6.22	7.90	7.95	7.14	6.61	7.33	5.09	6.99
Ho	1.35	1.72	1.73	1.54	1.44	1.61	1.10	1.52
Er	3.65	4.85	4.76	4.31	4.03	4.45	3.02	4.18
Yb	3.75	4.63	4.77	4.26	4.04	4.47	3.17	4.19
Lu	0.58	0.72	0.73	0.65	0.63	0.69	0.49	0.65
Hf	2.89	3.79	3.88	3.31	2.96	3.58	2.27	3.29
Ta	0.14	0.25	0.24	0.20	0.18	0.22	0.11	0.21
Pb	0.37	0.43	0.49	0.42	0.00	0.45	0.30	0.00
Th	0.12	0.21	0.21	0.17	0.14	0.19	0.08	0.19
U	0.04	0.07	0.08	0.06	0.05	0.06	0.03	0.06
$^{87}Sr/^{86}Sr$		0.702429	0.702434	0.702443			0.702573	

Table 8 (continued)

Sample	D09-2	D10-2	D11-2	D12-1	D13-1	D14-5	D15-2	D16-1
Latitude	2.24	2.21	2.22	2.22	2.21	2.22	2.21	2.21
Longitude	-101.37	-101.37	-101.31	-101.28	-101.27	-101.20	-101.15	-101.10
Depth	4059	4418	4083	4169	3972	3803	3606	3594
Segment	2	2	3	3	3	3	4	4
SiO_2 (wt. %)	50.41	50.23	51.69	51.19	50.46	50.58	50.63	51.16
MgO	8.25	8.24	8.45	7.51	8.67	8.11	7.98	8.64
CaO	11.52	11.55	12.33	11.80	12.13	11.62	12.00	12.99
MnO	0.18	0.18	0.18	0.19	0.18	0.18	0.19	0.18
TiO_2	1.67	1.67	1.28	1.46	1.28	1.56	1.53	1.12
FeO_T	10.16	10.27	9.68	10.77	9.74	10.24	10.57	9.60
Na_2O	2.67	2.60	2.52	2.62	2.35	2.64	2.59	2.21
K_2O	0.09	0.14	0.06	0.07	0.07	0.08	0.16	0.13
Al_2O_3	15.54	15.21	15.22	14.19	15.22	15.01	14.75	14.63
P_2O_5	0.15	0.15	0.09	0.12	0.09	0.14	0.14	0.09
SUM	100.64	100.24	101.50	99.92	100.19	100.15	100.54	100.75
Sr (ppm)	105.04	95.79	88.89	91.43	83.85	104.23	92.10	81.22
Ba	6.00	6.53	2.77	5.37	24.35	9.41	6.93	5.63
Zn	91.38	91.19	63.84	85.20	73.33	89.96	81.37	65.80
Cu	62.39	69.26	82.24	75.65	78.22	69.09	80.84	89.40
Ni	115.17	115.69	77.60	60.54	106.78	98.52	83.84	76.27
V	318.13	333.08	291.82	340.70	289.60	320.98	326.05	296.62
Sc	37.95	39.93	41.86	41.36	38.83	40.06	41.20	40.81
Cr	276.52	306.58	342.56	128.53	333.43	265.35	285.49	255.24
Y	39.39	42.22	30.99	34.90	31.16	36.16	36.67	28.75
Zr	120.24	121.20	58.92	81.78	74.66	109.66	93.91	65.31
Co	49.42	49.36	43.85	50.21	45.41	49.34	48.42	46.31
Rb	0.61	0.64	0.30	0.29	0.36	0.82	0.59	0.25
Nb	2.07	2.07	1.04	1.32	1.23	2.43	1.84	0.94
Cs	0.01	0.01	0.00	0.00	0.00	0.01	0.01	0.00
La	3.08	2.96	1.93	2.54	1.99	3.09	2.58	1.66
Ce	10.83	10.55	6.91	8.23	7.28	10.48	9.02	6.17
Pr	1.95	1.89	1.32	1.53	1.33	1.84	1.62	1.11
Nd	10.86	10.40	7.62	8.83	7.62	10.24	9.07	6.41
Sm	3.97	3.83	2.84	3.32	2.89	3.69	3.40	2.54
Eu	1.31	1.30	1.04	1.17	1.04	1.25	1.20	0.95
Gd	5.33	5.23	4.13	4.48	4.16	4.94	4.76	3.61
Tb	1.00	0.98	0.77	0.88	0.79	0.92	0.90	0.69
Dy	6.50	6.41	5.12	5.87	5.16	6.05	5.86	4.63
Ho	1.38	1.40	1.11	1.25	1.15	1.30	1.27	1.01
Er	3.84	3.78	3.06	3.64	3.18	3.65	3.54	2.80
Yb	3.82	3.78	3.04	3.55	3.13	3.64	3.54	2.85
Lu	0.59	0.59	0.46	0.55	0.49	0.56	0.55	0.45
Hf	3.10	3.03	2.15	2.47	2.17	2.87	2.59	1.87
Ta	0.15	0.15	0.15	0.11	0.09	0.17	0.13	0.08
Pb	0.38	0.36	0.29	0.00	0.29	0.43	0.30	0.21
Th	0.13	0.13	0.06	0.09	0.08	0.15	0.11	0.06
U	0.04	0.04	0.02	0.03	0.02	0.05	0.04	0.02
$^{87}Sr/^{86}Sr$	0.702461			0.702465		0.70247	0.702566	

Table 8 (continued)

Sample	D17-2	D18-1 (WR)	D19-4	D20-3	D21-5	D22-3	D23-4	D24-2
Latitude	2.20	2.07	2.20	2.24	2.24	2.23	2.22	2.21
Longitude	-101.04	-101.02	-100.97	-100.99	-100.93	-100.89	-100.83	-100.76
Depth	3796	3226	3802	3566	3518	3560	3372	3501
Segment	4	Off Axis	4	5	5	5	5	5
SiO_2 (wt. %)	51.90	49.77	50.96	50.96	50.83	50.83	50.30	50.94
MgO	8.57	9.77	8.83	8.44	8.16	8.51	9.00	8.28
CaO	12.44	12.34	12.60	12.22	11.26	11.86	12.27	12.04
MnO	0.17	0.21	0.17	0.18	0.18	0.17	0.17	0.17
TiO_2	1.16	1.04	1.11	1.43	1.62	1.38	1.20	1.31
FeO_T	9.30	8.04	9.47	10.04	10.62	9.76	9.10	9.61
Na_2O	2.41	2.57	2.31	2.57	2.63	2.54	2.38	2.53
K_2O	0.05	0.17	0.10	0.16	0.13	0.11	0.12	0.09
Al_2O_3	15.21	16.55	15.51	15.01	15.23	15.83	15.83	15.14
P_2O_5	0.08	0.08	0.08	0.13	0.13	0.10	0.10	0.09
SUM	101.30	100.54	101.14	101.14	100.80	101.11	100.47	100.21
Sr (ppm)	89.94	88.09	74.36	123.13	97.51	100.63	86.19	100.00
Ba	3.79	5.80	4.04	11.76	6.12	5.77	9.61	6.11
Zn	56.89	81.48	65.37	81.77	93.36	95.98	69.05	77.88
Cu	83.61	90.70	89.96	82.57	65.34	79.80	86.07	75.46
Ni	75.03	194.57	111.78	108.26	118.51	107.16	110.66	98.02
V	277.82	216.46	284.89	293.97	331.02	293.60	275.11	302.44
Sc	40.35	34.88	40.03	41.32	39.21	38.60	37.61	41.15
Cr	345.44	370.45	390.94	343.23	277.49	308.86	321.09	337.33
Y	27.40	24.68	27.85	31.74	37.80	32.63	29.84	32.09
Zr	48.29	57.10	61.00	95.60	105.95	91.84	72.06	82.69
Co	42.22	44.94	46.81	48.42	50.75	48.90	45.20	45.71
Rb	0.30	1.06	0.29	1.06	0.50	0.46	0.49	0.56
Nb	1.02	0.55	1.00	2.91	1.61	1.46	1.50	1.64
Cs	0.00	0.02	0.00	0.01	0.01	0.01	0.01	0.01
La	1.76	1.45	1.49	3.21	2.55	2.28	2.02	2.49
Ce	6.50	5.04	5.60	10.39	9.36	8.27	7.24	8.34
Pr	1.17	0.96	1.04	1.73	1.68	1.47	1.29	1.54
Nd	6.63	5.91	6.17	9.38	9.49	8.18	7.35	8.53
Sm	2.55	2.36	2.49	3.22	3.60	3.08	2.83	3.11
Eu	0.95	0.92	0.93	1.16	1.23	1.09	1.00	1.12
Gd	3.59	3.32	3.68	4.41	4.93	4.30	3.90	4.41
Tb	0.68	0.61	0.68	0.80	0.92	0.79	0.73	0.81
Dy	4.53	4.06	4.62	5.31	6.10	5.26	4.88	5.40
Ho	0.97	0.90	1.00	1.16	1.32	1.12	1.04	1.17
Er	2.72	2.47	2.77	3.15	3.58	3.08	2.93	3.23
Yb	2.71	2.34	2.87	3.23	3.62	3.15	2.85	3.26
Lu	0.42	0.37	0.42	0.48	0.56	0.49	0.44	0.50
Hf	1.89	1.69	1.76	2.48	2.72	2.37	2.06	2.36
Ta	0.07	0.05	0.07	0.20	0.12	0.11	0.11	0.11
Pb	0.23	0.26	0.22	0.37	0.34	0.29	0.30	0.34
Th	0.07	0.06	0.06	0.18	0.10	0.09	0.10	0.10
U	0.02	0.06	0.02	0.05	0.03	0.03	0.03	0.03
$^{87}Sr/^{86}Sr$	0.702499		0.702512	0.702565				

Table 8 (continued)

Sample	D25-1	D26-3	D27-1	D28-1	D29-3	D30-1	D31-1	D32-2
Latitude	2.20	2.19	2.17	2.15	2.14	2.13	2.13	2.21
Longitude	-100.68	-100.63	-100.59	-100.52	-100.45	-100.33	-100.39	-100.30
Depth	3396	3467	3490	3446	3621	3654	3714	3644
Segment	5	5	5	5	5	5	5	6
SiO_2 (wt. %)	50.70	50.41	50.80	51.26	50.50	48.39	50.86	51.32
MgO	8.21	7.94	8.31	7.99	8.14	9.18	7.98	8.42
CaO	11.69	11.50	12.16	11.97	11.96	10.78	11.40	12.35
MnO	0.18	0.18	0.18	0.18	0.18	0.19	0.18	0.18
TiO_2	1.56	1.53	1.42	1.44	1.49	1.22	1.60	1.23
FeO_T	10.15	10.19	9.70	10.07	10.05	10.64	10.24	9.56
Na_2O	2.62	2.67	2.70	2.53	2.54	2.32	2.68	2.47
K_2O	0.15	0.07	0.17	0.09	0.13	0.05	0.11	0.11
Al_2O_3	15.35	14.95	15.22	14.70	14.46	15.67	15.23	14.97
P_2O_5	0.14	0.13	0.14	0.13	0.13	0.11	0.14	0.10
SUM	100.75	99.57	100.81	100.36	99.58	98.54	100.43	100.71
Sr (ppm)	115.04	110.53	117.86	104.35	106.25	93.42	110.29	92.79
Ba	9.69	8.45	11.44	8.55	9.45	5.02	9.22	8.47
Zn	85.22	83.94	73.27	86.26	84.53	73.43	81.94	74.94
Cu	68.05	68.63	75.11	68.90	71.48	78.57	65.19	84.45
Ni	113.15	97.45	98.91	78.10	97.16	170.97	104.91	69.42
V	322.57	320.25	310.48	329.98	327.79	299.92	333.89	297.62
Sc	40.38	39.85	40.38	41.26	41.54	42.39	39.80	41.80
Cr	302.46	253.75	329.68	277.26	330.69	271.56	256.18	357.55
Y	37.02	35.62	33.39	33.77	34.72	31.82	36.78	28.99
Zr	105.33	105.82	96.37	98.47	103.79	64.85	114.06	75.25
Co	47.38	49.04	46.42	48.51	47.63	49.69	48.58	45.55
Rb	0.88		0.98	0.69	0.73	0.42	0.76	0.49
Nb	2.63		2.54	2.28	2.11	1.53	2.45	1.50
Cs	0.01		0.01	0.01	0.01	0.00	0.01	0.00
La	3.32		3.09	2.92	2.81	3.69	3.17	2.43
Ce	10.53		10.23	9.80	9.49	7.21	10.72	7.63
Pr	1.85		1.76	1.72	1.68	1.34	1.92	1.35
Nd	10.08		9.41	9.27	9.32	7.54	10.37	7.69
Sm	3.53		3.37	3.35	3.42	2.79	3.68	2.83
Eu	1.26		1.19	1.17	1.17	0.97	1.25	1.04
Gd	4.99		4.51	4.62	4.62	3.86	5.05	3.97
Tb	0.91		0.83	0.87	0.86	0.73	0.93	0.74
Dy	5.93		5.49	5.72	5.66	5.04	6.17	4.93
Ho	1.29		1.18	1.25	1.22	1.12	1.33	1.09
Er	3.54		3.23	3.44	3.39	3.16	3.69	2.94
Yb	3.53		3.24	3.33	3.38	3.20	3.68	2.94
Lu	0.54		0.51	0.53	0.52	0.51	0.58	0.46
Hf	2.76		2.54	2.54	2.64	1.88	2.97	2.04
Ta	0.21		0.17	0.16	0.15	0.11	0.16	0.11
Pb	0.44		0.38	0.38	0.34	0.00	0.37	0.27
Th	0.15		0.16	0.14	0.13	0.10	0.14	0.12
U	0.05		0.05	0.05	0.04	0.03	0.05	0.04
$^{87}Sr/^{86}Sr$	0.702507	0.702528			0.7025		0.702518	0.70247

Table 8 (continued)

Sample	D34-5	D35-1	D36-1	D37-2	D38-1	D39-1	D40-1	D42-1
Latitude	2.27	2.27	2.25	2.25	2.23	2.22	2.22	2.33
Longitude	-100.23	-100.18	-100.15	-100.07	-99.99	-99.92	-99.87	-99.89
Depth	3456	3388	3540	3420	3460	3670	3637	3636
Segment	6	6	6	6	6	6	6	7
SiO_2 (wt. %)	50.13	50.53	50.74	51.38	50.04	50.37	48.66	51.03
MgO	9.04	8.57	8.56	8.12	8.28	9.36	9.03	8.66
CaO	12.58	11.31	11.92	11.93	11.60	12.32	11.55	12.14
MnO	0.16	0.17	0.16	0.20	0.17	0.16	0.17	0.18
TiO_2	0.99	1.37	1.16	1.47	1.34	1.05	1.26	1.26
FeO_T	8.67	9.50	9.14	10.82	9.37	8.97	9.70	9.73
Na_2O	2.21	2.58	2.50	2.56	2.61	2.41	2.51	2.51
K_2O	0.13	0.10	0.07	0.05	0.06	0.09	0.06	0.09
Al_2O_3	16.14	15.51	15.61	14.37	15.80	16.07	16.09	14.96
P_2O_5	0.09	0.13	0.08	0.12	0.13	0.08	0.12	0.10
SUM	100.13	99.77	99.94	101.01	99.40	100.88	99.15	100.66
Sr (ppm)	85.33	111.84	87.83	88.51	111.71	100.07	104.27	92.93
Ba	3.30	6.74	7.76	6.46	4.00	3.47	2.87	6.38
Zn	64.13	75.36	71.32	84.23	74.28	73.70	71.21	77.30
Cu	95.34	74.74	79.47	76.48	75.37	93.09	83.64	81.16
Ni	136.76	138.00	94.58	77.35	118.44	116.43	155.94	107.50
V	262.31	294.34	268.51	338.03	280.71	251.32	272.01	301.31
Sc	37.47	39.54	38.73	42.28	38.47	36.89	38.44	41.01
Cr	426.43	314.27	398.10	205.71	331.17	357.00	345.53	336.66
Y	26.43	31.71	27.40	35.65	30.74	26.43	30.34	31.27
Zr	60.29	86.35	68.43	95.64	82.79	73.81	77.49	79.10
Co	45.70	45.01	44.54	50.53	43.85	47.15	45.65	47.85
Rb		0.56	0.39	0.68	0.26		0.19	0.59
Nb		1.92	1.19	1.74	1.33		1.19	1.51
Cs		0.01	0.00	0.01	0.00		0.01	0.01
La		2.84	2.09	2.74	2.30		2.21	2.32
Ce		9.09	6.87	8.95	8.19		7.43	7.77
Pr		1.65	1.23	1.60	1.53		1.39	1.44
Nd		8.97	6.87	8.81	8.58		7.95	8.06
Sm		3.10	2.70	3.14	3.04		2.85	3.01
Eu		1.12	0.98	1.14	1.10		1.04	1.09
Gd		4.30	3.72	4.66	4.18		3.89	4.30
Tb		0.82	0.71	0.85	0.79		0.76	0.80
Dy		5.37	4.60	5.73	5.11		5.00	5.34
Ho		1.16	1.01	1.24	1.11		1.11	1.17
Er		3.28	2.80	3.47	3.11		3.06	3.22
Yb		3.25	2.70	3.45	3.04		3.05	3.23
Lu		0.50	0.42	0.54	0.48		0.47	0.51
Hf		2.31	1.95	2.45	2.30		2.17	2.28
Ta		0.13	0.09	0.13	0.10		0.09	0.11
Pb		0.00	0.31	0.52	0.00		0.00	0.33
Th		0.12	0.10	0.12	0.09		0.08	0.10
U		0.04	0.03	0.05	0.03		0.02	0.03
$^{87}Sr/^{86}Sr$			0.702501				0.70248	0.702485

Table 8 (continued)

Sample	D44-2	D45-1	D46-2	D48-1	D49-1	D50-3	D51-1	D53-1
Latitude	2.33	2.33	2.32	2.29	2.33	2.44	2.45	2.22
Longitude	-99.84	-99.79	-99.72	-99.62	-98.27	-98.54	-98.90	-98.89
Depth	3663	3561	3521	3229	3072	2873	3743	3684
Segment	7	7	7	7	9	9	9	8
SiO_2 (wt. %)	51.08	50.35	50.42	50.44	50.60	51.07	51.93	50.70
MgO	8.01	8.33	8.46	9.03	8.65	7.41	7.86	7.64
CaO	11.82	12.14	12.12	11.51	12.19	11.69	12.29	11.66
MnO	0.18	0.19	0.16	0.17	0.17	0.18	0.19	0.21
TiO_2	1.48	1.53	1.10	1.38	1.21	1.53	1.42	1.84
FeO_T	10.01	10.23	8.72	9.78	9.32	9.62	10.49	11.82
Na_2O	2.69	2.41	2.41	2.48	2.56	3.01	2.66	2.49
K_2O	0.09	0.09	0.06	0.10	0.09	0.27	0.10	0.15
Al_2O_3	15.16	14.84	15.31	15.17	16.05	14.93	14.82	14.21
P_2O_5	0.11	0.12	0.11	0.11	0.07	0.19	0.12	0.15
SUM	100.63	100.22	98.87	100.17	100.91	99.89	101.88	100.86
Sr (ppm)	106.08	105.04	102.39	95.86	106.05	157.38	107.13	88.17
Ba	6.87	6.82	4.03	10.47	6.41	26.61	8.58	11.30
Zn	75.25	77.63	65.92	93.05	60.31	79.39	86.58	101.67
Cu	74.78	72.09	85.94	70.91	81.47	74.62	78.63	69.97
Ni	95.70	102.97	104.72	108.75	107.05	57.75	63.14	80.24
V	319.30	304.30	271.42	308.18	263.77	293.88	318.66	371.76
Sc	40.95	40.44	40.47	39.65	39.47	40.78	42.22	41.37
Cr	333.55	353.56	408.28	336.98	337.92	161.29	177.24	245.43
Y	35.07	35.35	26.45	33.53	28.43	31.30	34.20	43.35
Zr	94.25	99.95	64.69	89.86	62.67	117.12	97.03	119.10
Co	44.55	44.74	42.12	48.63	42.83	44.98	49.49	51.00
Rb	0.60	0.65	0.27	0.71	0.59	2.23	0.88	1.19
Nb	1.54	2.12	1.05	1.90	1.51	5.30	1.94	3.06
Cs	0.01	0.01	0.01	0.01	0.01	0.02	0.01	0.02
La	2.62	3.11	1.81	3.16	2.20	5.04	2.77	3.51
Ce	9.05	10.11	6.60	9.24	7.40	14.00	9.26	11.34
Pr	1.65	1.85	1.24	1.63	1.34	2.22	1.69	2.03
Nd	9.19	9.95	6.88	9.05	7.55	11.34	9.20	11.25
Sm	3.27	3.51	2.48	3.40	2.74	3.68	3.31	4.04
Eu	1.14	1.21	0.95	1.18	1.00	1.31	1.19	1.35
Gd	4.64	4.82	3.53	4.54	3.82	4.70	4.63	5.80
Tb	0.86	0.91	0.66	0.87	0.69	0.86	0.85	1.06
Dy	5.79	6.07	4.35	5.85	4.72	5.55	5.62	7.22
Ho	1.23	1.34	0.96	1.27	1.02	1.19	1.24	1.58
Er	3.43	3.68	2.68	3.51	2.83	3.15	3.45	4.31
Yb	3.33	3.62	2.62	3.38	2.83	3.05	3.43	4.34
Lu	0.53	0.55	0.40	0.53	0.45	0.47	0.54	0.68
Hf	2.62	2.67	1.78	2.54	2.09	2.81	2.51	3.19
Ta	0.11	0.14	0.08	0.15	0.12	0.34	0.13	0.20
Pb	0.47	0.00	0.00	0.33	0.34	0.73	0.48	0.46
Th	0.10	0.13	0.08	0.16	0.10	0.35	0.13	0.17
U	0.03	0.04	0.02	0.05	0.03	0.11	0.04	0.06
$^{87}Sr/^{86}Sr$	0.702465	0.702473			0.702605	0.702571		

Table 8 (continued)

Sample	D54-1	D56-1	D57-5	D58-1 (WR)	D59-1	D60-4	D61-1	D62-1
Latitude	2.22	2.24	2.29	2.26	2.28	2.29	1.27	1.36
Longitude	-99.05	-99.23	-99.37	-99.40	-99.46	-99.56	-101.54	-101.78
Depth	3456	3231	3454	3159	3320	3269	2636	2324
Segment	8	8	8		7	7	DD.V.	DD
SiO_2 (wt. %)	50.77	50.56	51.76	49.60	50.65	51.00	49.17	51.86
MgO	8.55	9.09	8.85	7.85	8.87	8.39	9.92	7.91
CaO	12.35	12.99	12.86	12.91	12.35	12.23	11.31	12.30
MnO	0.18	0.17	0.19	0.15	0.17	0.18	0.15	0.17
TiO_2	1.23	1.04	1.51	1.02	1.17	1.40	1.09	1.33
FeO_T	9.71	9.19	10.65	8.04	9.43	9.74	8.47	9.20
Na_2O	2.43	2.06	2.25	2.26	2.22	2.63	2.72	2.99
K_2O	0.08	0.06	0.08	0.22	0.06	0.08	0.15	0.17
Al_2O_3	15.30	15.43	14.52	17.10	15.35	15.38	16.88	15.26
P_2O_5	0.11	0.12	0.22	0.10	0.10	0.13	0.11	0.16
SUM	100.71	100.69	102.89	99.24	100.38	101.17	99.97	101.36
Sr (ppm)	91.20	88.73	97.66	107.15	90.37	105.97	169.97	156.51
Ba	3.44	5.57	7.09	7.98	9.69	5.64	16.01	23.51
Zn	77.59	68.49	91.42	66.57	77.52	91.28	63.41	82.70
Cu	78.27	86.05	69.09	72.40	80.88	77.92	78.92	84.07
Ni	101.48	116.06	91.33	106.02	111.41	106.34	240.25	60.23
V	294.66	276.51	357.27	245.66	282.61	299.87	194.42	252.97
Sc	41.10	38.98	39.68	34.75	38.64	41.62	32.13	40.37
Cr	336.28	416.21	235.96	323.64	368.82	325.97	359.49	226.95
Y	30.40	25.42	31.24	24.51	28.17	34.90	23.55	27.25
Zr	38.31	62.92	90.48	69.13	68.79	104.26	71.59	59.54
Co	47.59	43.14	46.07	41.21	45.44	50.38	45.08	46.67
Rb	0.53	0.46	0.74	1.87	0.74	0.51	1.37	2.03
Nb	1.39	1.46	1.90	1.17	1.68	1.45	3.22	4.62
Cs	0.01	0.00	0.01	0.01	0.01	0.01	0.01	0.02
La	2.06	1.97	3.74	1.77	2.59	2.50	3.22	4.17
Ce	6.93	6.38	9.43	5.97	7.44	8.70	9.69	8.63
Pr	1.27	1.16	1.62	1.09	1.30	1.60	1.55	1.89
Nd	7.20	6.26	8.86	5.97	7.08	8.84	8.02	9.71
Sm	2.67	2.27	3.30	2.20	2.66	3.25	2.64	3.08
Eu	0.97	0.86	1.15	0.84	0.94	1.15	1.01	1.14
Gd	3.94	3.28	4.46	3.17	3.66	4.57	3.45	4.07
Tb	0.74	0.61	0.84	0.59	0.71	0.84	0.62	0.72
Dy	4.93	4.20	5.73	3.86	4.80	5.56	3.91	4.67
Ho	1.10	0.91	1.24	0.86	1.02	1.21	0.84	0.99
Er	3.01	2.56	3.45	2.36	2.87	3.35	2.30	2.67
Yb	3.07	2.54	3.39	2.39	2.84	3.30	2.20	2.60
Lu	0.48	0.40	0.52	0.37	0.44	0.53	0.34	0.40
Hf	2.05	1.74	2.45	1.67	1.92	2.49	2.03	2.35
Ta	0.10	0.10	0.14	0.18	0.12	0.11	0.21	0.32
Pb	0.29	0.00	0.37	0.22	0.22	0.35	0.55	0.48
Th	0.08	0.10	0.15	0.07	0.13	0.09	0.21	0.31
U	0.03	0.03	0.05	0.10	0.04	0.03	0.07	0.09
$^{87}Sr/^{86}Sr$	0.702504		0.702512					0.702556

Table 8 (continued)

Sample	D63-3	D64-1	D65-4	D66-1
Latitude	1.28	1.22	1.16	3.65
Longitude	-101.95	-102.08	-102.17	102.17
Depth	2523	2826	2965	2921
Segment	DD	DD	EPR	EPR
SiO_2 (wt. %)	51.45	51.46	51.76	51.84
MgO	7.21	7.65	7.08	6.54
CaO	11.44	12.29	11.17	10.60
MnO	0.19	0.20	0.21	0.22
TiO_2	1.52	1.58	1.88	2.19
FeO_T	10.38	10.65	11.47	12.72
Na_2O	3.20	2.92	2.83	2.88
K_2O	0.16	0.12	0.20	0.19
Al_2O_3	14.79	14.09	14.23	13.56
P_2O_5	0.16	0.04	0.19	0.20
SUM	100.49	101.00	101.00	100.93
Sr (ppm)	137.80	128.22	104.17	100.04
Ba	20.07	20.44	16.41	15.76
Zn	95.86	72.69	104.83	99.07
Cu	79.73	77.69	58.83	56.81
Ni	35.19	52.62	66.58	54.70
V	295.01	267.85	374.40	409.11
Sc	40.71	39.95	40.72	41.25
Cr	68.20	114.35	157.43	78.13
Y	32.55	30.25	43.08	45.69
Zr	79.96	99.21	116.11	151.89
Co	49.62	45.38	51.44	50.79
Rb	1.88	1.74	1.97	1.39
Nb	4.42	4.07	3.87	3.73
Cs	0.02	0.02	0.03	0.01
La	4.21	3.87	4.26	5.02
Ce	12.31	9.69	13.20	15.82
Pr	2.06	2.00	2.31	2.74
Nd	10.93	10.64	12.36	14.76
Sm	3.60	3.57	4.27	5.10
Eu	1.32	1.29	1.41	1.74
Gd	4.93	4.82	5.89	6.98
Tb	0.88	0.87	1.10	1.29
Dy	5.73	5.65	7.18	8.51
Ho	1.21	1.20	1.54	1.85
Er	3.31	3.27	4.28	5.08
Yb	3.25	3.22	4.28	4.99
Lu	0.49	0.49	0.66	0.77
Hf	2.79	2.71	3.37	4.01
Ta	0.35	0.28	0.27	0.27
Pb	0.48	0.46	0.50	0.48
Th	0.28	0.26	0.26	0.26
U	0.09	0.08	0.08	0.09
$^{87}Sr/^{86}Sr$		0.702525		0.702451

In order to explore the origin of the highly depleted trace element concentration, and non-canonical HFSE ratios in Cocos-Nazca lavas, a two-stage melting model described by Lundstrom et al. (1998) was drawn upon, in which the residuum of the first stage forms the source for the second stage melting event. Here, an initial lherzolite source (0.57 Ol + 0.28 Opx + 0.13 Cpx, Workman and Hart, 2005) is assumed, with trace element concentrations of primitive mantle (Sun and McDonough, 1995). Mineral-melt distribution coefficients shown in Table 9.

Table 9: Mineral-melt distribution coefficients used in melting calculations.

Element	Olivine[1]	Opx[1]	Cpx[2]
Ba	0.000005	0.000006	0.00024
Th	0.00005	0.012	0.0059
Nb	0.005	0.004	0.006
Ta	0.005	0.004	0.019
La	0.005	0.0031	0.03
Nd	0.00042	0.012	0.088
Sm	0.0011	0.0065	0.299
Zr	0.001	0.0099	0.2
Hf	0.0022	0.03	0.43

[1]Salters and Stracke (2004); [2]Lundstrom et al. (2005)

The 1 GPa melting reaction; $0.56\ Opx\ +\ 0.72\ Cpx\ +\ 0.04\ Spin\ =\ 0.34\ Oliv\ +\ 1\ Melt$ of Wasylenki et al. (2003) is used to estimate the residuum mineral mode after 5 % melt extraction (0.63 Ol + 0.27 Opx + 0.1 Cpx). The trace element concentration of the residuum is given in Table 10 and is estimated using the equation (eq. 14);

$$C_r = \frac{C_i * D_{bulk}}{(D_{bulk} + F * (1 - D_{bulk}))} \tag{14}$$

Where C_r is the residual concentration of the trace element of interest, C_i is the initial concentration of the trace element of interest, F is the melt fraction, and D_{bulk} is the bulk partition coefficient given by (eq. 15);

$$D_{bulk} = \sum D^{mnrl/melt} X_{mnrl} \tag{15}$$

Where $D^{mnrl/melt}$ is the mineral-melt partition coefficient given in Table 9 and X_{mnrl} is the mass fraction of each mineral in the source lithology.

Table 10: Trace element concentrations (ppm) used in melting calculations.

Element	PM[1]	PM - 5 % Melt
Ba	6.600	0.005
Th	0.080	0.002
Nb	0.658	0.028
Ta	0.037	0.003
La	0.648	0.063
Nd	1.250	0.317
Sm	0.406	0.204
Zr	10.500	3.956
Hf	0.283	0.165

[1]From Sun and McDonough (1995)

Batch melts are calculated using the batch melting equation of Shaw (1970) (eq. 16);

$$C_{melt} = \frac{C_i}{(D_{bulk} + F*(1 - D_{bulk}))} \quad (16)$$

Where C_{melt} is the concentration of a given trace element in the batch melt. An example of this calculation is given in Table 11.

Table 11: Example batch melting calculation using the PM - 5% Melt concentrations.

F	La	Sm	La/Sm_N
0.01	4.5	4.5	0.64
0.02	2.6	3.7	0.45
0.03	1.9	3.1	0.38
0.04	1.4	2.7	0.34
0.05	1.2	2.4	0.31
0.06	1.0	2.2	0.29
0.07	0.9	2.0	0.28
0.08	0.8	1.8	0.27
0.09	0.7	1.7	0.26
0.1	0.6	1.5	0.25

Pooled melt compositions are calculated using the adiabatic decompression melting program *REEBOX PRO* (Brown and Lesher, 2016). The initial source composition consists of 0.6 harzburgite + 0.4 lherzolite. Harzburgite trace element concentrations are assumed to be refractory and are calculated using equation 14 assuming 10 % melting of DMM (Workman and Hart, 2005). Depleted DMM (Workman and Hart, 2005) trace element concentrations are assigned to the lherzolite. Trace element concentrations for each lithology and the bulk residuum are given in Table 12 and user-specified program inputs are given Table 13.

Table 12: Trace element concentrations (ppm) for each lithology (harzburgite and lherzolite).

Element	Trace Element Conc. (Harzburgite)	[1]Trace Element Conc. (Lherzolite)	Bulk Residuum
Rb	0.0008	0.0200	0.0085
Ba	0.0025	0.2270	0.0923
Th	0.0000	0.0040	0.0016
U	0.0000	0.0018	0.0007
Nb	0.0071	0.0864	0.0388
Ta	0.0003	0.0056	0.0024
La	0.0180	0.1340	0.0644
Ce	0.0790	0.4210	0.2158
Pr	0.0180	0.4830	0.2040
Sr	1.5600	6.0920	3.3728
Nd	0.1600	0.4830	0.2892
Sm	0.0860	0.2100	0.1356
Zr	1.1900	4.2690	2.4216
Hf	0.0560	0.1270	0.0844
Eu	0.0470	0.0860	0.0626
Gd	0.1800	0.3240	0.2376
Dy	0.2300	0.4710	0.3264
Er	0.1600	0.3290	0.2276
Yb	0.1800	0.3480	0.2472
Lu	0.0290	0.0560	0.0398

[1]Depleted DMM from Workman and Hart (2005)

Table 13: REEBOX PRO model inputs.

Parameter	Input	Notes
Lithology 1	DMM	40 % of the source. Composition given in Table 12
Lithology 2	Harzburgite	60 % of the source. Composition given in Table 12
Mantle Potential Temperature	1330	Program default
Half-Spreading Rate (cm/year)	2	Mean Cocos-Nazca spreading rate; Smith et al. (2020)
Pre-Existing Lithosphere (km)	0	
Mixing Function	Standard RMC (Langmuir)	Program default
Partition Coefficients	Temperature Dependent	Program default

The model output is the pooled melt from each lithology for each decompression step. The thermodynamic output of the model is given in Figure 43.

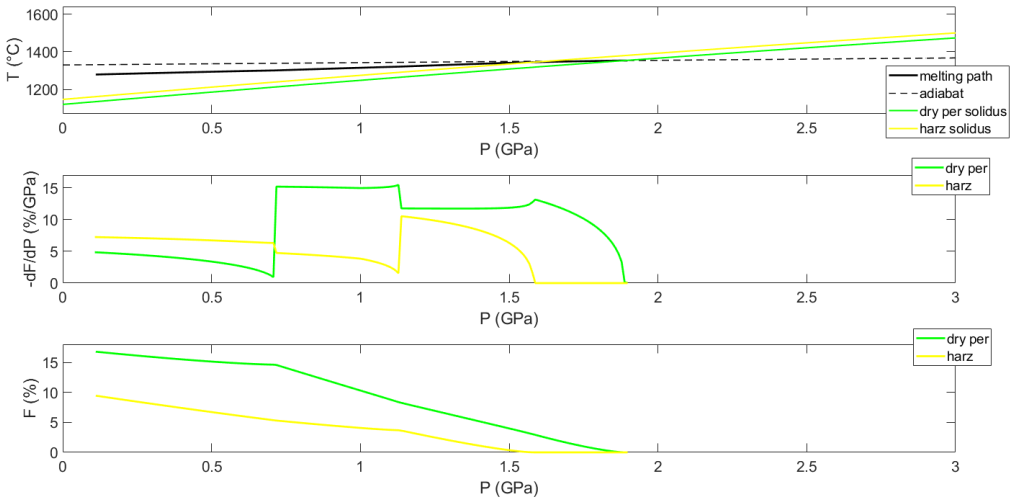

Figure 43: ***REEBOX PRO*** **thermodynamic output.**

In general, the pooled melts adequately account for the depleted nature of the Cocos-Nazca, Incipient Rift, and local EPR lavas. One notable exception is that the pooled melt Nb/Ta values do not drastically differ from those of DMM and do not account for the unusually low Nb/Ta values observed for some Cocos-Nazca and Garrett lavas. This is a consequence of two factors; 1) The *REEBOX PRO* default partition coefficients for the two elements differ from those of Lundstrom et al. (1998) and 2) The lherzolite crosses the solidus deeper than the harzburgite leading to initial melts that are elevated with respect to Nb/Ta. The harzburgite generates less melt than the lherzolite such that the Nb/Ta of the lherzolite source dominates the composition of the pooled melts. While different in a number of ways, the two calculations illustrate that the highly-depleted nature of the Cocos-Nazca, Incipient Rift, and local EPR lavas is explained by a two-stage melting model whereby the enriched components are removed during the initial melting event leaving behind a more refractory, depleted, residue that undergoes subsequent melting.

Appendix C: Supplementary Material for Chapter 3

Slabs of phyric lavas from the Cocos-Nazca Spreading Center were scanned and imported into the image processing software *ImageJ* (Schneider et al., 2012). Images of plagioclase ultra-phyric basalts (PUB) from other spreading centers were taken from Hellevang and Pederson (2008) and Lange et al. (2013a). Plagioclase were identified by adjusting the color threshold in *ImageJ*. Examples of a scanned slab (sample D22-1) and the resulting plagioclase outlines are given below (Figure 44). Following the methods of Boorman et al. (2004), measurements included the plagioclase area, centroid, fit ellipse, and feret's diameter. Partial plagioclase crystals and plagioclase with a measured area < .01 mm^2 were omitted (Figure 44).

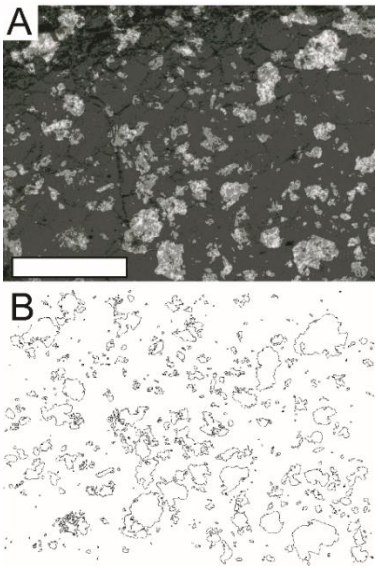

Figure 44: Example of a scanned plagioclase-bearing MORB (sample D22-1, A) and the outlines generated and measured by *ImageJ* (B). Scale bar in (A) is 1 cm.

ImageJ measurements were imported into *CSDSlice* (Morgan and Jerram, 2008), a program designed to convert 2-D measurements into 3-D. *CSDSlice* utilizes a database of crystal morphologies and short-axis/long-axis ratios to match crystal distributions to the best-fit short-intermediate-long axis. Best-fit shapes have R^2 values ranging from 0.70 to 0.95 with a mean value ≈ 0.85. Examples of the *CSDSlice* modelled shape compared to the actual shape distribution for two samples (KN-63D/1 and D22-1) are given in Figure 45. Goodness of fit is not correlated with the number of crystals ($R^2 = 0.17$) or plagioclase volume ($R^2 = 0.01$). It is possible that image resolution influences the accuracy of *CSDSlice* conversions and ultimately CSD calculations. However, among images taken from the literature, modelled best-fit shapes have R^2 ranging from 0.70 to 0.92 similar to the range observed for Cocos-Nazca lavas (R^2 from 0.72 to 0.95).

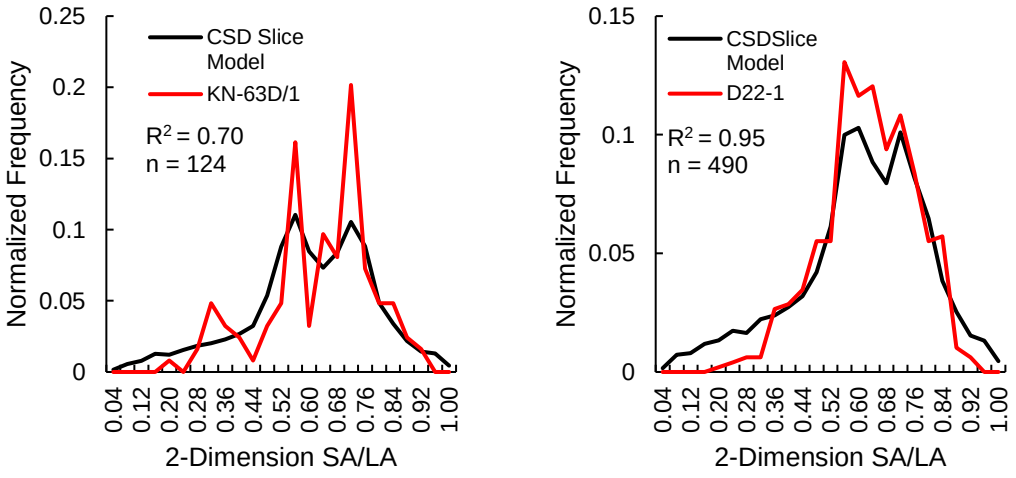

Figure 45: Examples of end-member *CSDSlice* models. KN-63D/1 is from the Knipovich ridge while D22-1 is from the Cocos-Nazca Spreading Center.

Core-rim pairs for one sparsely phyric lava (D15-2) and two plagioclase ultra-phyric basalts (D20-3 and D49-1) were analyzed using the Cameca CAMEBAX Microprobe at Duke University. For plagioclase analysis, a defocused beam (15 μm) was used with a beam current of 15 nA and an accelerating voltage of 15 KeV. Repeat analysis of an in-house bytownite standard reveals an overall variation of approximately 1.6 % leading to a deviation of An# of ± 2.5. Major element compositions of individual plagioclase cores and rims can be found in Table 14.

Table 14: Microprobe determined plagioclase core and rim major element compositions for plagioclase from the Cocos-Nazca Spreading Center.

ID	Core or Rim	SiO_2	MgO	CaO	FeO	Na_2O	K_2O	Al_2O_3	SUM	An No.
D15-2_1	core	48.05	0.13	14.78	0.39	2.55	0	32.78	98.67	76.9
D15-2_1	rim	46.94	0.22	15.46	0.48	2.19	0.02	32.66	97.96	80.1
D15-2_2	core	46.85	0.14	15.8	0.33	1.9	0.01	33.35	98.38	82.65
D15-2_2	rim	47.66	0.17	15.33	0.4	2.3	0.01	32.79	98.67	79.18
D15-2_3	core	47.22	0.16	15.88	0.41	1.95	0.01	32.93	98.56	82.3
D15-2_3	rim	46.51	0.24	15.04	0.52	2.33	0.02	32.38	97.05	78.57
D15-2_4	core	48.63	0.19	15.05	0.49	2.51	0	32.71	99.57	77.47
D15-2_4	rim	49.12	0.18	14.76	0.36	2.71	0	31.15	98.28	75.75
D15-2_5	core	50.36	0.28	13.99	0.45	3.24	0.03	30.93	99.28	71.09
D15-2_5	rim	49.04	0.18	14.78	0.48	2.84	0.01	32.32	99.66	74.84
D15-2_6	core	47.17	0.15	16.44	0.3	2.04	0.03	33.83	99.95	82.09
D15-2_6	rim	46.49	0.13	16.63	0.36	1.86	0	34.12	99.6	83.61
D15-2_7	core	47.78	0.17	15.94	0.48	2.23	0	33.12	99.74	80.37
D15-2_7	rim	50.23	0.21	14.77	0.58	2.73	0.03	31.28	99.83	75.51
D15-2_8	core	48.44	0.19	14.35	0.5	3.34	0.01	31.5	98.33	71.11
D15-2_8	rim	47.57	0.2	14.66	0.47	2.8	0.04	31.48	97.22	74.82
D15-2_9	core	50.81	0.16	13.59	0.48	3.51	0.02	30.69	99.26	68.83
D15-2_9	rim	50.23	0.29	13.21	0.51	4.44	0.03	30.61	99.31	62.94
D15-2_10	rim	49.41	0.22	14.32	0.54	3.27	0.02	31.41	99.18	71.43
D15-2_11	core	48.15	0.16	15.41	0.53	2.36	0.01	32.9	99.52	78.88
D15-2_11	rim	48.46	0.19	15.43	0.45	2.95	0.01	32.4	99.88	74.98
D15-2_12	core	51.38	0.26	13.65	0.49	4.08	0.02	31.76	101.63	65.67

Table 14 (continued)

D15-2_12	rim	50.37	0.15	13.87	0.43	3.32	0.02	31.45	99.61	70.47
D15-2_13	core	50.95	0.25	13.73	0.49	4.06	0.02	30.46	99.98	65.86
D15-2_13	rim	50.01	0.23	14.55	0.42	4.23	0.02	31.56	101.02	66.28
D15-2_14	core	48.45	0.19	15.84	0.38	2.81	0.02	32.98	100.67	76.25
D15-2_14	rim	50.18	0.24	14.74	0.47	3.38	0.02	30.95	99.98	71.35
D15-2_15	core	48.41	0.14	15.86	0.45	3.04	0	32.08	99.99	74.95
D15-2_15	rim	50.47	0.23	14.85	0.47	2.9	0.03	31.8	100.76	74.44
D20-3_1	core	49.19	0.24	14.34	0.35	2.87	0.01	30.71	97.72	74.03
D20-3_1	rim	47.39	0.23	14.76	0.41	2.69	0.02	32.19	97.69	75.79
D20-3_2	core	45.86	0.24	16.63	0.31	1.64	0.02	33.36	98.06	85.24
D20-3_2	rim	48.59	0.24	14.28	0.46	3.06	0.01	31.71	98.36	72.75
D20-3_3	core	47.55	0.21	13.7	0.4	3.03	0.02	31.86	96.78	72.06
D20-3_3	rim	48.97	0.21	13.54	0.54	3.02	0.02	31.01	97.31	71.9
D20-3_4	core	47.35	0.21	13.86	0.38	2.9	0.01	31.31	96.03	73.19
D20-3_4	rim	48.44	0.23	14.28	0.37	2.65	0.01	31.06	97.04	75.47
D20-3_5	core	49.11	0.16	14.65	0.28	2.76	0.02	32.04	99.02	75.21
D20-3_5	rim	48.6	0.2	15.48	0.34	2.4	0.01	33.01	100.06	78.63
D20-3_6	core	44.27	0.2	16.23	0.26	1.65	0.01	33.48	96.11	84.92
D20-3_6	rim	49.02	0.21	14.13	0.41	2.93	0.02	30.51	97.23	73.33
D20-3_7	core	47.63	0.2	13.87	0.33	2.71	0.01	31.85	96.59	74.56
D20-3_7	rim	47.36	0.18	15.02	0.39	2.23	0.01	32.69	97.89	79.34
D20-3_8	core	49.95	0.24	14.2	0.33	3.13	0.03	32.18	100.05	72.12
D20-3_8	rim	47.4	0.17	15.58	0.4	2.33	0.01	33.46	99.34	79.27
D20-3_9	core	45.4	0.19	17.36	0.24	1.33	0.03	33.67	98.22	88.07
D20-3_9	rim	47.61	0.24	15.32	0.36	2.46	0.05	32.16	98.21	77.91
D20-3_11	core	49.48	0.2	14	0.33	3.23	0.01	31.5	98.75	71.25
D20-3_11	rim	48.34	0.29	14.05	0.53	2.94	0.03	30.68	96.87	73.12
D20-3_12	core	48.98	0.18	14.72	0.35	2.81	0.01	31.63	98.7	74.98
D20-3_12	rim	49.76	0.2	14.21	0.43	3.01	0.02	31.31	98.94	72.97
D20-3_13	core	47.6	0.13	16.96	0.31	1.9	0	33.25	100.15	83.69
D20-3_13	rim	47.26	0.16	16.81	0.38	1.81	0.01	33.48	99.92	84.13
D20-3_14	core	49.43	0.19	15.09	0.31	2.82	0	31.58	99.42	75.43
D20-3_14	rim	47.87	0.15	15.4	0.42	2.31	0	32.98	99.13	79.23
D20-3_15	core	47.36	0.15	15.91	0.29	1.97	0	33.04	98.71	82.24
D20-3_15	rim	50.58	0.21	13.89	0.47	3.41	0	30.98	99.55	69.99
D49-1_1	core	47.39	0.1	17.75	0.32	1.78	0.01	33.89	101.25	85.06
D49-1_1	rim	46.17	0.07	17.49	0.36	1.77	0.01	33.97	99.86	84.9
D49-1_2	core	46.47	0.24	17.83	0.35	1.39	0	34.37	100.65	88.06
D49-1_2	rim	46.94	0.26	17.07	0.32	1.89	0.02	33.32	99.81	83.7
D49-1_3	core	46.3	0.14	17.51	0.37	1.22	0.02	33.75	99.31	89.07
D49-1_3	rim	47.92	0.19	16.26	0.43	2.47	0	32.14	99.42	79.06
D49-1_4	core	47.04	0.16	16.36	0.39	2.03	0.01	32.95	98.95	82.11
D49-1_4	rim	47.16	0.19	16.59	0.38	1.98	0.01	33	99.3	82.75
D49-1_5	core	46.59	0.17	17.6	0.34	1.53	0.02	33.36	99.6	86.77

Table 14 (continued)

D49-1_5	rim	46.4	0.16	17.81	0.33	1.36	0.01	33.28	99.34	88.17
D49-1_6	core	44.7	0.14	18.89	0.32	1.06	0.02	34.86	99.99	90.95
D49-1_6	rim	45.99	0.19	17.59	0.31	1.67	0.01	34.08	99.83	85.77
D49-1_7	core	47.56	0.16	17.22	0.3	2	0.01	33.25	100.5	83.13
D49-1_7	rim	45.98	0.09	17.95	0.28	1.41	0	33.68	99.39	87.96
D49-1_8	core	46.36	0.19	17.47	0.32	1.82	0.02	34.08	100.26	84.53
D49-1_8	rim	45.77	0.16	17.62	0.33	0.84	0	33.95	98.68	92.29
D49-1_9	core	45.75	0.14	18.17	0.41	1.5	0.01	34.48	100.45	87.39
D49-1_9	rim	46.81	0.13	17.61	0.42	1.13	0.01	33.99	100.11	89.92
D49-1_10	core	49.6	0.18	15.33	0.31	2.82	0.02	31.94	100.2	75.67
D49-1_10	rim	47.28	0.18	17.18	0.41	2.01	0	33.56	100.62	83.03
D49-1_11	core	49.02	0.16	15.97	0.31	1.61	0.03	33.72	100.81	84.87
D49-1_11	rim	48.46	0.22	16.84	0.28	2.07	0	33.37	101.25	82.3
D49-1_12	core	47.1	0.14	17.92	0.3	1.14	0.03	34.1	100.74	89.84
D49-1_12	rim	47.05	0.12	17.74	0.23	1.61	0.01	34.16	100.93	86.28
D49-1_13	core	48.28	0.17	17.04	0.29	1.86	0.02	33.11	100.76	83.95
D49-1_13	rim	49.19	0.14	15.81	0.39	2.64	0.02	32.51	100.7	77.34
D49-1_14	core	47.5	0.16	18.14	0.3	1.3	0.01	34	101.41	88.8
D49-1_14	rim	48.31	0.17	16.52	0.37	1.93	0.02	32.93	100.24	83.02
D49-1_15	core	47.2	0.11	17.31	0.36	1.75	0	33.74	100.48	84.95
D49-1-15	rim	46.19	0.2	16.71	0.42	1.41	0	33.31	98.24	87.14
D49-1_16	core	46.56	0.17	17.4	0.34	1.77	0.01	33.27	99.53	84.88
D49-1_16	rim	46.74	0.13	16.87	0.44	1.78	0.01	34.45	100.42	84.4
D49-1_17	core	46.16	0.17	17.94	0.23	1.54	0.01	34.83	100.88	86.96
D49-1_17	rim	47.8	0.18	16.71	0.36	2.39	0.01	33.91	101.36	80
D49-1_18	core	46.55	0.08	17.43	0.34	1.67	0	34.5	100.59	85.65
D49-1_18	rim	46.96	0.14	16.91	0.4	2.34	0.01	33.62	100.37	80.5
Bytownite	std	52.05	0.15	13.73	0.38	3.65	0.14	31.16	101.26	67.82
Bytownite	std	52.31	0.11	13.86	0.46	3.26	0.14	31.06	101.19	70.35
Bytownite	std	51.99	0.17	13.74	0.34	3.9	0.1	31.4	101.63	66.54
Bytownite	std	51.82	0.1	13.74	0.48	3.66	0.09	30.77	100.66	67.94
Bytownite	std	52.28	0.08	13.69	0.44	3.35	0.08	30.89	100.83	69.75
Bytownite	std	51.46	0.11	13.57	0.41	3.73	0.11	30.92	100.33	67.17
Bytownite	std	51.58	0.13	13.74	0.46	3.72	0.1	31.72	101.45	67.52
Bytownite	std	51.68	0.19	13.7	0.43	3.67	0.07	31.23	100.96	67.88
Bytownite	std	51.69	0.1	13.76	0.39	3.58	0.05	31.44	101	68.59
Bytownite	std	51.51	0.11	13.51	0.36	3.74	0.06	31.1	100.39	67.17
Bytownite	std	51.04	0.11	13.59	0.38	3.44	0.05	31.53	100.17	69.21
Bytownite	std	51.74	0.1	13.85	0.43	3.73	0.11	31.57	101.53	67.63
Bytownite	std	52.17	0.11	13.85	0.36	4.29	0.13	31.48	102.41	64.48
Bytownite	std	52.66	0.09	13.94	0.38	4.59	0.12	29.99	101.78	63.15

Images of plagioclase ultraphyric basalts were taken from the literature (Lange et al., 2013; Hellevang and Pederson, 2008) and their CSDs were calculated following the methods outlined above. A list of samples, their location, and the calculated CSD parameters are given in Table 15.

Table 15: Crystal size distribution results for plagioclase ultraphyric basalts (PUB) from the literature.

Sample	[1]1AR91_3R	[1]1TT170-47-11	[1]CT-14	[1]1A91_5R	[1]115-1-2	[2]2KN-63D/1
Spreading Domain	Blanco	Axial	Juan de Fuca	Blanco	SWIR	KNIP
Longitude	-129.64	-130.03	-129.07	-129.64	40.21	
Latitude	44.21	45.98	48.39	44.21	-43.43	
No. of Crystals	1914	582	126	75	133	124
S:I:L	1:1.4:2.0	1:1.4:2.2	1:1.4:1.9	1:1.4:1.4	1:1.4:2.0	1:1.4:1.9
Shape Score	0.84	0.84	0.92	0.72	0.73	0.7
Max L (mm)	15.16	16.84	9.169	9.67	13	5.5
Volume %	36.89	43.65	32.96	35.91	30.29	41.6
Intercept	-2.85	-2.09	-2.04	-2.59	-3.22	1
Slope	-0.724	-0.702	-0.897	-0.867	-0.61	-1.52
Intercept < 1 mm	-0.2	-0.58	-1.58	-0.62	-0.96	2.81
Slope < 1 mm	-5.12	-2.21	-0.69	-3.76	-3.06	-5
Intercept > 1 mm	-3.62	-3.92	-3.024	-3.97	-5.17	-2.26
Slope > 1 mm	-0.57	-0.43	-0.659	-0.614	-0.384	-0.77

[1]Data from Lange et al. (2013) and Nielsen et al. (2020)

[2]Data from Hellevang and Pederson (2008)

[a]Number of crystals analyzed

[b]Shape score refers to the fit between the modelled 3-D shape using CSDSlice and the actual distribution of the data

References

Adam, J., and Green, T., 2006, Trace element partitioning between mica- and amphibole-bearing garnet lherzolite and hydrous basanitic melts: 1. Experimental results and the investigation of controls on partitioning behavior: Contributions to Mineralogy and Petrology, v. 152, p. 1-17, doi: 10.1007/s00410-006-0085-4.

Aird, H.M., and Boudreau, A.E., 2013, High-temperature carbonate minerals in the Stillwater Complex, Montana, USA: Contributions to Mineralogy and Petrology, v. 116, p. 1143-1160, doi: 10.1007/s00410-013-0913-2.

Andersen, J.C.Ø., Rasmussen, H., Nielsen, T.F.D., and Ronsbo, J.G., 1998, The Triple Group and the Platinova gold and palladium reefs in the Skaergaard Intrusion; stratigraphic and petrographic relations: Economic Geology, v. 93, p. 488-509, doi: 10.2113/gsecongeo.93.4.488.

Andersen, J.C.Ø., Rollinson, G.K., McDonald, I., Tegner, C., and Lesher, C.E., 2017, Platinum-group mineralization at the margin of the Skaergaard intrusion, East Greenland: Mineralium Deposita, v. 52, p. 929-942, doi: 10.1007/s00126-016-0707-3.

Anderson, J.C.Ø., 2006, Postmagmatic Sulphur loss in the Skaergaard Intrusion: Implications for the formation of the Platinova Reef: Lithos, v. 92, p. 198-221, doi: 0.1016/j.lithos.2006.03.033.

Ariskin, A.A., Frenkel, M.Y., Barmina, G.S., and Nielsen, R.L., 1993, Comagmat: a Fortran program to model magma differentiation processes: Computers and Geosciences, v. 19, p. 1155-1170, doi: 10.1016/0098-3004(93)90020-6.

Asimow, P.D., and Ghiorso, M.S., 1998, Algorithmic Modifications Extending MELTS to Calculate Subsolidus Phase Relations: American Mineralogist, v. 83, p. 1127-1131, doi: 10.2138/am-1998-9-1022.

Asimow, P.D., Hirschmann, M.M., and Stolper, E.M., 1997, An analysis of variations in isentropic melt productivity: Philosophical Transactions of the Royal Society of London, v. 355, p. 255-281, doi: 10.1098/rsta.1997.0009.

Ballhaus, C.G., and Stumpfl, E.F., 1985, Occurrence and petrological significance of graphite in the Upper Critical Zone, western Bushveld Complex, South Africa: Earth and Planetary Science Letters, v. 74, p. 58-68, doi: 10.1016/0012-821X(85)90166-9.

Batiza, R., and Niu, Y., 1992, Petrology and Magma Chamber Processes at the East Pacific Rise ~ 9°30'N: Journal of Geophysical Research, v. 97, p. 6779-6797, doi: 10.1029/92JB00172.

Bender, J.F., Hodges, F.N., and Bence, A.E., 1978, Petrogenesis of basalts from the project FAMOUS area: experimental study from 0 to 15 kbars: Earth and Planetary Science Letters, v. 41, 277-302, doi: 10.1016/0012-821X(78)90184-X.

Bennett, E.M., Lissenberg, C.J., and Cashman, K.V., 2019, The significance of plagioclase textures in mid-ocean ridge basalt (Gakkel Ridge, Artic Ocean): Contributions to Mineralogy and Petrology, v. 174, doi: 10.1007/s00410-019-1587-1.

Bird, D.K., Brooks, C.K., Gannicott, R.A., Turner, P.A., 1991, A Gold-Bearing Horizon In the Skaergaard Intrusion, East Greenland: Economic Geology, v. 86, p. 1083-1092, doi: 10.2113/gsecongeo.86.5.1083.

Bird, D.K., Rogers, R.D., and Manning, C.E., 1986, Mineralized fracture systems of the Skaergaard intrusion, East Greenland. Meddelelser om Grønland: Geoscience 16, p. 68

Boorman, S., Boudreau, A., and Kruger, F.J., 2004, The Lower Zone – Critical Zone Transition of the Bushveld Complex: A Quantitative Textural Study: Journal of Petrology, v. 45, p. 1209-1235, doi: 10.1093/petrology/egh011.

Boudreau, A.E., and McCallum I.S., 1989, Investigations of the Stillwater Complex: Part V. Apatites as indicators of evolving fluid composition: Contributions to Mineralogy and Petrology, v. 102, p. 138-153, doi: 10.1007/BF00375336.

Boudreau, A.E., and McCallum I.S., 1992, Concentration of platinum-group elements by magmatic fluids in layered intrusions: Economic Geology, v. 87, p. 1830-1848, doi: 10.2113/gsecongeo.87.7.1830.

Boudreau, A.E., Mathez, E.A., and McCallum, I.S., 1986, Halogen Geochemistry of the Stillwater and Bushveld Complexes: Evidence for Transport of the Platinum-Group Elements by Cl-Rich Fluids: Journal of Petrology, v. 27, p. 967-986, doi: 10.1093/petrology/27.4.967.

Boudreau, A.E., Stewart, M.A., and Spivack, A.J., 1997, Stable Cl isotopes and origin of high-Cl magmas of the Stillwater Complex, Montana: Geology, v. 25, p. 791-794, doi: 10.1130/0091-7613(1997)025<0791:SCIAOO>2.3.CO;2.

Brooks, C.K., and Gleadow, A.J.W., 1977, A fission-track age for the Skaergaard intrusion and the age of the East Greenland basalts: Geology, v. 5, p. 539-540, doi: 10.1130/0091-7613(1977)5<539:AFAFTS>2.0.CO;2.

Brown, E.L., and C.E. and Lesher, 2016, REEBOX PRO: A forward model simulating melting of thermally and lithologically variable upwelling mantle: Geochemistry, Geophysics, Geosystems, vol. 17, p. 3929-3968, doi: 10.1002/2016GC006579.

Bryan, W.B., 1983, Systematics of Modal Phenocryst Assemblages in Submaris Basalts: Petrologic Implications: Contributions to Mineralogy and Petrology, v. 83, p. 62-74, doi: 10.1007/BF00373080.

Cabri, L.J., Beattie, M., Rudashevsky, N.S., and Rudashevsky, V.N., 2005, Process mineralogy of Au, Pd and Pt ores from the Skaergaard intrusion, Greenland, using new technology: Minerals Engineering, v. 18, p. 887-897, doi: 10.1016/j.mineng.2005.01.021.

Campbell, I.H., and Naldrett, A.J., 1979, The Influence of Silicate: Sulfide Ratios on the Geochemistry of Magmatic Sulfides: Economic Geology, v. 74, p. 1503-1506, doi: 10.2113/gsecongeo.74.6.1503.

Canales, J.P., Danobeitia, J.J., Detrick, R.S., Hooft, E.E.E., Bartolome, R., and Naar, D.F., 1997, Variations in axial morphology along the Galapagos spreading center and the influence of the Galapagos hotspot: Journal of Geophysical Research, v. 102, p. 27341-27354, doi: 10.1029/97JB01633.

Candela, P.A., and Holland, H.D., 1984, The partitioning of copper and molybdenum between silicate melts and aqueous fluids: Geochimica et Cosmochimica Acta, v. 48, p. 373-380, doi: 10.1016/0016-7037(84)90257-6.

Cann, J.R., 1974, A model for Oceanic Crustal Structure Developed: Geophysical Journal International, v. 39, p. 169-187, doi: 10.1111/j.1365-246X.1974.tb05446.x.

Cannat, M., 1993, Emplacement of mantle rocks in the seafloor at mid-ocean ridges: Journal of Geophysical Research Solid Earth, v. 98, doi: 10.1029/92JB02221.

Cannat, M., 1996, How thick is the magmatic crust at slow spreading oceanic ridges?: Journal of Geophysical Research, v. 101, doi: 10.1029/95JB03116.

Carbotte, S.M., Small, C., and Donnelly, K., 2004, The influence of ridge migration on the magmatic segmentation of mid-ocean ridges: Nature, v. 429, p. 743-746, doi: 10.1038/nature02652.

Carbotte, S.M., Smith, D.K., Cannat, M., and Klein, E.M., 2015, Tectonic and magmatic segmentation of the Global Ocean Ridge System: a synthesis of observations, in Wright, T.J., Ayele, A., Ferguson, D.J., Kidane, T. and Vye-Brown, C., eds., Magmatic Rifting and Active Volcanism: Geological Society London, Special Publication 420, doi: 10.1144/SP420.18.

Cashman, K.V., and Ferry, J.M., 1988, Crystal size distribution (CSD) in rocks and the kinetics and dynamics of crystallization III: Metamorphic crystallization: Contributions to Mineralogy and Petrology, v. 99, p. 401-415, doi: 10.1007/BF00371933.

Cashman, K.V., and Marsh, B.D., 1988, Crystal size distribution (CSD) in rocks and the kinetics and dynamics of crystallization II: Makaopuhi lava lake: Contributions to Mineralogy and Petrology, v. 99, p. 292-305, doi: 10.1007/BF00375363.

Castillo, P.R., Klein, E., Bender, J., Langmuir, C., Shirey, S., Batiza, R., and White, W., 2000, Petrology and Sr, Nd, and Pb isotope geochemistry of mid-ocean ridge basalt glasses from the 1145'N to 1500'N segment of the East Pacific Rise: Geochemistry, Geophysics, Geosystems, v. 1, doi: 10.1029/1999GC000024.

Chaplygin, I., Yudovskaya, M., Vergasova, L., and Mokhov, A., 2015, Native gold from volcanic gases at Tolbachik 1975-76 and 2012-13 Fissure Eruptions, Kamchatka: Journal of Volcanology and Geothermal Research, v. 307, p. 200-209, doi: 10.1016/j.jvolgeores.2015.08.018.

Cheatham, M.W., Sangrey, W.F., and White, W.M., 1993, Sources of error in external calibration ICP-MS analysis of geological samples and an improved non-linear drift correction procedure: Spetrochimica Acta, v. 48, E487-E506, doi: 10.1016/0584-8547(93)80054-X.

Chen, Y.J., 1992, Oceanic crustal thickness versus spreading rate: Geophysical Research Letters, v. 19, doi: 10.1029/92GL00161.

Christie, D.M, and Sinton, J.M., 1981, Evolution of abyssal lavas along propagating segments of the Galapagos spreading center: Earth and Planetary Science Letters, v. 56, p. 321-335, doi: 10.1016/0012-821X(81)90137-0.

Christie, D.M., Werner, R., Hauff, F., Hoernle, K., and Hanan, B.B., 2005, Morphological and geochemical variations along the Eastern Galapagos Spreading Center: Geochemistry, Geophysics, Geosystems, v. 6, doi: 10.1029/2004GC000714.

Colman, A., Sinton, J.M., White, S.M., McClinton, J.T., Bowles, J.A., Rubin, K.H., Behn, M.D., Cushman, B., Eason, D.E., Gregg, T.K.P., Gronvold, K., Hidlago, S., Howell, J., Neill, W., and Russo, C., 2012, Effects of variable magma supply on mid-ocean ridge eruptions: Constraints from mapped lava flow fields along the Galapagos Spreading Center: Geochemistry, Geophysics, Geosystems, v. 13, Q08014, doi: 10.1029/2012GC004163.

Combier, V., Seher, T., Singh, S., Crawford, W., Cannat, M., Escartin, J., and Dusunur, D., 2015, Three-dimensional geometry of axial magma chamber roof and faults at Lucky Strike volcano on the Mid-Atlantic Ridge: Journal of Geophysical Research, v. 120, p. 5379-5400, doi: 10.1002/2015JB012365.

Costa, F., Coogan, L.A., and Chakraborty, S., 2010, The time scales of magma mixing and mingling involving primitive melts and melt-mush interaction at mid-ocean ridges: Contributions to Mineralogy and Petrology, v. 159, p. 371-387, doi: 10.1007/s00410-009-0432-3.

Cullen, A., Vicenzi, E., and McBirney, A.R., 1989, Plagioclase-ultraphyric basalts of the Galapagos archipelago: Journal of Volcanology and Geothermal Research, v. 37, p. 325-337, doi: 10.1016/0377-0273(89)90087-5.

Cushman, B., Sinton, J., Ito, G., and Dixon, J.E., 2004, Glass compositions, plume-ridge interaction, and hydrous melting along the Galapagos Spreading Center, 90.5W to 98W: Geochemistry, Geophysics, Geosystems, v. 5, Q08E17, doi: 10.1029/2004GC000709.

D'Ericco, M.E., Warran, J.M., and Godard, M., 2016, Evidence for chemically heterogenous Arctic mantle beneath the Gakkel Ridge: Geochimica et Cosmochimica Acta, v. 174, p. 291-312, doi: 10.1016/j.gca.2015.11.017.

Danyushevsky, L.V., Leslie, R.A., Crawford, A.J., and Durance, P., 2004, Melt Inclusions in Primitive Olivine Phenocrysts: the Role of Localized Reaction Processes in the Origin of Anomalous Compositions: Journal of Petrology, v. 45, p. 2531-2553, doi: 10.1093/petrology/egh080.

Danyuskevsky, L.V., Perfitt, M.R., Eggins, S.M., and Falloon, T.J., 2003, Crustal origin for coupled 'ultra-depleted' and 'plagioclase' signatures in MORB olivine-hosted melt inclusions: evidence from the Siqueiros Transform Fault, East Pacific Rise: Contributions to Mineralogy and Petrology, v. 144, p. 619-637, doi: 10.1007/s00410-002-0420-3.

DeHoff, R.T., 1991, A geometrically general theory diffusion controlled coarsening: Acta Metallurgica et Materialia, v. 39, p. 2349-2360, doi: 10.1016/0956-7151(91)90016-T.

DeMets, C., Gordon, R.G., Argus, D.F., and Stein, S., 1994, Effect of recent revisions to the geomagnetic reversal time scale on estimates of current plate motions: Geophysical Research Letters, v. 21, p. 2191-2194, doi: 10.1029/95GL02118.

Detrick, R.S., Sinton, J.M., Ito, G., Canales, J.P., Behn, M., Blacic, T., Cushman, B., Dixon, J.E., Graham, D.W., and Mahoney, J.J., 2002, Correlated geophysical, geochemiscal, and volcanological manifestations of plume ridge interaction along the Galapagos Spreading Center: Geochemistry, Geophysics, Geosystems, v. 3, 8501, doi: 10.1029/2002GC000350.

Drignon, M., Nielsen, R.L., Tepley III, F.J., and Bodnar, R.J., 2018, Upper mantle origin of plagioclase megacrysts from plagioclase-ultraphyric mid-oceanic ridge basalt: Geology, v. 47, p. 43-46, doi: 10.1130/G45542.1.

Eason, D., and Sinton, J., 2006, Origin of high-Al N-MORB by fractional crystallization in upper mantle beneath the Galapagos Spreading Center: Earth and Planetary Science Letters, v. 252, p. 423-436, doi: 10.1016/j.epsl.2006.09.048.

Fleet, M.E., Chryssoulis, S.L., Stone, W.E., and Weisener, C.G., 1993, Partitioning of platinum-group elements and Au in the Fe-Ni-Cu-S system: experiments on the fractional crystallization of sulfide melt: Contributions to Mineralogy and Petrology, v. 115, p. 36-44, doi: 10.1007/BF00712976.

Fornari, D.J., Perfit, M.R., Allan, J.F., Batiza, R., Haymon, R., Barone, A., Ryan, W.B.F., Smith, T., Simkin, T., and Luckman, M.A., 1988, Geochemical and structural studies of the Lamont seamounts: seamounts as indicators of mantle processes: Earth and Planetary Science Letters, v. 89, p. 63-83, doi: 10.1016/0012-821X(88)90033-7.

Francheteau, J., Armijo, R., Cheminee, J.L., Hekinian, R., Lonsdale, P., and Blum, N., 1990, 1 Ma East Pacific Rise oceanic crust and uppermost mantle exposed by rifting in Hess Deep (equatorial Pacific Ocean): Earth and Planetary Science Letters, v. 101, p. 281-295, doi: 10.1016/0012-821X(90)90160-Y.

Francheteau, J., Armijo, R., Cheminee, J.L., Hekinian, R., Lonsdale, P., and Blum, N., 1992, Dyke complex of the East Pacific Rise exposed in the walls of Hess Deep and the structure of the upper oceanic crust: Earth and Planetary Science Letters, v. 111, p. 109-121, doi: 10.1016/0012-821X(92)90173-S.

Frank, M.R., Simon, A.C., Pettke, T., Candela, P.A., and Piccoli, P.M., 2011, Gold and copper partitioning in magmatic-hydrothermal systems at 800°C and 100 MPa: Geochimica et Cosmochimica Acta, v. 75, p. 2470-2482, doi: 10.1016/j.gca.2011.02.012.

Gale, A., Dalton, C.A., Langmuir, C.H., Su, Y., and Schilling, J.-G., 2013, The mean composition of ocean ridge basalts: Geochemistry, Geophysics, Geosystems, v. 14, doi: 10.1029/2012GC004334.

Garrido, C.J., Kelemen, P.B., and Hirth, G., 2001, Variation of cooling rate with depth in lower crust formed at an oceanic spreading ridge: Plagioclase crystal size distributions in gabbros from the Oman ophiolite: Geochemistry, Geophysics, Geosystems, v. 2, doi: 10.1029/2000GC000136.

Geldmacher, J., Hofig, T.W., Hauff, F., Hoernle, K., Garbie-Schonberg, D., and Wilson, D.S., 2013, Influence of the Galapagos hotspot on the East Pacific Rise during Miocene superfast spreading: Geology, v. 41, p. 183-186, doi: 10.1130/G33533.1.

Ghiorso, M.S., and Sack, R.O., 1995, Chemical Mass Transfer in Magmatic Processes. IV. A Revised and Internally Consistent Thermodynamic Model for the Interpolation and Extrapolation of Liquid-Solid Equilibria in Magmatic Systems at Elevated Temperatures and Pressures: Contributions to Mineralogy and Petrology v. 119, p. 197-212, doi: 10.1007/s004100050036.

Gillis, K., Mevel, C., Allan, J., et al., 1993, Proceedings of the Ocean Drilling Program, Initial Reports, v. 147: College Station, TX, doi: 10.2973/odp.proc.ir.147.1993

Gillis, K.M., Muehlenbachs, K., Stewart, M., Gleeson, T., and Karson, J., 2001, Fluid flow patterns in fast spreading East Pacific Rise crust exposed at Hess Deep: Journal of Geophysical Research, v. 106, p. 26311-26329, doi: 10.1029/2000JB000038.

Gillis, K.M., Snow, J.E., Klaus, A., Abe, N., Adriao, A.B., Akizawa, N., Ceuleneer, G., Cheadle, M.J., Faak, K., Falloon, T.J., Friedman, S.A., Godard, M., Guerin, G., Harigane, Y., Horst, A.J., Hoshide, T., Ildefonse, B., Jean, M.M., John, B.E., Koepke, J., Machi, S., Maeda, J., Marks, N.E., McCaig, A.M., Meyer, R., Morris, A., Nozaka, T., Python, M., Saha, A., Wintsch, R.P., 2014, Primitive layered gabbros from fast-spreading lower oceanic crust: Nature, v. 505, p. 204-207, doi: 10.1038/nature12778.

Gillis, K.M., Snow, J.E., Klaus, A., and the Expedition 345 Scientists, 2014, Proceedings of the Integrated Ocean Drilling Program, v. 345: College Station, TX, doi: 10.2204/iodp.proc.345.2014.

Giuliani, L., Iezzi, G., Vetere, F., Behrens, H., Mollo, S., Cauti, F., Ventura, G., and Scarlato, P., 2020, Evolution of textures, crystal size distributions and growth rates of plagioclase, clinopyroxene, and spinel crystallized at variable cooling rates from a mid-ocean ridge basaltic melt: Earth-Science Reviews, v. 204, doi: 10.1016/j.earscirev.2020.103165.

Godel, B., Rudashevsky, N.S., Nielsen, T.F.D., Barnes, S.J., and Rudashevsky, V.N., 2014, New Constraints on the origin of the Skaergaard intrusion Cu-Pd-Au mineralization: Insights from high-resolution X-ray computed tomography: Lithos, v. 190-191, p. 27-36, doi: 10.1016/j.lithos.2013.11.019.

Greaney, A., Rudnick, R.L., Helz, R.T., Gaschnig, R.M., Piccoli, P.M., and Ash, R.D., 2017, The behavior of chalcophile elements during magmatic differentiation as observed in Kilauea Iki lava lake, Hawaii: Geochimica et Cosmochimica Acta, v. 210, p. 71-96, doi: 10.1016/j.gca.2017.04.033.

Gregg, T.K.P., Fornari, D.J., Perfit, M.R., Haymon, R.M., and Fink, J.H., 1996, Rapid emplacement of a mid-ocean ridge lava flow on the East Pacific Rise at 9°46′-51′N: Earth and Planetary Science Letters, v. 144, doi: 10.1016/S0012-821X(96)00179-3.

Hall, L.S., Mahoney, J.J., Sinton, J.M., and Duncan, R.A., 2006, Spatial and temporal distribution of a C-like asthenosphere component in the Rano Rahi Seamount Field, East Pacific Rise, 15°-19°S: Geochemistry, Geophysics, Geosystems, v. 7, doi: 10.1029/2005GC000994.

Hanley, J.J., Mungall, J.E., Pettke, T., Spooner, E.T.C., and Bray, C.J., 2008, Fluid and Halide Melt Inclusions of Magmatic Origin in the Ultramafic and Lower Banded Series, Stillwater Complex, Montana, USA: Journal of Petrology, v. 49, p. 1133-1160, doi: 10.1093/petrology/egn020.

Hanna, H.D., 2004, Geochemical Variations in basaltic glasses from an incipient rift and upper level gabbros from Hess Deep, eastern equatorial Pacific [M.Sc. thesis]: Duke University.

Hansen, H., and Gronvold, K., 2000, Plagioclase ultraphyric basalts in Iceland: the mush of the rift zone: Journal of Volcanology and Geothermal Research, v. 98, p. 1-32, doi: 10.1016/S0377-0273(99)00189-4.

Harpp, K.S., Fornari, D.J., Geist, D.J., and Kurz, M.D., 2003, Genovesa Submarine Ridge: A manifestation of plume-ridge interaction in the northern Galapagos Islands: Geochemistry, Geophysics, Geosystems, v. 4, doi: 10.1029/2003GC000531.

Harpp, K.S., Hall, P.S., and Jackson, M.G., 2014, Galapagos and Easter: A Tale of Two Hotspots, in Harpp, K.S., Mittelstaedt, E., d'Ozouville, N., and Graham, D.W., eds., The Galapagos: A Natural Laboratory for the Earth Sciences: Geophysical Monograph Series v. 204, doi: 10.1002/9781118852538.ch3.

Hart, S., 1988, Heterogenous mantle domains: signatures, genesis, and mixing chronologies: Earth and Planetary Science Letters, v. 90, p. 273-296, doi: 10.106/0012-821X(88)90131-8.

Hays, M.R., 2004, Intra-transform volcanism along the Siqueiros fracture zone 8°20'N to 8°30'N, East Pacific Rise [M.Sc. thesis]: University of Florida.

Heinrich, C.A., Driesner, T., Stefansson, A., and Seward, T.M., 2004, Magmatic vapor contraction and the transport of gold from the porphyry environment to epithermal ore deposits: Geology, v. 32, p. 761-764, doi: 10.1130/G20629.1.

Hekinian R., Bideau, D., Cannat, M., Francheteau, J., and Hebert, R., 1992, Volcanic activity and crust-mantle exposure in the ultrafast Garrett transform faul near 13°28'S in the Pacific: Earth and Planetary Science Letters, v. 108, p. 259-275, doi: 10.1016/0012-821X(92)90027-S.

Hekinian, R., Bideau, D., Hebert, R., and Niu, Y., 1995, Magmatism in the Garrett transform fault (East Pacific Rise near 13°27'S): Journal of Geophysical Research, v. 100, p. 10163-10185, doi: 10.1029/94JB02125.

Hellebrand, E., Snow, J.E., Dick, H.J.B., and Hofmann, A.W., 2001, Coupled major and trace elements as indicators of the extent of melting in mid-ocean-ridge peridotites: Nature, v. 410, p. 677-681, doi: 10.1038/35070546.

Hellevang, B., and Pederson, R.B., 2008, Magma Ascent and Crustal Accretion at Ultraslow-Spreading Ridges: Constraints from Plagioclase Ultraphyric Basalts from the Artic-Mid-Ocean Ridge: Journal of Petrology, v. 49, p. 267-294, doi: 10.1093/petrology/egm081.

Herron T.J., Ludwig, W.J., Stoffa, P.L, Kan, T.K., and Buhl, P., 1978, Structure of the East Pacific Rise crest from multichannel seismic reflection data: Journal of Geophysical Research, v. 83, p. 798-804, doi: 10.1029/JB083iB02p00798.

Hey, R., 1977, Tectonic evolution of the Cocos-Nazca spreading center. Geological Society of America Bulletin: v. 88, p. 1404-1420, doi: 10.1130/0016 - 7606(1977)88<1404:TEOTCS>2.0.CO;2.

Higgins, M.D., 1996, Magma dynamics beneath Kameni volcano, Thera, Greece, as revealed by crystal size and shape measurements: Journal of Volcanology and Geothermal Research, v. 70, p. 37-48, doi: 10.1016/0377-0273(95)00045-3.

Higgins, M.D., 1998, Origin of megacrysts in granitoids by textural coarsening: a crystal size distribution (CSD) study of microcline in the Cathedral Peak Granodiorite, Sierra Nevada, California, in Castro, A., Fernandez, C., and Vigneresse, J.L., eds., Understanding Granites: Integrating New and Classical Techniques: Geological Society, London, Special Publications 168, p. 207-219, doi: 10.1144/GSL.SP.1999.168.01.14.

Higgins, M.D., 2000, Measurement of crystal size distributions: American Mineralogist, v. 85, p. 1105-1116, doi: 10.2138/am-2000-8-901.

Higgins, M.D., 2002, A crystal size-distribution study of the Kiglapait layered mafic intrusion, Labrador, Canada: evidence for textural coarsening: Contributions to Mineralogy and Petrology, v. 144, p. 314-330, doi: 10.1007/s00410-002-0399-9.

Hirschmann, M.M., Asimow, P.D., Ghiorso, M.S., and Stolper, E.M., 1999, Calculation of Peridotite Partial Melting from Thermodynamic Models of Minerals and Melts. III. Controls on Isobaric Melt Production and the Effect of Water on Melt Production: Journal of Petrology, v. 40, p. 831-851, doi: 10.1093/petroj/40.5.831.

Hirschmann, M.M., Renne, P.R., and McBirney, A.R., 1997, 40Ar/39Ar dating of the Skaergaard intrusion: Earth and Planetary Science Letters, v. 146, p. 645–658, doi: 10.1016/S0012-821X(96)00250-6.

Hofmann, A.W., 1997, Mantle geochemistry: the message from oceanic volcanism: Nature, v. 385, p. 219-229, doi: 10.1038/385219a0.

Holden, J.C., and Dietz, R.S., 1972, Galapagos gore, NazCoPac triple junction and Carnegie/Cocos ridges: Nature, v. 235, p. 266-269, doi: 10.1038/235266a0.
Holland, H.D., 1972, Granites, Solutions, and Base Metal Deposits: Economic Geology, v. 67, p. 281-301, doi: 10.2113/gsecongeo.67.3.281.

Holness, M.B., Nielsen, T.F.D., and Tegner, C., 2007, Textural maturity of cumulates: A record of chamber filling, liquidus assemblage, cooling rate and large scale convection in mafic layered intrusions: Journal of Petrology, v. 48, p. 141-157, doi: 10.1093/petrology/egl057.

Holwell, D.A., and Keays, R.R., 2014, The Formation of Low-Volume, High-Tenor Magmatic PGE-Au Sulfide Mineralization in Closed Systems: Evidence from Precious and Base Metal Geochemistry of the Platinova Reef, Skaergaard Intrusion, East Greenland: Economic Geology, v. 109, p. 387-406, doi: 10.2113/econgeo.109.2.387.

Holwell, D.A., Keays, R.R., McDonald, I., and Williams, M.R., 2015, Extreme enrichment of Se, Te, PGE, and Au in Cu sulfide microdroplets: evidence from LA-ICP-MS analysis of sulfides in the Skaergaard Intrusion, east Greenland: Contributions to Mineralogy and Petrology, v. 170, doi: 10.1007/s00410-015-1203-y.

Huber, C., Bachmann, O., Vigneresse, J.-L., Dufek, J., and Parmigiani, A., 2012, A physical model for metal extraction and transport in shallow magmatic systems: Geochemistry, Geophysics, Geosystems, v. 13, p. 2887-2905, doi: 10.1029/2012GC004042.

Jakobsen, J.K., Veksler, I.V., Tegner, C., and Brooks, C.K., 2011, Crystallization of the Skaergaard Intrusion from an Emulsion of Immiscible Iron- and Silica-rich Liquids: Evidence from Melt Inclusions in Plagioclase: Journal of Petrology, v. 52, p. 345-373, doi: 10.1093/petrology/egq083.

Jenkyns, H.C., Paull, C.K., Cummins, D.I., and Fullagar, P.D., 1995, Strontium-Isotope Stratigraphy of Lower Cretaceous Atoll Carbonates in the Mid-Pacific Mountains, in Winterer, E.L., Sager, W.W., Firth, J.V., and Sinton, J.M., eds., Proceedings of the Ocean Drilling Program, Scientific Results, v. 143, p. 89-97, doi: 10.2973/odp.proc/sr/143.212.1995.

Jenner, F.E., 2017, Cumulate causes for the low contents of sulfide-loving elements in the continental crust: Nature Geoscience, v. 10, p. 524-530, doi: 10.1038/ngeo2965.

Jenner, F.E., O'Neill, H.S.C., Arculus, R.J., and Mavrogenes, J.A., 2010, The magnetite crisis in the evolution of arc-related magmas and the initial concentration of Au, Ag, and Cu: Journal of Petrology, v. 51, p. 2445-2464, doi: 10.1093/petrology/egq063.

Karson, J.A., 2019, From Ophiolites to Oceanic Crust: Sheeted Dike Complexes and Seafloor Spreading, in Srivastava, R., Ernst, R., and Peng, P., eds., Dyke Swarms of the World: A Modern Perspective, doi: 10.1007/978-981-13-1666-1_13.

Keays, R.R., and Scott, R.B., 1976, Precious metal in ocean-ridge basalts; implications for basalts as source rocks for gold mineralization: Economic Geology, v. 71, p. 705-720, doi: 10.2113/gsecongeo.71.4.705.

Keays, R.R., and Tegner, C., 2016, Magma Chamber Processes in the Formation of the Low-sulfide Magmatic Au-PGE Mineralization of the Platinova Reef in the Skaergaard Intrustion, East Greenland: Journal of Petrology, v. 56, p. 2319-2340, doi: 10.1093/petrology/egv075.

Klein, E.M., and Langmuir, C.H., 1987, Global Correlations of Ocean Ridge Basalt Chemistry with Axial Depth and Crustal Thickness: Journal of Geophysical Research, v. 92, B8, doi: 10.1029/JB092iB08p08089.

Klein, E.M., Langmuir, C.H., and Staudigel, H., 1991, Geochemistry of basalts from the Southeast Indian Ridge: Journal of Geophysical Research, v. 96, p. 2089-2108, doi: 10.1029/90JB01384.

Kuo, L.-C., and Kirkpatrick, R.J., 1982, Pre-Eruption History of Phyric Basalts from DSDP Legs 45 and 46: Evidence from Morphology and Zoning Patterns in Plagioclase: Contributions to Mineralogy and Petrology, v. 79, p. 13-27, doi: 10.1007/BF00376957.

Lange, A.E., Nielsen, R.L., Tepley III, F.J., and Kent, A.J.R., 2013a, The petrogenesis of plagioclase-phyric at mid-ocean ridges: Geochemistry, Geophysics, Geosystems, v. 14, doi: 10.1002/ggge.20207.

Lange, A.E., Nielsen, R.L., Tepley III, F.J., and Kent, A.J.R., 2013b, Diverse Sr isotope signature preserved in mid-oceanic-ridge basalt plagioclase: Geology, v. 41, p. 279-282, doi: 10.1130/G33739.1.

Langmuir, C.H., Klein, E.M., and Plank, T., 1992, Petrological Systematics of Mid-Ocean Ridge Basalts: Constraints on Melt Generation Beneath Ocean Ridges, in Phipps Morgan, J., Blackman, D.K., and Sinton, J., eds, Mantle Flow and Melt Generation at Mid-Ocean Ridges: Geophysical Monograph Series, v. 71, doi: 10.1029/gm071p0183.

Larsen, R.B., Brooks, C.K., and Bird, D.K., 1992, Methane-bearing, aqueous, saline solutions in the Skaergaard intrusion, east Greenland: Contributions to Mineralogy and Petrology, v. 112, p. 428-437, doi: 10.1007/BF00310472.

Li, C., and Boudreau, A.E., 2017, The origin of high-Cu/S sulfides by shallow level degassing in the Skaergaard intrusion, East Greenland: Geology, v. 45, p. 1075-1078, doi: 10.1130/G39540.1.

Li, Y., and Audetat, A., 2012, Partitioning of V, Mn, Co, Ni, Cu, Zn, As, Mo, Ag, Sn, Sb, W, Au, Pb, and Bi between sulfide phases and hydrous basanite melt at upper mantle conditions: Earth and Planetary Science Letters, v. 355, p. 327-340, doi: 10.1016/j.epsl.2012.08.008.

Lifshitz, I.M., and Slyozov, V.V., 1961, The kinetics and precipitation from supersaturated solid solutions: Journal of Physics and Chemistry of Solids, v. 19, p. 35-50, doi: 10.1016/0022-3697(61)90054-3.

Lissenberg, C.J., MacLeod, C.J., Howard, K.A., and Godard, M., 2013, Pervasive reactive melt migration through fast-spreading lower oceanic crust (Hess Deep, equatorial Pacific Ocean): Earth and Planetary Science Letters, v. 361, p. 436-447, doi: 10.1016/j.epsl.2012.11.012.

Liu, B., and Liang, Y., 2017, The prevalence of kilometer-scale heterogeneity in the source region of MORB upper mantle: Science Advances, v. 3, doi: 10.1126/sciadv.1701872.

Lonsdale, P., 1988, Structural Pattern of the Galapagos Microplate and Evolution of the Galapagos Triple Junctions: Journal of Geophysical Research, v. 93, doi: 10.1029/JB093iB11p13551.
Lonsdale, P., 1995, Creation of the Cocos and Nazca plates by fisson of the Farallon plate: Tectonophysics, v. 404, p. 237-264, doi: 10.1016/j.tecto.2005.05.011.

Lundstrom, C.C., Shaw, H.F., Ryerson, F.J., Williams, Q., and Gill, J., 1998, Crystal chemical control of clinopyroxene-melt partitioning in the Di-Ab-An system: implications for elemental fractionations in the depleted mantle: Geochimica et Cosmochimica Acta, v. 62, p. 2849-2862, doi: 10.1016/S0016-7037(98)00197-5.

Mallick, S., Salters, V.J.M, and Langmuir, C.H., 2019, Geochemical Variability Along the Northern East Pacific Rise: Coincident Source Composition and Ridge Segmentation: Geochemistry, Geophysics, Geosystems, v. 20, doi: 10.1029/2019GC008287.

Manning, C.E., and Bird, D.K., 1986, Hydrothermal clinopyroxenes of the Skaergaard intrusion: Contributions to Mineralogy and Petrology, v. 92, p. 437-447, doi: 10.1007/BF00374426.

Marsh, B.D., 1988, Crystal size distribution (CSD) in rocks and the kinetics and dynamics of crystallization I: Theory: Contributions to Mineralogy and Petrology, v. 99, p. 277-291, doi: 10.1007/BF00375362.

Marsh, B.D., 1996, Solidification fronts and magmatic evolution: Mineralogical Magazine, v. 60, p. 5-40, doi: 10.1180/minmag.1996.060.398.03.

Marsh, B.D., 2013, On some fundamentals of igneous petrology: Contributions to Mineralogy and Petrology, v. 166, p. 665-690, doi: 10.1007/s00410-013-0892-3.

McBirney, A.R., 1975, Differentiation of the Skaergaard Intrusion: Nature, v. 253, p. 691-694, doi: 10.1038/253691a0.

McBirney, A.R., 1989, The Skaergaard Layered Series: I. Structure and Average Compositions: Journal of Petrology, v. 30, p. 363-397, doi: 10.1093/petrology/30.2.363.

McDonough, W.F., and Sun, S.-s., 1995, The composition of the Earth: Chemical Geology, v. 120, p. 223-253, doi: 10.1016/0009-2541(94)00140-4.

McKenzie, D., and O'Nions, R.K., 1991, Partial Melt Distributions from Inversion of Rare Earth Element Concentrations: Journal of Petrology, v. 32, p. 1021-1091, doi: 10.1093/petrology/32.5.1021.

Meurer, W.P., Klaber, S., and Boudreau, A.E., 1997, Discordant bodies from olivine-bearing zones III and IV of the Stillwater Complex, Montana – evidence for postcumulus fluid migration and reaction in layered intrusions: Contributions to Mineralogy and Petrology, v. 130, p. 81-92, doi: 10.1007/s004100050351.

Meurer, W.P., Willmore, C.C., and Boudreau, A.E., 1999, Metal redistribution during fluid exsolution and migration in the Middle Banded series of the Stillwater Complex, Montana: Lithos, v. 47, p. 143-156, doi: 10.1016/S0024-4937(99)00012-2.

Michael, P.J., and Cornell, W.C., 1988, Influence of spreading rate and magma supply on crystallization and assimilation beneath mid-ocean ridges: Evidence from chlorine and

major element chemistry of mid-ocean ridge basalts: Journal of Geophysical Research Solid Earth, v. 103, doi: 10.1029/98JB00791.

Michael, P.J., McDonough, W.F., Nielsen, R.L., and Cornell, W.C., 2002, Depleted melt inclusions in MORB plagioclase: messages from the mantle or mirages from the magma chamber?: Chemical Geology, v. 183, p. 43-61, doi: 10.1016/S0009-2541(01)00371-0.

Miller, J.S., Glazner, A.F., Walker, J.D., and Martin, M.W., 1995, Geochronologic and isotopic evidence for Triassic-Jurassic emplacement of the eugeoclinal allochthon in the Mojave Desert region, California: Geological Society of America Bulletin, v. 107, p. 1441–1457, doi: 10.1130/0016-7606(1995)107<1441:GAIEFT>2.3.CO;2.

Mills, R.D., Ratner, J.J., and Glazner, 2011, Experiment evidence for crystal coarsening and fabric development during temperature cycling: Geology, v. 39, p. 1139-1142, doi: 10.1130/G32394.1.

Mitchell, G.A., Montesi, L.G.J., Zhu, W., Smith, D.K., and Schouten, H., 2011, Transient rifting north of the Galapagos Triple Junction: Earth and Planetary Science Letters, v. 307, p. 461-469, doi: 10.1016/j.epsl.2011.05.027.

Mitchell, G.A., Montesi, L.G.J., Zhu, W., Smith, D.K., and Schouten, H., 2011, Transient rifting north of the Galapagos Triple Junction: Earth and Planetary Science Letters, v. 307, p. 461-469, doi: 10.1016/j.epsl2011.05.027.

Mock, A., and Jerram, D.A., 2005, Crystal Size Distributions (CSD) in Three Dimensions: Insights from the 3D Reconstruction of Highly Porphyritic Rhyolite: Journal of Petrology, v. 46, p. 1525-1541, doi: 10.1093/petrology/egi024.

Morgan and D.J., and Jerram, D.A., 2006, On estimating crystal shape for crystal size distribution analysis: Journal of Volcanology and Geothermal Research, v. 154, p. 1-7, doi: 10.1016/j.jvolgeores.2005.09.016.

Morgan, D.J., Jerram, D.A., Chertkoff, D.G., Davidson, J.P., Pearson, D.G., Kronz, A., and Nowell, G.M., 2007, Combining CSD and isotopic microanalysis: Magma supply and mixing processes at Stromboli Volcano, Aeolian Islands, Italy: Earth and Planetary Science Letters, v. 260, p. 419-431, doi: 10.1016/j.epsl.2007.05.037.

Mungall, J.E., and Brenan, J.M., 2014, Partitioning of platinum-group elements and Au between sulfide liquid and basalt and the origins of mantle-crust fractionation of the chalcophile elements: Geochimica et Cosmochimica Acta, v. 125, p. 265-289, doi: 10.1016/j.gca.2013.10.002.

Naslund, H.R., 1984, Petrology of the Upper Border Series of the Skaergaard Intrusion: Journal of Petrology, v. 25, p. 185-212, doi: 10.1093/petrology/25.1.185.

Neal, C.R., Donohue, P., Fagan, A.L., O'Sullivan, K., Oshrin, J., and Roberts, S., 2015, Distinguishing between basalts produced by endogenic volcanism and impact processes: A non-destructive method using quantitative petrography of lunar basaltic samples: Geochimica et Cosmochimica Acta, v. 148, p. 62-80, doi: 10.1016/j.gca.2014.08.020.

Ni, H., Keppler, H., Walte, N., Schiavi, F., Chen, Y., Masotta, M., and Li, Z., 2014, In situ observation of crystal growth in a basalt melt and the development of crystal size distribution in igneous rocks: Contributions to Mineralogy and Petrology, v. 167, doi: 10.1007/s00410-014-1003-9.

Nielsen, R.L., Crum. J., Bourgeois R., Hascall, K., Forsythe, L.M., Fisk, M.R., and Christie, D.M., 1995, Melt inclusions in high-An plagioclase from the Gorda Ridge: an example of the local diversity of MORB parent magmas: Contributions to Mineralogy and Petrology, v. 122, p. 34-50, doi: 10.1007/s004100050111.

Nielsen, R.L., Ustunisik, G., Lange, A.E., Tepley III, F.J., and Kent, A.J.R., 2020, Trace Element and Isotopic Characteristics of Plagioclase Megacrysts in Plagioclase Ultraphyric Basalts (PUB): Geochemistry, Geophysics, Geosystems, v. 21, doi: 10.1029/2019GC008638.

Nielsen, R.L., Ustunisik, G., Wensteiger, A.B., Tepley III, F.J., Johnston, A.D., and Kent, A.J.R, 2017, Trace element partinioning between plagioclase and melt: An investigation of the impact of experimental and analytical procedures: Geochemistry, Geophysics, Geosystems, v. 18, doi: 10.1002/2017GC007080.

Nielsen, T.F.D., 1975, Possible mechanism of continental breakup in the North Atlantic: Nature, v. 253, p. 182-184, doi: 10.1038/253182a0.

Nielsen, T.F.D., 2004, The Shape and Volume of the Skaergaard Intrusion, Greenland: Implications for Mass Balance and Bulk Composition: Journal of Petrology, v. 45, p. 507-530, doi: 10.1093/petrology/egg092

Nielsen, T.F.D., Andersen, J.C.O., Holness, M.B., Keiding, J.K., Rudashevsky, N.S., Rudashevsky, V.N., Salmonsen, L.P., Tegner, C., and Veksler, I.V., 2015, The Skaergaard PGE and Gold Deposit: the Result of in situ Fractionation, Sulphide Saturation, and Magma Chamber-scale Precious Metal Redistribution by Immiscible Fe-rich Melt: Journal of Petrology, v. 56, p. 1643-1676, doi: 10.1093/petrology/egv049.

Nikolaeva, I.V., Palesskii, S.V., Koz'menko, O.A., and Anoshin, G.N., 2008, Analysis of geologic reference materials for REE and HFSE by inductively coupled plasma-mass spectrometry (ICP-MS): Geochemistry Internation, v. 46, p. 1016-1022, doi: 10.1134/S0016702908100066.

Niu, Y., and Batiza, R., 1997, Trace element evidence from seamounts for recycled oceanic crust in the Eastern Pacific mantle: Earth and Planetary Science Letters, v. 148, p. 471-483, doi: 10.1016/S0012-821X(97)00048-4.

Niu, Y., and Hekinian, R., 1997, Spreading-rate dependence of the extent of mantle melting beneath ocean ridges: Nature, v. 385, p. 326-329, doi: 10.1038/385326a0.

Pagli, C., Wright, T.J., Ebinger, C.J., Yun, S.-H., Cann, J.R., Barnie, T., and Ayelee, A., 2012, Shallow axial magma chamber at the slow-spreading Erta Ale Ridge: Nature Geoscience, v. 5, p. 284-288, doi: 10.1038/ngeo1414.

Patten, C., Barnes, S.-J., Mathez, E.A., and Jenner, F.E., 2013, Partition Coefficients of chalcophile elements between sulfide and silicate melts and the early crystallization history of sulfide liquid: LA-ICP-MS analysis of MORB sulfide droplets: Chemical Geology, v. 358, p. 170-188, doi: 10.1016/j.chemgeo.2013.08.040.

Pendergast, M.D., 2000, Layering and Precious Metals Mineralization in the Rincon del Tigre Complex, Eastern Bolivia: Economic Geology, v. 95, p. 113-130, doi: 10.2113/gsecongeo.95.1.113.

Perfit, M.R., Fornari, D.J., Ridley, W.I., Kirk, P.D., Casey, J., Kastens, K.A., Reynolds, J.R., Edwards, M., Desonie, D., Shuster, R., and Paradis, S., 1996, Recent volcanism in the Siqueiros transform fault: picritic basalts and implications for MORB magma genesis: Earth and Planetary Science Letters, v. 141, p. 91-108, doi: 10.1016/0012-821X(96)00052-0.

Pertermann, M., and Hirschmann, M.M., 2003, Partial melting experiments on a MORB-like pyroxenite between 2 and 3 GPa: Constraints on the presence of pyroxenite in basalt source regions from solidus location and melting rate: Journal of Geophysical Research, v. 108, doi: 10.1029/2000JB000118.

Plank, T., Spiegelman, M., Langmuir, C.H., Forsyth, D.W., 1995, The meaning of 'mean F': clarifying the mean extent of melting at ocean ridges: Journal of Geophysical Research, v. 100, p. 15045-15052, doi: 10.1029/95JB01148.

Pupier, E., Duchene, S., and Toplis, M.J., 2008, Experimental quantification of plagioclase crystal size distribution during cooling of basaltic liquid: Contributions to Mineralogy and Petrology, v. 155, p. 555-570, doi: 10.1007/s00410-007-0258-9.

Rhodes, J.M., Dungan, M.A., Blanchard, D.P., and Long, P.E., 1979, Magma mixing at mid-ocean ridges: Evidence from basalts drilled near 22N on the Mid-Atlantic Ridge: Tectonophysics, v. 55, p. 35-61, doi: 10.1016/0040-1951(79)90334-2.

Rubin, K.H, Sinton, J.M, Maclennan, J., and Hellebrand, E., 2009, Magmatic filtering of mantle compositions at mid-ocean-ridge volcanoes: Nature Geoscience, v. 2, p. 321-328, doi: 10.1038/ngeo504.

Rubin, K.H., and Sinton, J.M., 2007, Inferences on mid-ocean ridge thermal and magmatic structure from MORB compositions: Earth and Planetary Science Letters, v. 260, p. 257-276, doi: 10.1016/j.epsl.2007.05.035.

Salters, V.J.M., and Stracke, A., 2004, Composition of the depleted mantle: Geochemistry, Geophysics, Geosystems, v. 5, doi: 10.1029/2003GC000597.

Sarda, P., and Graham, D., 1990, Mid-ocean ridge popping rocks: implications for degassing at ridge crests: Earth and Planetary Science Letters, v. 97, p. 268-289, doi: 10.1016/0012-821X(90)90047-2.

Saunders, A.D., Norry, M.J., and Tarney, J., 1988, Origin of MORB and Chemically-Depleted Mantle Resevoirs: Trace Element Constraints: Journal of Petrology, Special Volume 1, p. 415-445, doi: 10.1093/petrology/Special_Volume.1.415.

Schilling, J.-G., Fontignie, D., Blichert-Toft, J., Kingsley R., and Tomza, U., 2003, Pb-Hf-Nd-Sr isotope variations along the Galapagos Spreading Center (101°-83°W): Constraints on the dispersal of the Galapagos mantle plume: Geochemistry, Geophysics, Geosystems, v. 4, 8512, doi: 10.1029/2002GC000495.

Schneider, C.A., Rasnad, W.S., and Eliceiri, K.W., 2012, NIH Image to ImageJ: 25 years of image analysis: Nature Methods, v. 9, p. 671-675, doi: 10.1038/nmeth.2089.

Schouten, H., Smith, D.K., Montesi, L., Zhu, W., and Klein, E.M., 2008, Cracking of lithosphere north of the Galapagos triple junction: Geology, v. 36, p. 339-342, doi: 10.1130/G24431A.1.

Shaw, D.M., 1970, Trace element fractionation during anataxis: Geochimica et Cosmochimica Acta, v. 34, p. 237-242, doi: 10.1016/0016-7037(70)90009-8.

Shinohara, H., 1994, Exsolution of immiscible vapor and liquid from a crystallizing silicate melt: Imlications for chlorine and metal transport: Geochimica et Cosmochimica Acta, v. 58, p. 5215-5221, doi: 10.1016/0016-7037(94)90306-9.

Simon, A.C., Candela, P.A., Piccoli, P.M., Mengason, M., and Englander, L., 2008a, The effect of crystal-melt partitioning on the budgets of Cu, Au, and Ag: American Mineralogist, v. 93, p. 1437-1448, doi: 10.2138/am.2008.2812.

Simon, A.C., Pettke, T., Candela, P.A., and Piccoli, P.M., 2008b, The partitioning behavior of silver in a vapor-brine-rhyolite melt assemblage: Geochimica et Cosmochimica Acta, v. 72, p. 1638-1659, doi: 10.1016/j.gca.2008.01.003.

Singh, S.C., Crawford, W.C., Carton, H., Seher, T., Combier, V., Cannat, M., Canales, J.P., Düsünür, D., Escartin, J., and Miranda, J.M., 2006, Discovery of a magma chamber and faults beneath a Mid-Atlantic Ridge hydrothermal field: Nature, v. 442, p. 1029-1032, doi: 10.1038/nature05105.

Sinton, J., Detrick, R., Canales, J.P., Ito, G., and Behn, M., 2003, Morphology and segmentation of the western Galapagos Spreading Center, 90.5-98W: Plume-ridge interaction at an intermediate spreading rate: Geochemistry, Geophysics, Geosystems, v. 4, doi: 10.1029/2003GC000609.

Sinton, J.M, and Detrick, R.S., 1992, Mid-ocean ridge magma chambers: Journal of Geophysical Research, v. 97, p. 197-216, doi: 10.1029/91JB02508.

Smith, D.K., and Schouten, H., 2018, Opening of Hess Deep Rift at the Galapagos Triple Junction: Geophysical Research Letters, v. 45, p. 3942-3950, doi: 10.1029/2018GL077555.

Smith, D.K., Schouten, H., Montesi, L., and Zhu, W., 2013, The recent history of the Galapagos triple junction preserved on the Pacific Plate: Earth and Planetary Science Letters, v. 371-372, p. 6-15, doi: 10.1016/j.epsl.2013.04.018.

Smith, D.K., Schouten, H., Parnell-Turner, R., Klein, E.M., Cann, J., Dunham, C., Alodia, G., Blasco, I., Wernette, B., Zawadzki, D., Latypova, E., Afshar, S., and Curry, S., 2020, The Evolution of Seafloor Spreading Behind the Tip of the Westward Propagating Cocos-Nazca Spreading Center: Geochemistry, Geophysics, Geosystems, v. 21, doi: 10.1029/2020GC008957.

Smith, D.K., Schouten, H., Zhu, W.., Montesi, L.G.J., and Cann, J.R., 2011, Distributed deformation ahead of the Cocos-Nazca Rift at the Galapagos triple junction: Geochemistry, Geophysics, Geosystems, v. 12, Q11003, doi: 10.1029/2011GC003689.

Smithka, I.N., and Perfit, M.R., 2013, New Geochemical Analyses Reveal Crustal Accretionary Processes at The Overlapping Spreading Center Near 3N East Pacific Rise: Abstract OS43A-1882 presented at 2013 Fall Meeting, AGU, San Francisco, California, 9-13 December.

Sonnenthal, E.L., 1992, Geochemistry of dendritic anorthosites and associated pegmatites in the Skaergaard Intrusion, East Greenland: Evidence for metasomatism by a chlorine-rich fluid: Journal of Volcanology and Geothermal Research, v. 1-3, p. 209-230, doi: 10.1016/0377-0273(92)90141-Y.

Sours-Page, R., Johnson, K.T.M., Nielsen, R.L., and Karsten, J.L., 1999, Local and regional variation of MORB parent magmas: evidence from melt inclusions from the Endeavour Segment of the Juan de Fuca Ridge: Contributions to Mineralogy and Petrology, v. 134, p. 342-363, doi: 10.1007/s00410050489.

Sparks, R.S.J., Meyer, P., and Sigurdsson, H., 1980, Density variation amongst mid-ocean ridge basalts: Implications for magma mixing and the scarcity of primitive lavas: Earth and Planetary Science Letters, v. 46, p. 419-430, doi: 10.1016/0012-821X(80)90055-2.

Stolper, E., 1980, A Phase Diagram for Mid-Ocean Ridge Basalts: Preliminary Results and Implications for Petrogenesis: Contributions to Mineralogy and Petrology, v. 74, p. 13-27, doi: 10.1007/BF00375485.

Sun, S.-s., and McDonough, W.F., 1989, Chemical and isotopic systematics of oceanic basalts: implication for mantle composition and processes, in Saunders, A.D., and Norry, M.J., eds., Magmatism in the Ocean Basins: Geological Society Special Publication 44, p. 313-345.

Toomey, D.R., Purdy, G.M., Solomon, S.C., and Wilcock, W.S.D., 1990, The three-dimensional seismic velocity structures of the East Pacific Rise near latitude 9°30′N: Nature, v. 347, p. 639-645, doi: 10.1038/347639a0.

Valer, M., Bachelery, P., and Schiano, P., 2017, The Petrogenesis of Plagioclase-ultraphyric Basalts from La Reunion Island: Journal of Petrology, v. 58, p. 675-698, doi: 10.1093/petrology/egx030.

Voorhees, P.W., 1992, Ostwald Ripening of Two-Phase Mixtures: Annual Review of Material Science, v. 22, p. 197-215, doi: 10.1146/annurev.ms.22.080192.001213.

Wager, L.R., and Deer, W.A., 1939, Geological investigations in East Greenland, Part III. The petrology of the Skaergaard Intrusion, Kangerdlugssuaq, East Greenland: Meddelelser om Grønland 105, p. 1-352.

Wager, L.R., Vincent, E.A., and Smales, A.A., 1957, Sulphides in the Skaergaard intrusion, east Greenland: Economic Geology, v. 52, p. 855–903, doi: 10.2113/gsecongeo.52.8.855.

Wagner, C., 1961, Theorie der Alterung von Niederschlagen durch Umlosen: Zeitschrift fur Elektrochemie, v. 65, p. 581-591.

Wang, S., Yu, H., Zhang, Q., and Zhao, Y., 2018, Absolute plate motions relative to deep mantle plumes: Earth and Planetary Science Letters, v. 490, p. 88-99, doi: 10.1016/j.epsl.2018.03.021.

Wang, Z., and Becker, H., 2015, Abundances of Ag and Cu in mantle peridotites and the implications for the behavior of chalcophile elements in the mantle: Geochimica et Cosmochimica Acta, v. 160, p. 209-226, doi: 10.1016/j.gca.2015.04.006.

Wanless, V.D., and Behn, M.D., 2017, Spreading rate-dependent variations in crystallization along the global mid-ocean ridge system: Geochemistry, Geophysics, Geosystems, v. 18, p. 3016-3033, doi: 10.1002/2017GC006924.

Wanless, V.D., and Shaw, A.M., 2012, Lower crustal crystallization and melt evolution at mid-ocean ridges: Nature Geoscience, v. 5, p. 651-655, doi: 10.1038/ngeo1552.
Warren, J.M., 2016, Global variations in abyssal peridotite compositions: Lithos, v. 248-251, p. 193-219, doi: 10.1016/j.lithos.2015.12.023.

Wasylenki, L.E., Baker, M.B., Kent, A.J.R., and Stolper, E.M., 2003, Near-solidus Melting of the Shallow Upper Mantle: Partial Melting Experiments on Depleted Peridotite: Journal of Petrology, v. 44, p. 1163-1191, doi: 10.1093/petrology/44.7.1163.

Webster, J.D., Kinzler, R.J., and Mathez, E.A., 1999, Chloride and water solubility in basalt and andesite melts and implications for magmatic degassing: Geochimica et Cosmochimica Acta, v. 65, p. 729-738, doi: 10.1016/S0016-7037(99)00043-5.

Wendt, J.I., Regelous, M., Niu, Y., Hekenian, R., and Collerson, K.D., 1999, Geochemistry of lavas from the Garrett Transform Fault: insights into mantle heterogeneity beneath the eastern Pacific: Earth and Planetary Science Letters, v. 173, p. 271-284, doi: 10.1016/S0012-821X(99)00236-8.

White, W.M., and Klein, E.M., 2014, Composition of the Oceanic Crust: Treatise on Geochemistry, v. 4, p. 457-496, doi: 10.1016/B978-0-08-095975-7.00315-6.

White, W.M., McBirney, A.R., and Duncan, R.A., 1993, Petrology and geochemistry of the Galapagos Islands: Portrait of a pathological mantle plume: Journal of Geophysical Research Solid Earth, v. 98, p. 19533-19563, doi: 10.1029/93JB02018.

Wohlgemuth-Ueberwasser, C.C., Fonseca, R.O.C., Ballhaus, C., and Berndt, J., 2013, Sulfide oxidation as process for the formation of copper-rich magmatic sulfides: Mineralium Deposita, v. 48, p. 115-127, doi: 10.1007/s00126-012-0420-9

Workman, R.K., and Hart, S.R., 2005, Major and trace element composition of the depleted MORB mantle (DMM): Earth and Planetary Science Letters, v. 231, p. 53-72, doi: 10.1016/j.epsl.2004.12.005.

Xu, M., Canales, J.P., Carbotte, S.M., Carton, H., Nedimovic, M.R., and Mutter, J.C., 2014, Variations in axial magma lens properties along the East Pacific Rise (9°30′N-10°00′N) from swath 3-D seismic imaging and 1-D waveform inversion: Journal of Geophysical Research, v. 119, p. 2721-2744, doi: 10.1002/2013JB010730.

Yin, Y., and Zajacz, Z., 2018, The solubility of silver in magmatic fluids: Implications for silver transfer to the magmatic-hydrothermal ore-forming environment: Geochemica et Cosmochemica Acta, v. 238, p. 235-251, doi: 10.1016/j.gca.2018.06.041.

Yokoyama, T., Makishima, A., and Nakamura, E., 1999, Evalution of the coprecipitation of incompatible trace elements with fluoride during silicate rock dissolution by acid digestion: Chemical Geology, v. 157, p. 175-187, doi: 10.1016/20009-2541(98)00206-X.

Yudovskaya, M.A., Distler, V.V., Chaplygin, I.V., Mokhov, A.V., Trubkin, N.V., Gorbacheva, S.A., 2006, Gaseous transport and deposition of gold in magmatic fluid: evidence from the active Kudryavy volcano, Kurile Islands: Mineralium Deposita, v. 40, p. 828-848, doi: 10.1007/s00126-005-0034-6.

Yudovskaya, M.A., Tessalina, S., Distler, V.V., Chaplygin, I.V., Chugaev, A.V., and Dikov, Y.P., 2008, Behavior of highly-siderophile elements during magma degassing: A case study at the Kudryavy volcano: Chemical Geology, v. 248, p. 318-341, doi: 10.1016/j.chemgeo.2007.12.008.

Zajacz, Z., Candela, P.A., Piccoli, P.M., Sanchez-Valle, C., and Walle, M., 2013, Solubility and partitioning behavior of Au, Cu, Ag and reduced S in magmas: Geochimica et Cosmochimica Acta, v. 112, p. 288-304, doi: 10.1016/j.gca.2013.02.026.

Zajacz, Z., Halter, W.E., Pettke, T., and Guillong, M., 2008, Determination of fluid/melt partition coefficients by LA-ICPMS analysis of co-existing fluid and silicate melt inclusions: Controls on element partitioning: Geochemica et Cosmochemica Acta, v. 72, p. 2169-2197, doi: 10.1016/j.gca.2008.01.034.

Zellmer, G.F., Rubin, K.H., Dulski, P., Iizuka, Y., Goldstein, S.L., and Perfit, M.R., 2011, Crystal growth during dike injections of MOR basaltic melts: evidence from preservation of local Sr diseuilibria in plagioclase: Contributions to Mineralogy and Petrology, v. 161, p. 153-173, doi: 10.1007/s00410-010-0518-y.

Zheng, T., Lin, J., Schouten, H., Smith, D.K., Parnell-Turner, R.E., Tucholke, B.E., Cann, J.R., and Klein, E.M., 2019, Variations in crustal structure in the region of the Galapagos triple junction: Abstract T43F-0504 presented at 2019 Fall Meeting, AGU, San Francisco, California, 9-13 December.